Parameterization of Hurricane Surge for the State of Texas Coastline

Jennifer L. Irish
Texas A&M University

Final Report

prepared for
Texas General Land Office

October 10, 2009

Introduction to Report

Coastal hazard response requires a quick and reliable method for estimating hurricane surge. The Saffir-Simpson Hurricane Scale was developed in 1969 to provide weather forecasters and emergency planners with a simple method for estimating wind damage potential. This scale is based solely on estimated maximum wind speed within a hurricane. In spite of the narrow scope of its formulation, this scale has proven to be a reasonable indicator of hurricane wind damage. However, it is also important to quickly and reliably indicate storm surge, which requires consideration of storm size and regional geographic conditions.

A fundamental understanding of how the physical system responds, in an idealized sense, to various combinations of hurricane parameters serves two functions. First, it provides coastal managers and planners with additional information for assessing expected damages to CNRAs, including flood hazard areas, coastal features such as shore and dune areas, and wetlands. Second, it provides information to help improve existing prediction resources such as those provided by the SLOSH1 model or FEMA flood maps. Specifically, this information will provide a better understanding of possible surge generation limits for extreme events and of surge response in areas on the margins of numerical model basins or with unknown topography.

This project supported on M.S. student, one undergraduate student, and PI time to supervise additional students contributing to the outcomes of this work. The format of this reports is in the form of student theses chapters and journal papers. Specifically, the following items make up this report:

- **Part 1**: Irish, J.L., Resio, D.T., and Cialone, M.A., 2009, "A surge response function approach to coastal hazard assessment. Part 2: Quantification of spatial attributes of response functions," Nat. Hazards, Vol. 51, No. 1, 183-205.

- **Part 2:** Song, Y.K., 2009, “Extreme hurricane surge estimation for Texas coastal bridges using dimensionless surge response functions,” Masters Thesis, Texas A&M University. Chapters V through VII.

- **Part 3:** Katyal, R., 2009, “Development of parameterized surge response functions for coastal bays,” Masters Thesis, Texas A&M University. (Thesis supported by this grant).

- **Part 4:** Loder, N.M., Irish, J.L., Cialone, M.A., and Wamsley, T.V., 2009. "Sensitivity of hurricane surge to morphological parameters of coastal wetlands," Estuar. Coast. Shelf Sci., Vol. 84, 625-636.

- **Part 5:** Irish, J.L., Babbitt, C.W., 2009. “Hurricane surge primer.”

The following describes where information on each task is located within the report:

- Task 1. Develop and Validate ADCIRC Model – Idealized Scenario: Part 1

- Task 2. Select Hypothetical Storm Set and Develop ADCIRC Simulations – Idealized Scenario: Part 1, Part 2 (Chapter 5), and Part 3 (Chapter 4).

- Task 3. Analyze and Develop Surge Parameterization – Idealized Scenario: Part 1, Part 2 (Chapters 6 and 7), and Part 3 (Chapter 5.1).

- Task 4. Perform Simulations and Analyze Galveston Region – Complex Geometry Scenario: Part 3.

- Task 5. Develop and Provide Public and Agency Outreach: Part 5, the online surge primer is available at ceprofs.civil.tamu.edu/jirish, and copies of workshop presentations available upon request..

- Task 6. Prepare Documentation: all Parts.

Nat Hazards
DOI 10.1007/s11069-009-9381-4

ORIGINAL PAPER

A surge response function approach to coastal hazard assessment. Part 2: Quantification of spatial attributes of response functions

Jennifer L. Irish · Donald T. Resio · Mary A. Cialone

Received: 30 July 2008 / Accepted: 4 March 2009

Abstract In response to the 2004 and 2005 hurricane seasons, surge risk assessment approaches have been re-evaluated to develop more rapid, reliable methods for predicting the risk associated with extreme hurricanes. Here, the development of dimensionless surge response functions relating surge to hurricane meteorological parameters is presented. Such response functions present an opportunity to maximize surge data usage and to improve statistical estimates of surge probability by providing a means for defining continuous probability density functions. A numerical modeling investigation was carried out for the Texas, USA coastline to develop physical scaling laws relating storm surge response with hurricane parameters including storm size, intensity, and track. It will be shown that these scaling laws successfully estimate the surge response at any arbitrary location for any arbitrary storm track within the study region. Such a prediction methodology has the potential to decrease numerical computation requirements by 75% for hurricane risk assessment studies.

Keywords Storm surge · Coastal flooding · Coastal hazards · Tropical cyclones · Hurricanes · Risk assessment

List of symbols

ADCIRC	ADvanced CIRCulation model, a finite-element long-wave numerical model
B	Hurricane pressure profile peakedness parameter (Holland 1980)
c_p	Hurricane central barometric pressure, a measure of hurricane intensity
JPM	Joint probability method
JPM-OS	Joint probability method with optimal sampling
m_x	Location-dependent constant relating hurricane surge to intensity

J. L. Irish (✉)
Coastal and Ocean Engineering Division, Zachry Department of Civil Engineering,
Texas A&M University, College Station, TX 77843-3136, USA
e-mail: jirish@civil.tamu.edu

D. T. Resio · M. A. Cialone
Coastal and Hydraulics Laboratory, U.S. Army Engineer Research and Development Center,
Vicksburg, MS 39186, USA

Published online: 20 March 2009

R_{p}	Hurricane pressure radius, a measure of hurricane size
R_{thresh}	Threshold hurricane pressure radius for small storms
R'	Dimensionless hurricane pressure radius
X	Distance alongshore
x'	Preliminary dimensionless alongshore distance
$x_2{}'$	Dimensionless alongshore distance
x_{o}	Distance alongshore, x, at the eye location at landfall
$x_{\zeta_{\mathrm{peak}}}$	Distance alongshore, x, at the location of peak alongshore surge
(x, y)	Geographic position
$(x_{\mathrm{o}}, y_{\mathrm{o}})$	Geographic position of storm eye at landfall
Δp	Central pressure deficit
γ	Specific weight of water
λ	Constant relating location of peak alongshore surge to storm size
Φ	Dimensionless surge response surface
ϕ_{km}	Dimensional surge response function
ζ	Maximum hurricane surge at a given location (x, y)
ζ'	Dimensionless surge
ζ_{peak}	Peak alongshore surge
ζ_{sim}	Numerically simulated maximum hurricane surge at a given location (x, y)
ζ_{Φ}	Predicted maximum hurricanes surge at a given location (x, y) using surge response function

1 Introduction

Following the hurricane seasons of 2004 and 2005, the reliability of conventional methodologies for assessing flooding risk for extreme hurricane events has been brought into question. Resio et al. (2009) presented a comprehensive background and history on extreme-value statistics for coastal flooding and discussed their shortcomings when used to assess flooding. In order to overcome many of the shortcomings associated with existing statistical approaches, Resio et al. (2009) presented a new method for determining coastal flooding risk based upon the joint probability method (JPM) with optimal sampling (JPM-OS). This new approach allows for a more reliable estimate of extreme flood level risk, a better quantification of the uncertainty associated with these risk estimates, and a more efficient use of numerical analysis and historical observations. These benefits of the JPM-OS are derived from the proposed surge response function approach which suggests that a continuous surface for maximum surge (ζ) at a particular geographic location (x, y) for a given storm track angle with respect to the coastline k, storm forward speed m, and eye location at landfall $(x_{\mathrm{o}}, y_{\mathrm{o}})$ is given by:

$$\zeta(x, y) = \phi_{km}\left([x_{\mathrm{o}}, y_{\mathrm{o}}],\ [c_p, R_{\mathrm{p}}],\ [x, y]\right), \tag{1}$$

where ϕ_{km} is the dimensional surge response function for track angle k and forward speed m, c_p is the hurricane central pressure, and R_{p} is the hurricane pressure radius. The above definition for surge response allows for the development of a continuous, as opposed to discretized, probability density function from which flooding risk due to extreme coastal storms can be more accurately defined. This surge response surface approach also presents a means for optimally sampling the storm population in order to minimize computational

requirements for storm surge modeling studies for risk assessment, and for gleaning more information from historical observations.

The motivation for the investigation presented here is to show that surge response functions demonstrate continuous behavior with respect to both meteorological conditions and changes in coastal landscape, and that these surge response functions can be estimated based on a limited and discrete set of surge values.

The following sections first present an analysis of numerical surge simulation results for a regional coastline on the Gulf of Mexico to produce continuous surge response surfaces, then present a parameterization of the numerical results for use in estimating surge response functions from limited surge data.

2 Surge response surface development by numerical simulation

In order to verify the concept and validity of the surge response function approach, a numerical investigation was conducted for the northwestern Gulf of Mexico, along the coast of Texas. Below, the numerical modeling methodology and simulated storm surge results are discussed.

2.1 Numerical simulation methodology

Storm surges along the Texas coastline were computed using the finite-element long-wave numerical model ADCIRC (Westerink et al. 1992, 2007). The ADCIRC model domain included the entire Gulf of Mexico water body and the North Atlantic basin to 60°W longitude, and the domain highly resolved the entire northern Gulf of Mexico nearshore and inland bay system particularly along the Texas coast (Fig. 1). This numerical domain

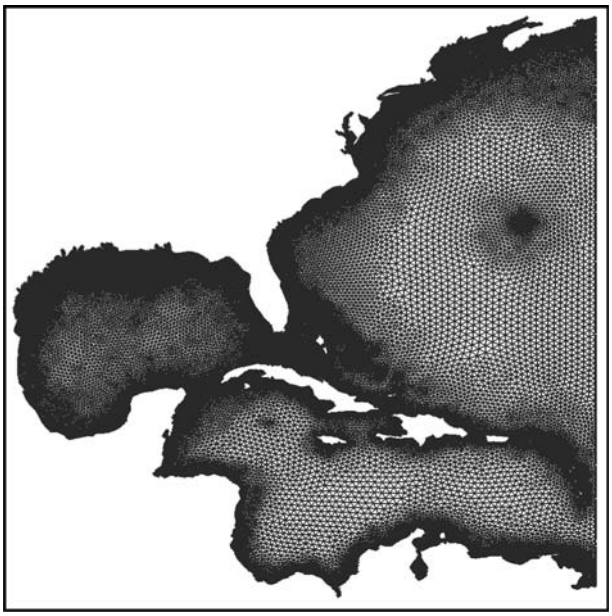

Fig. 1 ADCIRC computational domain

and associated calibration inputs were rigorously verified for surge simulation demonstrating accuracy well within 30 cm for most locations within inland bays and along the open coast throughout the northern Gulf of Mexico (U.S. Army Corps of Engineers 2006a, b). Storm surge modeled within ADCIRC for this investigation was forced with meteorological inputs for wind and barometric pressure fields. Tidal forcing and ocean wave setup, both of which can add to storm surge, are beyond the scope of this paper. Astronomical tide can typically be considered as a linear addition to surge level in many applications, and added surge level by wave-induced setup, which typically contributes much less to total flood level than wind-induced surge for high surge events, is anticipated to scale in a similar manner as the wind-induced surge considered here.

In order to develop surge response surfaces at multiple locations within a real coastal system, a parametric representation of tropical cyclone meteorology was adopted. Seeking a surge response surface in the form of Eq. 1, central pressure (c_p), storm size (R_p), storm forward speed (v_f), and peakedness B (Holland 1980), in conjunction with an assumed background pressure field, were used as input to a coupled hurricane vortex—planetary boundary layer (PBL) model (Thompson and Cardone 1996) to estimate sustained near-surface winds throughout the storm.

Hurricanes impacting the Texas coast may be divided into three classes: (1) those entering the Gulf of Mexico between Florida and Cuba which follow a northwesterly path, (2) those entering the Gulf of Mexico between Cuba and the Yucatan peninsula which follow a northwesterly path, and (3) those entering the Gulf of Mexico after passing over the Yucatan peninsula, or those forming initially within the Gulf of Mexico, which follow a north northeasterly path. This investigation focuses on four hurricanes of the first class, where the tracks are spaced 30 km apart. The selected hurricane tracks parallel each other and have track angles at landfall, with respect to the coastline, of less than 17° (Fig. 2). While storm track angle with respect to the coastline (Niedoroda et al. in review) and storm forward speed can alter maximum surge at the coast, in this investigation peak surge response to these parameters is not considered in order to simplify the analysis. Storm forward speed for all simulations was 5.7 m/s and represents a typical forward speed for hurricanes in the Gulf of Mexico (Dorst 2007). We acknowledge, however, that in more northern locations (such as the mid-Atlantic and Northeast coasts of the U.S.), the historical record shows average hurricane forward speeds to be greater than 5.7 m/s (Dorst

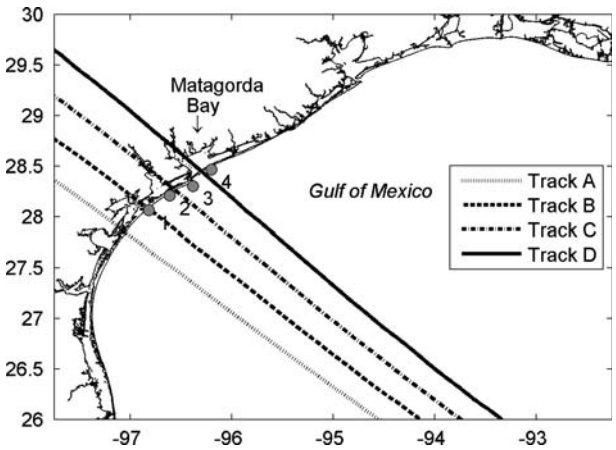

Fig. 2 Location map showing hurricane tracks considered in this analysis and sample output locations

2007). By holding track angle and hurricane forward speed constant, specific application of the results presented here will be limited in applicability to the track angles and storm forward speed considered here.

Sensitivity to variation in storm peakedness (Holland B), from 0.9 to 1.9, was evaluated with ADCIRC and demonstrated only small changes in peak surge, on the order of 15%. As such, surge variation with storm peakedness was not considered further in this investigation. Instead, Holland B for all simulations was held constant at 1.27 until the last 50 km before landfall at which point Holland B was decreased linearly to a value of 1.00 at landfall. These values for Holland B represent typical hurricane conditions in the Gulf of Mexico.

Multiple parameterized storms for simulation were created for each track by varying hurricane intensity (c_p) from 900 to 960 mb and size (R_p) from 11 to 65 km. Surges for a minimum of 17 storm intensity and storm size combinations were simulated for each track, with additional simulations added as needed to verify trends in surge response surfaces. In all, 75 numerical storm surge simulations were executed and evaluated.

2.2 Impact of hurricane intensity and size on surge magnitude and extent

For each simulation, modeled hurricane surge along the open coast was analyzed to determine the impact of both hurricane intensity and hurricane size on surge magnitude and on the distribution of surge along the coast. Figures 3 and 4 show the alongshore

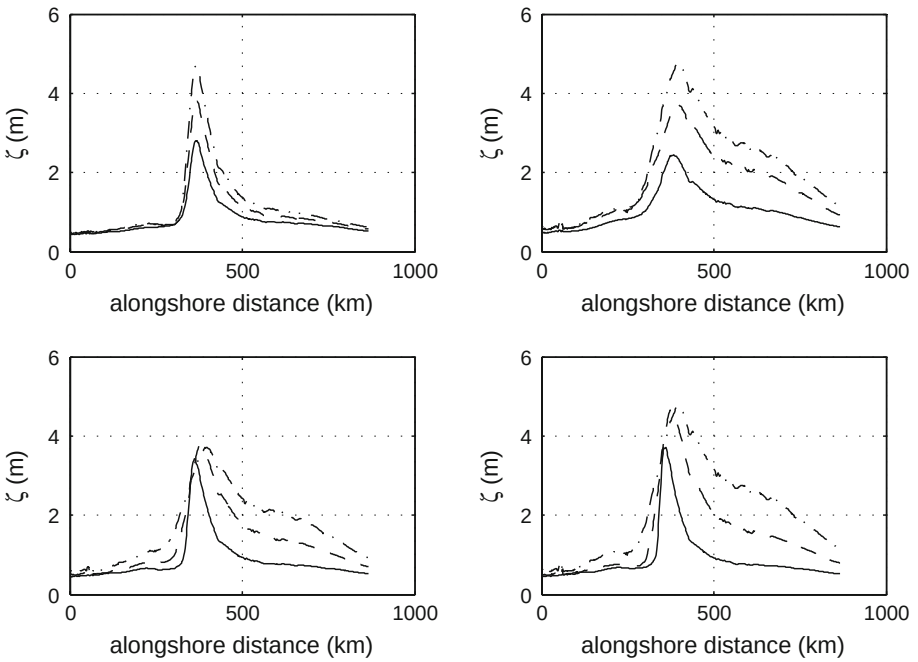

Fig. 3 Numerically simulated surge variation alongshore for selected storms on Track A. Top panes show surge variation with intensity [c_p = 960 mb (*solid*), 930 mb (*dashed*), and 900 mb (*dash-dot*)] when size R_p = 20.4 km (*top left*) and 65.9 km (*top right*); bottom panes show surge variation with size [R_p around 15 km (*solid*), 30 km (*dashed*), and 65 km (*dash-dot*)] when intensity c_p = 930 mb (*bottom left*) and 900 mb (*bottom right*)

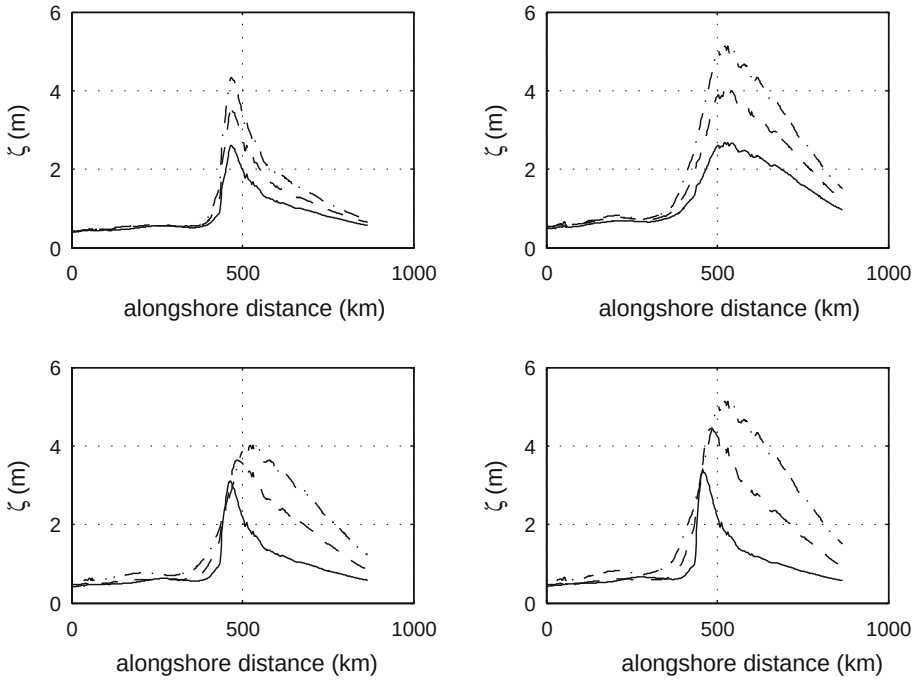

Fig. 4 Numerically simulated surge variation alongshore for selected storms on Track D. Top panes show surge variation with intensity [$c_p = 960$ mb (*solid*), 930 mb (*dashed*), and 900 mb (*dash-dot*)] when size $R_p = 20.4$ km (*top left*) and 65.9 km (*top right*); bottom panes show surge variation with size [R_p around 15 km (*solid*), 30 km (*dashed*), and 65 km (*dash-dot*)] when intensity $cp = 930$ mb (*bottom left*) and 900 mb (*bottom right*)

distribution of hurricane surge for selected simulations on Tracks A and D, respectively. The top panes in both figures, where hurricane size is held constant, demonstrate that the peak alongshore surge uniformly increases with increasing hurricane intensity. For small to moderately sized storms (top left panes), peak alongshore surge increases about 30 cm per 10 mb of intensification. Large storms result in a relatively large rate of increase of peak surge; for large storms (top right panes), peak alongshore surge increases about 40 cm per 10 mb. The top panes of Figs. 3 and 4 also show that the alongshore distribution from one intensity to the other is similar in shape and generally scales with peak alongshore surge.

The bottom panes of Figs. 3 and 4, where hurricane intensity is held constant, show that as hurricane size increases hurricane surge tends to increase as well (Irish et al. 2008). As hurricane size increases from small (10–15 km) to moderate (20–30 km), the largest relative rise in peak alongshore surge is observed on all Tracks, between 0.5 and 1.0 m per 10 km increase in R_p. As storm size continues to increase, the simulation results indicate that the relative rise in peak alongshore surge is milder, increasing up to 20 cm per 10 km. Unlike with intensity, the relative location of landfall appears to govern the degree to which surge increases with hurricane size. For example, along Track D peak alongshore surge gradually rises for all storm sizes. In contrast, along Track A peak alongshore surge rises initially with increasing size then appears to stabilize. This is most probably related to the relative size of the hurricane with respect to the continental shelf width. The cross-shore shelf width along and to the north of Track A is narrower than the cross-shore shelf width along and to the northeast of Track D. Therefore, for Track D the relatively large

shallow shelf region provides a larger area over which surge may be generated during larger storms.

From a regional risk-assessment perspective, the alongshore extent of elevated surge levels is important. Figures 3 and 4 demonstrate that for larger hurricanes the extent of high surge levels increases substantially with increasing size for all tracks and all storm intensities. For example, the alongshore extent of surge levels over 2 m increases by 20–100% per 10 km increase in R_p. This elevated surge along the coast is most dramatic to the right of hurricane landfall, as expected.

2.3 Simulated surge response surfaces

For each of the four tracks, surge response surfaces by track were developed at four locations at 10-m depth along the open coast (Fig. 5) based on hurricane meteorological characteristics taken ~165 km from landfall. In all cases, surge for a given storm track at a particular location varies relatively smoothly with changes in both hurricane intensity and hurricane size. In the vicinity of the landfall location and point of peak alongshore surge

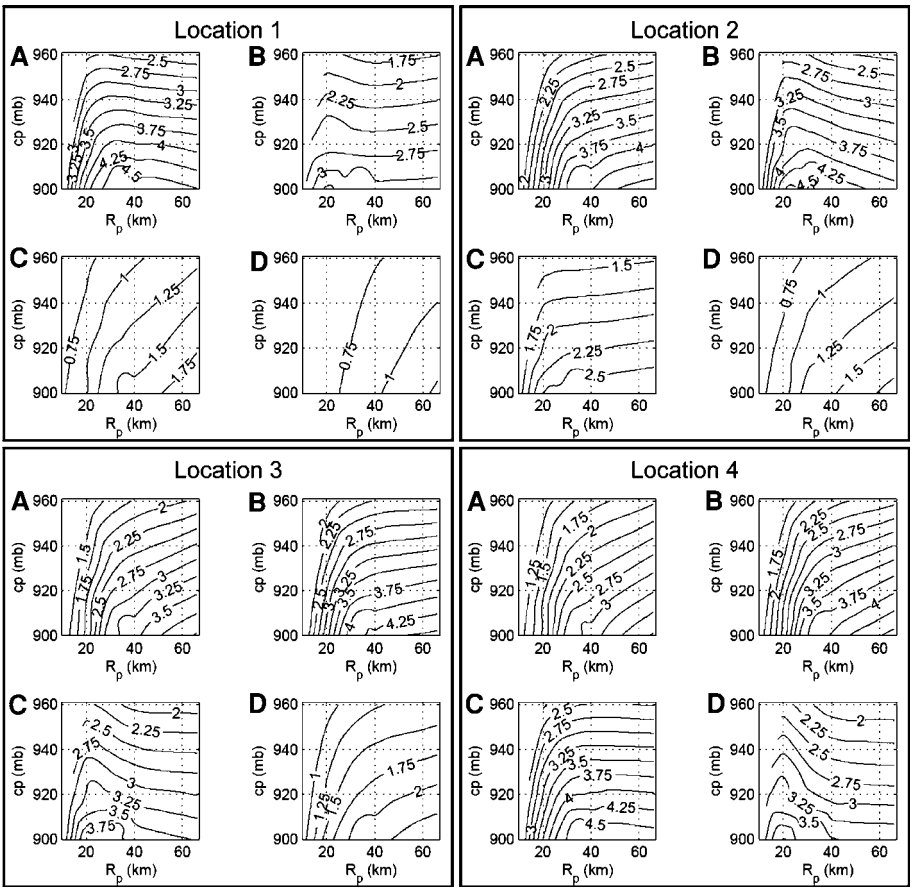

Fig. 5 Numerically simulated surge response surfaces at locations 1 through 4 (see Fig. 2) for all storms on Tracks A through D. Peak surge contours shown at 0.25-m intervals

(Fig. 5; Locations 1 and 2 for Track B, Location 3 for Track C, and Location 4 for Track D), the surge response surfaces have somewhat complex characteristics. In particular, the influence of storm size yields a positive bulge, or ridge, in the surge response surface for small storms for locations close to the landfall location. Further to the right of the landfall location, this bulge becomes relatively less peaked (Fig. 5; e.g., Location 1 for Track A) as the influence of storm size more broadly impacts the response surface at a distance on the order of one times the storm radius from the landfall location. This influence becomes less pronounced at a distance on the order of 1.5 times the storm radius to the right of the landfall location (Fig. 5; e.g., Location 2 for Track A and Location 3 for Track B).

Beyond this distance, the surge response surfaces vary more gradually with both storm intensity and size. Well to the right of the landfall location and point of peak alongshore surge (Fig. 5; e.g., Locations 3 and 4 for Track A and Location 4 for Track B), the surge response surfaces exhibit monotonically increasing surge values with both increasing storm size and increasing storm intensity. Furthermore, at these locations surge varies almost linearly with storm intensity for a given storm size, thus indicating that a small sample of storms can adequately define these surge response surfaces (Fig. 6). Locations to the left of the storm track, away from the landfall location, also exhibit uniformly increasing surge with both increasing storm size and intensity (Fig. 5; e.g., Locations 1, 2, and 3 for Track D).

When considering the surge response surface variation with track for a given alongshore location, storm size dictates which track yields a more severe surge level. At an alongshore location just to the right of Track B (Location 2 on Fig. 5), Track B's surge response surface yields the largest surge for all small to moderately sized storms. However, the surge response surface for Track A at this same location, which tracked about 50 km to the left of Location 2, demonstrates larger surges than Track B when storm size is very large.

The characteristic shapes described above for these numerically simulated surge response surfaces suggest that these surfaces may be reasonably described by a few storm parameters. The following section describes an approach for parameterizing the surge

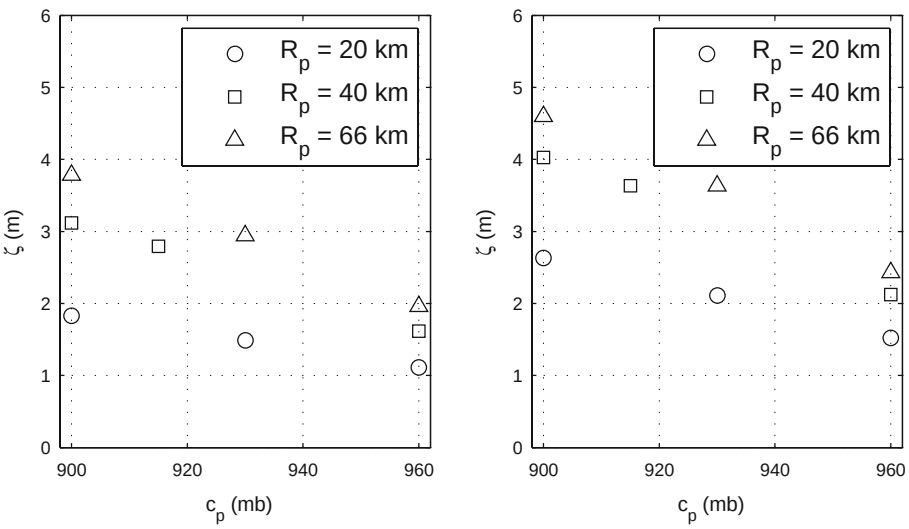

Fig. 6 Central pressure versus numerically simulated surge at Location 4 (see Fig. 2) for selected storms on Tracks A (*left pane*) and B (*right pane*)

response surfaces as a means to optimize numerical simulations and subsequent data analysis.

3 Surge response function estimation

Numerical storm surge simulations are highly computationally intensive with one individual storm simulation requiring more than 1,000 h of CPU time (based on simulations made on a Cray XT3 and on a Linux cluster). In addition, the physics solved within the surge model itself becomes more and more complex as effects due to waves, inland runoff, and morphodynamic change are dynamically coupled with the hydrodynamic model in order to achieve a higher degree of accuracy in the simulated surge estimate. Compounding the computational time requirements is the necessity for comprehensive coverage of all storm parameters to effectively implement traditional JPM-type extreme value statistics methods. Typically, such studies require an array of storm track orientations with a sequence of tracks spaced about 25 km apart per orientation. Thus, from a practical standpoint, the number of individual storm surge simulations required for a coastal flood risk-assessment study must be minimized.

In this section, physical scaling laws are introduced which cast the surge response into a dimensionless form in a way that lends itself to better interpolation of surge response for storm scenarios not explicitly represented by the simulated storm set.

3.1 Physical scaling laws for hurricane surge response

At a given alongshore location for a given storm track, the numerically simulated results suggest that storm surge at a location of interest scales with storm intensity and size and with proximity to the eye location at landfall. Using the numerically simulated surge values, a dimensionless surge response function was developed. First, an analysis of simulated surges demonstrated a strong correlation, with R^2 of 0.85 for all tracks, between storm size and distance between the location of peak alongshore surge and the eye location at landfall (Fig. 7). For all tracks, the numerical results also indicate that this distance between peak surge $\left(\zeta_{\text{peak}}\right)$ and storm eye can, to first order, be described by a linear function of storm size with slope, λ:

$$x_{\zeta_{\text{peak}}} - x_{\text{o}} \cong \lambda R_{\text{p}}, \tag{2}$$

where x is taken as distance measured along an axis running alongshore (Fig. 2) such that $x_{\zeta_{\text{peak}}}$ is the distance alongshore to the location of peak alongshore surge and x_{o} is the distance alongshore to the eye location at landfall. This relationship may also be used to determine the relative distance between an alongshore location of interest and the location of peak surge $\left(x - x_{\zeta_{\text{peak}}}\right)$. By performing a linear regression on the numerically simulated surges, the slope for all storms on all tracks was determined to be $\lambda = 0.87$. Average percent error for the numerically simulated distance between eye location at landfall and peak alongshore surge with respect to that distance predicted with Eq. 2 is better than 17% (calculated as the difference between the simulated and predicted values normalized by the simulated value). It should be noted, however, that the error in the predicted estimate can readily be accounted for in the uncertainty term in the JPM-OS approach to extreme-value statistics (Resio et al. 2009).

The numerically simulated surges (see Figs. 3, 4) suggest that the alongshore distribution of surge, when normalized by ζ_{peak}, decreases consistently with distance from $x_{\zeta_{\text{peak}}}$,

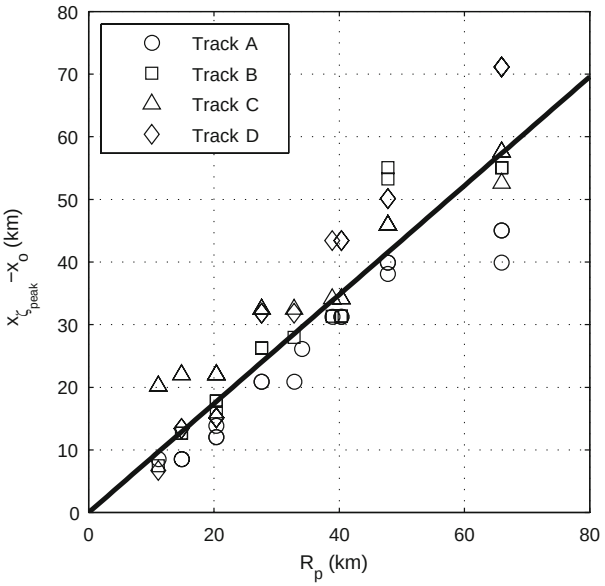

Fig. 7 Numerically simulated alongshore location of peak surge versus storm size for all simulated storms

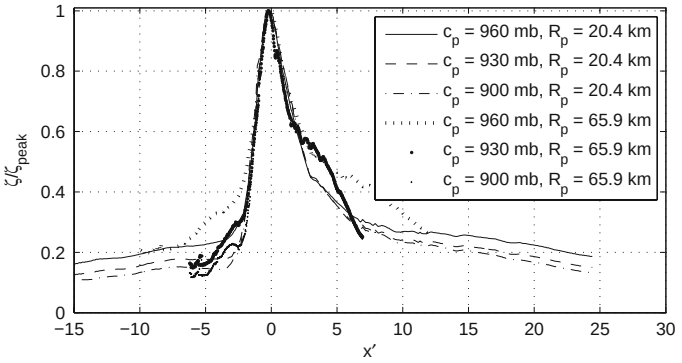

Fig. 8 Numerically simulated dimensionless alongshore surge distribution for selected storms on Track A

when alongshore distance is normalized by storm size (Fig. 8). For extreme-value statistics, the surge levels of interest are those at or near the peak surge value, and the normalized surge distribution for all simulated storms closely align when surge levels are >60% of the peak alongshore surge. Thus, a dimensionless alongshore dimension (x') is introduced:

$$x' = \frac{(x - x_o)}{R_p} - \lambda. \tag{3}$$

In order to develop a dimensionless surge parameter which is independent of surge at other locations e.g., (ζ_{peak}), a dimensionless surge (ζ') as a function of ζ at the location of interest (x) and c_p is defined as:

$$\zeta' = \frac{\gamma\zeta}{\Delta p} + m_x \Delta p, \tag{4}$$

where Δp is the pressure differential between the far-field barometric pressure and c_p, γ is specific weight of water, and m_x is a location-dependent constant determined by linear regression. From a physical perspective, the first term in Eq. 4 represents to first order the momentum balance for surge generation, where Δp can be considered proportional to wind speed squared. The second term in Eq. 4 can be considered representative of additional wind drag effects. Based on the numerical simulations and Texas locations considered here, values for m_x vary from 0.007 to 0.012 mb^{-1} (for Δp in mb).

Figure 9 shows the dimensionless surge response function for Locations 1 through 4 based on the dimensionless parameters ζ' and x' as defined by Eqs. 3 and 4. This figure shows that these two dimensionless parameters largely describe the surge response, by collapsing the dimensionless surge (ζ') into a single surge response function. Consider Location 1, which is located at the landfall location of Track B and well to the southwest of Tracks B and C and about 25 km to the northeast of Track A. At this location, all storms with $x' < 0$ follow the same response distribution while all storms at $x' = 0$ collapse to a single value of ζ'. Location 2, located just southwest of Track C and centered among the other tracks, similarly exhibits a single alongshore response distribution when $x' < 0$. Additionally, ζ' at Location 2 follows the same alongshore distribution for all storms when $x' > 0$. However, at Location 2 some scatter is evident near the peak of the distribution, around $x' = 0$.

At Location 3, however, there are a few notable exceptions which do not follow a single alongshore distribution. These storms, marked by circles in Fig. 9, are those storms which are relatively small and make landfall just southwest of Location 3 (Track C). These storms further coincide with the bulge, or ridge, observed in the surge response surface for Track C (Fig. 5, bottom left pane). From the simulated data, it is evident that there is a secondary effect related to the relative landfall proximity of small storms. By inspection of the simulated data (see location of ridge features in Fig. 5), a natural size threshold (R_{thres}) for the Texas location considered here for defining "small storms" is $R_{\text{p}} < 25$ km. In order to quantify this secondary effect, all storms with $R_{\text{p}} < R_{\text{thres}}$ and $-\lambda < x' < \lambda$ were identified (circled storms on Fig. 5) and compared to the dimensionless distributions presented in Fig. 5. In order to collapse this class of storms into the existing surge response function, a revised dimensionless alongshore dimension (x_2') was defined:

$$x_2' = x' - F(1 - R')H(1 - R'), \tag{5}$$

where $R' = R_{\text{p}}/R_{\text{thres}}$ is the dimensionless hurricane size, $H(1 - R')$ is the Heaviside function ($H(x) = 1$ for $x \geq 0$ and $= 0$ for $x < 0$), and $F(1 - R')$ is a ramp function defined as:

$$F(1-R') = \begin{array}{ll} a_1(1-R') + b_1, & -\lambda \leq x' \leq 0, \\ a_2(1-R') + b_2, & 0 < x' \leq \lambda \\ 0, & \lambda < |x'|. \end{array}, \tag{6}$$

The coefficients a and b of this ramp function were determined by linear regression between the quantity $(1 - R')$ and the difference between the initial value of x' and the corresponding value of x' on the existing surge response function, where ζ' is kept constant (Fig. 9). In Eq. 6, the division into three ranges can be seen on Fig. 9. Small storms making landfall just to the southwest of the location (circles with $x' < 0$ in Fig. 9, bottom panes) are adjusted using the $a_1 - b_1$ ramp function, while small storms making landfall

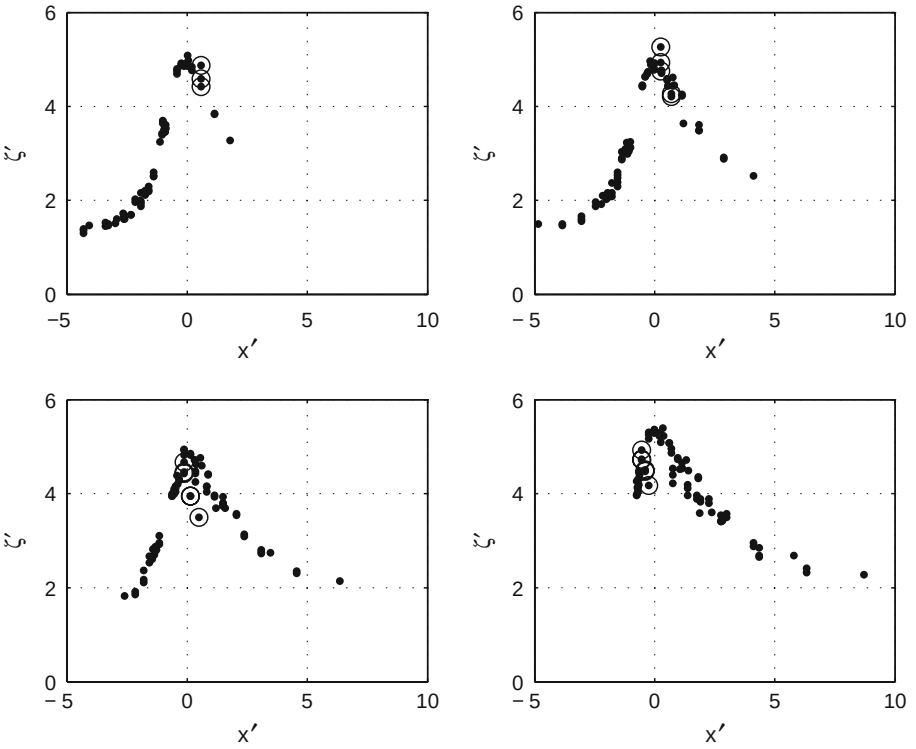

Fig. 9 Preliminary dimensionless surge response functions using all simulated storms on all four tracks for Locations 1 (*top left*), 2 (*top right*), 3 (*bottom left*), and 4 (*bottom right*). Circled storms are those with $R_p < 25$ km and $-\lambda < x' < \lambda$

just to the northeast of the location (circles with $x' > 0$ in Fig. 9, top panes) are adjusted using the $a_2 - b_2$ ramp function. Based on the full suite of numerical simulations, the coefficient values for this stretch of the Texas coast were determined to be $a_1 = -1.04$, $b_1 = 0.16$, $a_2 = 3.29$, and $b_2 = -0.67$.

Figure 10 shows the revised dimensionless relationships defined by ζ' versus $x_2{}'$. As this figure shows, the surge response is almost completely described by this new function, where the anomalous small storms now align with the rest of the distribution. While there is some scatter evident when $x' > 0$, the general trend is made clear. This small amount of scatter is most likely attributed to the combined effect of hurricane size and regional geometry, namely continental shelf width and orientation, and shoreline orientation.

It is worth noting that from location to location within the study area, the response function shape and magnitude along the open coast varies slowly. This indicates that in areas with slowly varying geographic features, interpolation of surge between locations for which surge data are available (e.g., water level measurement locations) to a reasonable degree of accuracy should be possible. It is important, however, to recognize that the response function shape and magnitude will likely vary more substantially within coastal embayments, so care should be given when interpolating between locations if using historical observations collected within coastal bays. Conversely, a response function developed from historical data at any given location (even within a coastal embayment)

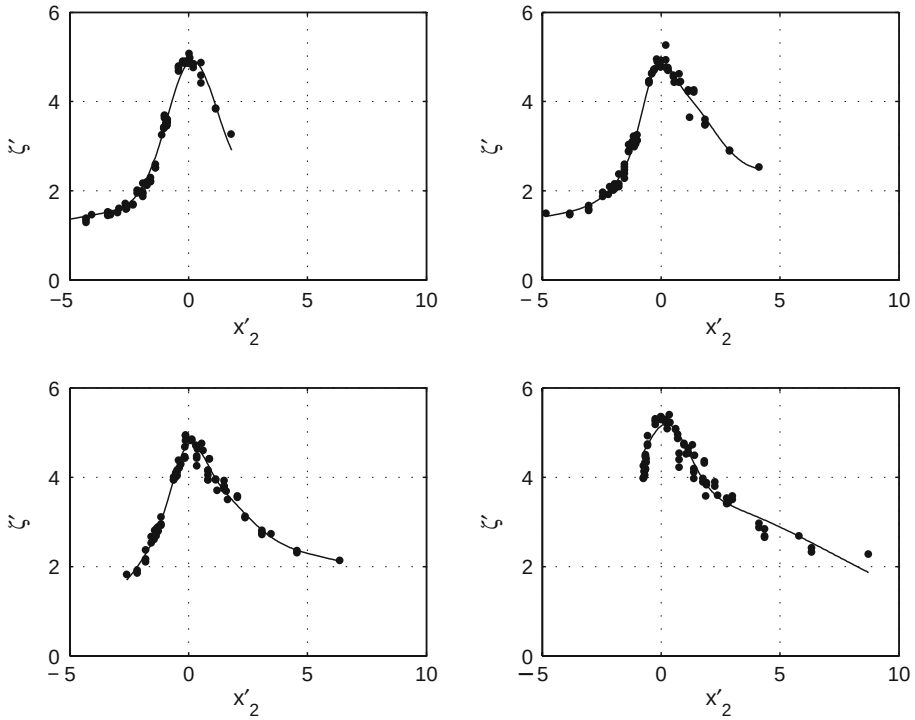

Fig. 10 Dimensionless surge response functions using modified dimensionless alongshore parameter and using all simulated storms on all four tracks for Locations 1 (*top left*), 2 (*top right*), 3 (*bottom left*), and 4 (*bottom right*). Solid line shows 3-term Gaussian fit to data

can be expected to perform well for estimating the surge response at that location for any hurricane event.

Equations 4 through 6 provide a means for predicting surge response functions from limited data, and as will be shown below, these relationships effectively predict surge response for storms not explicitly represented by numerical simulations.

3.2 Response function prediction from limited data

In this section, we examine the use and accuracy of dimensionless surge response functions developed from limited surge data sets to predict surge response over a range of conditions in order to optimize numerical simulations and to maximize the knowledge gained from field measurements. Specifically, we will consider spatial data sets limited by track spacing and range of c_p and data sets limited by spatial coverage. The dimensionless surge response functions (Φ) developed from the 75 numerically simulated surges appear to be generally described by a Gaussian distribution in the form:

$$\Phi\left(x_2'\right) = a_1 e^{-\left(\frac{x_2'-b_1}{c_1}\right)^2} + a_2 e^{-\left(\frac{x_2'-b_2}{c_2}\right)^2} + a_3 e^{-\left(\frac{x_2'-b_3}{c_3}\right)^2}, \tag{7}$$

where a_1, b_1, c_1, a_2, b_2, c_2, a_3, b_3, and c_3 are curve-fitting coefficients determined by least-squares regression. As seen in Fig. 10, the Gaussian distributions reasonably represent the numerically simulated data, where R^2 values for these curve-fits are between 0.97 and 0.99

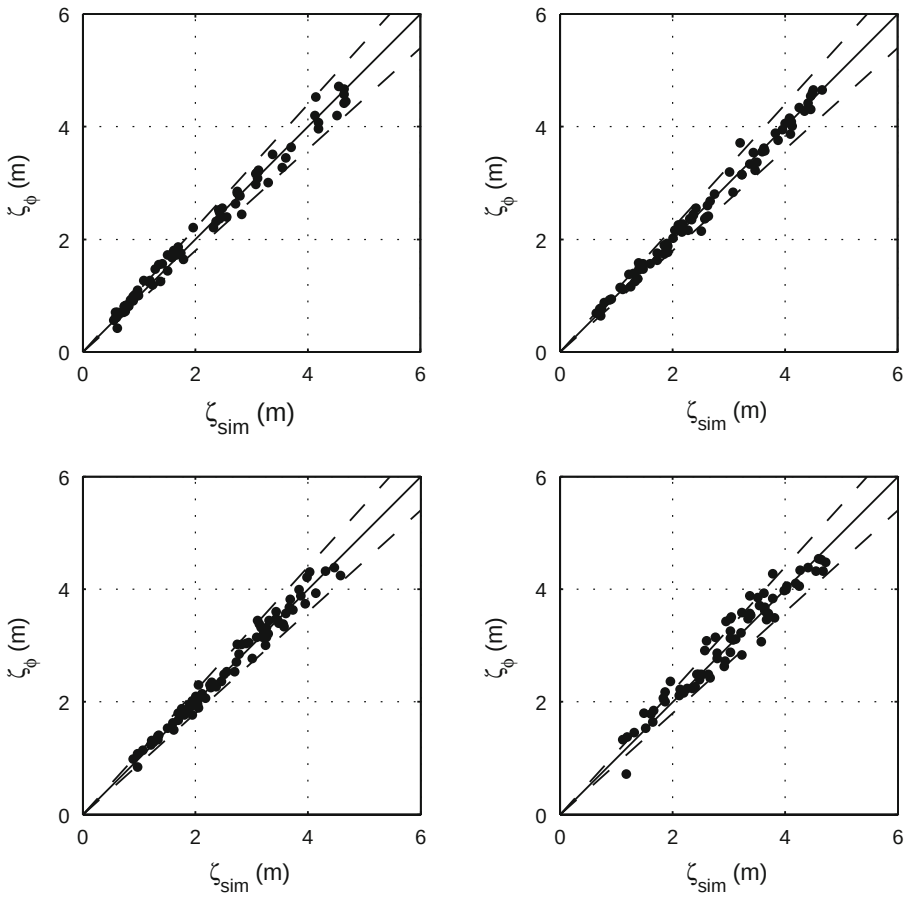

Fig. 11 Predicted surge using curve-fitted surge response function, based on all four tracks, versus numerically simulated surge at Locations 1 (*top left*), 2 (*top right*), 3 (*bottom left*), and 4 (*bottom right*). Solid line indicates an exact match while dashed lines indicate ±10% about an exact match

at Locations 1 through 3 and 0.91 at Location 4. To test the skill of Φ for surge response estimation, we first used the curve-fitted function of Eq. 7 was used to estimate surge (ζ_Φ) based on the suite of 75 meteorological input parameter combinations, namely $R_p - c_p - x_o$ sets. These estimated surges were then compared with the numerically simulated surges (ζ_{sim}, Fig. 11). At all locations, the mean ($\zeta_\Phi - \zeta_{sim}$) errors are between 0 and +4 cm (Table 1) and can be considered negligible, given expected error in the surge simulations on the order of 20–30 cm. At Locations 1 through 3, root-mean-square (RMS) error in ζ_Φ is between 13 and 14 cm while RMS error at Location 4 is somewhat larger, 24 cm. The RMS errors in ζ_Φ are the same order of magnitude as the expected simulation error (typically 20–30 cm) and for risk-analysis can be accounted for through an uncertainty term.

3.2.1 Limited number of discrete storm tracks

Next, the case where simulated surge data are available for a limited number of tracks was examined by considering an increase in track spacing from 30 km (0.25°) to 60 km (0.50°)

Table 1 Error statistics for surge prediction using surge response functions

Track spacing (km [°])	Tracks included	Statistics for storms within bounds of included data for all locations (range)			Statistics for all 75 storms for all locations (range)		
		Mean error [% mean error] (cm)[a]	RMS error [% RMS error] (cm)[a]	R^2	Mean error (cm)[a]	RMS error (cm)[a]	R^2
30 [0.25]	A, B, C, D (baseline)	+2 [+1.2] (0 to +4)	16 [7.3] (13 to 24)	0.97 (0.94–0.99)	All storms within data bounds		
60 [0.50]	A, C	−2 [−5.1] (−9 to +4)	15 [5.7] (10–19)	0.98 (0.97–0.99)	−4 (−15 to +6)	28 (10 to 43)	0.94 (0.91 to 0.99)
	B, D	+4 [+2.2] (+0 to +8)	19 [7.5] (11–25)	0.96 (0.92–0.98)	+12 (0 to +30)	43 (19 to 106[b])	0.89 (0.70[b] −0.97)
90 [0.75]	A, D	−6 [−1.0] (−16 to +9)	22 [7.7] (15–30)	0.96 (0.94–0.99)	All storms within data bounds		
90 [0.75]	A, D when $c_p = 900$ and 960 mb only	−6 [−2.7] (−17 to +10)	23 [8.4] (16–32)	0.97(0.94–0.99)	All storms within data bounds		
Spatial interpolation using Locations 1 and 4 to predict Locations 2 and 3 (Loc 2, Loc 3)		+20 [5.5], +23 [7.4]	27 [7.6], 32 [10.2]	0.95, 0.92	+25, +2	61, 71	0.83, 0.76

[a] Data in parenthesis () give range of error at all four locations, in cm

[b] Larger error values are associated with those locations without data coverage for $x_2' > 0$

Fig. 12 Dimensionless surge response functions using simulated storm surge for the 60-km spacing cases of Tracks A and C only (top pane) and Tracks B and D only (bottom pane). Within each pane are Locations 1 (*top left*), 2 (*top right*), 3 (*bottom left*), and 4 (*bottom right*). Solid line shows 3-term Gaussian fit to data ▶

and 90 km (0.75°). Figures 12 and 13 show the simulation data points and corresponding Φ curve-fit for these more sparsely spaced track conditions while Figs. 14 and 15 show the predicted ζ_Φ versus ζ_{sim} for these cases. For the 60-km spacing case using Tracks A and C (Figs. 12 and 14, top panes), at Locations 1 through 4 the simulated data points span a range of x_2' from negative, to near-zero, to positive, thereby providing sufficient information for curve-fitting, particularly in the region of highest surge potential $\left(x_2' \approx 0\right)$. The resulting ζ_Φ predictions yield error magnitudes (average mean error = −4 cm and average RMS error = 28 cm, Table 1) similar in order-of-magnitude to those characterizing the predictions with the full four-track suite of simulated data. Similar magnitudes of error are also observed for the ζ_Φ predictions for the 60-km Tracks B and C case at Locations 2 through 4 (Figs. 12 and 14, bottom panes, and Table 1). However, at Location 1 for the Tracks B and C cases more error is introduced, particularly for the more extreme surge levels. This is primarily a consequence of no data coverage about the peak of the surge response function distribution $\left(x_2' \approx 0\right)$ and secondarily a consequence of no data coverage when $\left(x_2' < 0\right)$. In other words, the response function is not as well represented when data are not available for storms tracking to the right of the location of interest, in the range $x_2' \geq 0$. However, it is anticipated, based on the results for the Tracks A and C case, that the addition of simulations along a track 60 km to the south of Location 1 should provide sufficient information for response function development.

For the case when two tracks spaced 90 km apart (Tracks A and D) are used to develop Φ and predict ζ_Φ (Figs. 13 and 15), at Locations 1 through 3 values of x_2' span a range from negative to positive, including simulated data near $x_2' = 0$. At these locations, the resulting ζ_Φ predictions yield error magnitudes (average mean error = −6 cm and average RMS error = 22 cm, Table 1) similar in order-of-magnitude to those characterizing the predictions with tracks spaced every 30 or 60 km. At Location 4, while values of x_2' do span from negative to positive there is a noticeable gap in x_2' coverage near the peak of the Φ distribution $\left(x_2' \approx 0\right)$. Unlike at Location 1 for the 60-km Tracks B and D case, here there are simulated data points available to either side of $x_2' = 0$. By estimating the peak value of ζ' at $x_2' = 0$, a Gaussian fit in the form of Eq. 7 which has a peak near $x_2' = 0$ may be developed. Here, this false data point was represented by the average between the linearly extrapolated values of ζ' using the available simulated ζ' values in the regimes $x_2' < 0$ and $x_2' > 0$. The resulting Φ curve-fits shown in Fig. 13 (bottom right), and Fig. 14 (bottom right) indicate that this extrapolation procedure shows promise for response function development in locations where data for most extreme surge values are not available. At Location 4, this modified curve-fit for Φ results in a surge prediction with mean and RMS errors of −16 and 30 cm.

The above analysis indicates that a numerical simulation set with tracks spaced at least 90 km apart, possibly more, is sufficient for predicting surge response at any open coast location between tracks. With track spacing increased from 30 km (0.25°) to 90 km (0.75°), the number of numerical simulations are reduced by half, from 75 to 38.

3.2.2 Limited number of discrete storm intensities

In this section, the accuracy of Φ and related surge predictions (ζ_Φ) was evaluated when the number of unique storms on each track is also limited. Since it is desirable to consider a

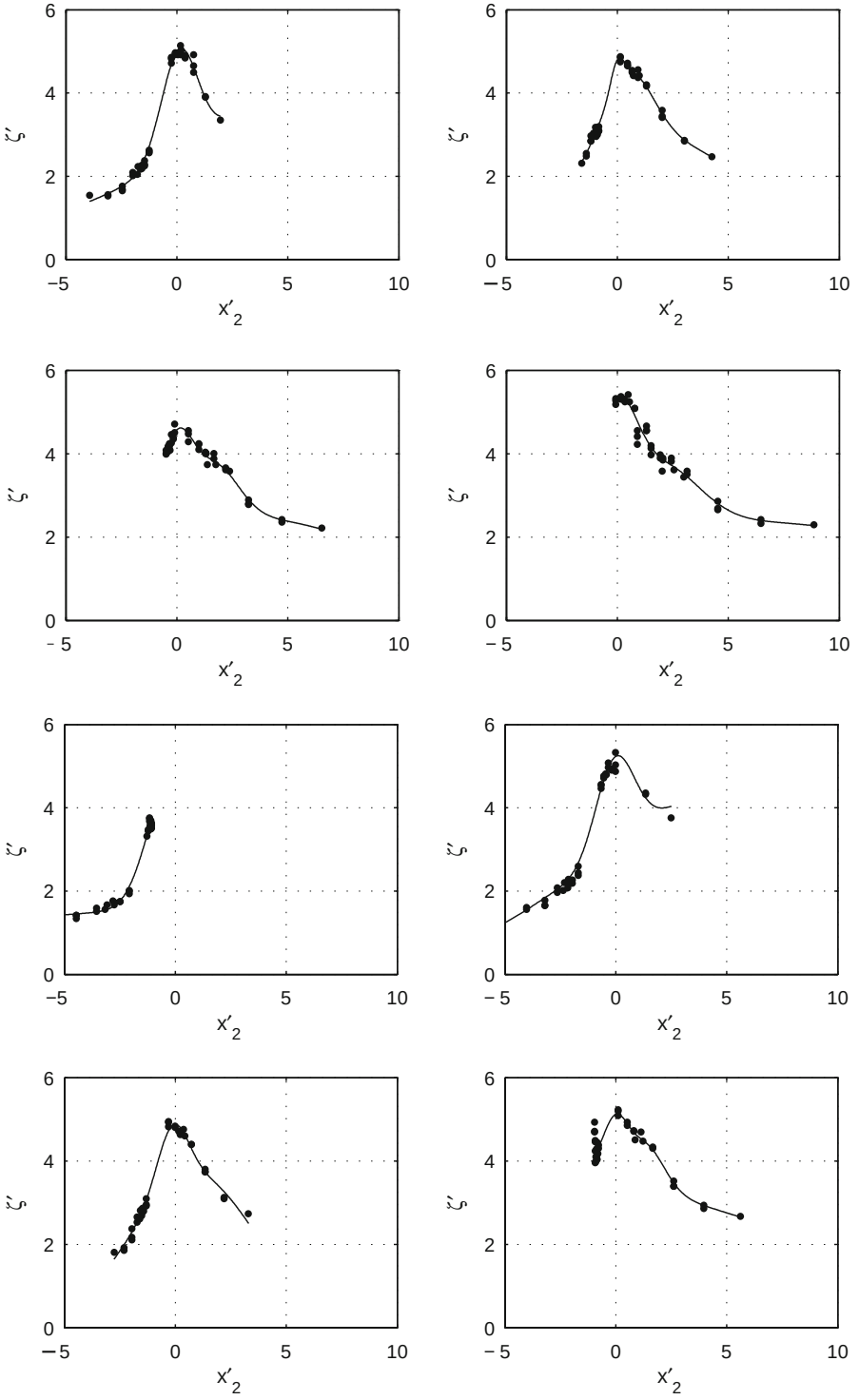
6
4
2
0
−5
0
5
10
ζ′
x′2

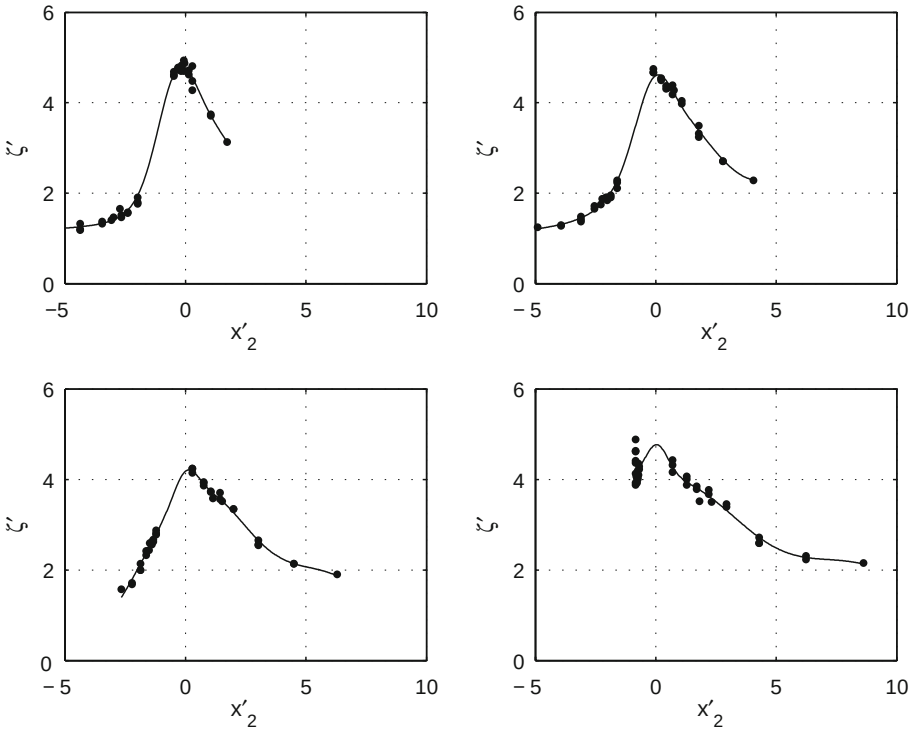

Fig. 13 Dimensionless surge response functions using simulated storm surge for Tracks A and D only (90-km spacing). Within each pane are Locations 1 (*top left*), 2 (*top right*), 3 (*bottom left*), and 4 (*bottom right*). Solid line shows 3-term Gaussian fit to data

range of x_2' values (or R_p values), here the along-track storm set is reduced by considering a limited set of c_p. Choosing the subset of simulated storms on Tracks A and D when $c_p = 900$ or 960 mb results in the response function and surge predictions shown in Figs. 16 and 17. It is worth noting that while the combined storm set on Tracks A and D was reduced by more than half, from 38 storms (Figs. 13 and 15) to 18 storms (Figs. 16 and 17), the response function and prediction accuracy (Table 1) is remarkably similar between these cases. This analysis shows that numerical simulations can be optimized by limiting both the number of tracks and the number of intensity scenarios considered. Here, the total realized computational reduction was 75%.

3.2.3 Limited spatial information

For many engineering investigations, budget and time constraints limit surge data analysis to interrogation of historical water level gauge measurements or high water marks. Given

Fig. 14 Predicted surge using curve-fitted surge response function, based on Tracks A and C only (top pane) and Tracks B and D (bottom pane), versus numerically simulated surge at Locations 1 (*top left*), 2 (*top right*), 3 (*bottom left*), and 4 (*bottom right*). Solid line indicates an exact match, dashed lines indicate ±10% about an exact match, and hollow circles indicate prediction is extrapolated beyond the bounds of the surge response function ▶

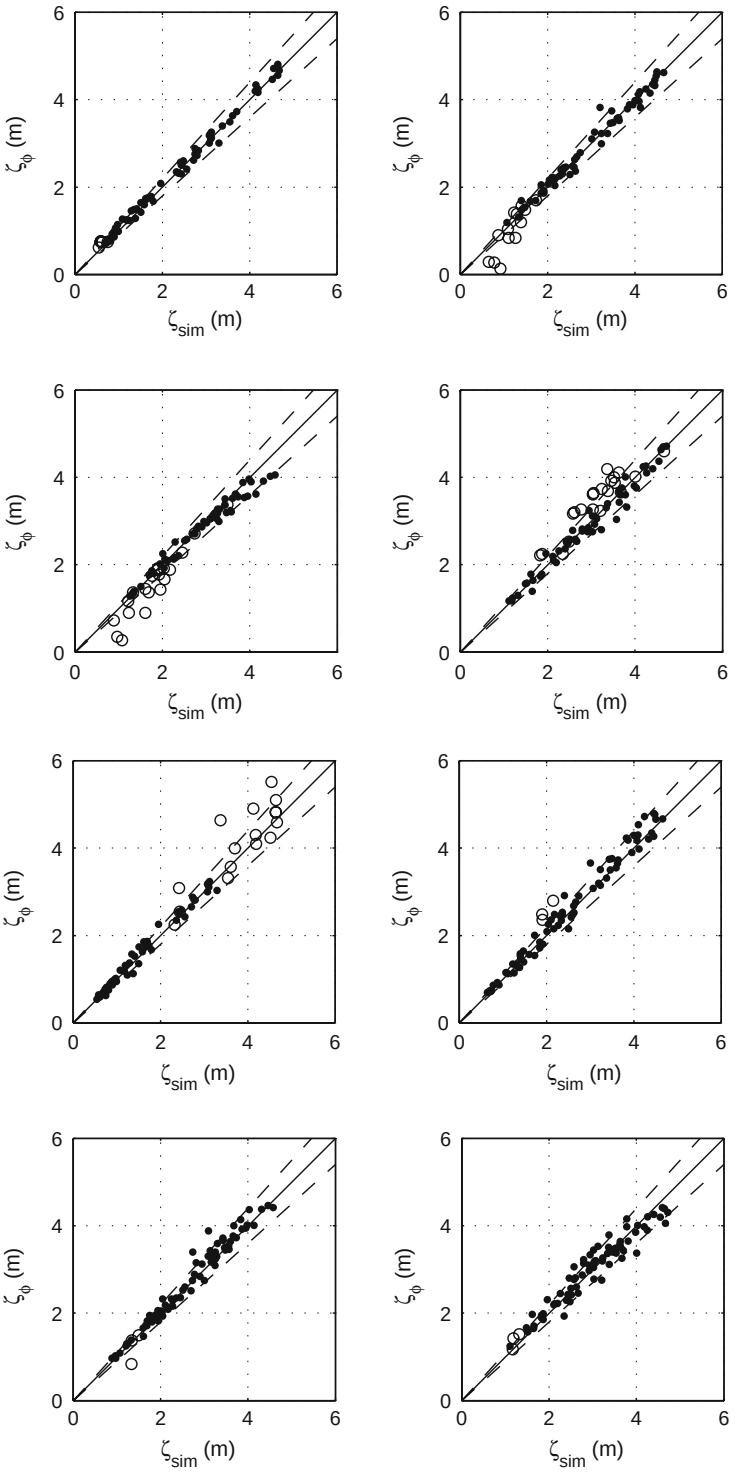
ζ_ϕ (m)
ζ_{sim} (m)
0
2
4
6

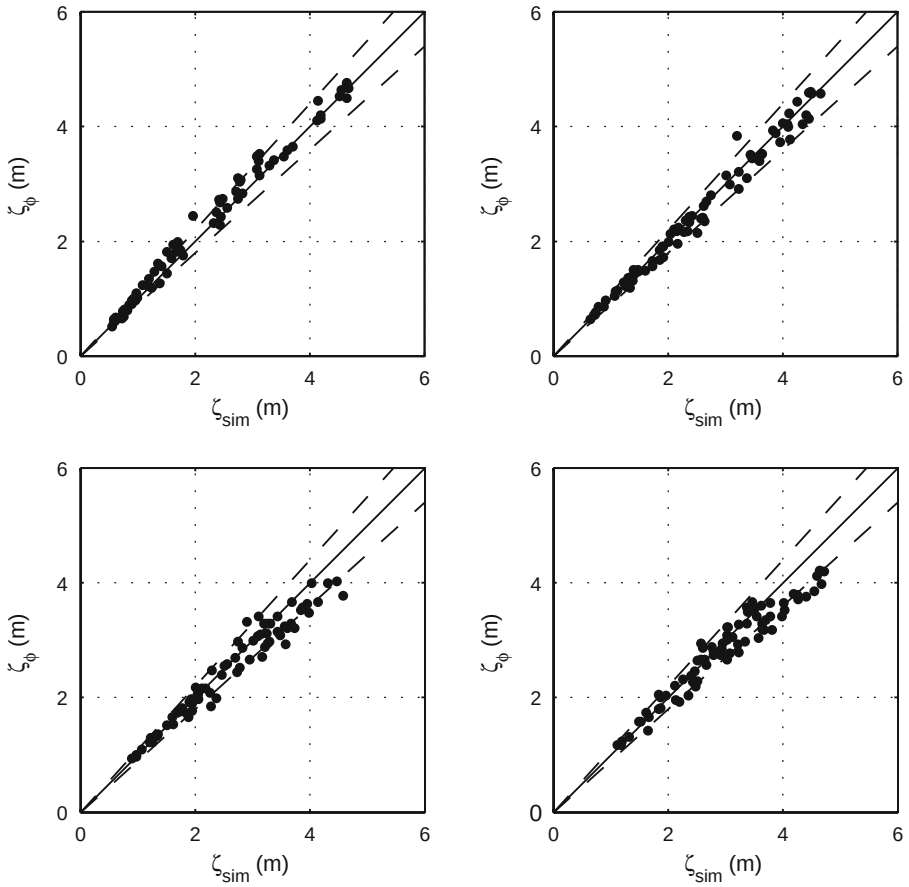

Fig. 15 Predicted surge using curve-fitted surge response function, based on Tracks A and D only, versus numerically simulated surge at Locations 1 (*top left*), 2 (*top right*), 3 (*bottom left*), and 4 (*bottom right*). Solid line indicates an exact match while dashed lines indicate ±10% about an exact match

the slowly varying changes in Φ with along-coast location, the accuracy and viability of using weighted-averaging to interpolate response functions along the coast was evaluated. Starting with the Track A and Track D functions for the full set of simulated storms the response functions at Locations 2 and 3 were estimated by taking an alongshore-distance weighted average between the response functions at Locations 1 and 4, within the region of x_2' overlap. The resulting surge predictions at Locations 2 and 3, within the range of $\Phi(x_2')$ computed explicitly shows good agreement with the simulated surges at both locations particularly for larger surge events (Fig. 18). Mean and RMS errors for this distance-weighted interpolation between gauges spaced 90 km apart is within 23 and 32 cm, respectively (Table 1). The surge predictions do, however, exhibit more scatter when determined by straight extrapolation of the surge response function. This evaluation indicates that the surge response function approach can expand the quantitative use of historical data to include locations for which no measurements are available.

The analysis described above demonstrates that a small sample of hurricane surges may be used to define the surge response over a wide range of meteorological and geographic

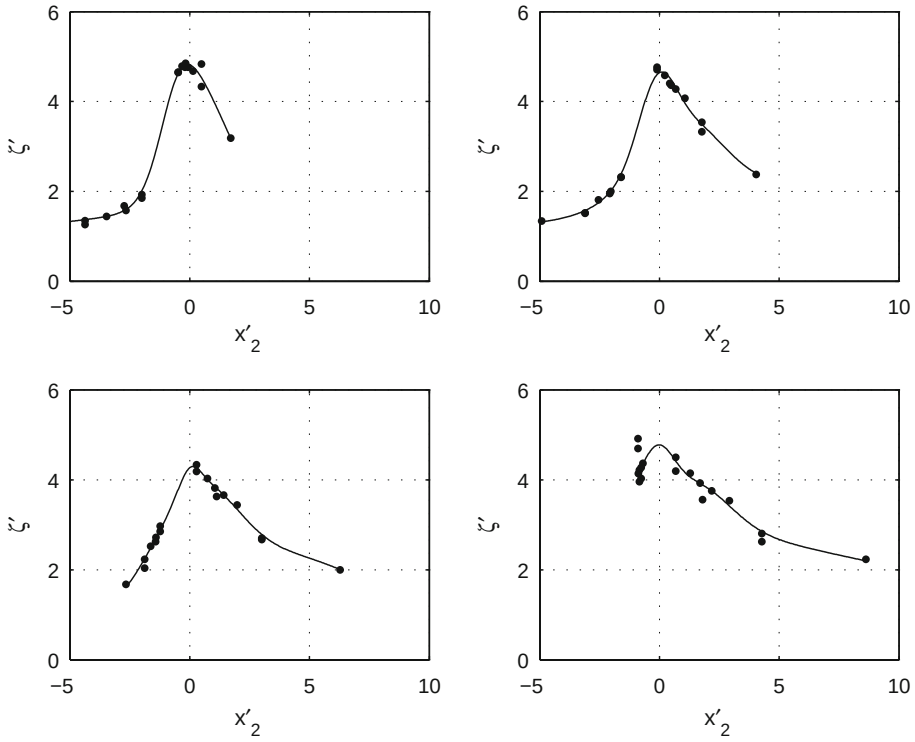

Fig. 16 Dimensionless surge response functions using simulated storm surge for Tracks A and D with $c_p = 900$ or 960 mb only (90-km spacing). Within each pane are Locations 1 (*top left*), 2 (*top right*), 3 (*bottom left*), and 4 (*bottom right*). Solid line shows 3-term Gaussian fit to data

conditions. Such a method may be used to identify storm conditions to be combined with an optimal sampling method for hazard risk assessment (Neidoroda et al. in review).

4 Summary and conclusions

The surge response surface approach to coastal storm surge statistics with the JPM-OS method allows the use of a continuous probability density function. Resio et al. (2009) showed that such an approach can provide a more effective risk assessment for extreme events. Here, the authors first showed that surge response surfaces exhibit continuous behavior with respect to storm intensity, storm size, and storm track over a large coastal area. Secondly, it was demonstrated that a dimensionless surge response function exists and can reasonably be described in terms of physical scaling laws relating the location of peak alongshore surge to storm size and the surge magnitude to storm intensity. Finally, the numerically simulated data were decimated to demonstrate the use of the developed scaling laws to estimate surge response functions with a high degree of accuracy.

The dimensionless surge response function and interpolation scheme introduced here can readily be applied in open coastal areas. Because this response function approach produces reliable surge estimates, particularly for the high surge levels important to extreme-value statistics, this approach has the potential to reduce numerical simulation

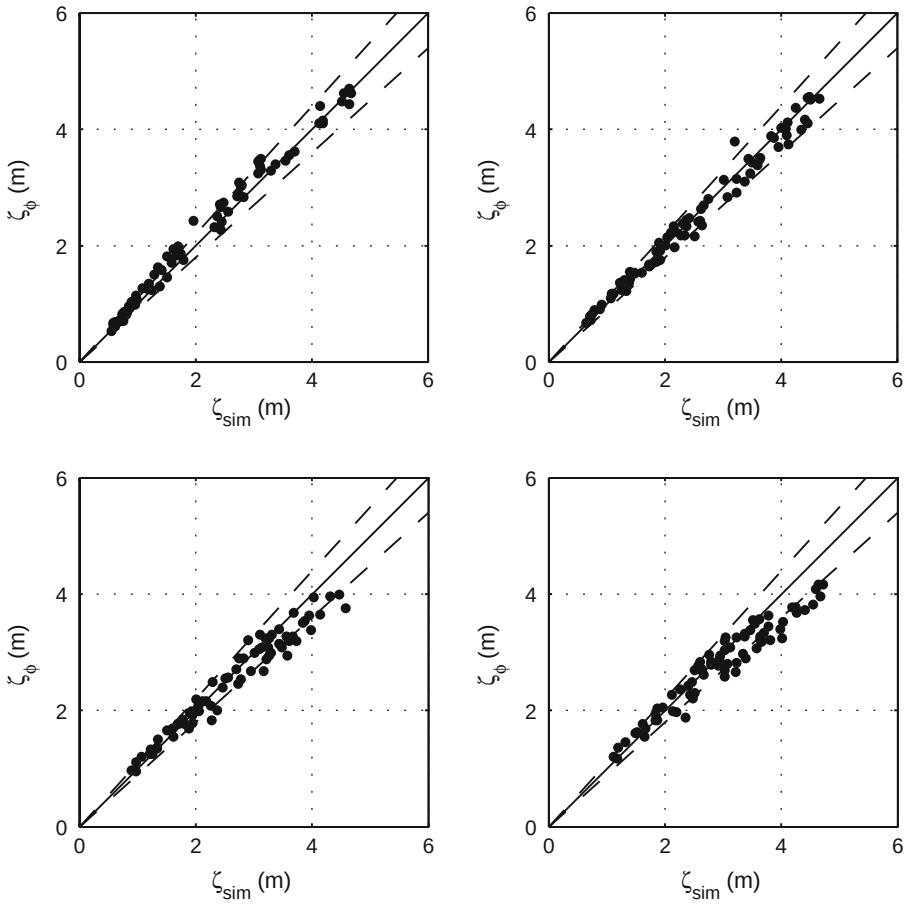

Fig. 17 Predicted surge using curve-fitted surge response function, based on Tracks A and D with $c_p = 900$ or 960 mb only, versus numerically simulated surge at Locations 1 (*top left*), 2 (*top right*), 3 (*bottom left*), and 4 (*bottom right*). Solid line indicates an exact match while dashed lines indicate $\pm 10\%$ about an exact match

requirements by at least 75% for coastal hazard assessment studies. Such computational time savings will lead to significant project time and cost savings. Similarly, this dimensionless response function approach shows promise for historical data interpretation. Limited surge level observations at discrete locations along with information on intensity, size, and track of those hurricanes captured in the surge observation record may be analyzed in the context of these response functions in order to estimate surge levels for alternate events at the measurement location, or at other locations along the same stretch of coast.

Finally, for more comprehensive application in hurricane surge studies, the response functions developed here should be expanded to include the impacts of other physical processes such as storm angle of approach and forward speed, wave setup, inland runoff, and locally generated wind setup. It is expected that a more generalized dimensionless response function exists and can be described in a similar manner as that presented here.

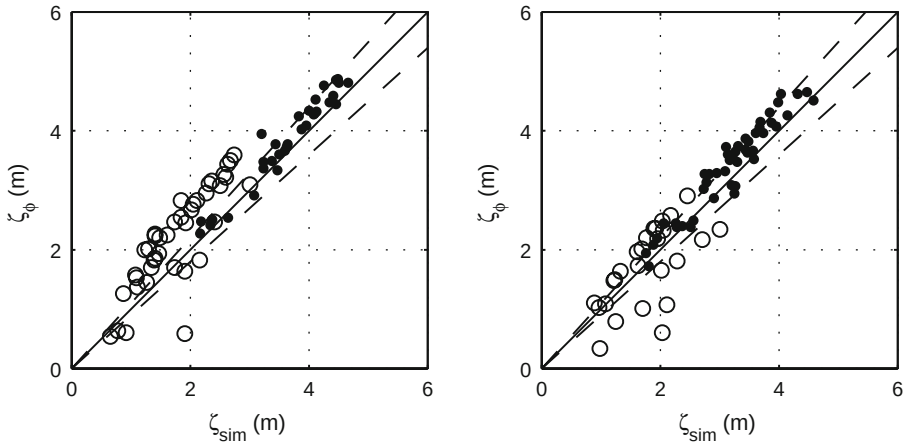

Fig. 18 Predicted surge at Locations 2 (*left*) and 3 (*right*) using a weighted-average of curve-fitted surge response functions at Locations 1 and 2 (see Fig. 10). Solid line indicates an exact match, dashed lines indicate ±10% about an exact match, and hollow circles indicate prediction is extrapolated beyond the bounds of the interpolated surge response function

Acknowledgments The research presented herein was funded by the U.S. Army Engineer Research and Development Center and in part by a Grant/Cooperative Agreement from the National Oceanic and Atmospheric Administration. The views expressed herein are those of the authors and do not necessarily reflect views of NOAA or any of its subagencies. The use of trade names does not constitute an endorsement in the use of these products by the U.S. Government.

References

Dorst N (2007) What is the average forward speed of a hurricane? In Hurricane Research Division Frequently Asked Questions. National Oceanic and Atmospheric Administration. http://www.aoml.noaa.gov/hrd/tcfaq/G16.html

Holland GJ (1980) An analytic model of the wind and pressure profiles in hurricanes. Mon Weather Rev 108:1212–1218. doi:10.1175/1520-0493(1980)108<1212:AAMOTW>2.0.CO;2

Irish JL, Resio DT, Ratcliff JJ (2008) The influence of storm size on hurricane surge. J Phys Oceanogr (online) doi:10.1175/2008JPO3727.1

Niedoroda AW, Resio DT, Toro G, Divoky D, Reed C (in review) Emerging methods for evaluation of the coastal hurricane storm surge hazard. *Ocean Engineering*

Resio DT, Irish JL, Cialone MA (2009) A surge response function approach to coastal hazard assessment – part 1: basic concepts. Nat Hazards. doi:10.1007/s11069-009-9379-y

Thompson EF, Cardone VJ (1996) Practical modeling of hurricane surface wind fields. J Waterw Port C ASCE 122(4):195–205

U.S. Army Corps of Engineers (2006a) Performance evaluation of the New Orleans and southeast Louisiana hurricane protection system draft final report of the Interagency Performance Evaluation Task Force. U.S. Army Corps of Engineers Report, 259 pp

U.S. Army Corps of Engineers (2006b) Louisiana Coastal Protection and Restoration (LACPR) preliminary technical report—appendix B—history of hurricane occurrences. U.S. Army Corps of Engineers New Orleans District Report

Westerink JJ, Luettich RA, Baptista AM, Scheffner NW, Farrar P (1992) Tide and storm surge predictions using finite element model. J Hydr Eng 118(10):1373–1390. doi:10.1061/(ASCE)0733-9429(1992)118:10(1373)

Westerink JJ, Luettich RA, Feyen JC, Atkinson C, Dawson MD, Powell JP, Roberts HJ, Kubatko EJ, Pourtaheri H (2007) A basin to channel scale unstructured grid hurricane storm surge model as implemented for southern Louisiana. Mon Weather Rev 136:833–864

EXTREME HURRICANE SURGE ESTIMATION

FOR TEXAS COASTAL BRIDGES

USING DIMENSIONLESS SURGE RESPONSE FUNCTIONS

A Thesis

by

YOUN KYUNG SONG

Submitted to the Office of Graduate Studies of
Texas A&M University
in partial fulfillment of the requirements for the degree of

MASTER OF SCIENCE

August 2009

Major Subject: Civil Engineering

CHAPTER V

NUMERICAL SIMULATION STRATEGY

To develop sufficient surge data to define and refine SRFs at the selected coastal bridges, numerical hurricane simulations were conducted to compute storm surge levels in the region of interest. In this section, a detailed description is presented on the numerical hurricane simulations is presented. The following presents the numerical storm surge model, ADCIRC, and its setup, hurricane selection, and specification of elevation stations on the open coast.

5 .1 ADCIRC Hydrodynamic Model

For accurate and detailed surge analysis, a storm surge model has to incorporate the key features discussed in this section including:

- A large scale grid domain specifying the open boundary in deep water
- The sufficient grid refinement on the coastal regions including the adjacent basins, and
- The flexibility in node density.

In this study, storm surge elevation was simulated using the advanced hydrodynamic model, ADCIRC-2DDI (Luettich et al., 1991; Westerink et al., 1994). ADCIRC is a surface water circulation model coded using a finite element scheme in space and using a finite different method in time to solve the GWCE, discussed previously in section 2.3.

ADCIRC can be forced by specifying free surface elevations (due to tidal potential or barometric pressures deficit), normal flow, surface stress (due to hurricane wind or wave radiation), and landscape features such as barriers, bridge piers, and so forth. These boundary conditions can be specified on the nodes along the circumference of and/or within the grid domain.

The ADCIRC model provides several options that improve its computational performance. These include the selection of operational mode; the external mode (ADCIRC-2DDI) or internal mode (ADCIRC-3DL), and parallel (MPI-run) or serial processing. In internal mode, ADCIRC computes the vector form of surface water velocities by solving the three-dimensional wave equation with the primitive conservation of momentum. In external mode, ADCIRC computes the scalar of surface water elevations by solving the depth-integrated, two dimensional wave equations with the primitive conservation of mass. ADCIRC execution in external mode saves both CPU time and data storage, requiring on the order of one third that required for the three-dimensional computation. Westerink et al. (2008) showed ADCIRC with this configuration to perform well for surge simulations. Typical computation error for surge simulation is estimated at 20 to 30 cm.

ADCIRC is capable of running on multiple processors in parallel by decomposing the mesh grid and related input files into multiple numbers of smaller pieces, assigning each piece of work to an independent CPU, and then reassembling the output from each CPU back together. In this way, it saves real time taken to complete the total simulation as well as eases the computational burden laid on a single CPU.

ADCIRC is currently utilized to solve the free surface circulation and sediment transport problem by various professional research groups in national institutions including the U.S. Army Corps of Engineers, Federal Emergency Management Agency (FEMA), National Laboratory for Civil Engineering (LNEC), National Oceanic and Atmospheric Administration (NOAA), and U.S. Naval Research Laboratory (NRL).

5.1.1 Computational Domain

As a model domain, the east coast computation domain of Westerink et al. (2008) was used. This grid include the Western North Atlantic Ocean, the Caribbean Sea, and the Gulf of Mexico is used (Fig. 19). The east coast domain specifies open boundaries along the 60°W meridian, and the grid refinement widely varies from about 0.400° in the deep ocean to 0.005° nearshore and in inland bays (Weterink et al., 1992 and 1994). Especially, it highly resolves the regional bathymetry near the Texas coast and adjacent bays and waterways. Detailed grid information lists in Table 2.

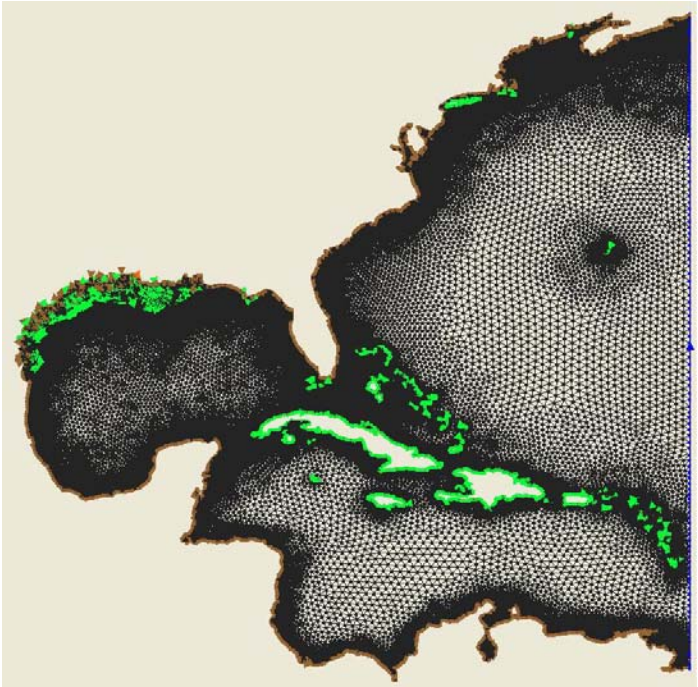

Fig. 19 East coast ADCIRC domain grid.

Table 2. East coast domain triangular mesh information

Area [km^2]	Maximum Bathymetry [m]	Minimum Bathymetry [m]	Number of Nodes	Number of Elements	Grid size (Approximation, degree)		Grid size (Approximation, meter)	
					Maximum	Minimum	Maximum	Minimum
8.3522×10^6	7,858.09	(-)71.67	1,344,247.00	2,628,785.00	0.400	0.005	46,000	100

5.2 Hurricane Surface Wind Field Modeling

Besides the capability of the storm surge model itself, the accuracy of the surge prediction heavily depends on the accuracy of the specified hurricane forcing. For hurricane simulations, ADCIRC takes hurricane wind and boundary field files containing the information on surface wind and pressure at each time step as input for forcing. Several input wind field sources are available, including reanalyzed historical wind fields (i.e. HWINDS, Powell and Reinhold, 2007). In this thesis, however, we

emphasize parameterization of the surge response, so a parametric wind field model is used. Thus, to develop hurricane wind fields, the Planetary Boundary Layer (PBL) model of Thompson and Cardone (1996) is utilized. This PBL model is derived from the vertically averaged, horizontal equation of motion with respect to a moving cartesian coordinate system with its origin at the center of the eye (Chow, 1971; Cardone et al., 1992). The vertically integrated momentum flux is related to the surface stress, and the wind and pressure fields are represented with respect to hurricane parameters including central pressure (c_p), storm size (R_p), storm forward speed (v_f), and peakedness (B, Holland, 1980). During model development, it was assumed that the vortex flux within the PBL is horizontally homogeneous, steady state, and that the structure of a hurricane wind field changes slowly (over periods longer than one hour). Therefore, properties of those hurricane parameters are specified at one hour interval, and based on this information the PBL model computes the wind velocities and pressure at the nested grid points at specified time steps. For this study, in order to adequately resolve the temporal surge response as the hurricane moves over the continental shelf and the landmass, wind speed and pressure were set to be read every fifteen minutes in a format compatible to ADCIRC file specification. The PBL model uses a moving coordinate system so the origin of the nested grid always coincides at the center of the hurricane. The nested domain is constructed by overlapping seven regular grids, each with progressively coarser grid spacing (1.25km, 2.5km, 5km, 10km, 20km, 40km, and 80km) from the origin of the coordinate system. Therefore, grid refinement can be efficiently adjusted so the complete grid has high resolution near the center of the eye and low resolution

outside the radius where spatial variation in hurricane wind diminishes. The PBL model converts wind (x and y direction, respectively) and pressure information into a format compatible to ADCIRC specification so the PBL output is directly used as wind and pressure field input forcing for ADCRIC storm surge simulation. Given the hurricane forcing, ADCIRC calculates surface wind stress following Garratt's (1977) relationship as

$$\frac{\tau_x}{\rho_o} = C_{D,x}\frac{\rho_a}{\rho_o}|W_{10}|W_{10,x} \tag{5.1}$$

$$\frac{\tau_y}{\rho_o} = C_{D,x}\frac{\rho_a}{\rho_o}|W_{10}|W_{10,y} \tag{5.2}$$

where

τ_x, τ_y is wind stress in the x and y direction, respectively,

$\frac{\rho_a}{\rho_o}$ is ratio of air density to average density ofseawater,

$W_{10,x}, W_{10,y}$ is x and y component of wind velocity vector at a 10m height in units of m/s,

$|W_{10}|$ is wind speed at a 10m height in units of m/s, and

C_D is Garratt's (1977) frictional drag coefficient defined as

$$C_{D,x} = (0.75 + 0.067W_{10,x}) \times 10^{-3}$$
$$C_{D,y} = (0.75 + 0.067W_{10,y}) \times 10^{-3}$$

The PBL specifies the hurricane pressure field, P_c following the exponential law (Holland B, 1980) as

$$P_c = P_{eye} + \Delta P e^{-(R_p/r)^B} \tag{5.3}$$

where

P_{eye} is pressure at the eye of the storm,

ΔP is pressure deficit,

r is the distance from the eye of the storm, and

R_p is a pressure scale radius used in PBL model.

Including Holland B for the parametric expression of observed hurricane intensity also improves the accuracy in the maximum wind speed estimation for the hurricane, $U_{\max}$ as

$$U_{\max} = \left(\frac{B}{\rho_a e} \right)^{1/2} (p_n - p_c)^{1/2} \tag{5.4}$$

where e is the base of the natural logarithms. Consequently, the storm surge levels, which would be related to the square of the wind speeds (Irish et al, 2008), were also estimated by linear proportion to the Holland B.

5.3 Hurricane Selection Based on Optimal Sampling

For this study, the sensitivities of surge response to the variation in both forward speed and approach angle were assumed insignificant. Therefore, the storms propagating with 5.7m/s forward speed and less than 17° of angle with respect to shoreline orientation, a typical forward speed and angle of historical hurricanes in Gulf of Mexico (Irish et al., 2009), were only considered. Holland B was held constant at 1.27 until the hurricane is over 50km from landfall; at this point, the hurricane's Holland B was to decrease slowly to 0.9.

As demonstrated previously, the SRF redefines a continuous surge response surface, with respect to relative alongshore distance from the location of the hurricane

eye to the position of interest. In order to measure the alongshore distance, and to investigate the surge responses to varying continental shelf slope, additional 215 elevation stations were specified along the ocean coastline. Accepting the concept of an idealized shoreline, that the surge response at 10m-depth nearshore can represent the overall surge response behavior along the adjacent continental shelf (Irish et al, 2009), the stations were specified along the 10m-depth contour throughout the Texas open coast (Fig. 20).

In addition to the 4 tracks investigated through the preceding work of Irish et al. (2009), a total of 18 storm tracks, 30km apart from each other, were specified to compromise the entire study area (Fig. 20). Specifically, the synthetic storms along eight parallel tracks were selected for surge investigation in the Galveston area, and for the Corpus Christi region, six more parallel tracks were selected.

The properties for the storm size (Rp) and intensities (cp) were specified based on the investigation of the discrete data set of Irish and Resio. (2009). While the storm tracks were somewhat densely placed in order to capture the effect of spatial variability in continental shelf width, if any, subsets for storm size and intensity combinations were alternately applied for each track to optimize numerical simulation requirements. That is, if the subset for the first, third, and fifth track, respectively, near Galveston, consists of at least nine different combinations of size and intensity properties (subset I), the second and the fourth tracks were specified with combinations of only two discrete intensities (960mb and 900mb) and a single moderate size (subset II) (see Fig. 21). Table 3 lists the combinations of storm size and intensity selected for subset I and subset II,

respectively. On the basis of these two setups, synthetic hurricane wind fields were created with intensity between 960mb and 900mbs, and size between 11 and 65km.

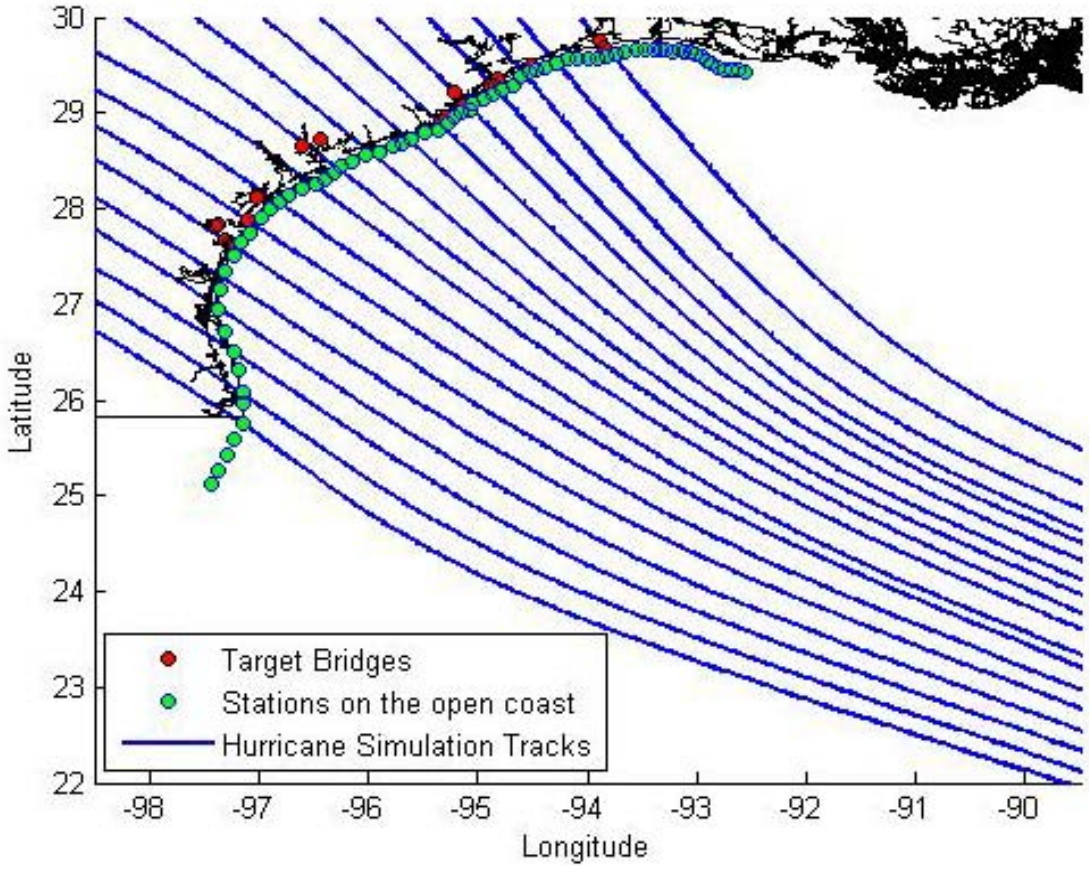

Fig. 20 Storm tracks (solid line) with respect to stations along the Texas coast. The green dots aligned along the shoreline represent the elevation stations while red dots indicate target bridges.

As mentioned previously, the computation of barometric pressures and wind velocities were specified every 900 seconds and saved in two separate files in a format compatible to ADCIRC model specification. With these wind field files as meteorological forcing input, along with the other inputs for grid and boundary conditions, more than 105 ADCIRC hurricane simulations were conducted. With the

refined grid, approximately 1300 CPU hours were requested to complete a single run for a storm of 6 days duration with 0.5 second time increment. To alleviate the computational burden, in terms of time and facilities available, the simulations were run on multiple processors (32, 64, 72, or 88), depending on platform and parallel configuration of the computational platform. The ADCRIC computation produced the time history of the storm surges with the typical accuracy of 20 to 30 cm (Westerink et al., 2008).

Table 3. *Rp* and c_p Combinations for subset I & II

Subset I				
x_{eye} [Lon.]	y_{eye} [Lat.]	v_f [km/s]	c_p [mb]	R_p [km]
-95.65	28.75	5.7	960	20.4
-95.65	28.75	5.7	960	38.9
-95.65	28.75	5.7	960	66.0
-95.65	28.75	5.7	930	14.8
-95.65	28.75	5.7	930	32.8
-95.65	28.75	5.7	930	47.8
-95.65	28.75	5.7	900	11.1
-95.65	28.75	5.7	900	27.6
-95.65	28.75	5.7	900	40.4

Subset II				
x_{eye} [Lon.]	y_{eye} [Lat.]	v_f [km/s]	c_p [mb]	R_p [km]
-95.35	28.90	5.7	960	32.8
-95.35	28.90	5.7	900	32.8

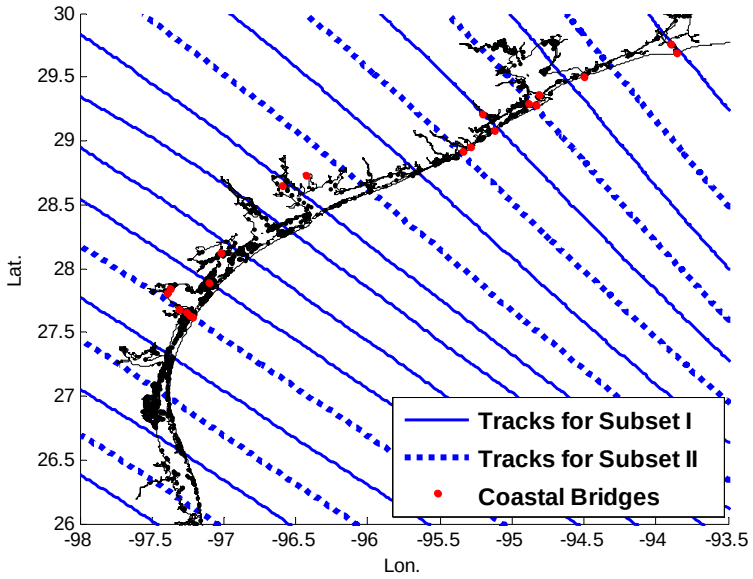

Fig. 21 Tracks for subset I & II. The solid lines are the tracks for hurricane simulations for subset I consisting of minimum 9 combinations of Rp and Cp. The dashed lines are the tracks for hurricane simulations for subset II consisting of minimum 2 combinations of Rp and Cp as shown in XXXTable 3

CHAPTER VI

EXTREME SURGE ESTIMATION USING SURGE RESPONSE FUNCTION

6.1 Surge Response Function Advancements

The storm simulation data was analyzed to determine the dimensionless SRF parameters based on the physical scaling laws of Irish et al. (2009), and then refined to account for continental shelf width

First, the effect of varying coastline configuration on the spatial extent of storms peak surges was studied. As discussed in section 4.3, the location of the peak surge should be analyzed in relation with the continental shelf width, or L_{30}. To measure the L_{30}, several pairs of two ocean stations were specified to locate at the 10m and 30m water depth, respectively, on the virtual orthogonal to shoreline orientation. Alongshore distance between two 10m depth stations were set with simulated hurricane landfall spacing, which is 30km (Fig. 22). To measure the alongshore peak surge distance (x-x_{peak}), however, a minimum of nine combinations of storm surge results along the 10 tracks were utilized (Fig. 23). The size parameter λ was determined from surge data simulated throughout the Texas coast, as a means to account the effect of varying L_{30} for the SRF. By linear regression, the relationship between L30 and the alongshore extent to highest surge was investigated, with respect to the storm size. The increase in steepness of the linear interpolation (or λ) with wider L_{30} and increasing storm size (R_P) resulted from the analysis (Fig. 24). Therefore, it was concluded that the simplification of slowly

varying coastal geography was not valid for SRF development within the wide range of conditions seen on the Texas coast.

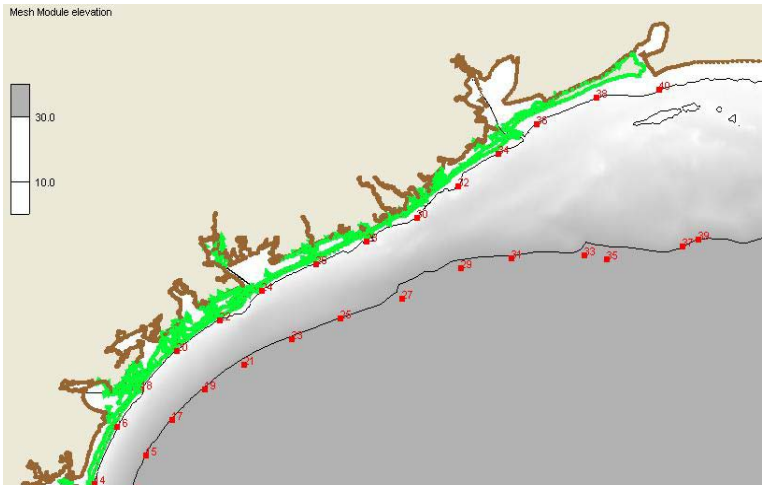

Fig. 22 Locations of 10m and 30m water depth on the continental shelf. A pair of two depth indicators were specified on virtual orthogonal line with respect to shoreline orientation to measure L30

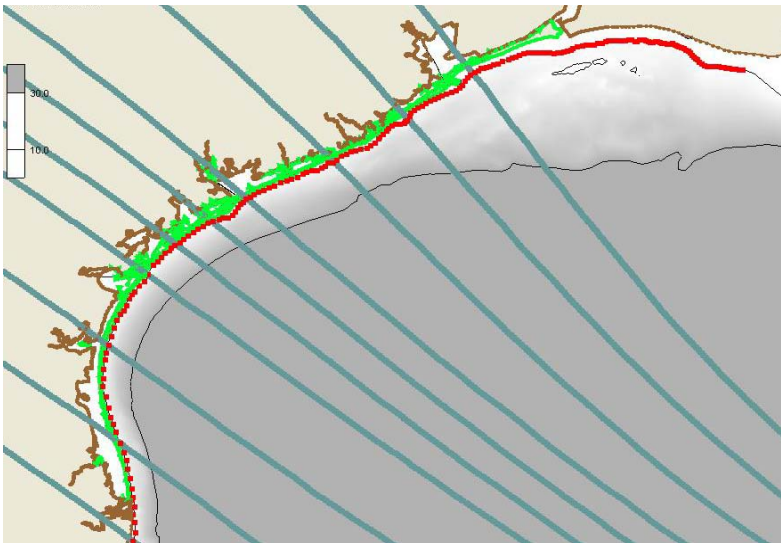

Fig. 23 Hurricane tracks selected (green solid lines) to measure the effect of varying continental shelf width (L30). From the bottom left across the top right, track 1, 3, 5, 7, 8, 9, 10, 12, 14, 16, and 17, respectively. The solid line in black marks the 30m water depth contour while the red dots represent the elevation stations specified at 10m- water depth in the coast.

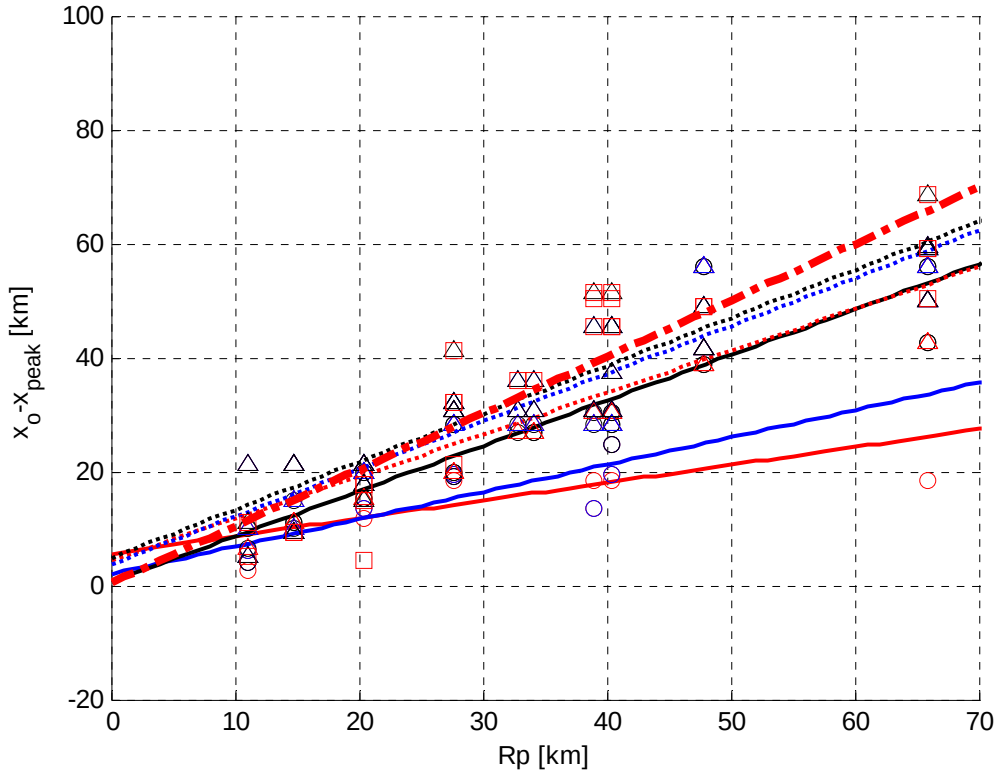

Fig. 24 Linear regression of storm size (Rp) and the distance between the location of hurricane eye at landfall and the alongshore peak surge location. The slope of each interpolation is used to determine t the slope parameter, λ.

To incorporate the different geographical conditions, the total study area was divided into three parts depend on the variability in the parameter λ (

Table 4); the coastal regions near Corpus Christi, Matagorda Bay, and Galveston, respectively. By partitioning the continuous coastal regions into three spatial ranges, the previously used simplification of slowly varying coastal configuration is then applicable within each segment of the coast (i.e., Galveston, Matagorda Bay, and Corpus Christi).

Table 4. Properties of the parameter λ for each segmentation of the Texas coastal region

Selection of λ and storm tracks applied for each study area		
Coastal Region	λ	Track I.D.
Corpus Christi	0.74	5,7,8,9
Matagorda Bay	0.84	7,8,9,10,12
Galveston	0.99	10,12,14

Table 5 lists the variation in λ estimated from storms propagating over the corresponding L30. These were plotted in Fig. 25. This figure shows that the distribution of the λ with respect to varying L30 can be categorized into three groups depending on their slopes – the magnitude of increase in the λ with uniform variation in L30. If we visualize the range of the continental shelves classified in the same group on the continental shelf map (Fig. 25), it is seen that the overall geography of the continental shelf shape along the Texas coast can be divided into three segments (Fig. 26, separated with the solid lines) based on the lambda variation.

In addition to the correlation between L30 and λ, it is seen that the lambda variations also corresponded to the changes in the shoreline orientation. Therefore, it is expected that, by examining the correlation between L30, Rp, parameter λ, and the shoreline orientation θf, the SRF could also provide a means to characterizing the regional geographical features in parametric function. Meanwhile, the effects of such a varying costal shape can be resolved by assuming that the interaction between the hurricane meteorology and the geographical factors in the region can be captured by the surge responses to the hurricanes approaching the vicinity of the area of interest. Therefore, when determining the site-dependent coefficients, such as λ and mx,

reflecting the regional characteristics, storm simulation results from selectively chosen tracks were only utilized. For example, for the evaluation of λ and mx for bridges located in the Corpus Christi area, the storm surge data obtained from storms simulated along the track No.5 to No. 9, and in-betweens was only used.

Table 5. Lambda variation change in the continental shelf width

3 - pair		
Track ID	L30 [km]	Lambda
1,2,3	19.6	0.26
2,3,4	20.6	0.36
3,4,5	21.3	0.49
4,5,6	23.5	0.70
5,6,7	25.4	0.69
6,7,8	28.0	0.79
7,8,9	30.1	0.74
8,9,10	33.1	0.84
9,10,11	35.7	0.81
10,11,12	39.5	1.01
11,12,13	41.7	1.12
12,13,14	47.9	1.01

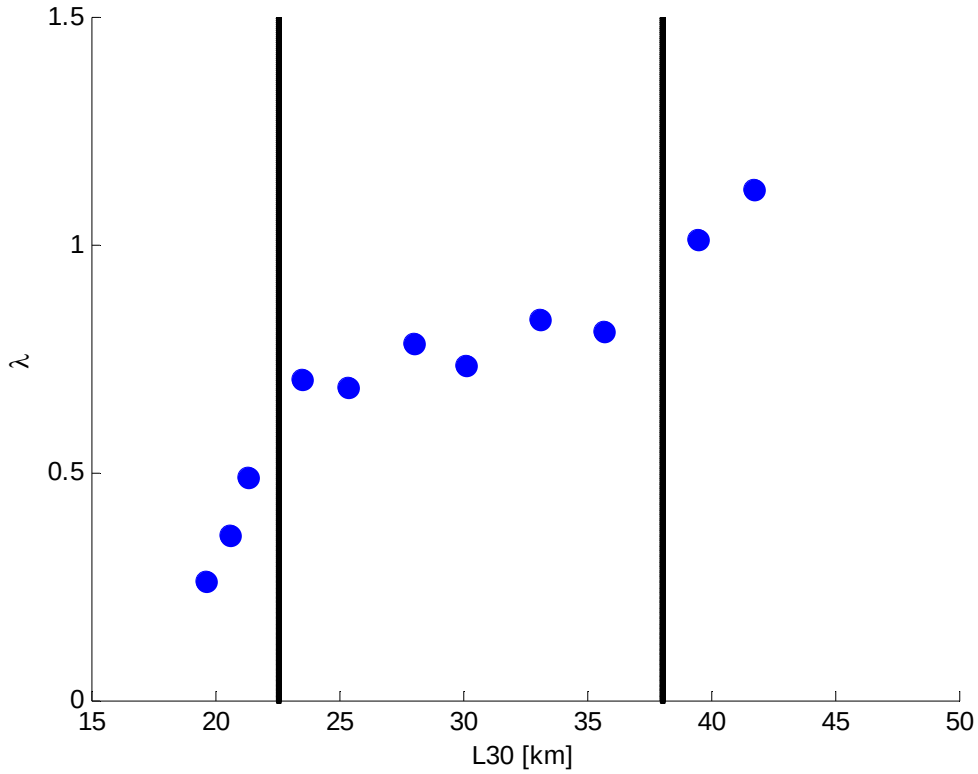

Fig. 25 The parameter λ variations with respect to varying continental shelf width. The solid lines separate the research area into three segments.

Fig. 26 Continental shelf map of the Texas coast. The dark shade represents the continental shelf extension to the 30m water depth (L30). The red box represents the alongshore range of L30 within which the parameter λ shows the similar tendency in the distribution with respect to L30.

The properties for λ, along with the surge simulation data, were used to determine the dimensionless SRF parameters (x2' and ζ') following the methods presented the previous sections. The obtained sets of x2' and ζ', were curve-fitted. As a conclusion, the flexibility of the three-term Gaussian function in adjusting peak width was found to be the most suitable for defining the SRF, as applied during previous preceding work by Irish et al. (2009). However, the region to the right side of the hurricane eye is the most influenced by the hurricane forcing, due to the hurricane meteorology in the northern hemisphere. Therefore, SRF behavior has some asymmetry with respect to x2'=0. In an effort to find a way to improve the flexibility in the shape of the function, two pairs of three-term Gaussian functions were defined based on the right and left side of the data, independently. In this way, the scatter near the peak of SRF was minimized, and thus a smoother curve, with its peak well-posed at the center (the location of x2'=0), could be developed. This curve fitting approach also reflects the asymmetry of the surge behavior. Therefore, the SRF near the 20 selected bridge locations were developed in a format of an asymmetric three-term Gaussian function.

As discussed before, the SRF is a site-dependent function. Therefore, for the 20 target bridges, 20 independent SRFs were developed. The SRFs for each bridge are presented in the Appendix, and three of these SRFs are presented here for discussion (Fig. 27).

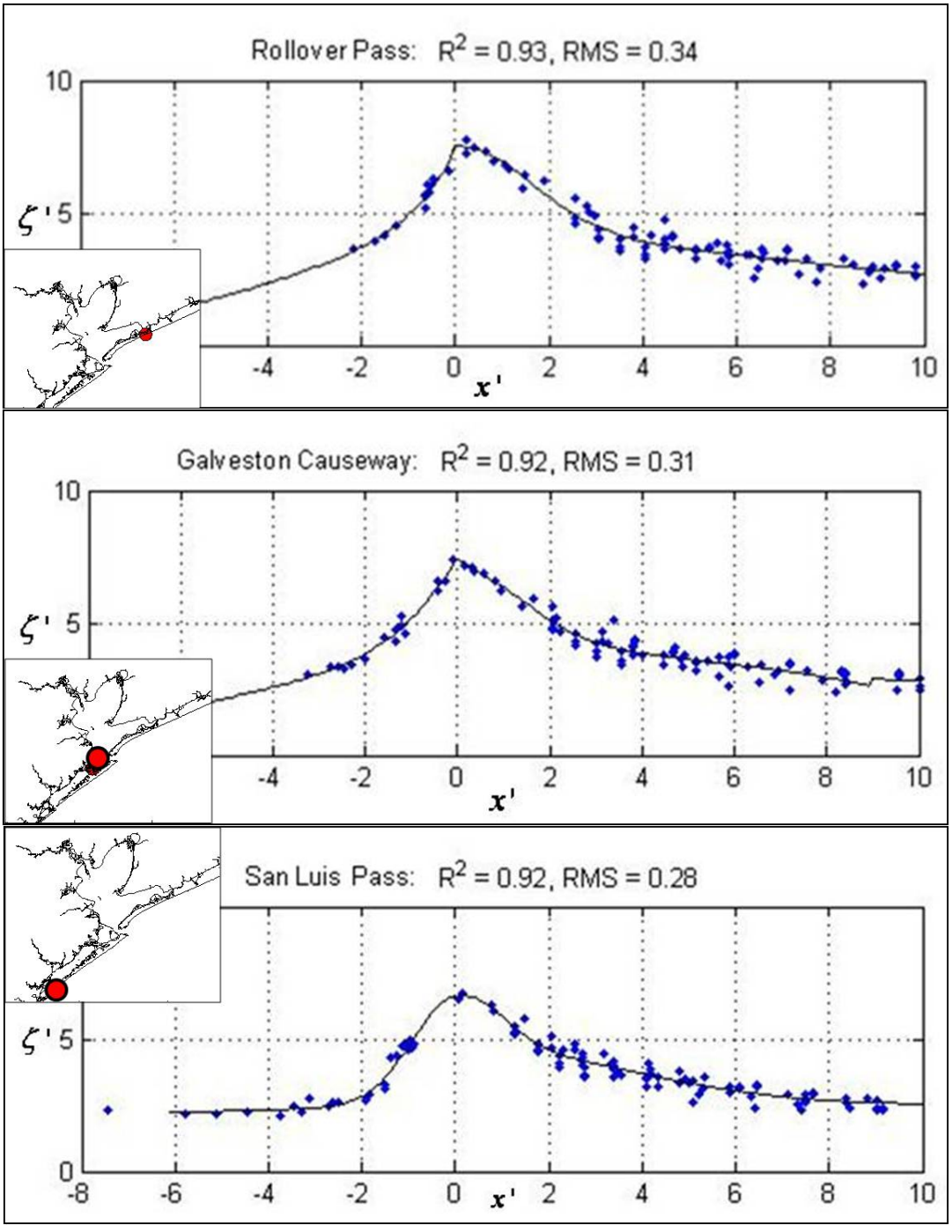

Fig. 27 Surge response functions developed at the three locations in Galveston. The SRFS are developed at the location of Rollover Pass(top), Galveston Causeway (middle), and San Luis Pass (bottom). Solid line represents the three-term Gaussian fit to the data.

6.2 Validation and Justification of the Surge Response Function Methodology for Hurricane Flood Probability Analysis

By comparing the surge predictions made by SRFs to the original numerical simulation output, the accuracy of each SRF could be estimated. Since the SRF is a developed by the data-fit function of the dimensionless parameters, inherently the SRF itself is a dimensionless, continuous function of the hurricane parameters. Therefore, with given hurricane conditions, the SRF provides the general use of itself for predition of dimensional surges by back-calculating from the SRF.

The SRF was used in this way to make predictions of storm surges (ζsrf) based on the hurricane conditions applied for generating synthetic wind fields earlier as forcing input for storm surge simulations (ζsim). Using the SRFs presented inFig. 27, the SRF predictions (ζsrf) were compared to the ADCIRC model simulation results (ζsim), as shown in Fig. 28. The solid line crossing on the center represents an exact match between the two results.

At the elevation stations on the open coast, the root mean square errors (RMS) of (ζsrf – ζsim) were estimated to be between 15cm and 32cm. This is consistent with the results resulted by Irish et al. (2009). Considering the accumulative errors due to model computation capability is the order of 20 to 30 cm (U.S. Army Corps of Engineers, 2006), the magnitude of RMS errors between the two predictions is reasonable. Therefore, we concluded that the obtained SRFs for the 20 bridge locations of interest accurately represent the surge behavior along the Texas coast.

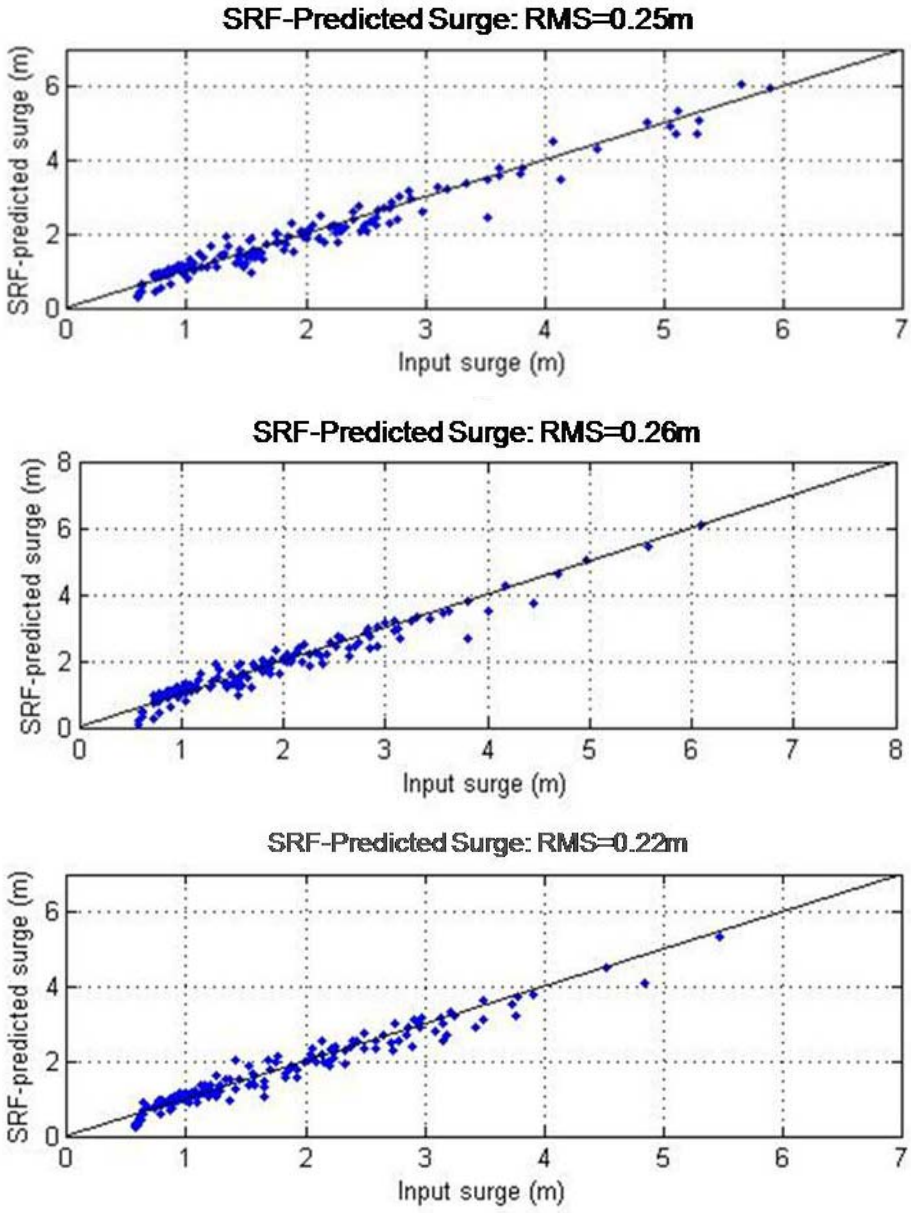

Fig. 28 ζsrf - ζsim plots. The values on the vertical axis are SRF surge predictions while those on the horizontal axis are ADCIRC surge simulation results. Rollover Pass(top), Galveston Causeway (middle), and San Luis Pass (bottom). Solid line indicates the exact match.

To better optimize SRF performance, further study on the interaction between surges and the bay site environment is in process (Katyal, Personal communications).

Note that all surge levels predicted by the SRFs are based on the surge data computed from the numerical model. During ADCIRC simulations, only the hurricane wind stress and pressure forcing forced the surge. Therefore, these SRFs do not account for additional water level due to wave radiation, astronomical tide, and surface water runoff. Finally, static topography within the ADCIRC model was employed, so any additive flooding due to lowering of the barrier islands during the storm is not included.

CHAPTER VII

APPLICATION OF SURGE RESPONSE FUNCTION FOR PEAK SURGE ESTIMATION

By virtue of its continuous form across hurricane meteorological parameters, the SRF can be utilized to calculate storm surge levels at given locations for any hurricane, once the properties for storm size, intensity, and the distance from a point of interest to the hurricane eye at landfall are known. For extreme surge analysis, the SRF was developed based on the peak surges extracted from the entire surface water level history from each ADCIRC simulation. Therefore, the surge prediction made by SRFs may be considered to be the peak surge level at that location for the given hurricane meteorology.

To demonstrate and validate the use of the SRF methodology, storm surge predictions for two historical hurricanes (Carla (1961) and Ike (2008)) were carried out. The SRF-predicted surge levels were compared to high water marks (HWMs) and water level gauge measurement taken during and after these hurricane events.

The focus of this study is on evaluating the extreme surge level response against the hurricane forcing represented by the surface wind stress, pressure deficit, and their interaction with the local bathymetry. Flood levels derived by other forcing mechanisms were not included in the surges predicted by SRF, but it is noted that processes including wave setup and tides can contribute substantially to overall flood elevation. Thus, when the SRF predictions are compared to observations, some of the differences between the two water levels were anticipated and can be attributed to the effects of wave setup, astronomical tide, land erosion, and runoff. For example, the wave setup contributes

approximately 10 to 20% of the total flood level at the open coast. In addition, there is inherently uncertainty with HWM data, due to the nature of its collection with respect to debris lines, visual observations, and so forth. Moreover, it has to be noted that HWMs often include individual wave runup.

For comparison between the SRF predicted peak surges and the Hurricane Carla observation, the HWMs as given by debris or drift lines on the buildings were used. The HWMs were measured with respect to the Geodetic Vertical Datum (NGVD29), while the SRF predictions were made with respect to MSL. The HWM data were converted to MSL using datum information for the 1983-2001 tidal epoch. This conversion gives MSL to be higher than NGVD29 by about 0.2m in the vicinity of the Galveston and 0.3m in the vicinity of Corpus Christi, based on the benchmark information for the NOAA Galveston Pier 21 and the NOAA Rockport, respectively.

For the comparison between the SRF predicted peak surges with the Hurricane Ike high water levels, peak observed water levels computed from the time history collected with pressure gauges were used. The water level time series were obtained from pressure gauges deployed by U.S. Geological survey (USGS, 2005 and 2008) prior to Hurricane Ike's passage. The water level data used for comparison were measured with respect to North America Vertical Datum (NAVD) of 1988. To make it comparable with SRF prediction, these data were converted to MSL. The benchmark data indicate MSL is higher than NAVD88, about 0.35 m.

7.1 Hurricane Carla Description

Hurricane Carla was one of the most powerful hurricanes seen in the United States hurricane record, especially for the state of Texas. Hurricane Carla was first classified as a hurricane as it passed through the western Caribbean Sea on September 6, 1961, and this storm steadily evolved to a Category 5 hurricane while approaching the Texas coast in Gulf of Mexico (Fig. 29). At its landfall on September 11, 1961, between Port O'Connor and Port Lavaca in Texas, Carla was a Category 4 hurricane with a lowest pressure of 931mb, maximum sustain wind speed of 64 m/s, and radius to maximum wind of 56km (NOAA, 2009) As it was a large and intense hurricane moving slowly, at 1.8 m/s, a wide span of the Texas coast, from Port Lavaca to Galveston, experienced some of the highest storm surges ever recorded in this area, 3.3-3.7m (NOAA unknown)

7.2 Comparison of the Peak Surges from Surge Response Function Predictions with High Water Mark Observations

Using the hurricane parameters for Hurricane Carla, SRF predictions were made and compared to the HWMs published by NOAA (1982). The peak storm surge levels evaluated from SRF prediction and observed from the HWMs, with respect to MSL, are listed in Table 6. In addition, the surge levels listed in this table are also plotted on the same graph (Fig. 30) in order to visualize the comparison.

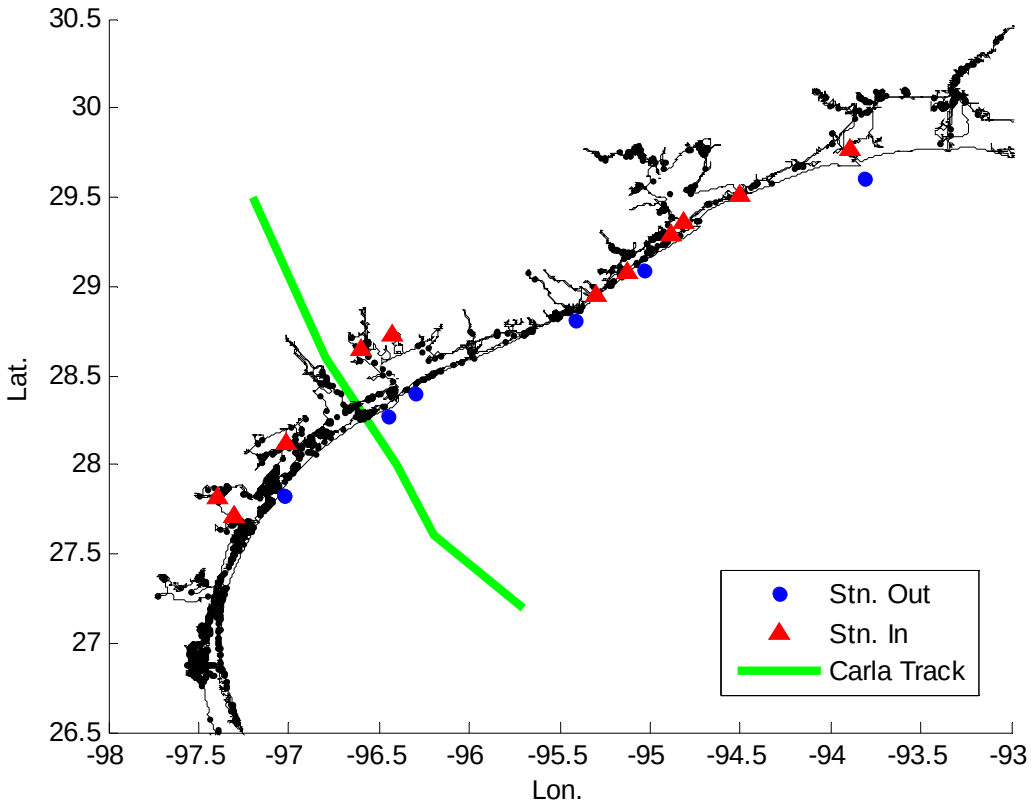

Fig. 29 Hurricane tracking map and elevation stations. SRF prediction was made at stations marked with triangles and compared to the HWM reported by National Weather Service, NOAA (Miller 1982) at the corresponding locations. The solid line shows the Hurricane Carla's storm track* with respect to the elevation stations. *Based on information from National Hurricane Center (2008).

Table 6. Hurricane Carla surge estimation from HWM and SRF

Hurricane Carla Surge Comparison			
Stnation No.	distance from landfall [km]	HWM above MSL [m]	SRF Prediction [m]
51	-43.7	2.8	2.1
53	-41.6	1.6	1.4
58	-30.5	2.6	2.1
65	-16.2	2.0	1.9
77	9.5	3.4	2.5
83	20.6	2.9	2.9
84	20.6	4.5	3.8
88	25.9	5.4	5.2
110	71.2	3.1	3.6
117	80.5	3.7	4.1
127	92.9	3.1	3.8
132	97.0	3.5	3.7
141	111.5	2.5	2.5
147	120.8	2.7	2.6
157	133.5	2.7	3.1
179	164.5	2.5	2.9
182	166.2	2.0	2.1

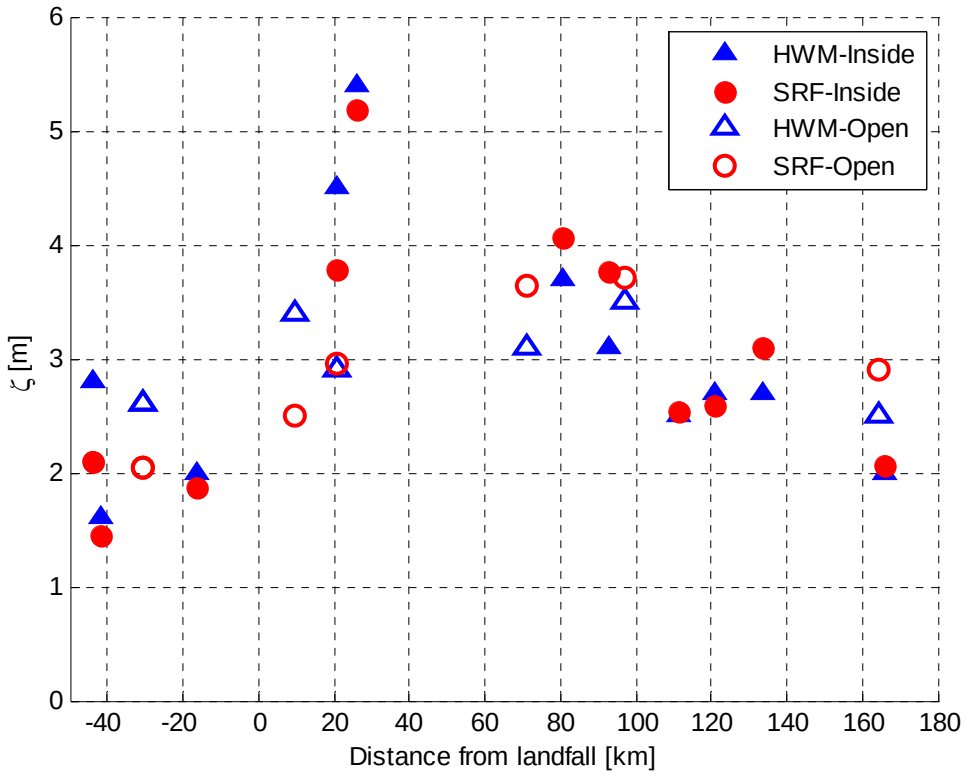

Fig. 30 Comparison of the SRF prediction to HWM for hurricane Carla. Surge levels were estimated with respect to MSL at the elevation stations as shown by Fig. 22.

From the comparison of the two data sets, it was shown that a clear correlation exists between the SRF predictions and the historical HWMs. Based on the pairs of data obtained at 17 stations located inside the coastal bays or along the open coast, the root-mean-square (RMS) error was estimated to be 48 cm, and a strong correlation, with the correlation coefficient of 0.87, between two data sources were found. The SRF predictions only included storm surge by wind and pressure deficit, whereas the HWMs include wave effects (i.e. setup and runup) and astronomical tides. The additional effects of waves and tides were more obvious when comparing the difference in two the surge levels at the stations located on the open coast (hollow marks on Fig. 30) than with

those located inside a coastal bays (solid marks on Fig. 30). Also, the fact that the flood levels recorded through HWM are known to have a high degree of uncertainty leads to differences in two data sources.

7.3 Hurricane Ike Description

On September 13, 2008, while this study was on going, Hurricane Ike struck the Galveston area and caused damage to several coastal bridges and roadways, including the Rollover Pass and Pelican Island Bridges. As Hurricane Ike began moving northwesterly into the Gulf of Mexico, it was upgraded to a Category 4 hurricane. Although Ike's intensity weakened to a Category 2 by the time it made landfall at Galveston, Texas, because of the wide extent of the hurricane force wind field, it resulted in huge storm surges along the Texas coast. Near landfall, the size of the eye was 58km, the center pressure was 952mb, and it approached the coast with speed of 19.3km/hr. With the given Hurricane Ike meteorology, surge predictions were made using the SRFs at several stations located near the eye of Hurricane Ike (Fig. 31). The positions of these SRF stations were specified to correspond to the locations of the pressure monitoring sensors deployed by the USGS prior to Ike's landfall. The SRF predictions were compared to the peak measured water level from the USGS gauges to verify its accuracy.

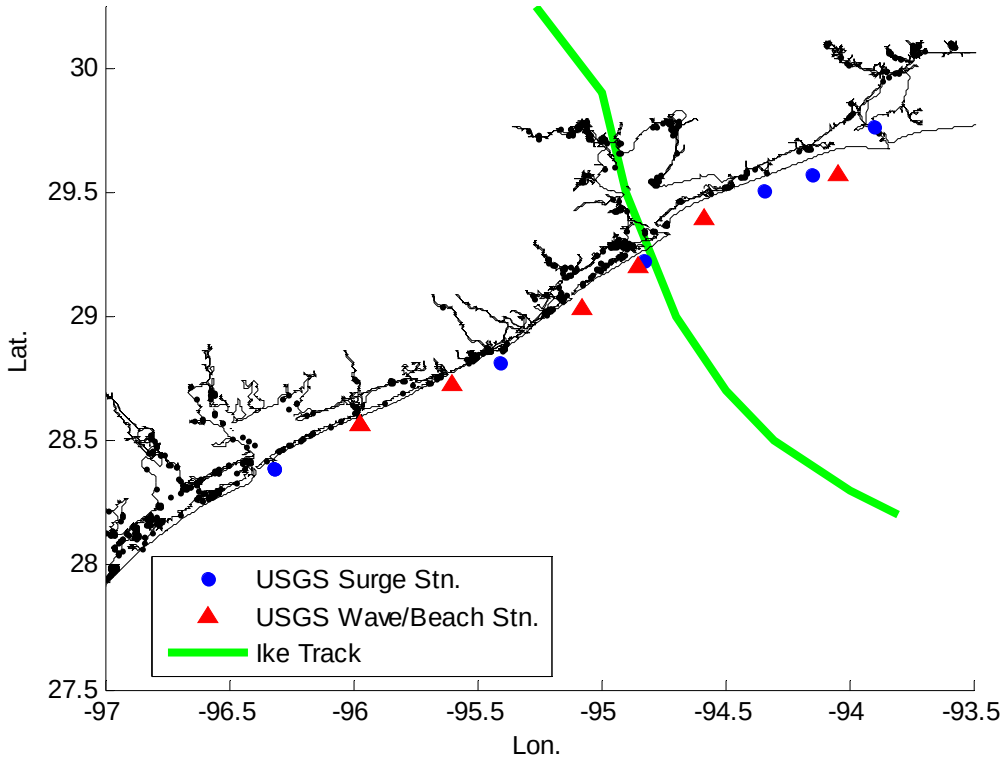

Fig. 31 Hurricane Ike tracking map and elevation stations. SRF prediction was made at stations marked with triangles and compared to the peak water level measured by USGS (2009) at the corresponding locations. The solid line shows the hurricane Ike's storm track* with respect to the elevation stations. ***Based on information from National Hurricane Center.**

7.4 Comparison of the Extreme Surges from SRF Predictions with Peak Water Level Observations

USGS (2009) has classified the site of recording the peak water level either as a surge station (Hollow on Fig. 32), or wave/beach station (Solid on Fig. 32) depending on the gauge configuration at the region. That is, in the surge-type flooding, the observed water level was presumed to have affected solely by the quasi-steady flood levels, including wave setup. On the other hand, some gauges which did not filter surface waves

are classified as a wave/beach type (USGS, 2009). With this discrimination, the surge predictions from the SRFs were compared to the peak water levels at the USGS stations. To examine the alongshore variation in the surge levels, the wave/beach stations located on the open coast were selected. However, at some locations, where the wave/beach stations did not exist nearby, the outer-most surge type stations, located behind barrier islands or in bays, were selected. In this way, the distance between consecutive stations was kept relatively constant. The numerical prediction results are listed in Table 7 and they are plotted in Fig. 32.

The data comparison shows a strong correlation, with a correlation coefficient 0.93, between the SRF values and the USGS measurements. Although the RMS for the 12 measurements is 75 cm, this was anticipated since the SRF predictions did not include the effect of wave setup or tides. However, since the effect of wave setup is smaller behind the barrier islands, much smaller differences between the SRF prediction and the surge-type flood levels are seen in; here, RMS error is 43 cm. Additionally, larger gaps between two sets of data and more scattering in USGS data are seen in the data distribution at the east side of Galveston, compared to that at the west side of stations. Considering the SRF prediction still shows consistency in surge level trend, the increase of inconsistency between SRF predictions and USGS observations near and on the right side of the location of the hurricane landfall can be explained by the effect of the changes in geographical features such as lowering of barrier islands due to relatively stronger hurricane impact in the east part of Galveston.

Table 7. Hurricane Ike surge estimation from peak surges and SRF

Hurricane Ike Surge Predictions			
Station No.	SRF Prediction [ft]	HWM above MSL [m]	SRF Prediction [m]
82	3.0	1.2	0.9
94	2.4	1.2	0.7
105	5.1	2.6	1.6
110	6.3	1.5	1.9
126	8.7	2.7	2.7
138	9.0	4.2	2.7
139	9.8	3.6	3.0
151	13.1	5.6	4.0
161	14.5	4.7	4.4
167	16.3	4.9	5.0
170	16.5	5.4	5.0
182	11.2	3.0	3.4

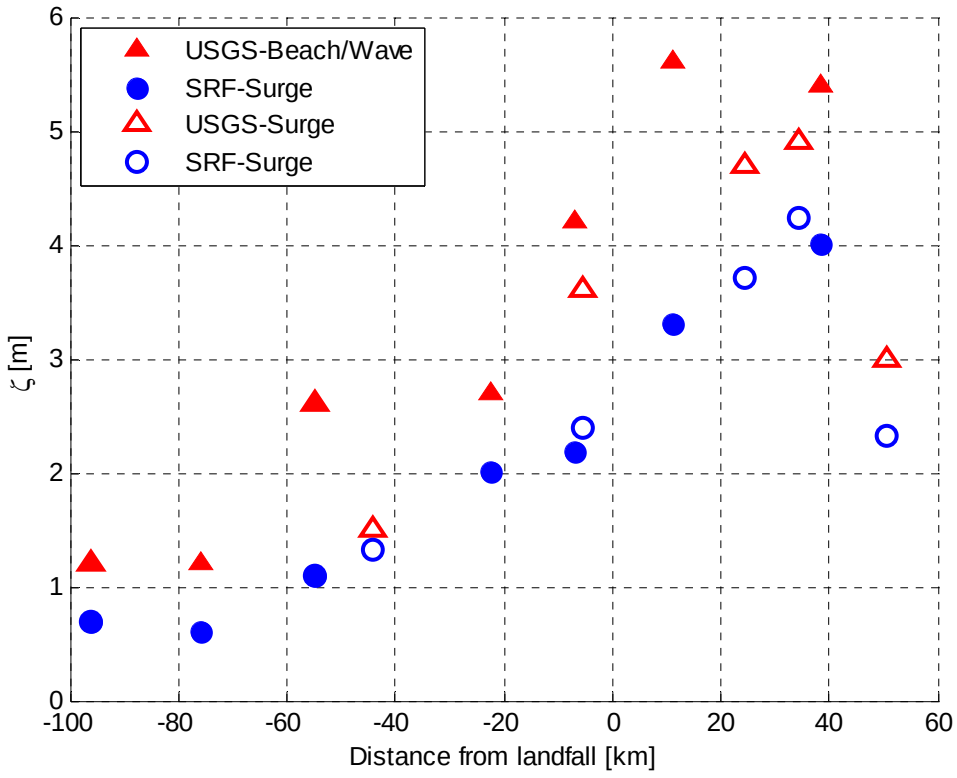

Fig. 32 Comparison of the SRF prediction to peak water level record during Hurricane Ike. Surge levels were estimated with respect to MSL at the elevation stations as shown by Fig. 18.

7.5 Discussion of the Comparisons

The two sets of comparisons between the SRF predictions and field measurements demonstrated the performance of the SRF in capturing the surge response trends with alongshore spatial changes. In particular, the information on the spatial variation in storm surge levels, produced by the SRFs, can be used in predicting the maximum flooding suspected location, along with the peak surge levels at that location.

Furthermore, the surge response predicted using several SRFs for a given hurricane condition showed a clear correlation with the observed data for both hurricanes considered. Owing to the SRF methods ability to utilize any set of hurricane

meteorological conditions by turning into the dimensionless input into a dimensionless surge, the study of two hurricanes with different meteorological conditions, making landfall at two different locations along the Texas coast, proved that the SRF can be applied for accurate storm surge predictions over a wide range of hurricane conditions.

On the other hand, as the SRF method presented here was developoed to predict the storm surge behavior with respect to the hurricane wind and pressure fields, the storm surge predictions made by these SRFs do not include the the additional surge generated by wave breaking (wave setup),), astronomical tides, and additional flooding induced by changes to geographical features (dune slope change and lowering of the barrier island) during the hurricane events. The exclusion of these factors in the SRFs, in addition to potential errors in the field measurements thhemselves, introduces a bias between the SRF predictions and the observed data., particularly along the open coast. However, even with the expected bias, the alongshore distributions between two sets of data showed strong correlation. That is to say, the difference in flood levels between two sources of data can be justified by the factors mentioned above. While the SRF method is based on parameterized meteorology, which does not account for natural variability in the hurricane wind field, for example, the relatively good correlation between the SRF predictions and the measurements gives a strong indication that the SRF method is robust enough for general application.

Development of Parameterized Surge Response Functions for Coastal Bays

A Thesis

by

RAJAT KATYAL

Submitted to the Office of Graduate Studies of
Texas A&M University
in partial fulfillment of the requirements for the degree of

MASTER OF SCIENCE

December 2009

Major Subject: Ocean and Coastal Engineering

Development of Parameterized Surge Response Functions for Coastal Bays

A Thesis

by

RAJAT KATYAL

Submitted to the Office of Graduate Studies of
Texas A&M University
in partial fulfillment of the requirements for the degree of

MASTER OF SCIENCE

Approved by:
Chairs of Committee, Jennifer L. Irish
Committee Members, David Brooks
Scott A. Socolofsky
Head of Department, David V. Rosowsky

December 2009

Major Subject: Ocean and Coastal Engineering

ABSTRACT

Development of Parameterized Surge Response Functions for Coastal Bays. (December 2009)

Rajat Katyal, B.E., Punjab Engineering College (Chandigarh)

Chair of Advisory Committee: Dr Jennifer L. Irish

In the past few years, there has been increase in number of hurricanes hitting the Gulf of Mexico coastline. These hurricanes have caused damage in the billions of dollars, and hundreds of people have been killed during these events. The damage from hurricanes is caused by four main factors: storm surges, waves, strong winds and rain. At the coast, the damage due to the storm surge and waves is dominant. Numerical simulation models like ADCIRC are available for estimating storm surge, but high computational time makes it impossible to use them for evacuation planning purposes. Public perception of storm surge hazard is based upon the Saffir Simpson scale. As demonstrated by Hurricanes Katrina and Ike, the Saffir Simpson scale does not work well for surge prediction.

The accurate and timely prediction of storm surge is very important. For this purpose, dimensionless Surge Response Functions (SRFs) for the open coast of Texas has been developed (Irish et.al 2008 and Song, 2009). The surge inside bays tends to be different than that at the open coast due to local geometric factors like shape, center of gravity, and characteristic size of the bay. To accurately predict the surge levels inside the bay,

scaling laws are developed based upon the above mentioned factors. These scaling laws are used along with SRFs for the open coast (Irish et. al. 2009) to develop dimensionless SRFs for bays. The SRFs for 3 bays, Matagorda, Galveston and Corpus Christi have been explored. Results have shown that the Surge Response method works reasonably well for Matagorda, Corpus Christi and Galveston Bay. For these bays the dimensionless surge lies within the 95% confidence interval of Surge Response Functions.

ACKNOWLEDGEMENT

I would like to thank Dr. Jennifer Irish, my advisor, for guiding me and improving my professional and technical skills throughout my studies and research at Texas A&M University. I would also like to thank my other members of committee, Dr David Brooks and Dr. Scott A. Socolofsky for reviewing my thesis and for their help in completing my master's program.

I would also like to thank my family and friends who have motivated me to attend graduate school and giving me the support to complete my master's degree.

I would also like to thank Texas General Land Office, who has provided the funds for this work to be completed.

Table of Contents

List of Figures

List of Tables

CHAPTER 1

INTRODUCTION

Development of Parameterized Surge Response Functions for Coastal Bays

According to Federal Emergency Management Agency (FEMA 2009), in the region of Atlantic Ocean, Caribbean Sea or Gulf of Mexico every year approximately ten tropical storms develop. Most of these storms dissipate over ocean and only few develop into hurricane and hit United States coastal areas. Every three years, five hurricanes have the probability of hitting the United States coastline. Two out of these five hurricanes have the probability of developing into a category 3 hurricanes as defined on the Saffir-Simpson scale. These storms cause damage in millions of dollars. Hurricanes cause damage mainly by two phenomena, first being the direct wind damage and second being the damage caused by storm surge. As hurricanes approach coast, rotating wind pushes the water at coast and generate storm surge. Storm surge is the major cause of damage at the coast and inside coastal bays.

Historically, hurricane surge had been considered to be primarily dependent upon its intensity, as represented by the Saffir-Simpson scale. But Saffir-Simpson scale fails to describe storm surge induced damage caused by hurricanes like Rita, Katrina and Ike. Thus for accurate and timely prediction of hurricane damage potential, storm surge due to various hurricane conditions should be predicted.

Various numerical models are available for predicting storm surge, but storm simulation with high resolution numerical models is highly computationally intensive with each simulation requiring of the order of 1000 hours of CPU time. Thus, use of these numerical models for planning purpose is limited. To predict hurricane surge accurately and quickly, the development of parameterized, dimensionless SRFs for Texas coastal bays (Galveston, Matagorda, and Corpus Christi) have been explored. SRFs (SRF, Irish et al., 2009) are parameterized dimensionless functions for defining continuous surge response surface. The SRF method for the open coast has been developed by identifying the relationship between the peak surge at station and the meteorological and geometrical parameters such as size, intensity and landfall location of storm. It has been shown that when SRFs approach is applied to open coast, error in surge prediction is 30 cm, which is comparable with the expected error in numerical simulations.

However, the relevant parameters influencing the form of SRFs inside coastal bays tends to differ from those along the open coast due to various local parameters related to bay configuration, including the center of gravity of bay, horizontal bay dimensions, relative position of the hurricane eye with respect to bay, mean water depth, and shoreline irregularities. Research results presented in this thesis show that the surge inside Matagorda, Galveston and Corpus Christi Bays can indeed be described in terms of these parameters by introducing additional physical scaling laws which account for bay geometry. Thus, these new parameters can be integrated with the open coast surge response to efficiently predict the storm surge inside the bay.

In the following sections first background and literature review for the work will be presented, then the study area will be described and finally the methodology and general form of SRFs developed for the bays will be presented along with its applications.

CHATER II

Background and Literature Review

2.1 Hurricanes

Hurricanes are defined as a weather system which has maximum wind speed of approximately 120 km/h or higher, is accompanied by thunderstorms and have well defined surface circulation system.

Historically hurricanes are categorized according to the Saffir-Simpson scale (Table 3) based upon their intensity and wind speed. But Hurricanes Katrina, Ike have demonstrated that intensity alone cannot be used to categorize hurricanes for predicting their damage potential.

Type	Maximum Wind Speed (km/h)	Pressure (mb)
Depression	<24.2	--
Tropical Strom	24.2-45.4	--
Category 1	46-59	>980
Category 2	59.6-68.3	965-980
Category 3	68.9-80.7	945-965
Category 4	81.4-96.3	920-965
Category 5	>96.3	<920

Table 1 Saffir-Simpson Scale

The main hazards associated with tropical cyclones and especially hurricanes are storm surge, high winds, heavy rain, and flooding. Parameters like hurricane forward speed and path are very difficult to predict, because these parameters depend upon the interaction between storm circulations, earth's atmosphere, and constantly changing

region of high and low pressure system. Based upon these complex interactions, some hurricanes follow a straight path, while other wavers along the path. Typically, the forward speeds of hurricanes are in range of 24 to 32 km/h.

2.2 Governing Equations for Storm Surge

Physics behind storm surge generation is very complex, particularly the interaction between the storms parameters and the geometric characteristics. Earlier surge prediction was based upon the historical surge data (Resio and wasterink, 2008). But due to low frequency of these events, the extent of data available was not enough to characterize the geometrical and metrological parameters. Thus use of such inadequate data leads to inaccurate prediction of storm surge.

Storm surge is generated by rotating wind and pressure deficit on its surface, which cause the water to pile up at coastline (NOAA 2009). Thus physics behind the storm surge is completely described by the 3-dimensional equations for mass and momentum conservation. Based upon these equations physics based numerical models were developed which consider both geometric and meteorological conditions for surge prediction.

Based upon the assumption that the water density in shallow water can be considered to be a constant and for storm surge generation horizontal scale is much more important than vertical scale. The 3-dimensional equations of mass and momentum conservation can be integrated over depth to generate 2-dimensional shallow water equations (Pritchard 1971). The mass conservation is represented as

$$\frac{\partial H}{\partial t} + \nabla_h \left(H \, \vec{u} \right) = 0 \tag{2.1}$$

and momentum conservation as

$$\frac{\partial \vec{u}}{\partial t} + \left(\vec{u} . \nabla_h \right) \vec{u} + g \nabla_h \xi + f \, \hat{k} \times \vec{u} + \tau_b \, \vec{u} = \psi \tag{2.2}$$

where

H is total fluid depth,

U is vertically averaged horizontal velocity,

ξ is elevation above the mean sea level

f is the Coriolis parameter,

τ is bottom stress parameter,

∇_h is the horizontal gradient operator, and

$\hat{k}$ is the vertical unit vector,

ψ is a forcing term.

The forcing for storm surge is due to the pressure difference and the wind stress (τ_s) produced at the surface of the water along with the other forces like the coriolis force, wave radiation stress, etc. The wind stress is defined as (Dean and Dalrymple, 2002)

$$\tau_s = \rho_a C_f U^2 \tag{2.3}$$

Where,

τ_s is wind stress,

ρ_a is density of air,

C_f is friction coefficient,

U is wind speed.

In deep water the rise in water level is contributed mainly by the pressure deficit at the center of the storm. The storm surge caused by the pressure deficit can be calculated (Dean and Dalrymple 2002) by

$$\xi_b = \frac{\Delta p}{\gamma} \tag{2.4}$$

where,

ξ_b is set up of surface water due to the barometric pressure deficit.

γ is the specific weight of water.

As mentioned earlier, storm surge in coastal area depends upon the interaction of meteorological parameters and coastal geometrical characteristics. The simplified storm surge at steady state near open coast can be represented as (Resio and Westerink 2008)

$$\xi_c = \left(\frac{\tau}{gh}\right) W \tag{2.5}$$

Where, ξ_c is storm surge at the coast

τ is hurricane induced wind and barometric pressure

h is depth of water

W is continental shelf width

g is the acceleration due to gravity

The dependence of surge on the characteristics like water depth and the shelf width is one of the reason for variation in surge generation from location to location for similar metrological conditions.

2.3 Numerical Studies

Accuracy of numerical models used is very important for this study. Thus it becomes very important to use a numerical model which gives result with sufficient accuracy. Provost et al. (1993) has investigated the feasibility of using a Finite Element Model (FEM) as an alternative to the Finite Difference method usually developed for high resolution large scale ocean circulation model and concluded that the Finite Element technique can be used as an alternative to more commonly used Finite Difference technique for ocean circulation models.

The effect of grid refinement on storm surge prediction was studied by Westerink et al. (1991). He found that to accurately simulate the interaction between the storm parameters and the geometrical parameters a high resolution grid is required near coastal regions. He also compared two grids, one with uniform nodal density and other with varying nodal density. He found that both grids gave similar results for storm surge prediction. Thus by adopting the finer grid in coastal regions and coarser grid in the offshore areas, computational time can be saved.

The effect of domain size on the surge prediction had been investigated by Westerink et al (1994), and it was found that the large domain containing the Western North Atlantic Ocean, the Caribbean Sea, and the Gulf of Mexico along with the boundary condition at a sufficiently offshore location gave surge predictions more accurately as compared to those obtained from computation using smaller grid domains. Regarding variable

density, Older (1981) have found that smoother and slower change in resolution helps in better prediction. Also the resolution should vary with the flow rather than across it.

2.3 Wind Models

The accuracy of storm surge prediction by any numerical model depends upon the accuracy of the wind and pressure inputs. Numerical models require specification of the surface wind, or the surface wind stress itself at high resolution throughout the life of the storm. Earlier surge model applications use simplified parametric models for atmospheric forcing while the response of the ocean is predicted based upon numerical models. In the simplest form, parametric atmospheric models use the relation between the maximum surface winds (V_{max}) and pressure drop across the storm (Δp) (Thompson et al. 1996). The relationship general form can be represented as:

$$\mathrm{V_{max}} = a(\Delta \mathrm{p}^{\mathrm{b}}) \tag{2.6}$$

Where a, b are constant and Δp is the difference in P_{far} and Pcentral.

Parametric approaches for atmospheric forcing are simplified representations of complicated processes in the atmosphere. Thus, these approaches does not always represent the wind and pressure profiles accurately, and the error induced at this stage gets carried over to the ocean response numerical models, which uses these wind and pressure fields as input. The tropical cyclone wind field can also be calculated by analysis of observation. But this approach requires large amount of measured data. Most

of the measured data available for tropical storms is for coastal areas, which does not correctly represent the data at the offshore locations.

Vortex boundary layer models based upon the primitive equations of motions have also been used for representing the tropical wind fields. The U.S Army Corps of Engineers vortex model was extensively used for storm surge modeling (Mark and Scheffner 1993). The model is based upon the concept that the tropical storm changes its structure relatively slowly. Thus, the tropical cyclone is represented by a small number of snapshots representing the different phase of storms and the intermediate transition between these storms. The model is based upon the equation of horizontal motion vertically averaged through the depth of the Planetary Boundary Layer (PBL) (Chow 1971, Cardone et al. 1992). The final form of equation represents the balance between the Coriolis force, the pressure gradient force and the frictional force at the outermost boundary

$$fK \times (V - V_g) = -\frac{1}{\rho}\nabla P_c - \frac{C_D}{h}|V + V_c|(V + V_c) \tag{2.7}$$

The simplest pressure field is defined by the exponential pressure law and is of the form

$$P_c(r) = Po + \Delta pe^{(\frac{-R_p}{r})} \tag{2.8}$$

These equations are solved over a grid which is a system of rectangular nests, with the very fine spacing near the hurricane center and relatively coarse spacing in the outer regions. Chow (1971) provides the detail of the grid and the computational scheme followed in the model. The limitation of the horizontal spatial resolution was addresses

in Cardone et al. (1994) in which the horizontal computational nests were increased from five to seven. The option has provided an increase in the spatial resolution around the centre of storm and also extends the computational nests which allow better application of far field boundary condition.

The wind model used for this study is PBL model (Thompson et al. 1996). Detailed description of model and its interaction with the numerical model is provided in Chapter 4.

2.6 Surge Response Functions (Open Coast):

To predict potential damage due to hurricanes, agencies like National Ocean and Atmospheric Administration (NOAA) and Federal Emergency Management System (FEMA) uses the Saffir Simpson scale. But damage caused by Hurricane Katrina, which was a Category 3 storm (NOAA) at landfall, cannot be explained by the Saffir-Simpson scale. Irish et al (2008) has shown that the storm size plays a key role in generating the surge in coastal areas. They have concluded that for a given intensity, storm surge varies by 30% for reasonable variation in storm size. SRFs for the open coast were developed by Irish et al (2009). It showed that the surge response surfaces changes continuously with the meteorological parameters like size, intensity of storm along with geometrical parameters like landfall location of storm and station location of interest. They investigated the surge response surfaces for the four tracks as shown in Figure 1 and gave relationship between the distance between the peak surge, the landfall location and the size of the storm. They represented this relationship as

$$X_{\xi peak} - X_o \cong \lambda R_p \tag{2.10}$$

Based upon this, they proposed the dimensionless distance in the form of

$$X' = \frac{X - Xo}{R_p} - \boldsymbol{\lambda} \tag{2.11}$$

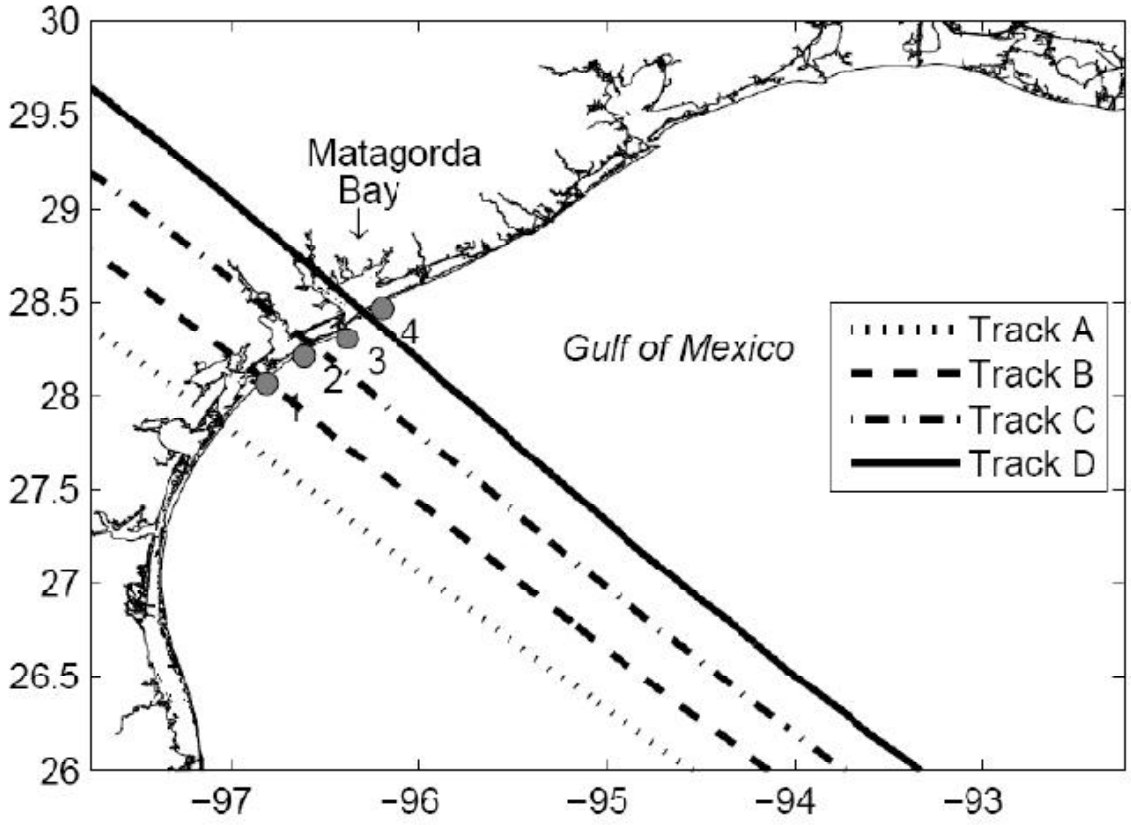

Figure 1 Matagorda Tracks for open coast SRF (from Irish et al. 2009)

After performing linear regression analysis on the numerical simulation results for the four tracks, they have found the slope (λ) to be 0.87. More recently, the values of λ along the Texas coastline have been shown to vary (SONG 2009) based upon the variation of the continental shelf width along Texas coastline**.** Irish et al. (2009) define a

dimensionless surge (ξ′) as a function of peak surge at the station and the pressure deficit:

$$\xi' = \frac{\gamma\xi}{\Delta p} + m_x \Delta p \tag{2.12}$$

where, m_x is a constant determined by linear regression analysis at each station. To account for secondary effect related to storms of size less than the threshold size($R_{thres} = 25km$), alongshore distance (X_2') was modified to a form

$$X_2' = X' - F(1 - R')H(1 - R') \tag{2.13}$$

Where R' is a dimensionless storm size defined as

$$R' = \frac{R_p}{R_{thres}} \tag{2.14}$$

R_{thres} = Threshold size of storm=25 km.

$H(1 - R')$ is a heaviside function defined as

$$H(1 - R') = \begin{matrix} 1 & for\ x \geq 0, \\ 0 & for\ x < 0. \end{matrix} \tag{2.15}$$

$F(1 - R')$ is a Ramp function defined as

$$F(1 - R') = \begin{matrix} a_1(1 - R') + b_1, & -\lambda \leq x' \leq 0, \\ a_2(1 - R') + b_2, & 0 < x' \leq \lambda, \\ 0, & \lambda < |x'|. \end{matrix} \tag{2.16}$$

The coefficients *a* and *b* for Texas coast were determined by linear regression to be

a_1 = -1.04, b_1 = 0.16, and

a_2 = 3.29, b_2 = -0.67.

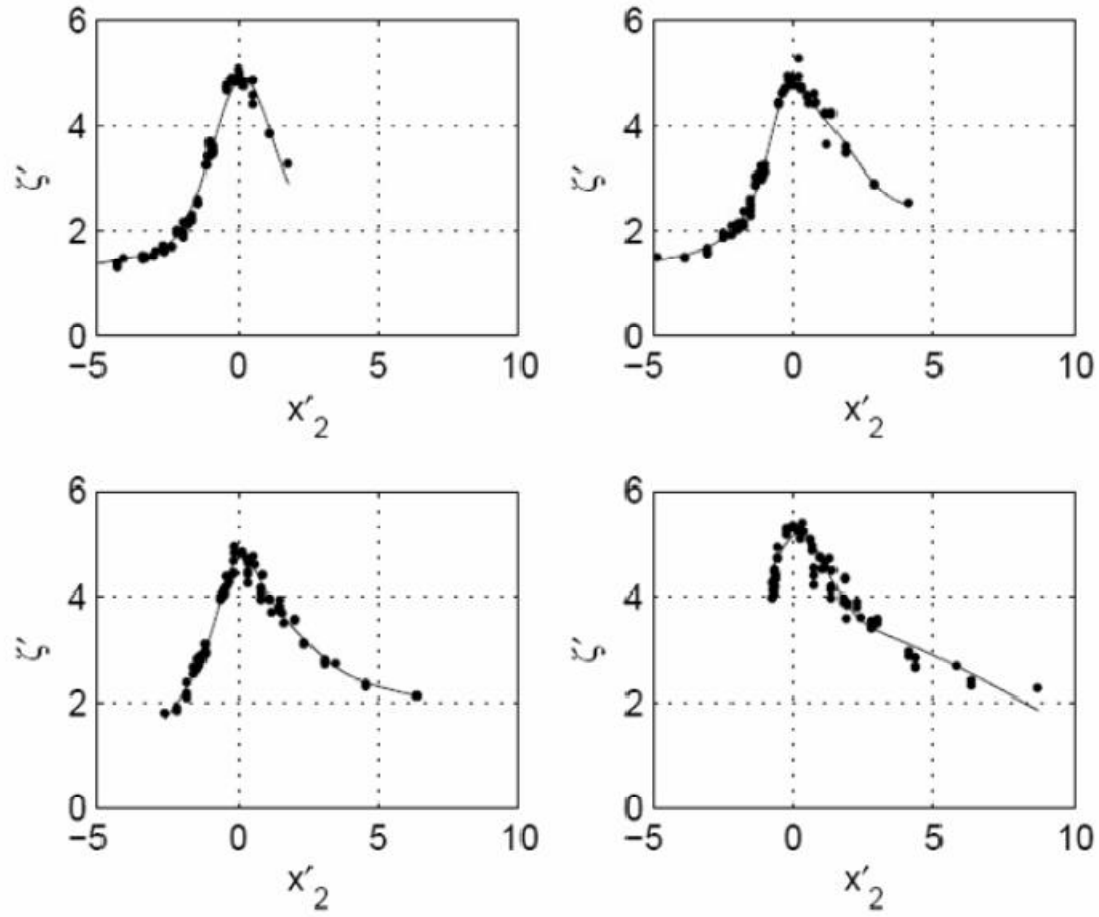

Figure 2 Open coast SRF (from Irish et al. 2009)

They have found that the Gaussian 3 term distribution represents non-dimensional data at most stations. The R-square value for fit at these stations is above 0.9 for Gaussian 3 term fit. The coefficients for Gaussian fit at these locations were determined based upon linear regression analysis. Figure 2 shows the SRFs predicted at four locations near the Matagorda Bay. At all of these locations the mean of error between the simulated surge

values and the predicted surge values was in range of 13 to 24 cm, which is comparable to the accuracy of numerical models for storm simulations. Irish et. al (2009) also showed, that the SRFs work well for limited data sets.

Chapter III

Study Area

3.1 Introduction

For the purpose of this study, three bays (Matagorda, Galveston and Corpus Christi Bay) have been selected along the Texas coastline. Hypothetical storms have been simulated and the peak surge values have been extracted at the various stations inside the bays for these simulations. Analysis at these stations is performed to extend the SRF method (Irish et al. 2009) for application inside the bays.

3.2 Matagorda Bay

Matagorda Bay is located between Calhoun and Matagorda counties on Texas coast. The bay has three inlets through which it interacts with the Gulf of Mexico. The average depth inside the bay is around 2.5 m with respect to geoid. On the west side of bay there is a deep shipping channel with a depth of 17m. The center of gravity of bay is shown in appendix A.

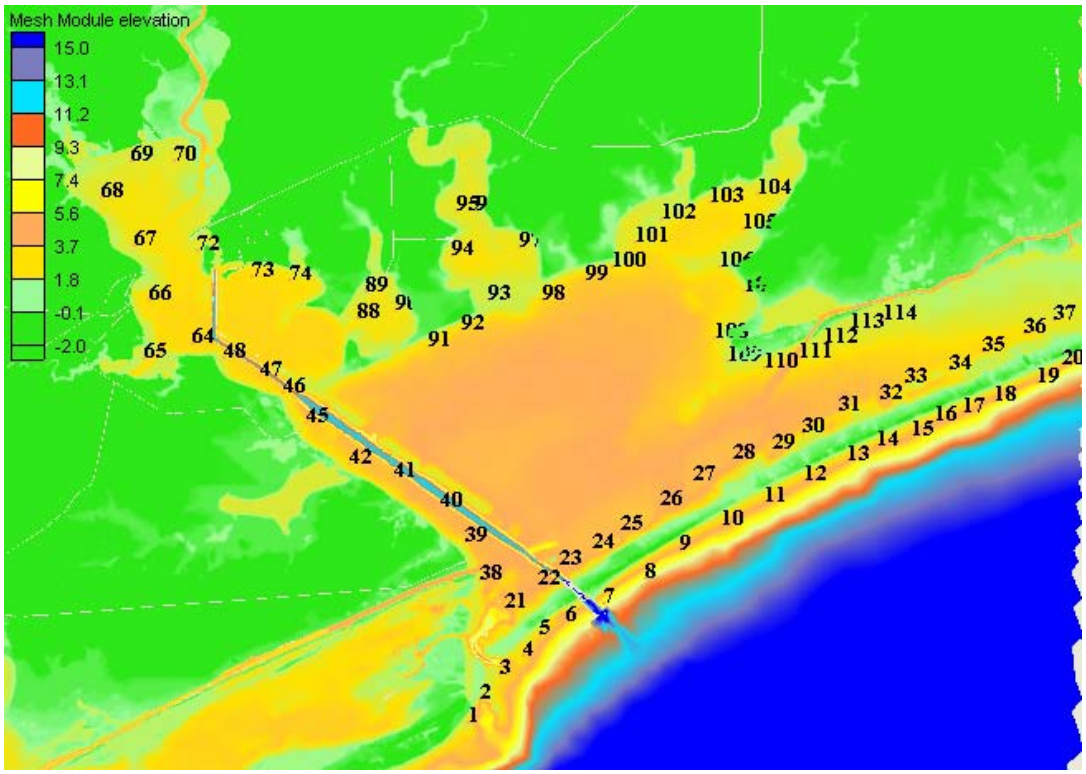

Figure 3 Matagorda contour and stations locations.

For the purpose of development of SRFs, a total of 128 stations were selected inside the bay as shown in Figure 3. The details of the station location have been attached in appendix A.

3.3 Galveston Bay

The Galveston Bay is the largest estuary on the Texas Coast (Gulf Base 2009). It consists of six sub bays systems. The bay covers approximately 1,500 km², and is 50 km long and 27 km wide. The average depth of Galveston Bay is 2.0m with respect to the geoid. The bay has three inlets at the Gulf of Mexico. Like Matagorda Bay, Galveston

also has a deep shipping channel on the west side of the bay. In Galveston Bay a total of 159 stations were selected for SRFs development as shown below in Figure 4.

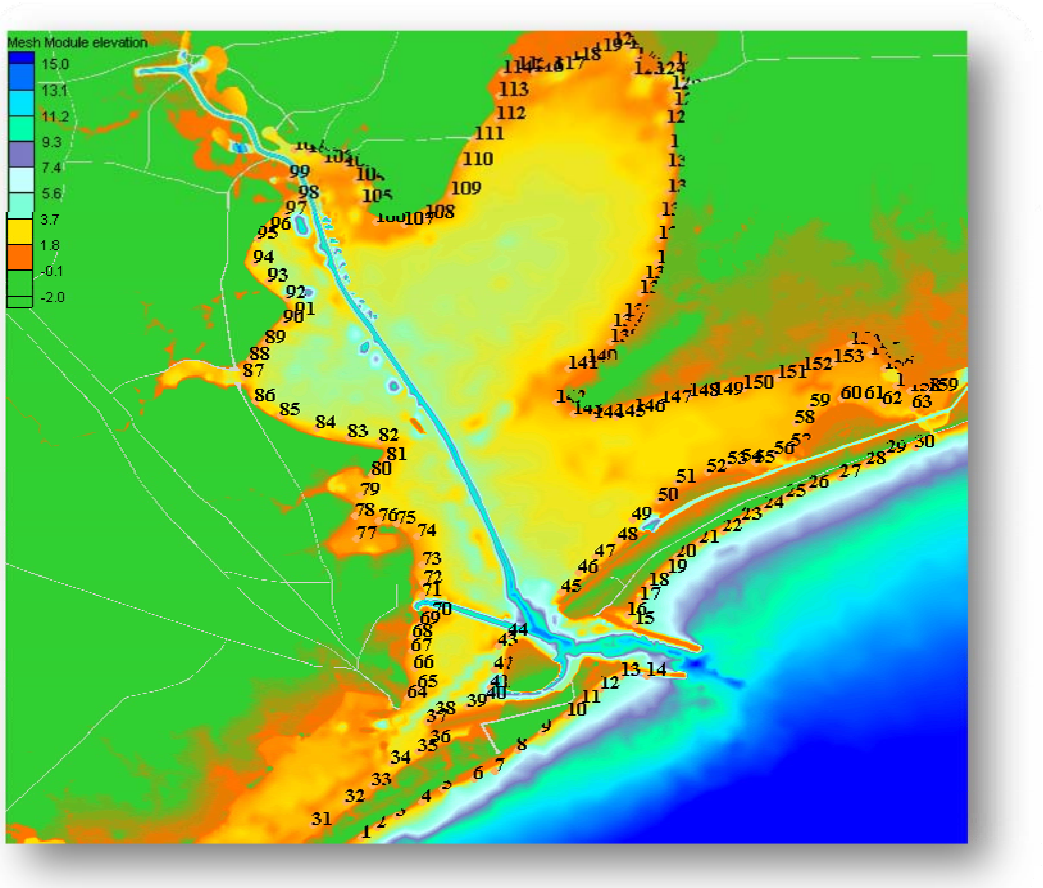

Figure 4 Galveston contour map and station locations

The details for the station locations (Latitude and Longitude) and Center of Gravity of bay are attached given in appendix A.

3.4 Corpus Christi Bay:

Corpus Christi is located in the southern Texas coast. The bay is 15km long and 22 km wide. The average depth of the bay is 3.0 m with respect to geoid.

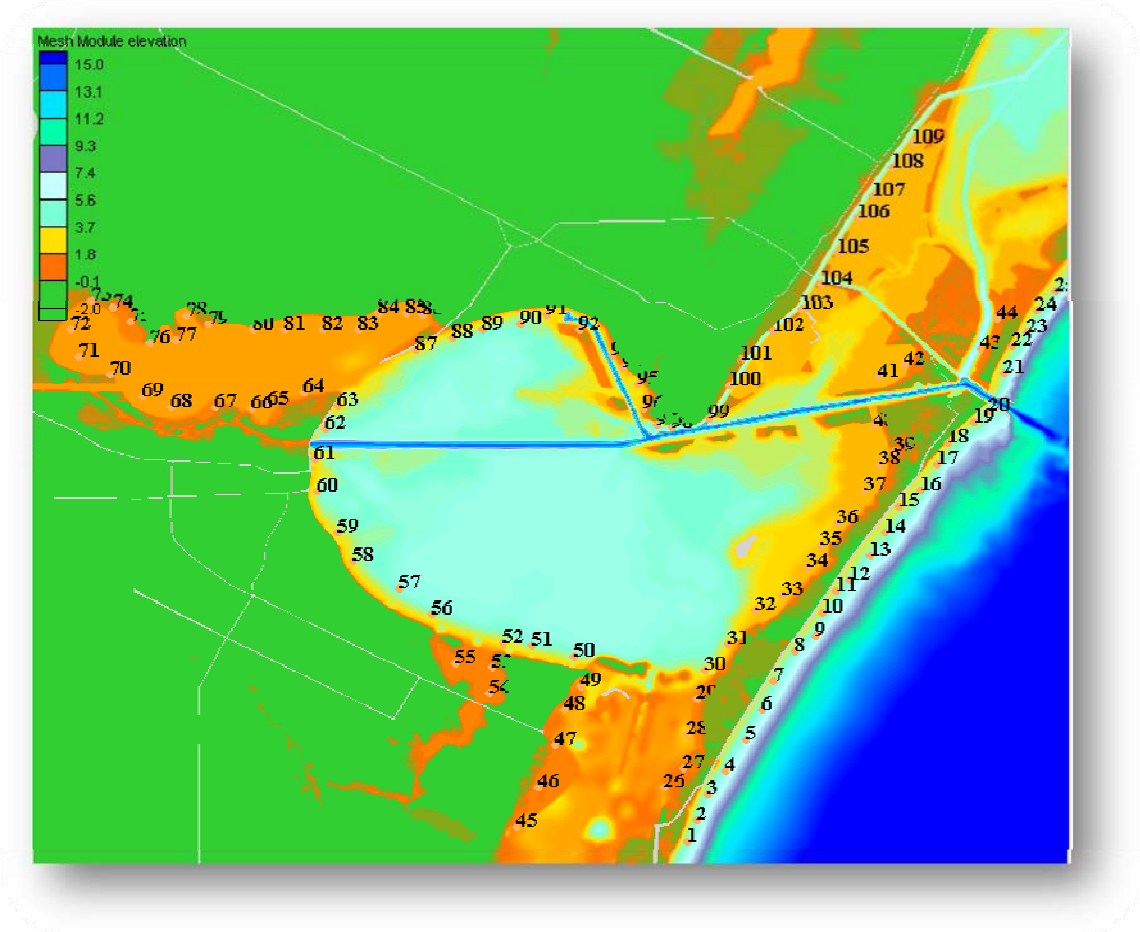

Figure 5 Corpus Christi Bay contour map and stations location.

The Figure 5 shows the contour map for the Corpus Christi Bay and the locations of 109 stations which are selected for SRF's analysis. The details of station locations (Latitude and Longitude) and Center of Gravity of bay are attached in appendix A.

Chapter IV

Numerical Simulations

The interaction between hurricane wind forcing and bay parameters like bathymetry, shape and size of a bay are very complex and needs to be understood for defining SRFs inside bays. To understand the response of bays to a hurricane wind forcing, sufficient amount of storm surge data is required in the area of interest. In this section, the numerical model used for simulations, model domain, wind model, and the storms parameters used for simulations are described.

4.1 ADCIRC Hydrodynamic Model

For accurate prediction of surge inside bays, the hydrodynamic numerical model needs to have a high resolution in area of interest and large domain size. A large domain helps in specifying the boundary conditions at offshore locations which reduces the errors caused by the boundary conditions. The variable grid density is required for more refined grid near coastal location as this helps in saving the computational time with less dense grid in offshore locations compared to coastal areas. For these reasons ADCIRC (Luettich et al., 1991 and 1994; Westerink et al, 1992) which is an advanced hydrodynamic model and uses a finite element scheme in space and finite different method in time to solve the Generalized Wave Continuity Equation (GWCE) (4.1) is chosen for simulating storm surge in area of interest. The GWCE is derived by differentiating continuity equation with respect to time and by spatially differentiating

the conservation of momentum equation. The GWCE in cartesian coordinates is as follows:

$$\frac{\partial^2\xi}{\partial t}+\tau_o\frac{\partial\xi}{\partial t}+\frac{\partial}{\partial x}\{U\frac{\partial\xi}{\partial t}-UH\frac{\partial U}{\partial x}-VH\frac{\partial V}{\partial x}+fVH-H\frac{\partial}{\partial x}\left[\frac{P_S}{p_o}+g(\xi-\alpha\eta)\right]$$
$$-E_{h2}\frac{\partial^2\xi}{\partial x\partial t}+\frac{\tau_{sx}}{\rho_o}-(\tau_*-\tau_o)UH+\frac{\partial}{\partial y}\{V\frac{\partial\xi}{\partial t}-UH\frac{\partial V}{\partial x}$$
$$-VH\frac{\partial V}{\partial y}-fUH-H\frac{\partial}{\partial y}\left[\frac{P_S}{p_o}+g(\xi-\alpha\eta)\right]-E_{h2}\frac{\partial^2\xi}{\partial y\partial t}+\frac{\tau_{sy}}{\rho_o}$$
$$-(\tau_*-\tau_o)VH=0 \qquad 4.1$$

ADCIRC-2DDI is a two dimensional depth integrated model which uses depth integrated mass and momentum equations subjected to incompressibility, Boussinesq and hydrostatic pressure approximations as its basis.

$$\frac{\partial\xi}{\partial t}+\frac{\partial UH}{\partial x}+\frac{\partial VH}{\partial y}=0 \qquad 4.2$$

$$\frac{\partial U}{\partial t}+U\frac{\partial U}{\partial x}+V\frac{\partial V}{\partial x}-fv=-\frac{\partial}{\partial x}\left[\frac{P_S}{p_o}+G(\xi-\alpha\eta)\right]+\frac{1}{H}M_x+\frac{\tau_{sx}}{\rho_{oH}}-\tau_*U \quad 4.3$$

$$\frac{\partial V}{\partial t}+U\frac{\partial V}{\partial x}+V\frac{\partial V}{\partial x}-fU=-\frac{\partial}{\partial y}\left[\frac{P_S}{p_o}+G(\xi-\alpha\eta)\right]+\frac{1}{H}M_y+\frac{\tau_{sy}}{\rho_{oH}}-\tau_*V \quad 4.4$$

where,

ξ= Free surface elevation relative to the geoid

U,V= depth averaged horizontal velocity

H=h+ξ= Total water column

h= bathymetric depth relative to geoid

f= coriolis parameter

Ps= atmospheric pressure at free surface

g= acceleration due to gravity

η= Newtonian equilibrium tide potential

α= effective earth elasticity factor

ρ_o= density of water

τ_{sx}, τ_{sy}= free surface applied stress

E_{h2} = horizontal eddy diffusion coefficient

$$\tau_* = C_f \frac{\sqrt{(U^2 + V^2)}}{H}$$

Cf= bottom friction coefficient

The ADCIRC-2DDI model can be forced with elevation boundary forcing, variable spatial or temporal free surface stress and atmospheric pressure forcing. ADCIRC can be run in parallel on a multiprocessor with a suitable platform (MPI). This feature reduces the computational burden imposed by simulating at high resolution domain on single CPU. In a parallel run, ADCIRC partitions the grid and other input files to assign them

to independent CPUs. After processing these files, ADCIRC reassembles the output generated by each CPU to give the final result. Thus through parallel run it saves the CPU time as well as computational requirement for simulating a large domain size.

4.2Model Domain

In this study, the east coast computation domain of Westerink et al. (2006) is used as the model domain. The grid includes the Western North Atlantic Ocean, the Caribbean Sea, and the Gulf of Mexico. The offshore boundary is defined at east coast which extends from Glace Bay to the Corocora Island in eastern Venezuela along the 60^oW meridian. Other boundaries are defined by the eastern coastlines of North, Central and South America. The approximate size of grid in Coastal areas is 0.006^o while in offshore it is 1.15^o. The bathymetry in Gulf of Mexico region is in accordance with detailed database used by Westerink et al. (1992). The key parameters of the grid are as follows

- Number of nodes 1,344,247
- Number of elements 2,628,785
- Area 8.352 X 10^6 km^2
- Maximum depth 7858.09 m
- Grid size in deep ocean 1.15^o
- Grid size in coastal areas 0.006^o

The model domain used for simulations is shown in Figure 6.

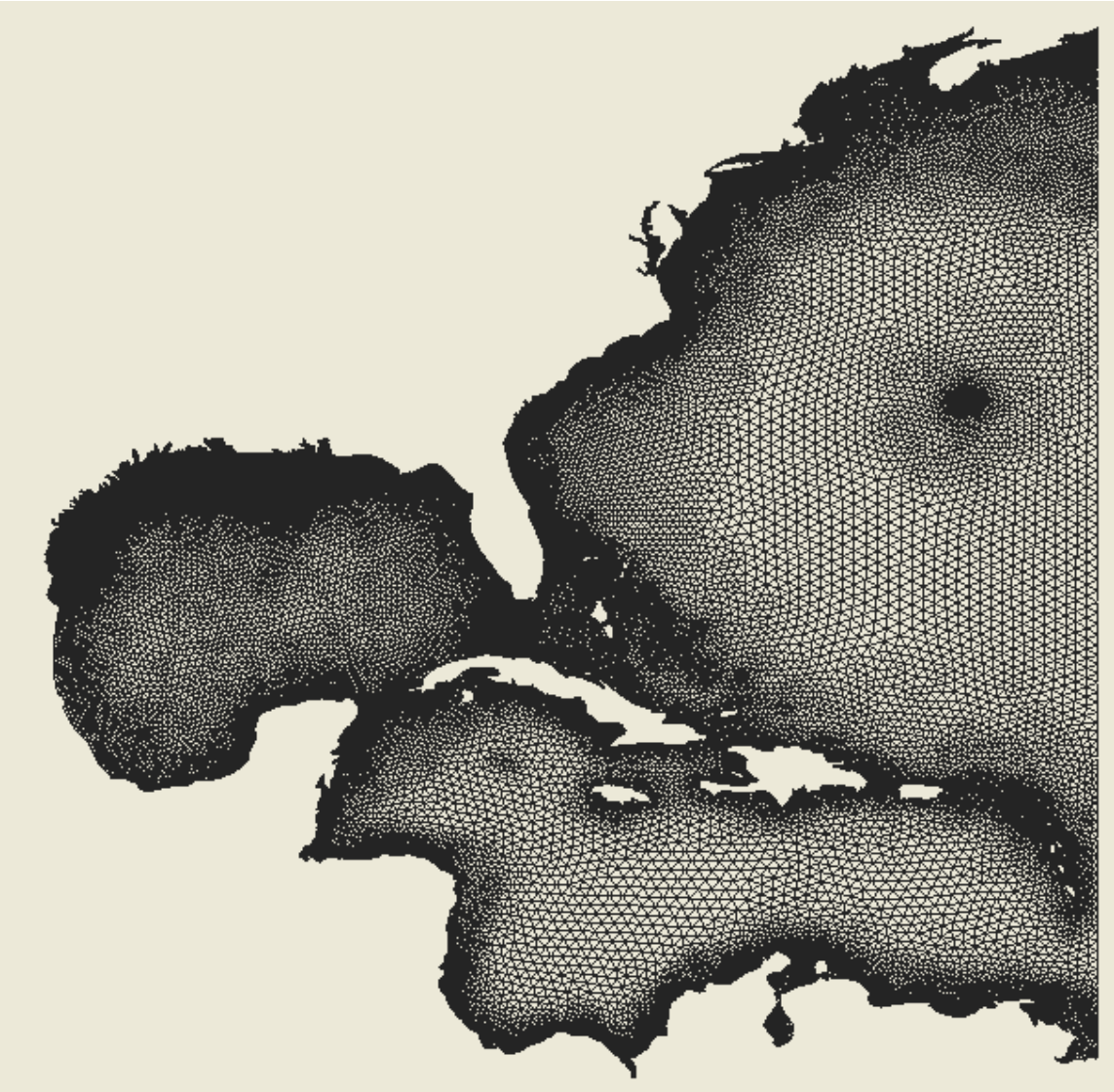

Figure 6 Computational domain

4.3 Wind Field Model

For predicting storm surge ADCIRC uses wind and pressure fields as inputs at every time step. Thus accuracy of results provided by ADCIRC depends upon how accurately wind and pressure field are fed into it. Therefore, the choice of wind model becomes very important to predict storm surge accurately. Development of various wind models

has been discussed in Section 2.3. In this study, the Planetary Boundary Layer (PBL) model of Thompson and Cardone (1996) is used to generate wind and pressure fields.

The PBL model is based upon vertically averaged, horizontal equation of motion in moving coordinate system (Chow, 1971; Cardone et al., 1992). The wind and pressure fields in PBL model are defined as a function of storm parameters like intensity, size, forward speed and Holland B parameter (B, Holland (1998)). In the PBL model Pressure field is defined as an exponential law given by

$$P_c = P_{eye} + \Delta P e^{-(\frac{R_p}{r})^B} \tag{4.5}$$

Where

P_{eye} is the pressure at eye of storm.

ΔP is difference in far away pressure and P_{eye}.

r is the distance from the eye of storm.

R_p is the pressure scale radius for PBL model.

B is a constant in the general range of 0.5-2.5

In PBL model it is assumed that the wind field pattern changes slowly and hurricane wind filed can be described by discrete number of snapshots representing the various phases of wind field and transformation of these phases. PBL computes the wind velocities and pressure at the grid points as described in Figure 7 at specified time steps

based upon storm parameters specified. For this study, inputs for wind speed and pressure were given after every fifteen minutes. The nested grid is obtained by using seven grids with linearly increasing grid spacing (1.25km, 2.5km, 5km, 10km, 20km, 40km, and 80km), with most dense grid near center of hurricane (Figure 8). The high resolution grid at the center of hurricane helps in predicting the variation in wind and pressure field at high resolution in this region as compare to the outer region where variation in wind and pressure field is comparatively less.

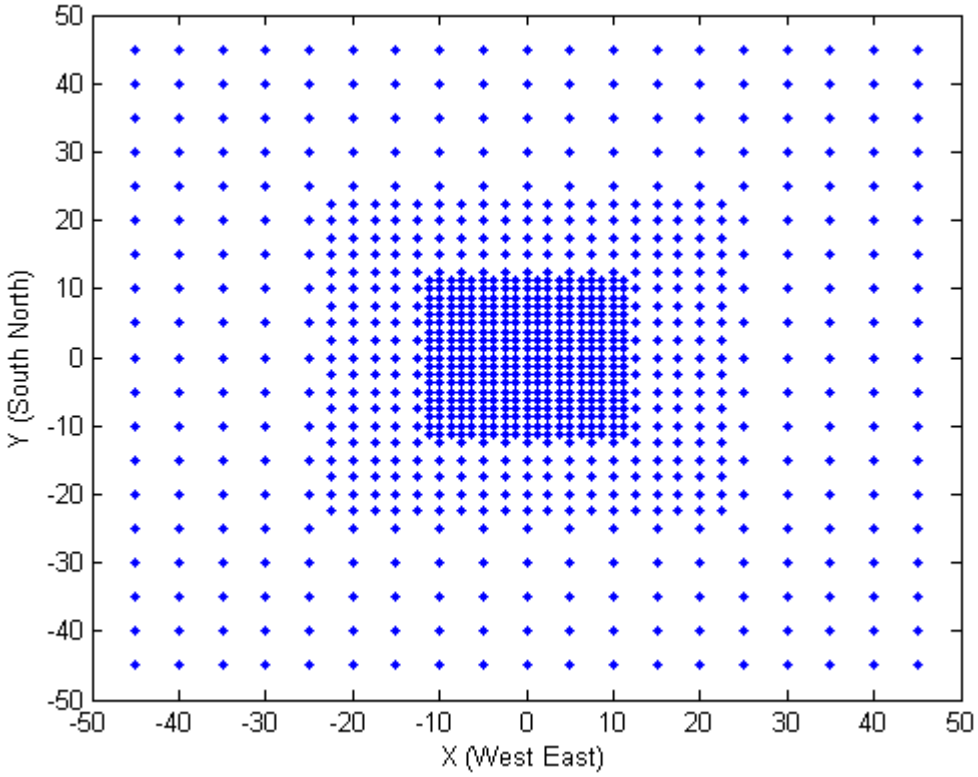

Figure 8 PBL grid nests

Iterative procedure to compute the wind and pressure field is used at each grid point starting with initial guess of gradient of wind field components from hurricane pressure field. Figure 9 shows the contour map and wind velocity for a storm on track near Matagorda Bay.

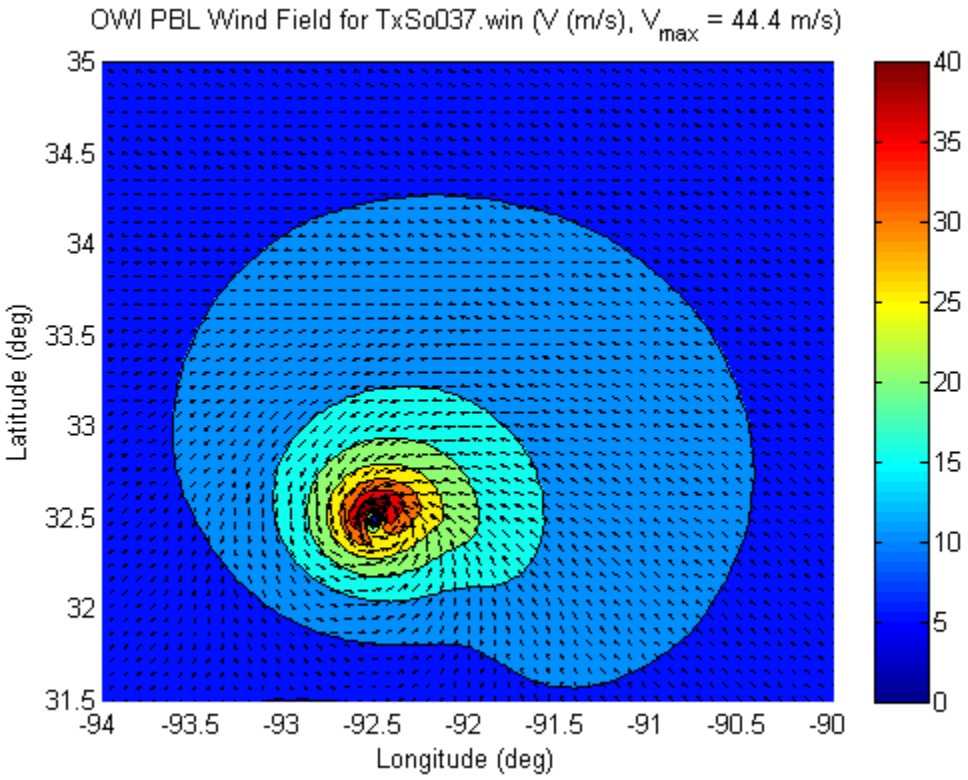

Figure 9 PBL wind field contour profile

4.4 Storms selection

For this study, total of 106 simulations were made on 9 tracks as shown in Figure 10. Along with variation in track, size and intensity of storms were varied from 11 km to 66

km and 900mb to 960mb respectively. The storm size and intensity for these simulations were specified based upon data set of Irish et al. (2009).

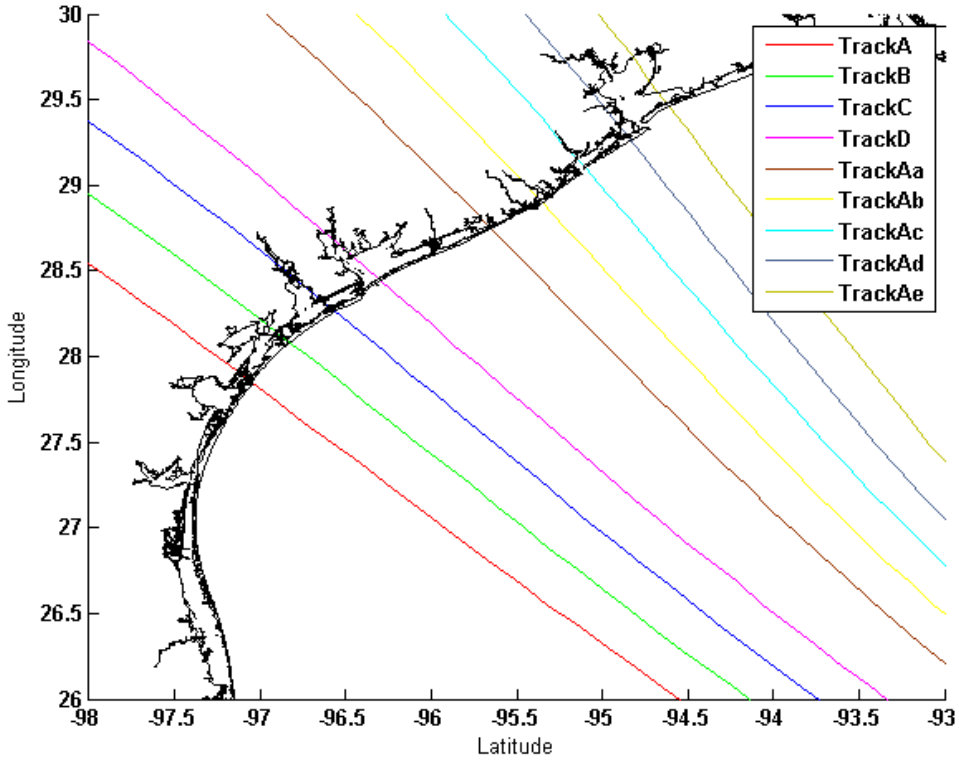

Figure 10 Tacks

Response due to forward speed (5.7 m/s) of hurricane and track angle (17^{o} or less) is assumed less important as compared to the variation in factors like intensity and size of storm, thus forward speed and track angle are kept constant (Irish et al. 2009). The Holland B parameter was kept to be constant (1.27) until the hurricane is 50 km away from the land fall and after that it was decreased to 0.9.

Chapter V

Methodology

5.1 SLOSH Database Comparison with Open coast SRFs

SLOSH (Sea Lake and Overland Surge from Hurricanes) is the model used by NOAA for predicting the surge level in case of hurricanes. Its database includes the results of several hypothetical storms for many different basins. The database provides the MEOW (Maximum Envelope of water), where MEOW represents the maximum level of water reached at a location for several storms of same category along with forward speed and direction, but for tracks parallel to each other. The category of hurricane is based upon the Saffir-Simpsons Scale (Table 1)

For the purpose of comparison of the results of SLOSH and the SRFs (open coast), two locations have been selected at an open coast area near Matagorda Bay as shown in the figure below. At these locations, SLOSH results have been extracted and plotted along with the surge levels calculated by SRFs.

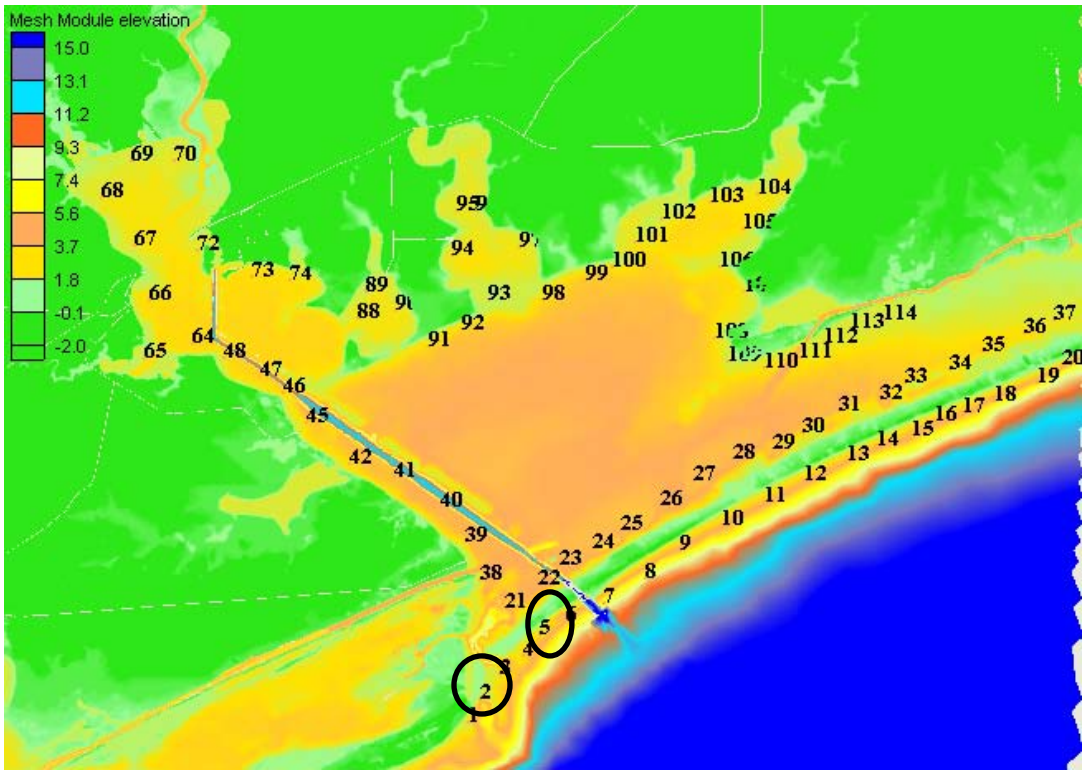

Figure 11 Stations location for SLOSH and SRF comparison

The SLOSH gives the range of surge levels at any station based upon Saffir Simpson category of hurricane and speed of the storm, whereas the surge values from the SRFs depend upon the intensity, size and location of the storm with respect to the station location. Figure 12 through Figure 13 show the results for station 2, and 5. As seen from the plots for both the stations, the SLOSH database gives higher surge values as compared to the SRF by 0.61 to 0.76 m. The reason for this seems to be wave setup which is not included in the SRF term. However, what is most important in comparison is that the SLOSH gives a constant value for each category of the storm, whereas SRF shows that we get a range of values depending upon the landfall location, size and

intensity of the storm. The SRF results show that with the change in landfall location (XXo) with respect to the station location surge value for a particular storm changes.

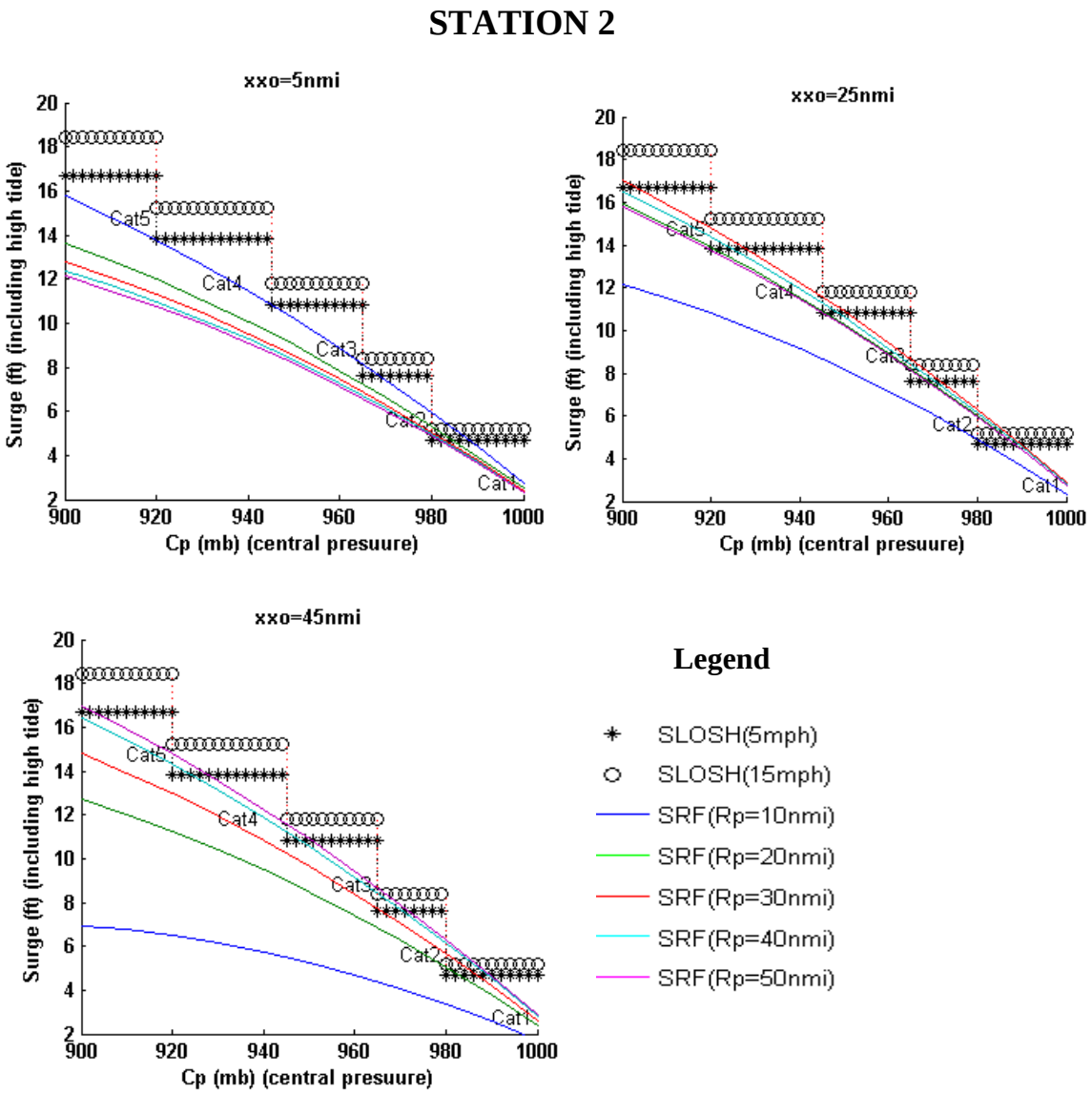

Figure 12 SLOSH and SRF comparison, station 2

STATION 5

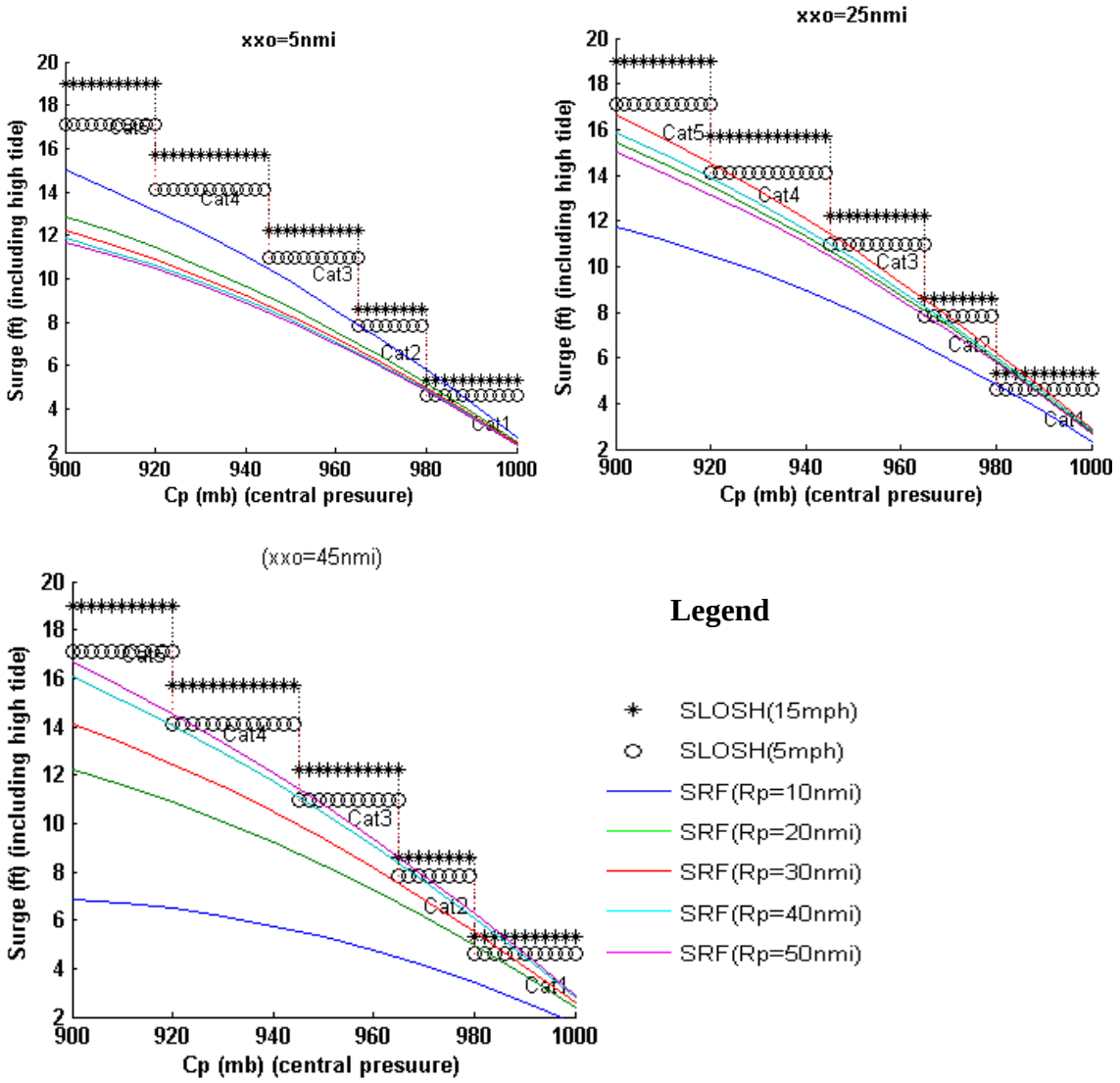

Figure 13 SLOSH and SRF comparison, Station 5

5.2 Application of Open Coast SRFs inside Matagorda Bay

SRFs for open coast, as described in section 2.6 use a linear distance for a station and land fall location. This methodology has worked well for open coast, but inside bay it is not possible to define these linear distances at all locations due to irregular shape of the bay. To check the effectiveness of the methodology inside the bay, inlet location of

Matagorda Bay has been selected to define the linear distances. For all locations inside the bay non-dimensional distances used are that of the inlet station and this non dimensional distance is plotted at each station with the corresponding non-dimensional surge values and other important assumption made is that the lambda value used at all stations inside the bay is obtained from open coast. With these two assumptions the non-dimensional distance and non-dimensional surge values are plotted and the results are shown in the figure below.

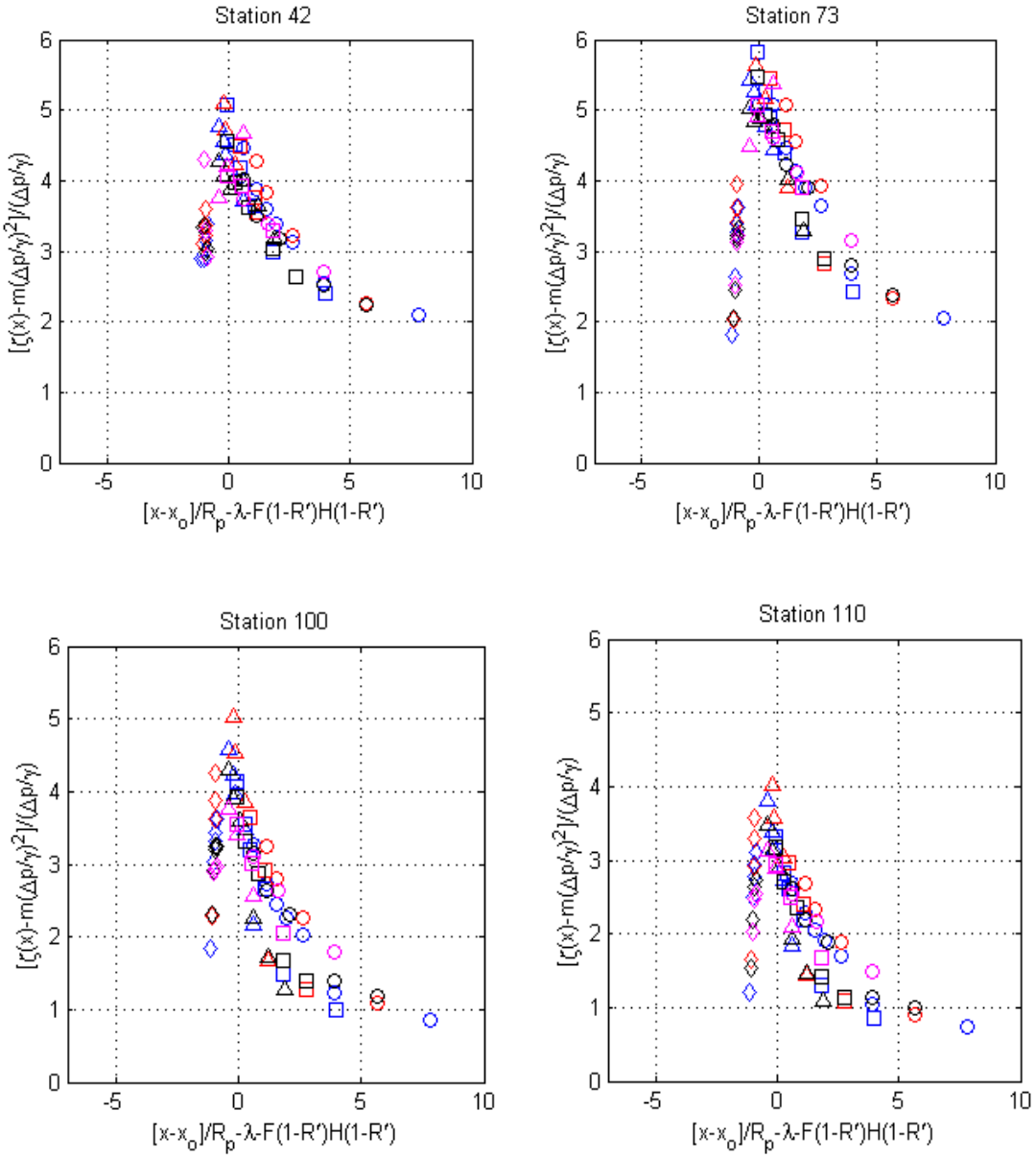

Figure 14 SRF inside the bay with open coast methodology.

SRFs give the same shape inside the bay as for the open coast, but simulations are much more scattered inside the bay as compared to the open coast. The R-square value for station at open coast is in range of 0.9 to 0.97, while for stations inside the bay R-square

values are in range of 0.55 to .68. Thus we can say that the SRF methodology for open coast does not work well inside the bay.

5.3 Effect of inlet opening:

As a storm approaches a bay, it pushes the water with it. Water enters into the bay through an inlet opening and sometime by overtopping of a barrier island. Thus the amount of water entering into the bay, and in turn the storm surge inside the bay, is dependent on the inlet opening.

This section deals with the effect of inlet opening on the storm surge inside Matagorda Bay. To study the effect of inlet opening on surge inside the bay, one of the Matagorda Bay openings was blocked as shown in Figure 15.

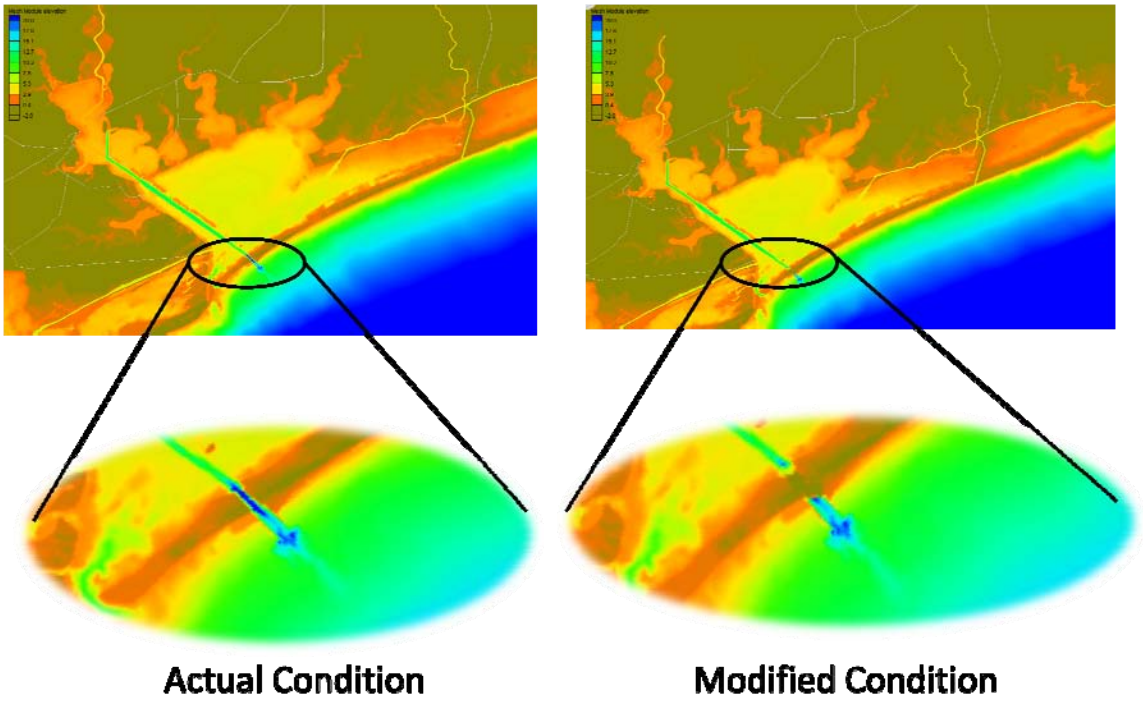

Figure 15 Matagorda Bay, showing actual and modified inlet condition.

With the modified grid configuration, storm of size (Rp) 11 km and central pressure 960 mb was simulated on three tracks(A,B,C) as shown in Figure 10.

The simulation results with the inlet opening blocked was compared with the results for inlet open conditions. Figure 16 and Figure 17 Time series for Station show time series of the simulation with two conditions for open coast stations 7, 12 for the three tracks.

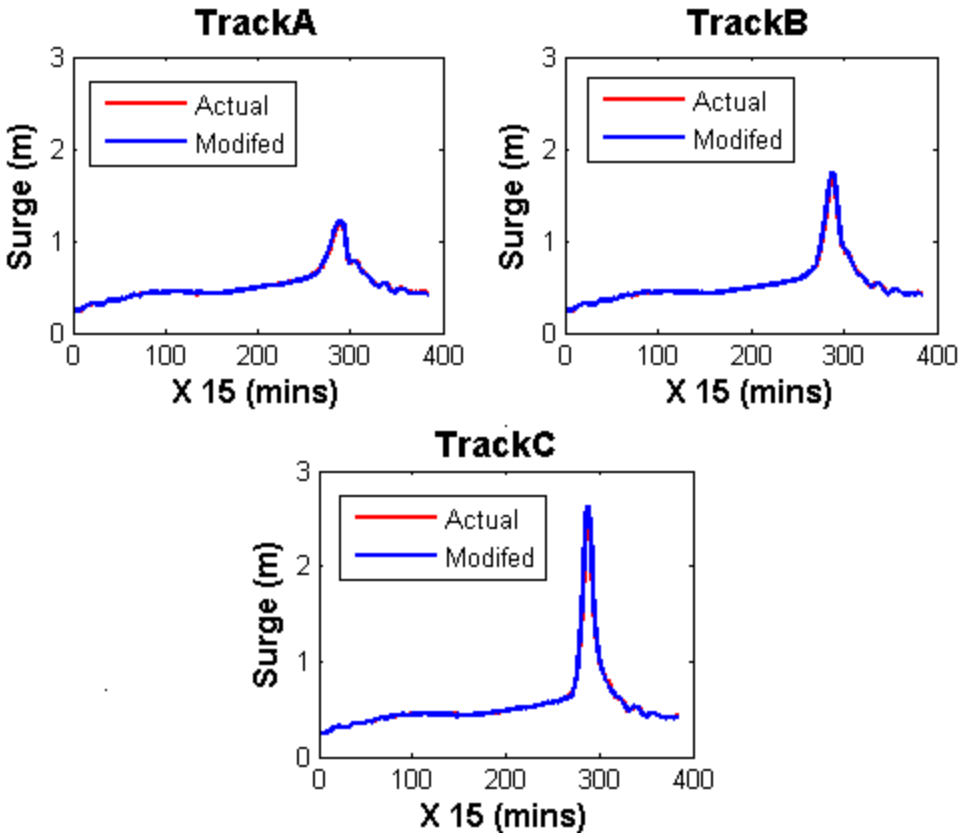

Figure 16 Time series for station 7

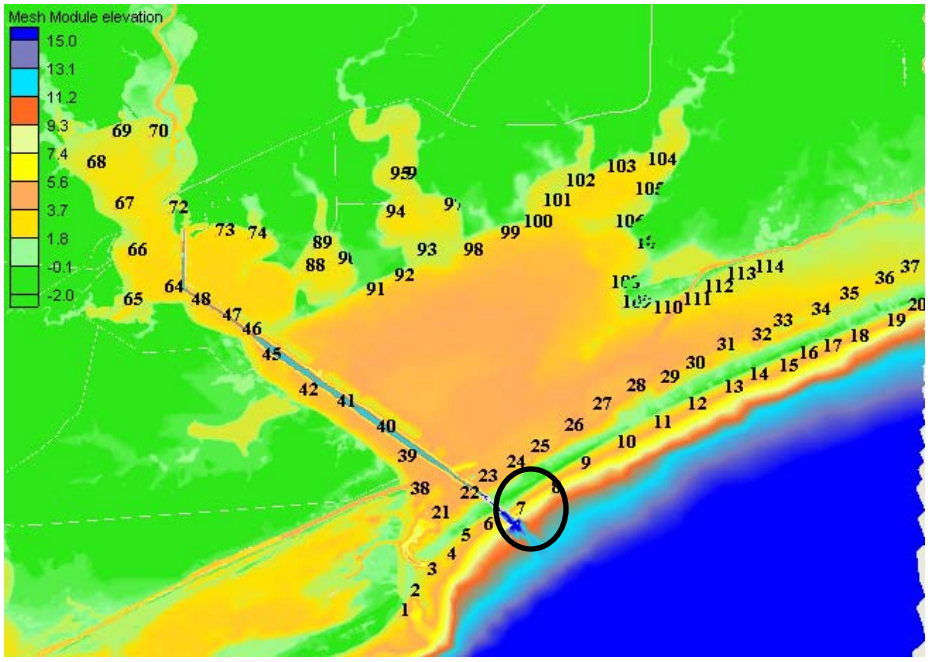

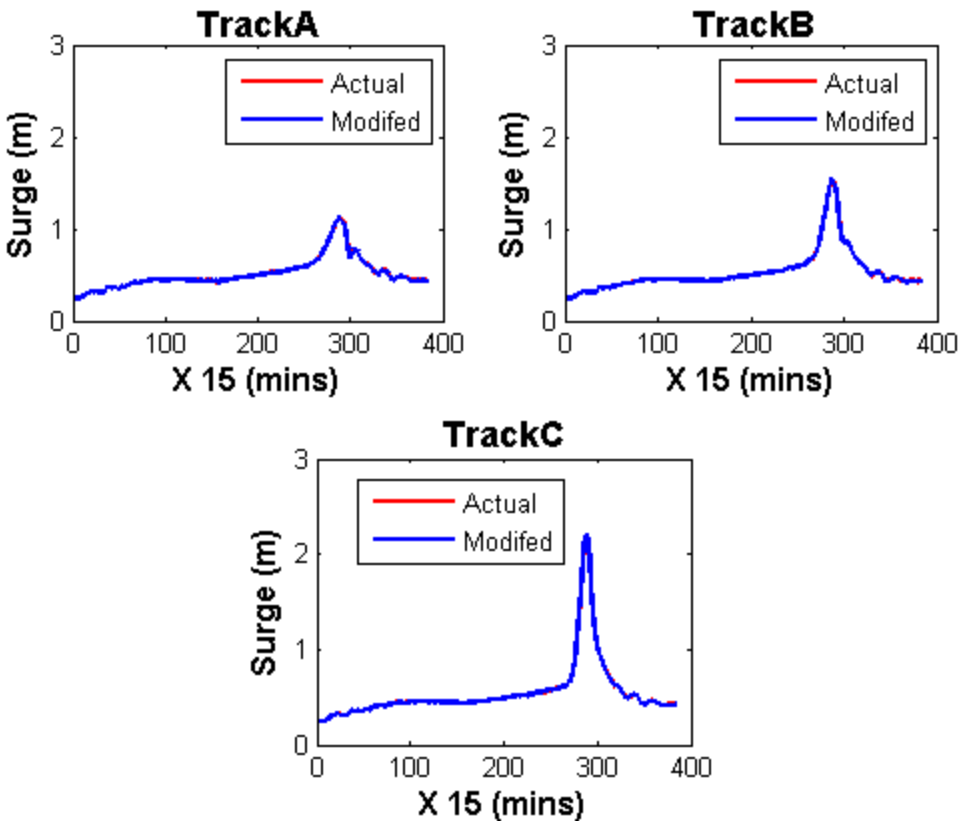

Figure 17 Time series for Station 12

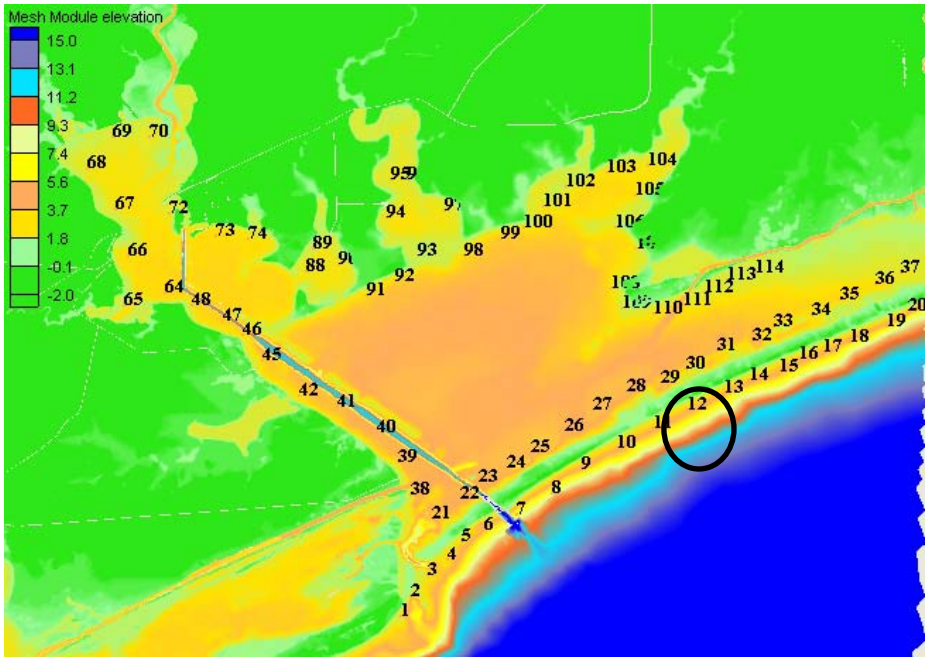

Time series for two inlet conditions, overlap each other at both the stations. Thus for open coast locations, time series and peak surge values are unaffected by two proposed inlet conditions. Also, the inlet location does not make any difference to the peak surge at open coast. To investigate the effect of inlet opening on peak surge inside the bay, time series for stations inside the bay area are plotted and results are shown below from Figure 18 to Figure 22.

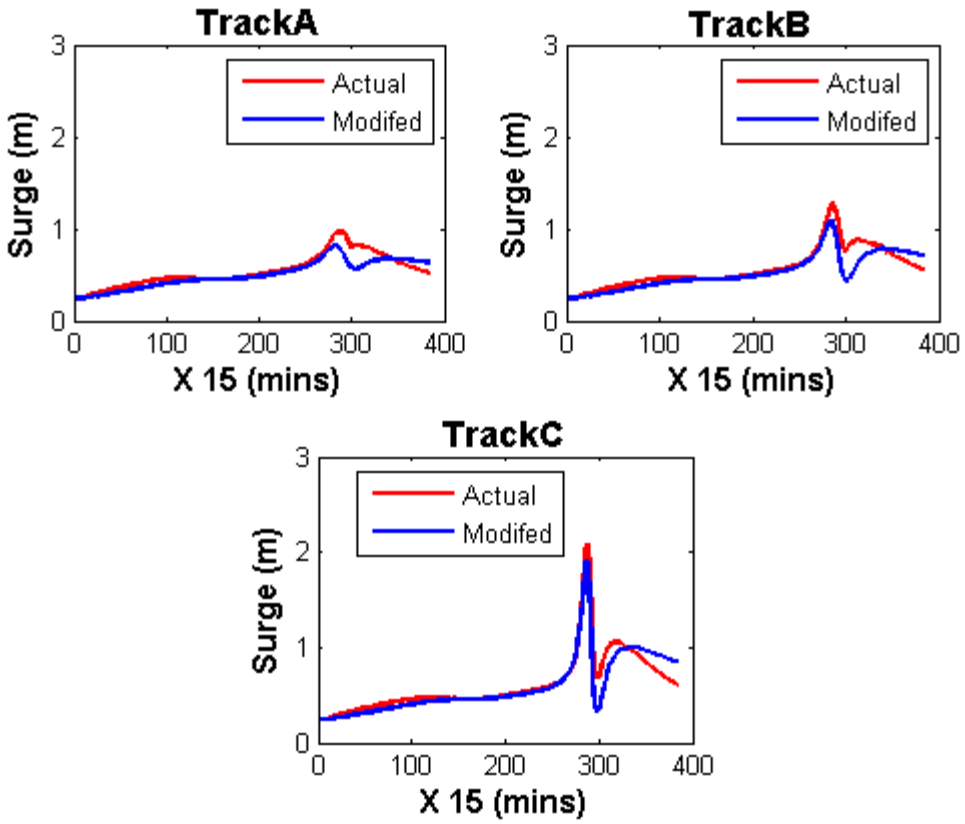

Figure 18 Time series station 38

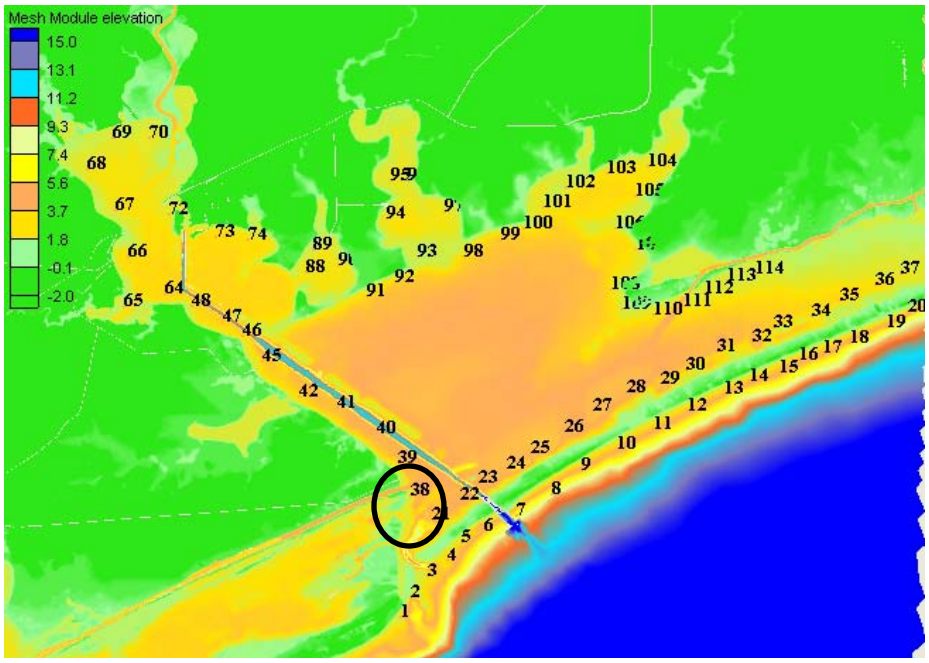

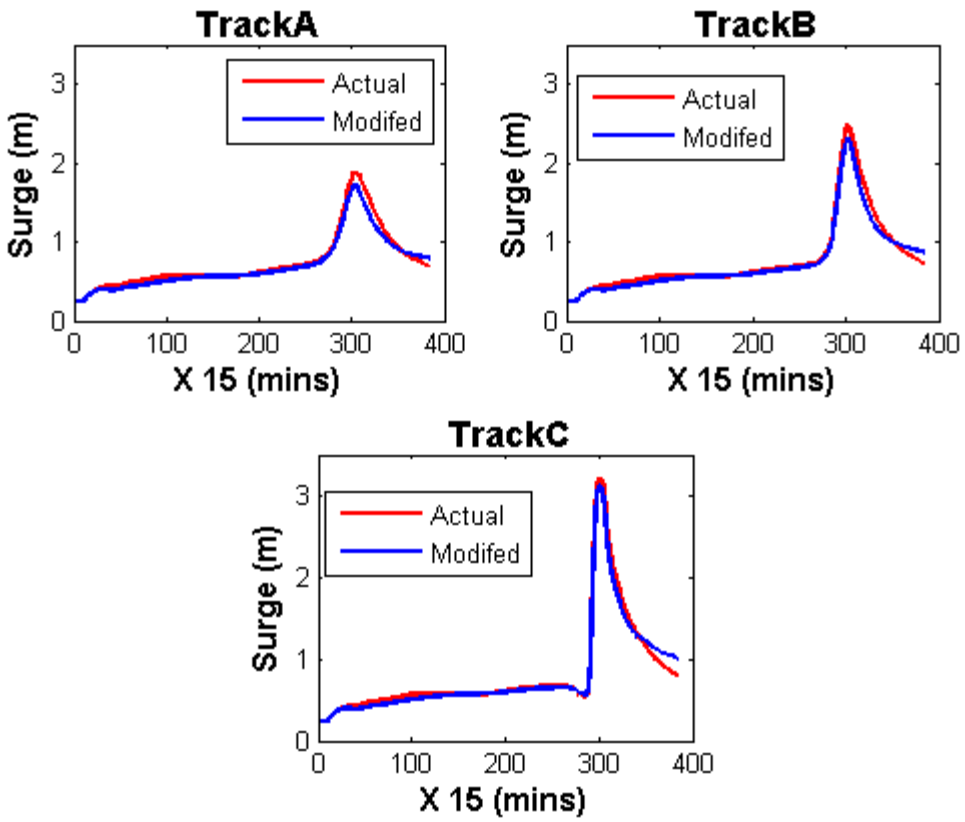

Figure 19 Time series for station 69

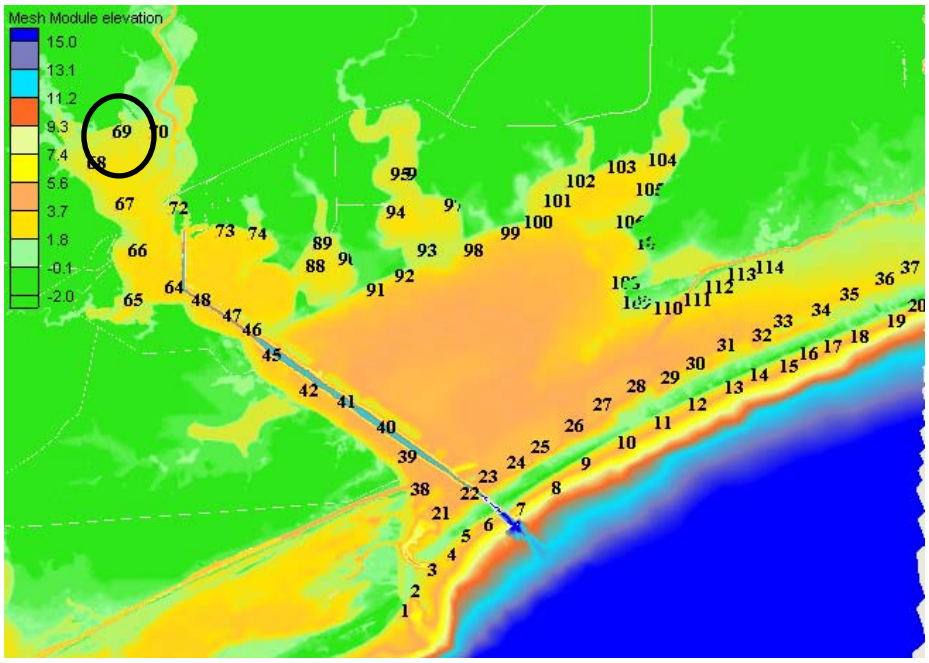

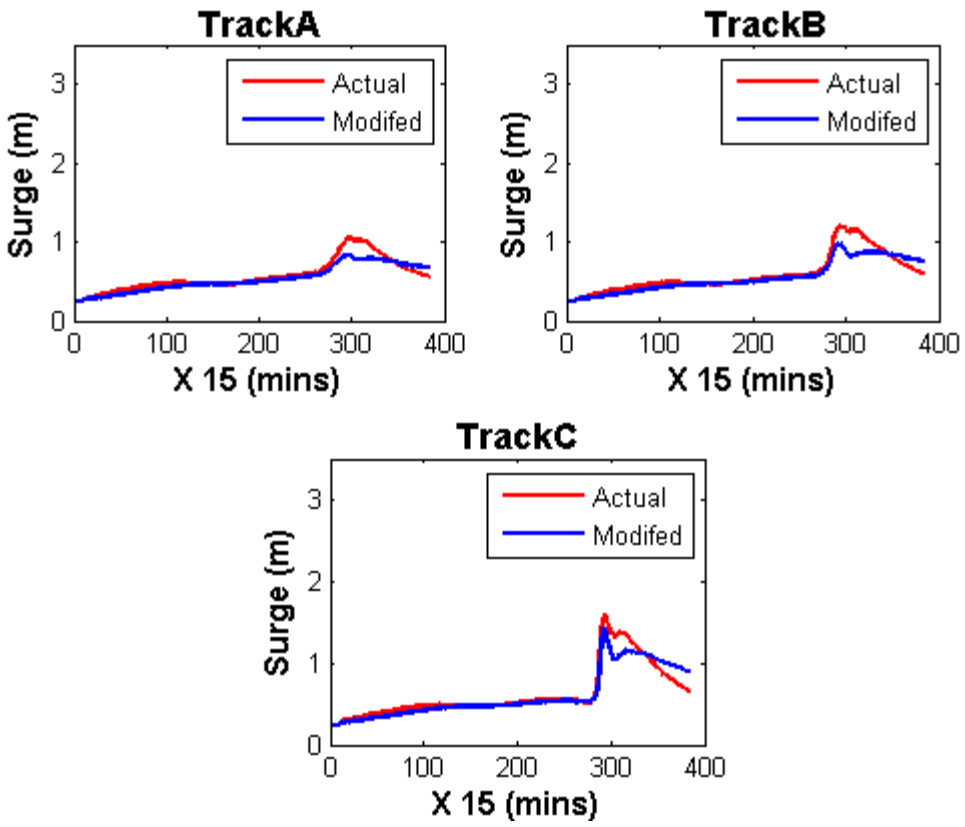

Figure 20 Time series for station 92

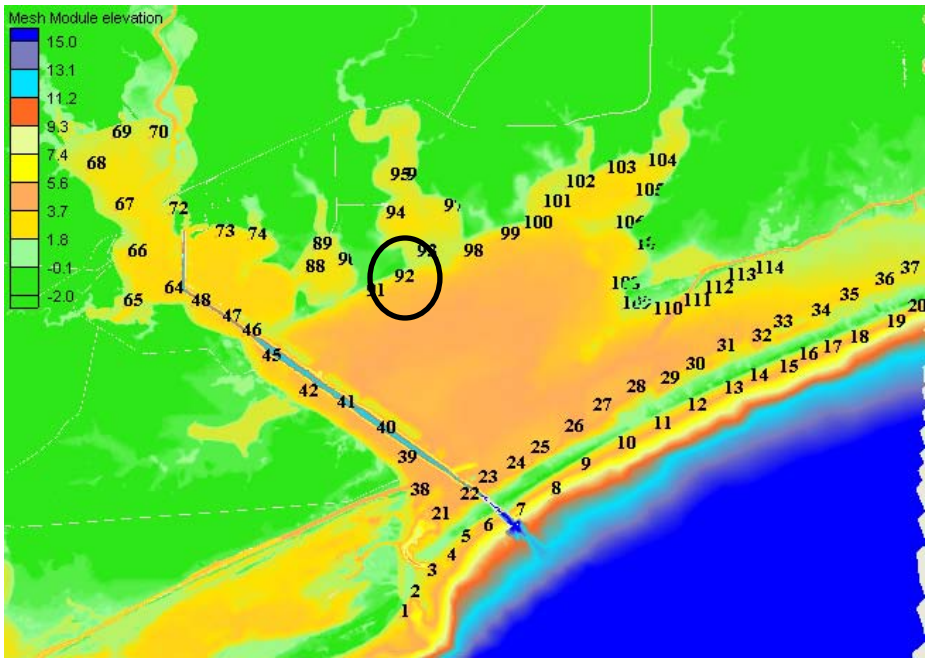

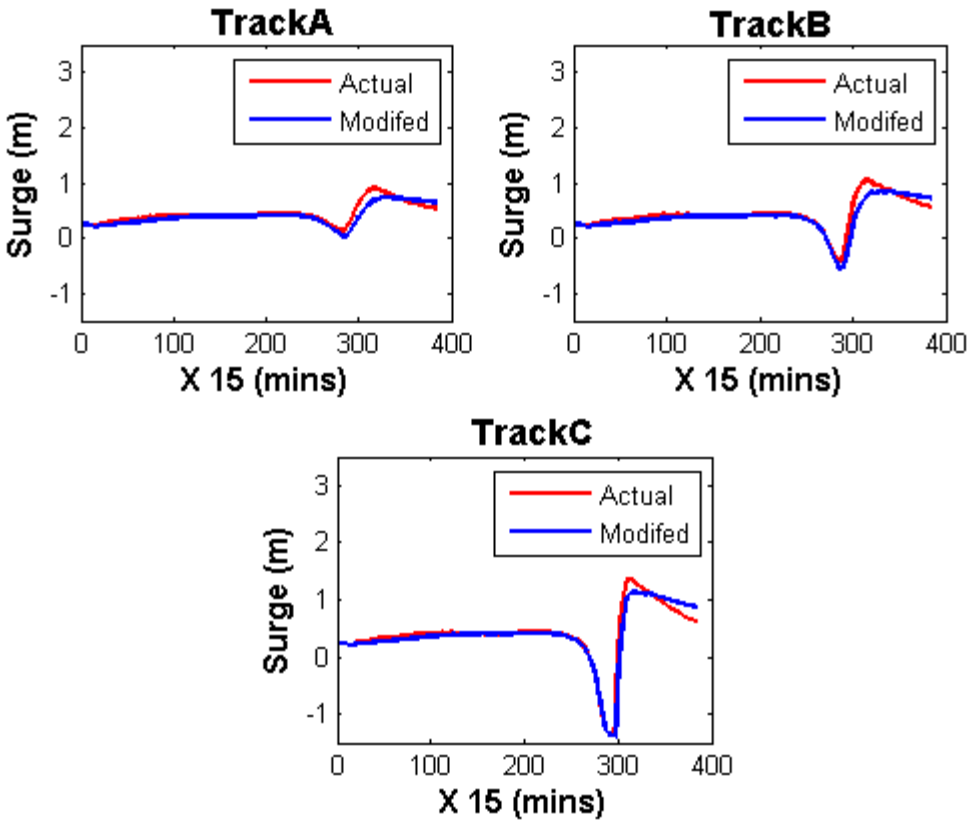

Figure 21 Time series for station 104

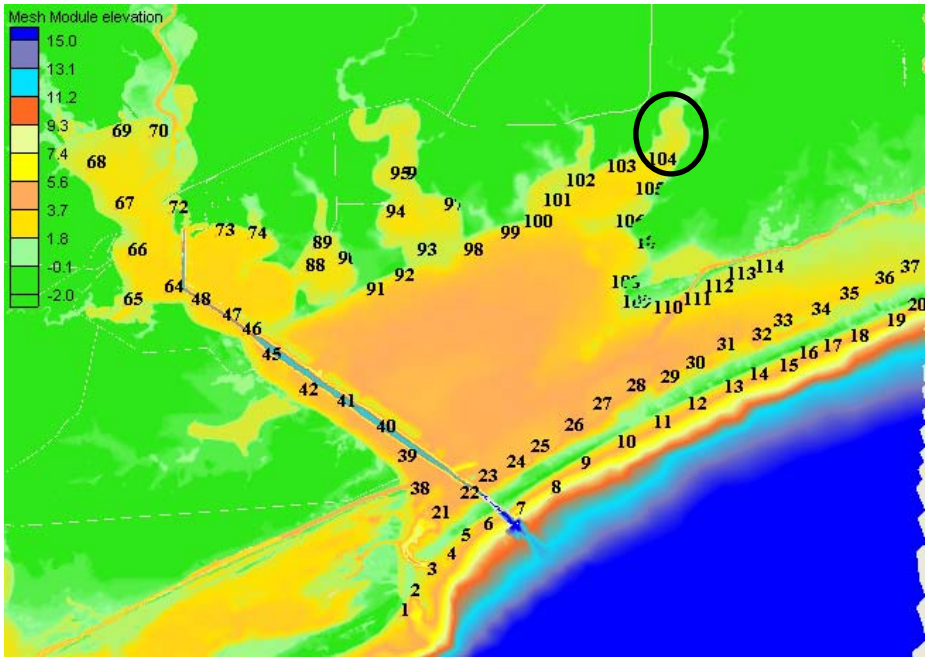

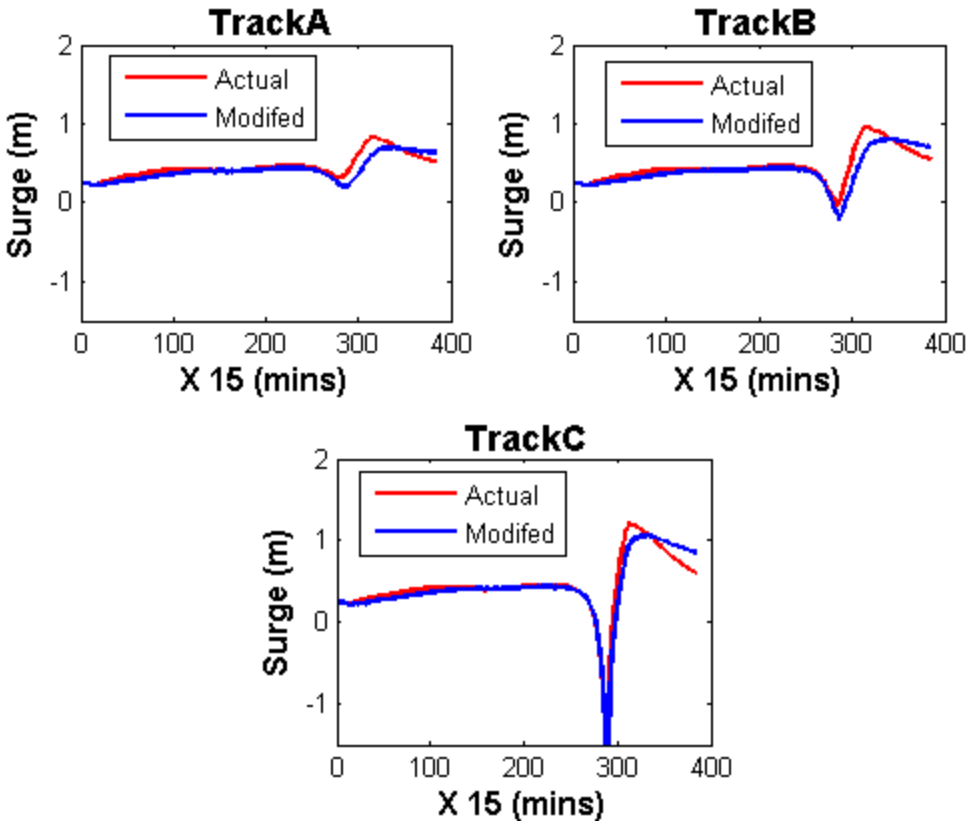

Figure 22 Time series for station 108

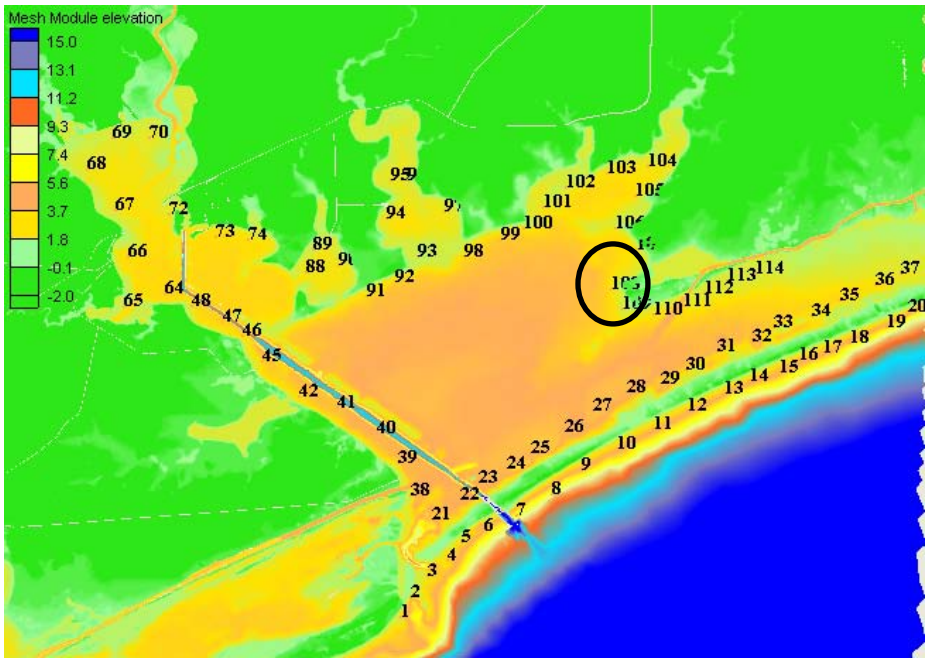

As is clear from Figure 18 to Figure 22, the peak surge value inside the bay for the blocked inlet case is less than that of the open inlet case. This is because with inlet closed there is relatively less amount of water entering inside the bay and thus the peak surge value inside the bay decreases.

Table 4 peak surge ratios for inlet blocked and open conditions

	Track A	**Track B**	**Track C**
Station 7	1.03	1.04	1.05
Station 12	1.00	1.00	1.00
Station 38	0.84	0.85	0.91
Station 69	0.91	0.94	0.97
Station 92	0.79	0.80	0.89
Station 104	0.82	0.79	0.82
Station 108	0.84	0.84	0.84
Average (Station 38 to 108)	0.84	0.84	0.89

Table 4 gives the ratio of peak surge for inlet closed condition versus inlet open condition. For station 7 and station 12, which are open coast stations, the ratio is about 1.00. But for stations 38 to 108, which are the station inside the bay, there is a decrease in the peak surge value as indicated by a ratio less than 1.00.

Further decrease in peak surge value lies between the 11 to 16%, which is same as the percentage of area blocked by closing the inlet (15%). The percentage decrease in peak surge value is similar throughout the bay. So based upon these observations we can conclude that, although inlet opening affect volume of water entering the bay, the percentage decrease in peak surge is similar throughout the bay. Thus the location of opening does not affect the surge distribution inside the bay. Although, change in an area of inlet opening, will affect the SRFs.

5.4 Importance of Center of Gravity

As a storm passes by a bay, there is a set up at one end and a set down at the other end of the bay. Figure 23 shows set-up and set- down in 2-dimensions.

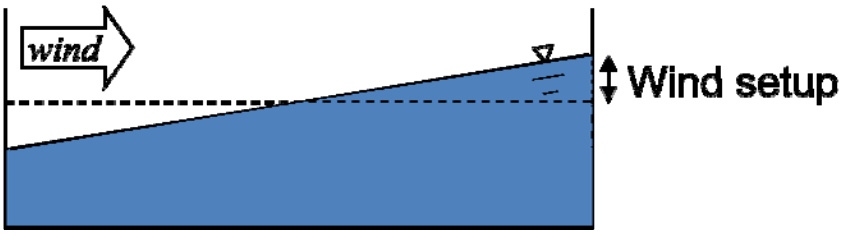

Figure 23 Set-up and set-down in bay (from Irish personal communication 2009)

Thus, Bay responds to an external forcing as a system. We investigated the effect of the center of gravity of the bay on peak storm surge distribution. Considering the volume of water inside the bay at calm state, the center of gravity of the volume of water is calculated. From the center of gravity of the bay, minimum distance of a storm as is passes by a bay is calculated. This distance is normalized by size of storm to give the

non-dimensional distance. The non-dimensional surge as defined in section 2.6 is plotted against this non dimensional distance and the results are shown below.

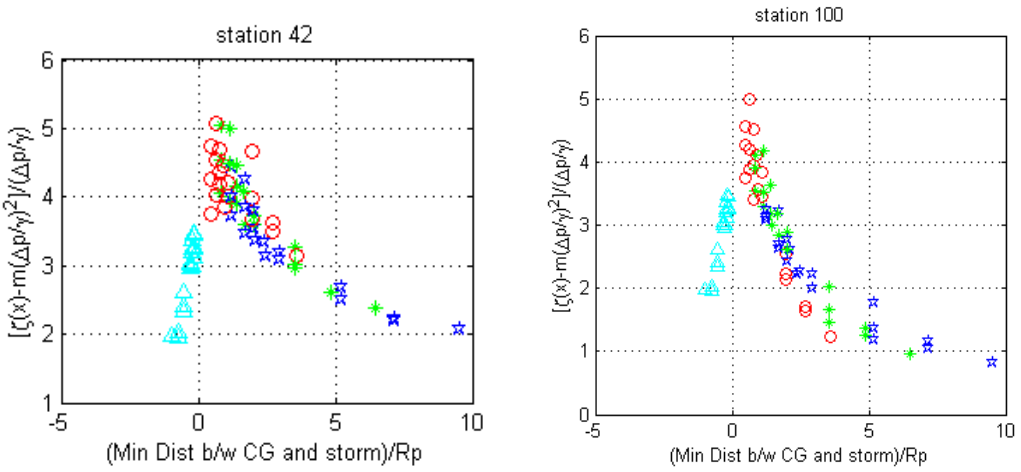

Figure 24 Importance of Centre of Gravity

As shown in Figure 24, the surge values do correlate to the size and minimum distance of storm from the center of gravity of bay. However there is a significant scatter in SRFs particularly for stations located on the west side of the bay, which corresponds to the channel location inside the bay.

5.5 Effect of Channel

As mentioned previously, Matagorda Bay has a deep channel on the west side of bay. To study the effect of channel on the peak surge distribution inside bay, simulations under two conditions were generated. First, using the actual condition i.e. with channel and second with the channel blocked. For both the cases simulation with storm size (R_p=15Km) and intensity (p=930mb) were used. Peak surge values were extracted from

the time series of the two simulations. The contour map of the peak surge obtained is shown in Figure 25 and Figure 26.

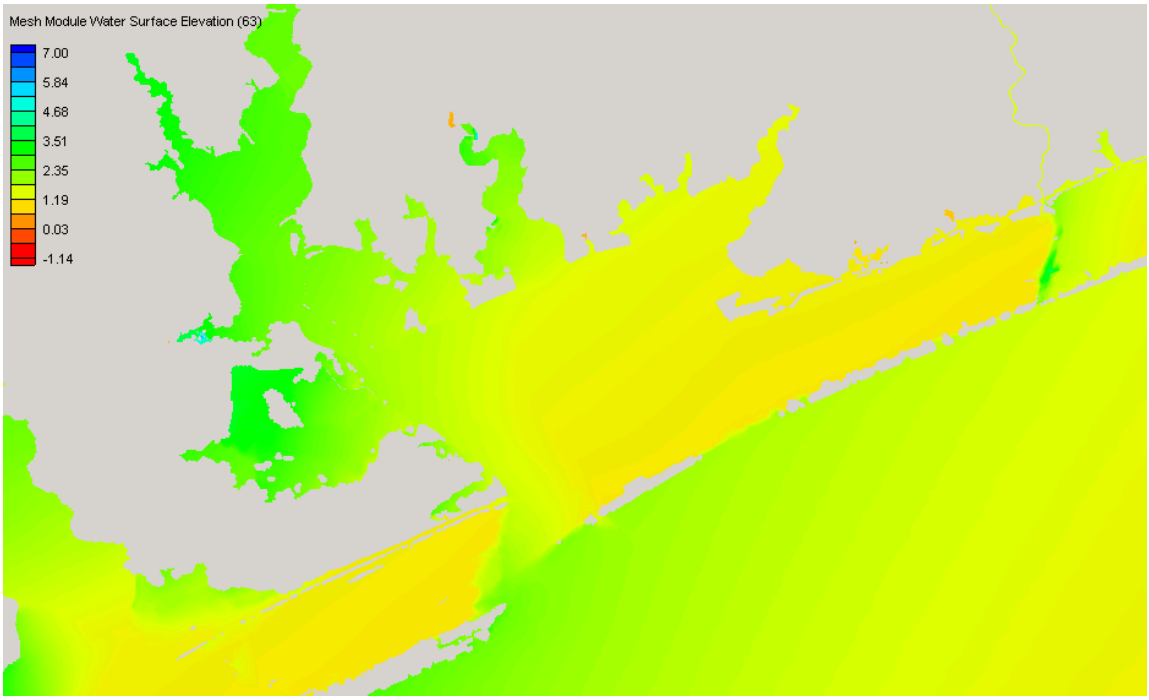

Figure 25 Peak surge in Matagorda Bay with channel

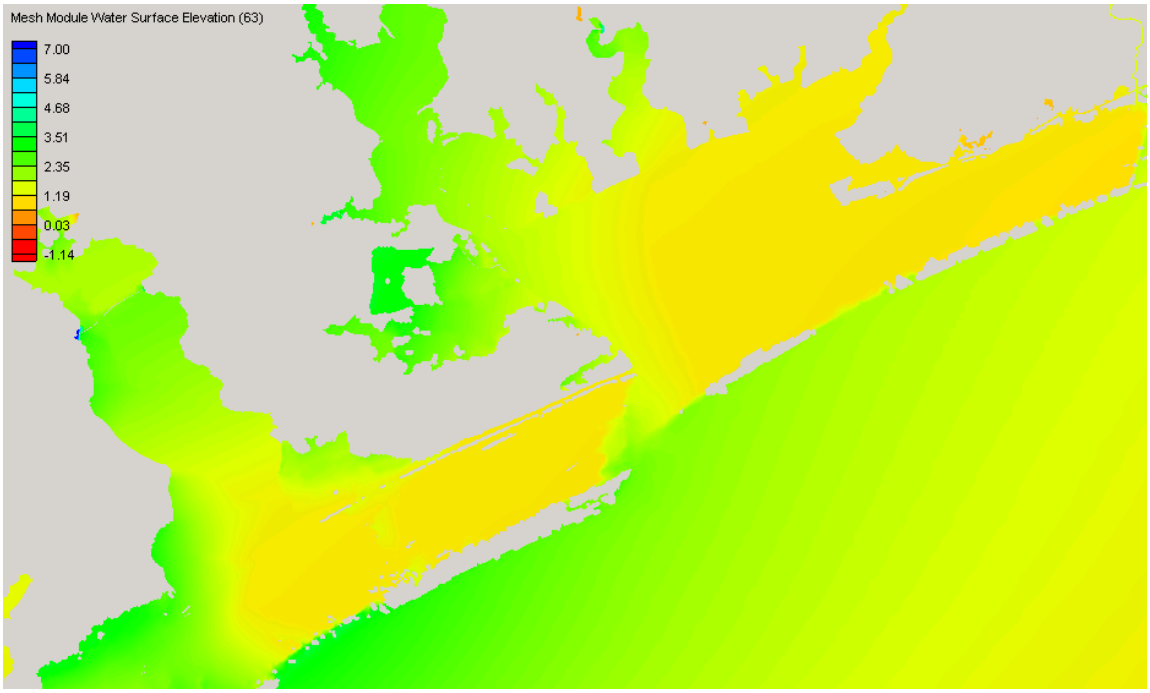

Figure 26 Peak surge in Matagorda Bay without channel

For both cases, peak surge values were same for all the 114 station(s) considered in this study. The contour map of peak surge inside the bay with and without channel shows similar region of peak values. Thus we can say that the existence of a channel does not affect the peak surge levels inside the bay.

5.6 Timing of peak surge

Storms on different tracks might cause peak surge values at a station at different times. This might affect a surge response inside the bay. To study this effect, we selected stations at various locations inside Matagorda Bay and water elevation time series were

compared for different tracks storms at these stations.

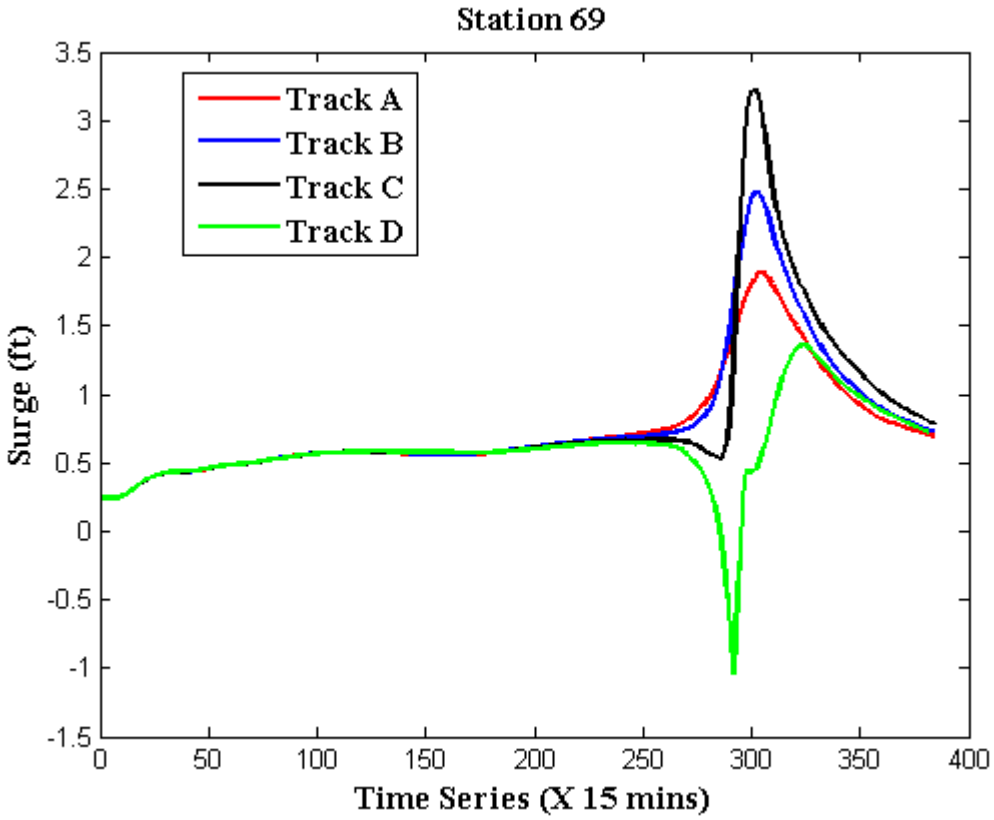

Figure 27 Time series for station 69, Matagorda Bay

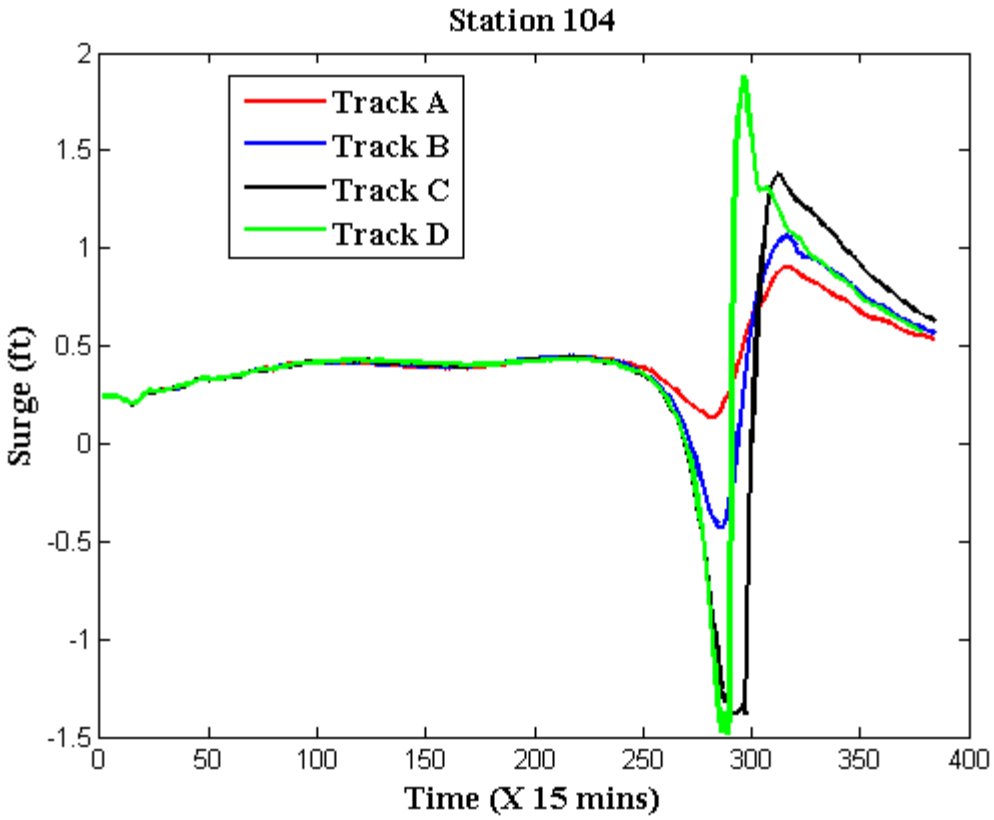

Figure 28 Time series for station 104, Matagorda Bay.

Figure 27 and Figure 28 show time series for the storm (R_p=15Km and intensity=960mb) on track A, B, C and D at station 69 and station 104 in Matagorda Bay. For both stations peak surge values for Track A, B, and C (Figure 10, all on west side of center of gravity of bay) occurs at the same time, while that of Track D (on east side of center of gravity) is shifted slightly in time but does not appear to be significantly different from trend. Thus, it can be assumed that to the first order, timing of peak surge does not affect the surge response inside the bay.

Chapter VI

SRFs Methodology and Application

6.1 Introduction: In this chapter, SRFs inside Matagorda Bay are discussed. The SRFs are based upon the parameters discussed in Chapter 5. The approach developed for SRFs in Matagorda Bay is validated by applying this formulation for SRFs in Galveston and Corpus Christi Bays. As shown in the previous Chapter, the Center of Gravity and the non-dimensional surge for open coast are important factors for peak surge distribution inside a bay while the timing of peak surge, inlet width and channel location inside a bay, to the first order, does not affect peak surge distribution inside a bay. In the following section, a methodology for SRFs in Matagorda Bay is defined based upon four tracks (A, B, C, D) as shown in Figure 29.

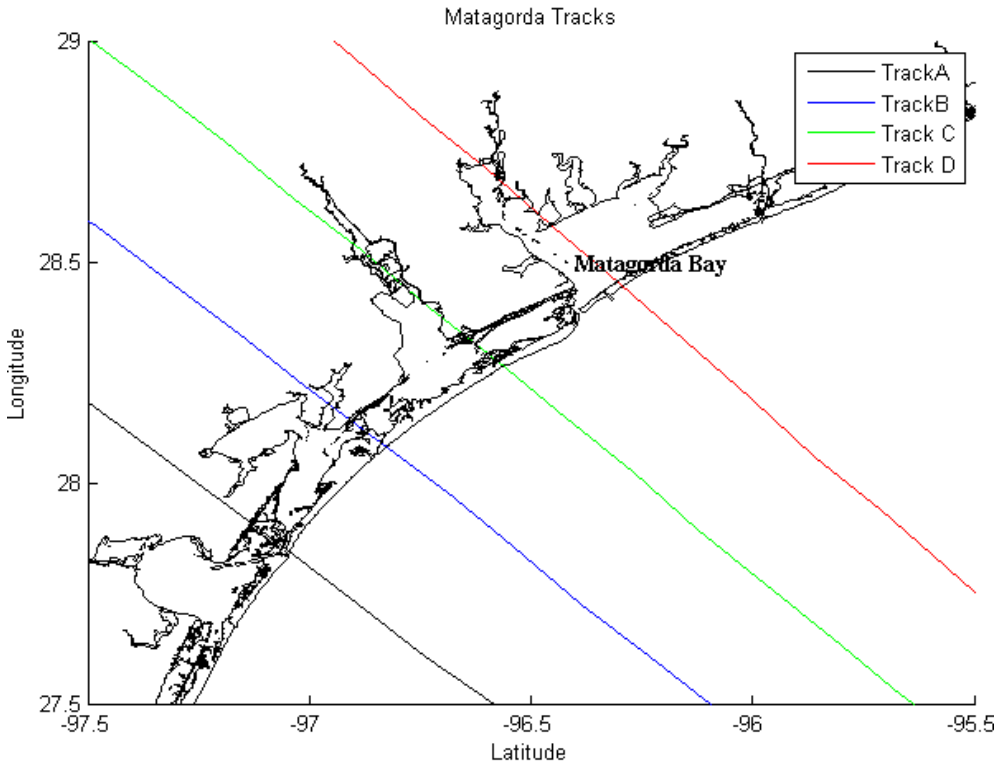

Figure 29 Matagorda Bay Tracks

6.2 **SRFs for Matagorda Bay**: Features of Matagorda Bay have been discussed in Chapter 3. Based upon the factors described in the previous chapter and analysis at 128 stations (Figure 3) in Matagorda Bay using 76 storms on tracks A, B, C, D (Figure 29), the following non-dimensional quantities for SRFs inside Matagorda Bay is (are) proposed.

Non-dimensional surge(ξ), which is given as

$$\xi' = \frac{\gamma\xi}{\Delta p} + m_\chi \Delta p + F(\Delta p, Rp, \xi, S_b) \tag{6.1}$$

The first two terms on the right hand side of equation are the same as that defined for the open coast SRFs. While F(Δp, Rp, ξ, S_b) is a function of intensity, storm size, surge at the station due to the storm and size of bayS_b. It is defined as

$$\mathrm{F}(\Delta p, \mathrm{Rp}, \xi, S_b) = \begin{cases} \xi c Rp & for\ \Delta p < 0.9\ \&\ Rp > S_b \\ 0 & \text{Otherwise} \end{cases} \quad (6.2)$$

where,

S_b is characteristic size of a bay.

c is a constant determined to be 0.03/m^2 for Matagorda Bay.

Thus, the main difference in the non-dimensional surge for inside the bay and the open coast is that, that for inside a bay, for storms which are larger in size than that of characteristic size of bay and have intensity such that Δp is greater than 0.9, there is an extra term $\xi c R_p$ added to non-dimensional surge for open coast.

Non-dimensional distance(X'), defined as

$$X' = \frac{X_c}{Rp} + \frac{S_b}{X_c} - \boldsymbol{\lambda} + F(\Delta p, R_p, S_b) \quad (6.3)$$

where

X_c is the minimum distance between the Center of Gravity of a bay and the eye of storm as storm passes by the bay.

F (Δp, Rp, S_b) is a function based upon the size of storm, size of bay and intensity of storm and is defined as

$$= \frac{(\Delta p - 0.84)}{(0.1 \times S_b)} \qquad \text{for, } R_p < S_b$$

$$\text{F}(\Delta p, R_p, S_b) = \frac{(\Delta p - 0.84)}{(0.1 \times S_b)} \qquad \text{for } \Delta p > 0.84 \text{ \& } R_p > S_b; \qquad (6.4)$$

$$= \frac{(0.84 - \Delta p)}{(0.1 \times S_b)} \qquad \text{for } \Delta p < 0.84 \text{ \& } R_p > S_b;$$

Plots between the non-dimensional surge and the non-dimensional distance at stations inside Matagorda Bay are shown in Figure 30 through Figure 33

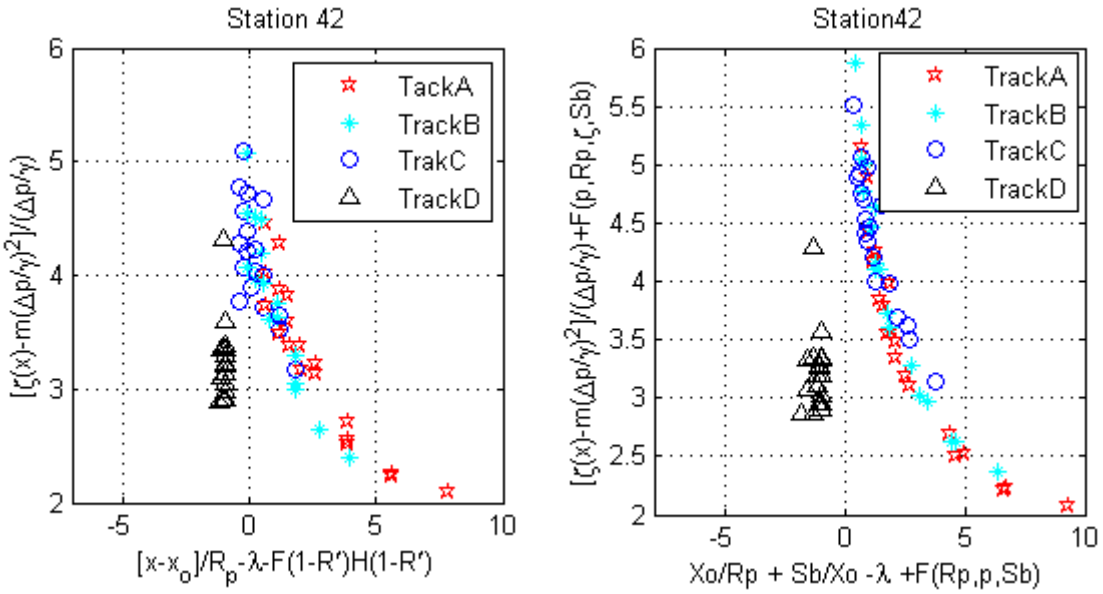

Figure 30 Open coast methodology (left plot), Inside Bay methodology (right plot) Matagorda Station 42.

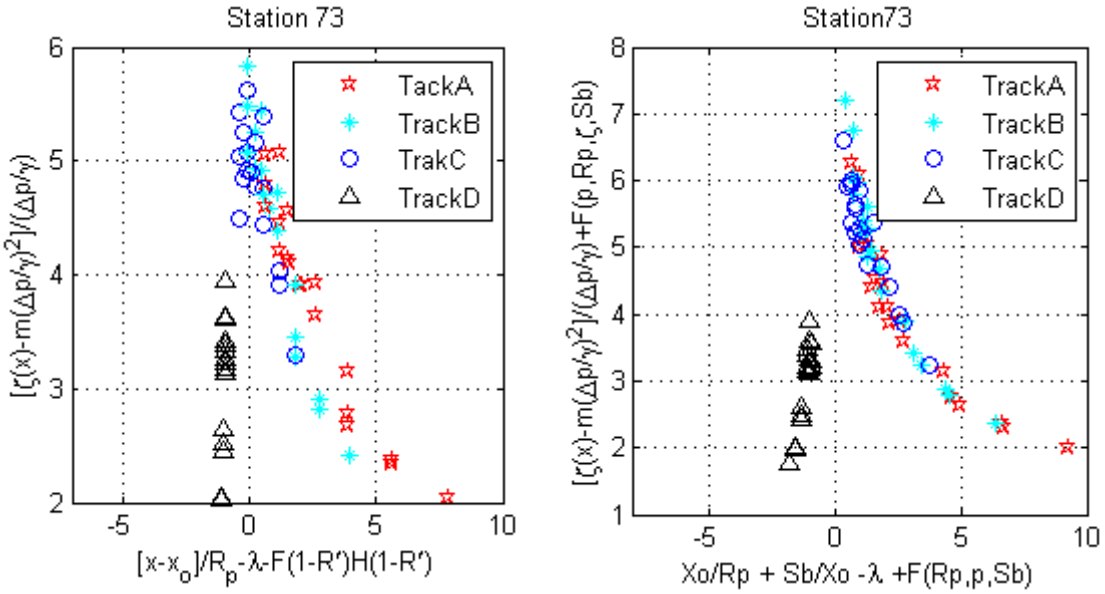

Figure 31 Open coast methodology (left plot), Inside Bay methodology (right plot)

Matagorda Station 73

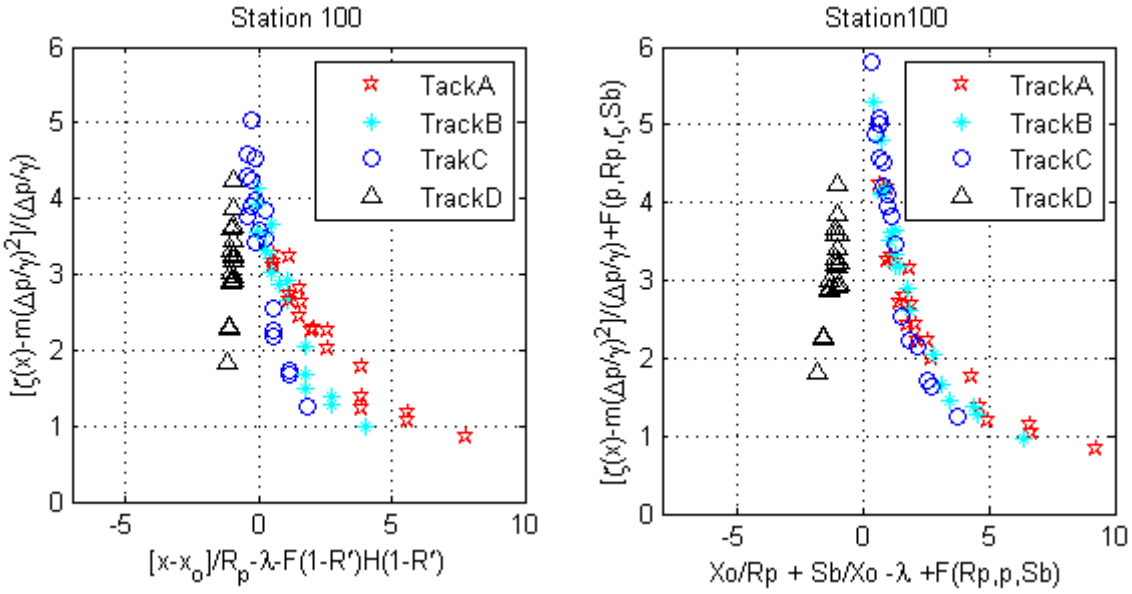

Figure 32 Open coast methodology (left plot), Inside Bay methodology (right plot)

Matagorda Station 100

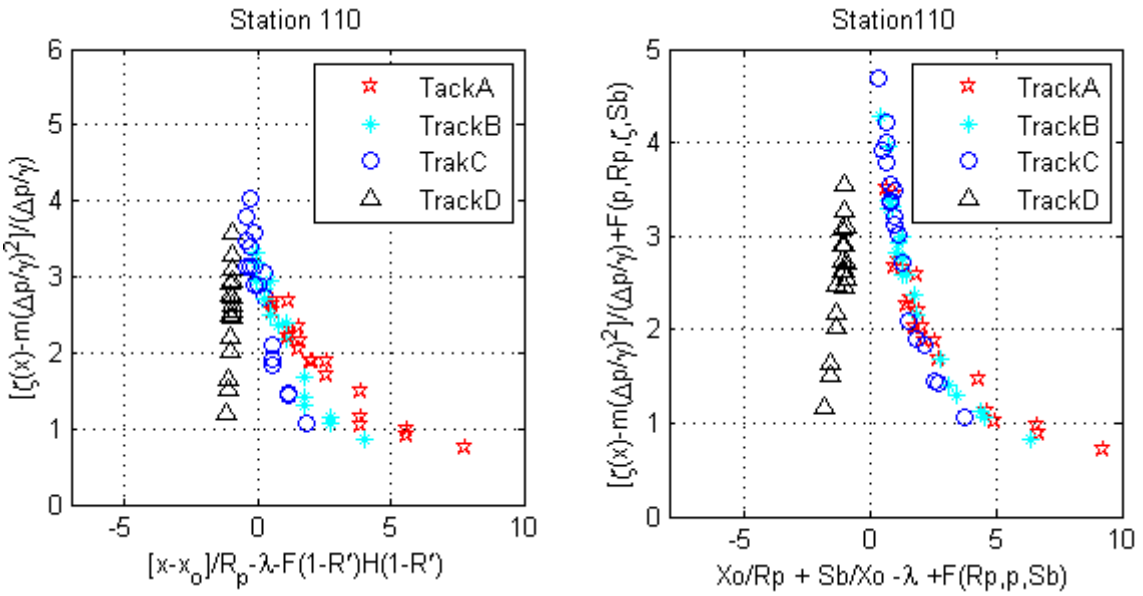

Figure 33 Open coast methodology (left plot), Inside Bay methodology (right plot)

Matagorda Station 110

For Figure 30 through Figure 33, left-hand side shows the non dimensional relationship obtained for bay locations based upon the open coast methodology while the right-hand side shows the non-dimensional relationship for bay stations based upon the new methodology developed for Matagorda Bay. With the open coast methodology we get scatter in the non-dimensional plots which can be attributed to factors like relative size of storm to the size of bay, intensity of the storm and relative location of the storm with respect to center of gravity of the bay. In contrast, with new methodology developed for Matagorda Bay scatter in non-dimensional plots reduced considerably. Thus, with the new methodology SRFs can be predicted more accurately.

Figure 34 though Figure 41 show the Gaussian function fit to the non-dimensional surge and non-dimensional distance data and comparison between the simulated and SRF predicted surge at station locations 42, 73, 100, and 110.

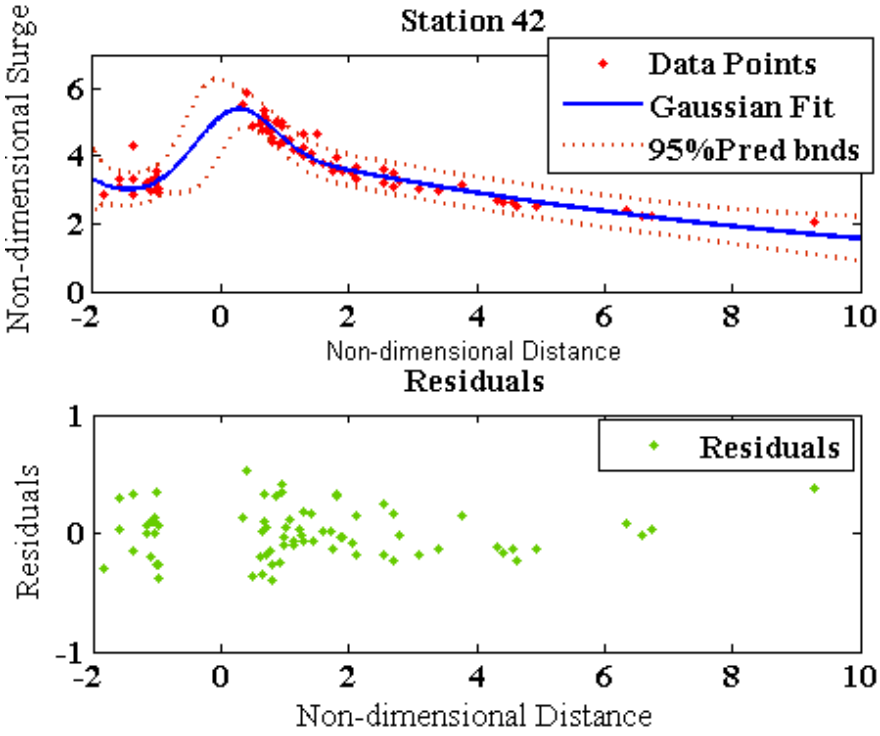

Figure 34 SRF for station 42, R-square = 0.93

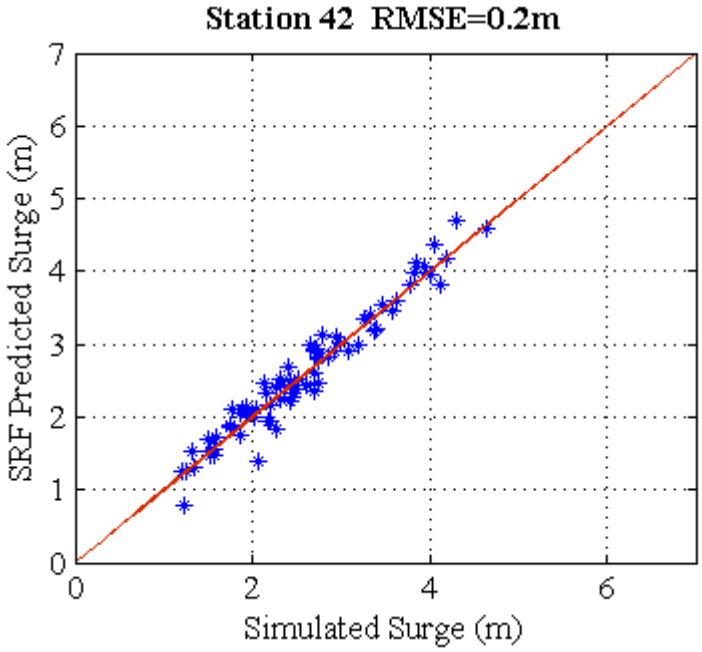

Figure 35 Simulated Vs SRF predicted.

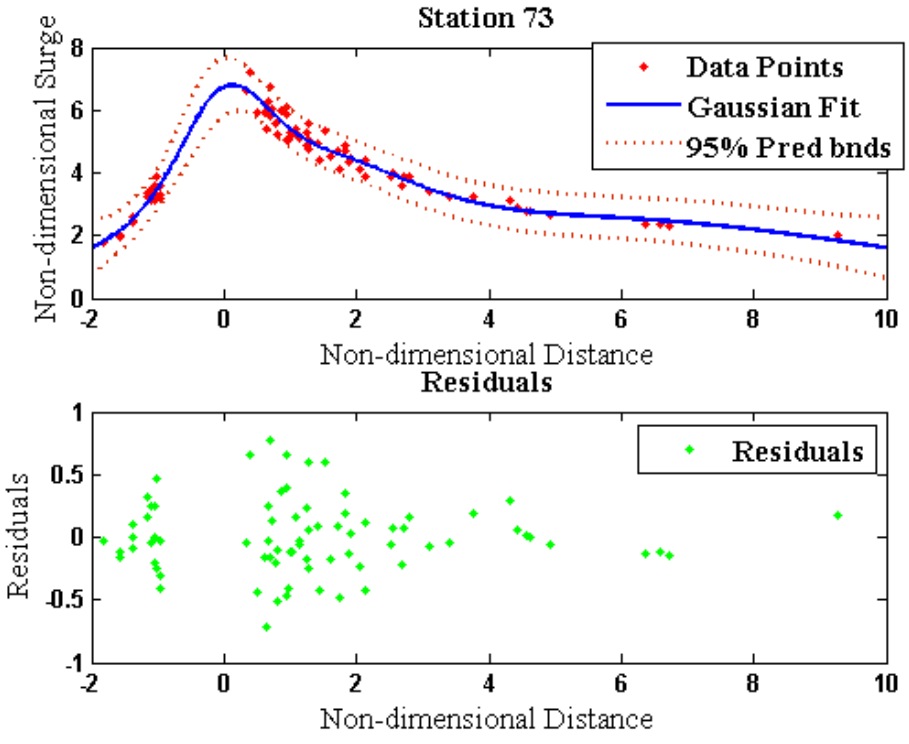

Figure 36 SRF for station 73, R-square = 0.95

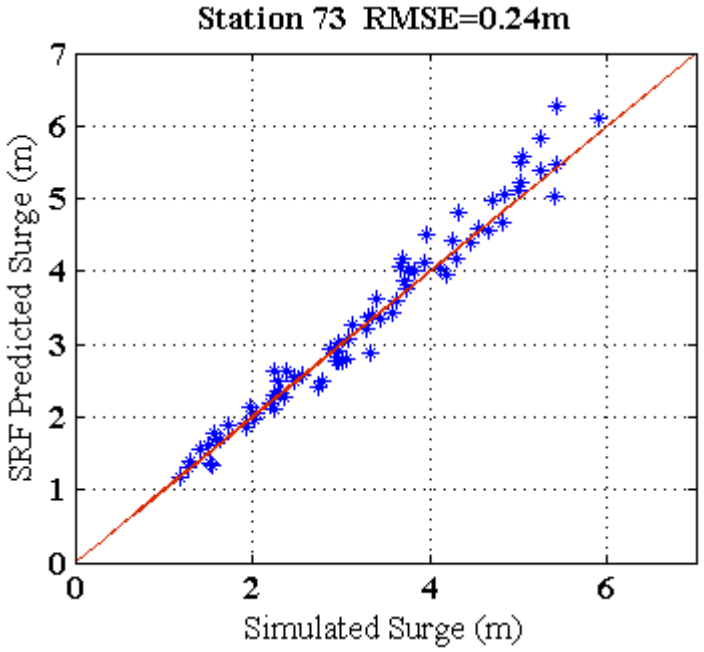

Figure 37 Simulated Vs SRF predicted

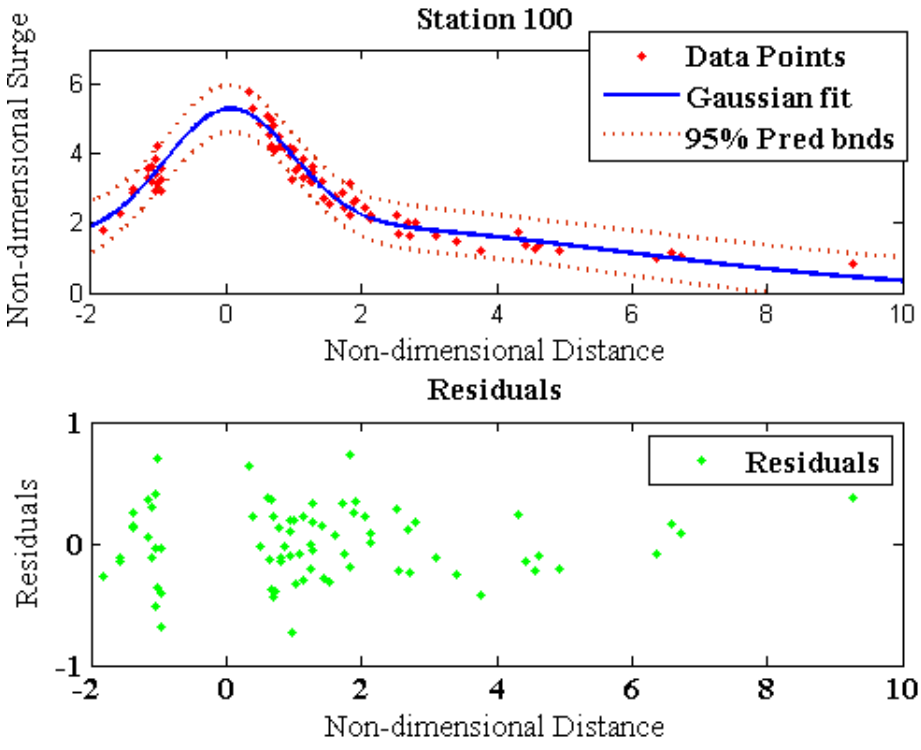

Figure 38 SRF for station 100, R-square 0.93

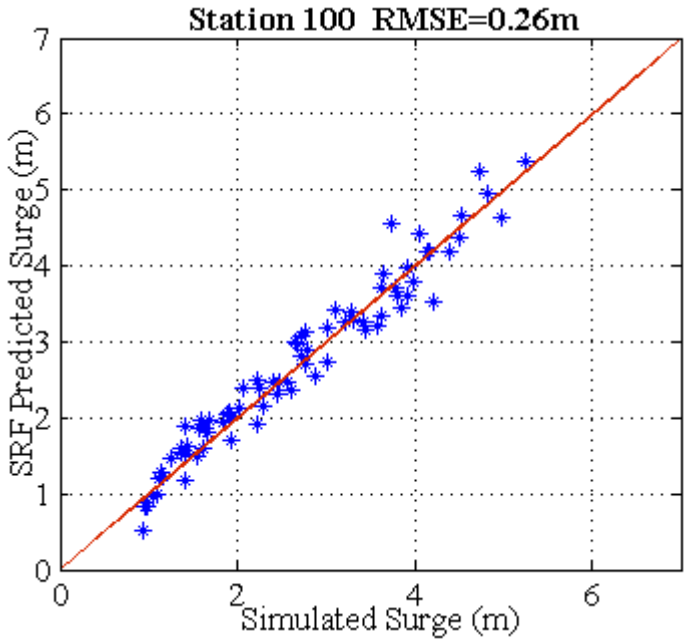

Figure 39 Simulated Vs SRF Predicted.

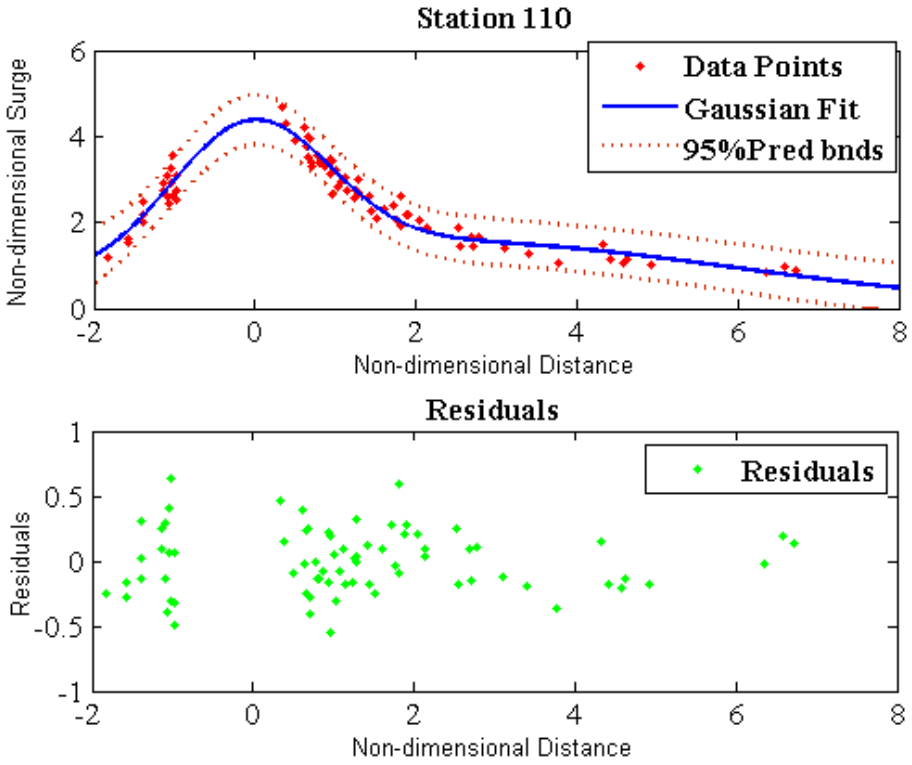

Figure 40 SRF for station 110, R-square 0.93

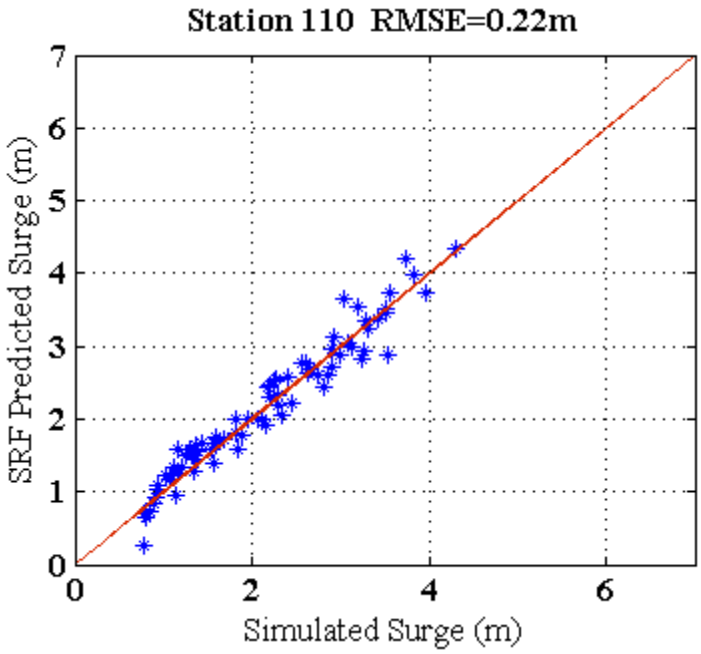

Figure 41 Simulated Vs SRF predicted.

These plots show the 95% prediction bounds for the Gaussian fit. As is clear from the figures most of the simulation results lie within 95% confidence interval. Figure 34 through Figure 41 also shows the residual (non-dimensional predicted surge – non-dimensional simulated surge) plots for the fit. As is clear from the residual plots there is random scatter about the zero line, thus there is no bias in predicted SRFs. With the open coast methodology, R-square values for SRF is approximately 0.67 as compared to 0.91 using the new methodology. R-square value for the Gaussian fit at Matagorda stations lies in 0.91 to 0.97. The plots also show the comparison between simulated surge and the surge predicted by SRF. Root Mean Square Error (RMSE) for Matagorda Bay is between 0.2 to 0.28 m as compared to RMSE of 0.52 to 0.64 m with open coast methodology. The plots also show that in region where non-dimensional distance is zero,

we do not have simulations results. Thus to define SRF in this region we need to have more simulations.

6.3 Application to Galveston

Features of Galveston Bay have been discussed in Chapter 3. Based upon the SRF methodology developed for Matagorda Bay, SRFs for 159 stations inside Galveston Bay are developed using 5 tracks (Aa, Ab, Ac, Ad, Ae) shown in Figure 42 with total of 30 storm simulations on them with R_p value varying from 5 to 35 km and the intensity of storm varying from the 900mb to 960mb.

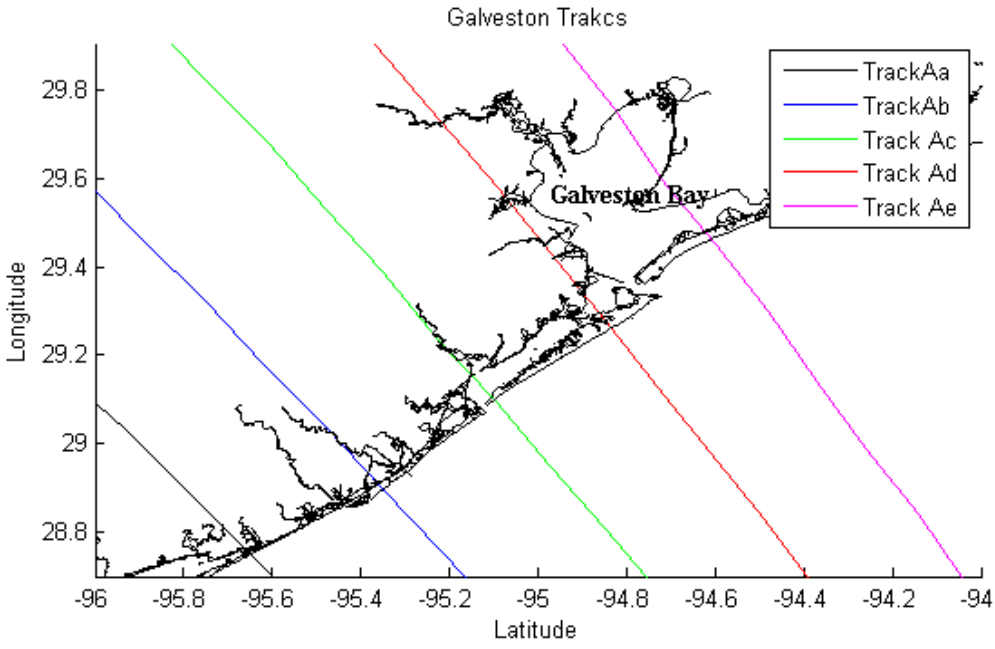

Figure 42 Galveston Bay Tracks

The parameters which changes for Galveston bay compared to Matagorda Bay for applying the SRF methodology inside Galveston bay are

- Center of gravity of bay
- Size of bay (20Km)
- Lambda value =0.99 (based upon the Song 2009)
- Constant c ($0.05/m^2$)

Figure 43 through Figure 48 show the non-dimensional relationship developed for Galveston Bay using 30 storms on five tracks (Aa, Ab, Ac, Ad, Ae).

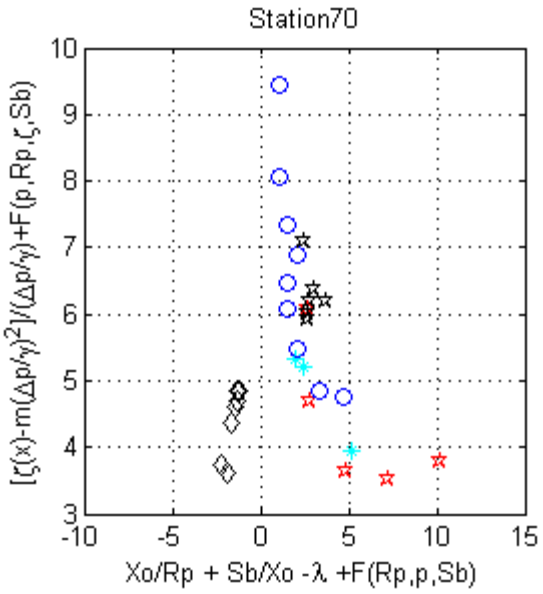

Figure 43 Non-dimensional Plot Galveston Station 70.

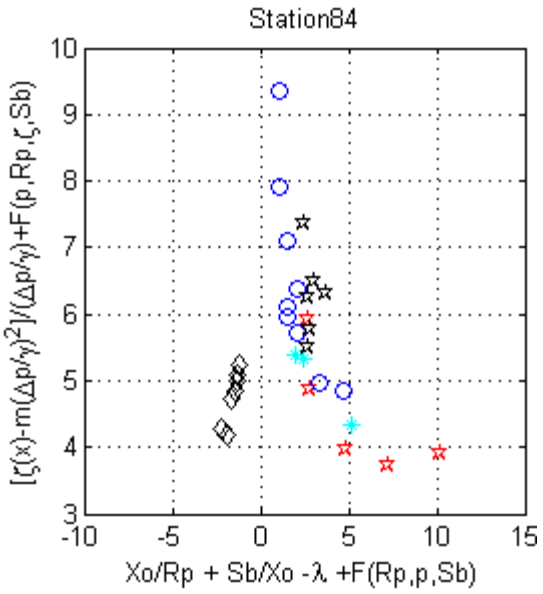

Figure 44 Non-dimensional plot Galveston Station 84

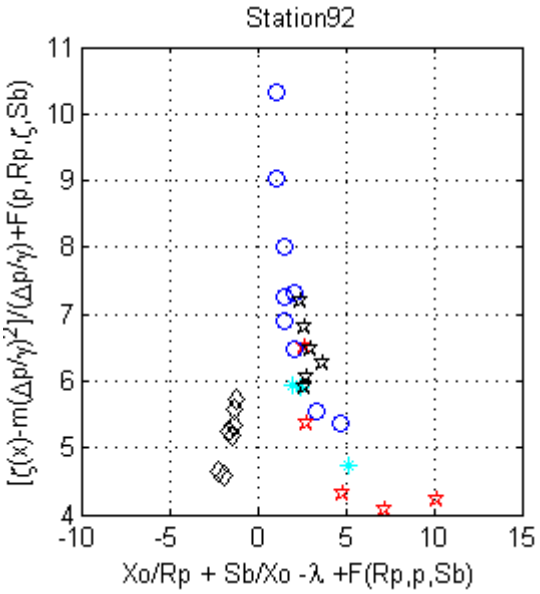

Figure 45 Non-dimensional Plot Galveston Station 92

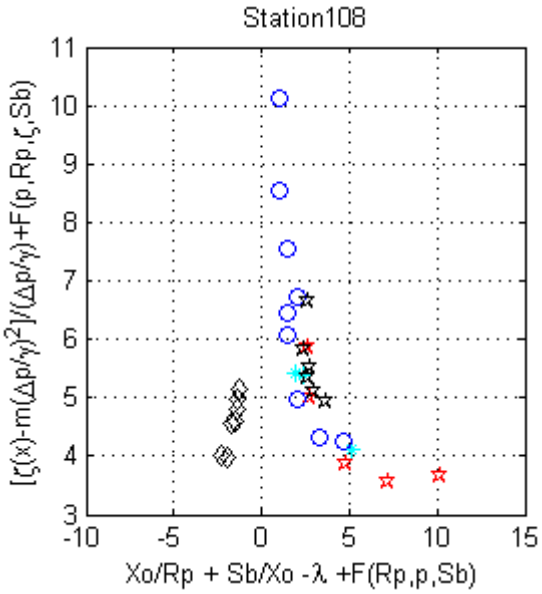

Figure 46 Non-dimensional Plot Galveston Station 108

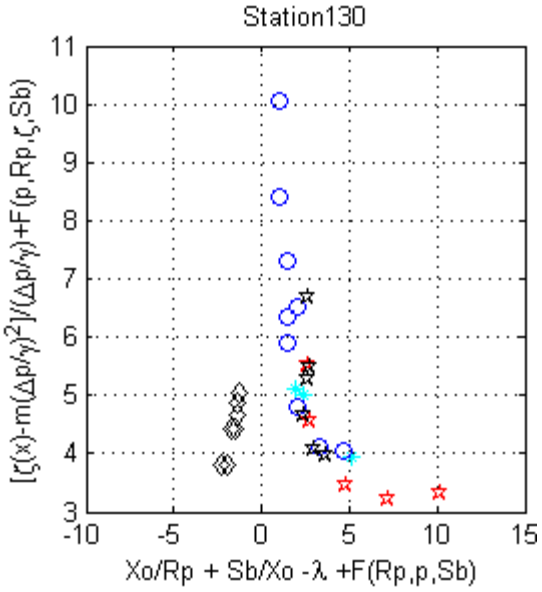

Figure 47 Non-dimensional Plot

Galveston Station 130

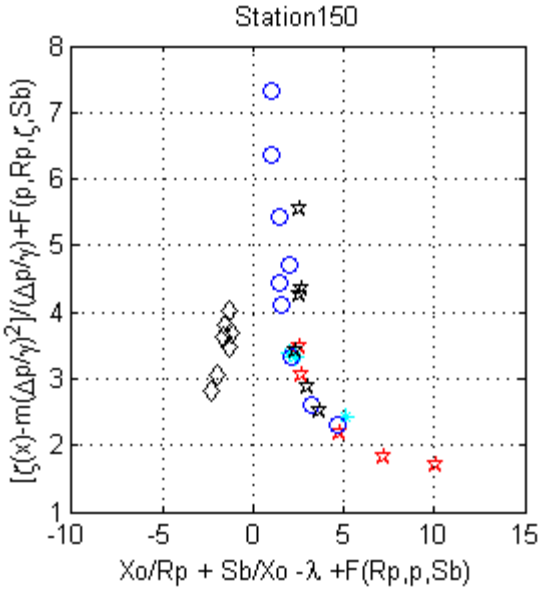

Figure 48 Non-dimensional Plot

Galveston Station 150

As is clear from Figure 43 through Figure 48, the methodology developed for the Matagorda Bay works well for the Galveston region. Figure 49 and Figure 52 show the curve fit to the data at locations 92 and 108 in Galveston Bay based upon the Gaussian fit.

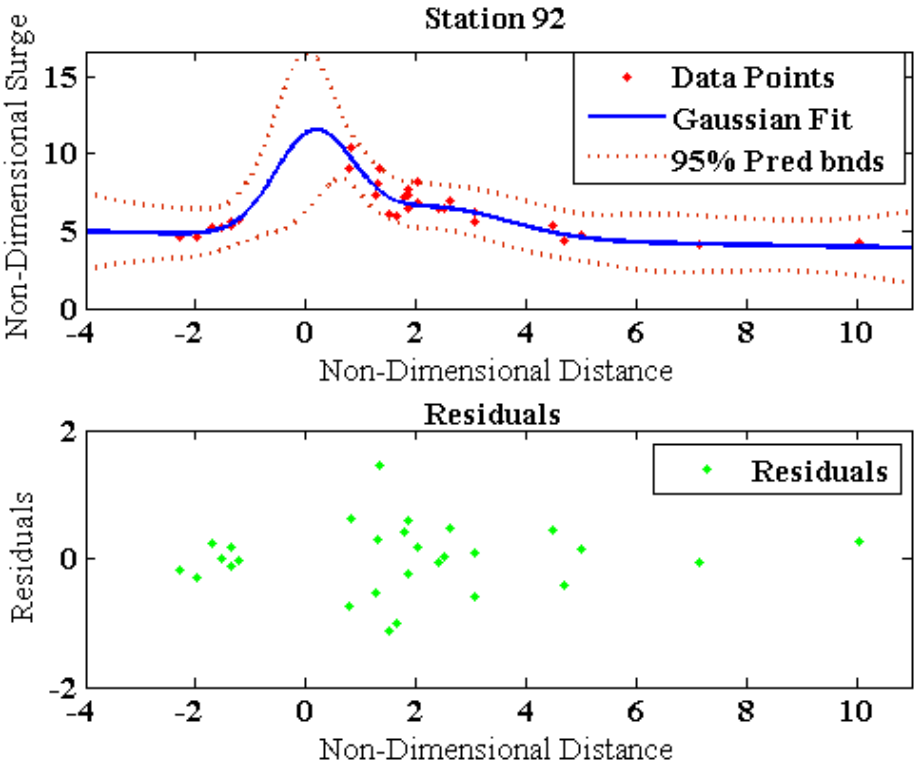

Figure 49 SRF for station 92, R-square 0.82

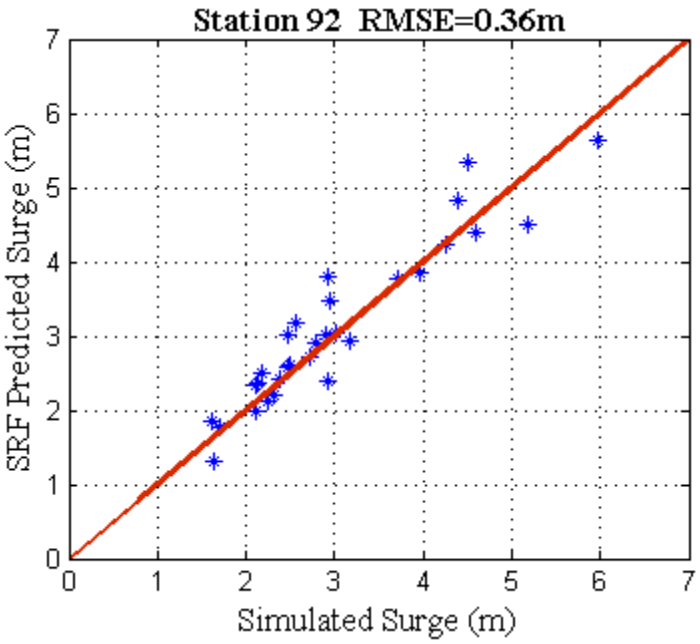

Figure 50 Simulated Vs SRF predicted

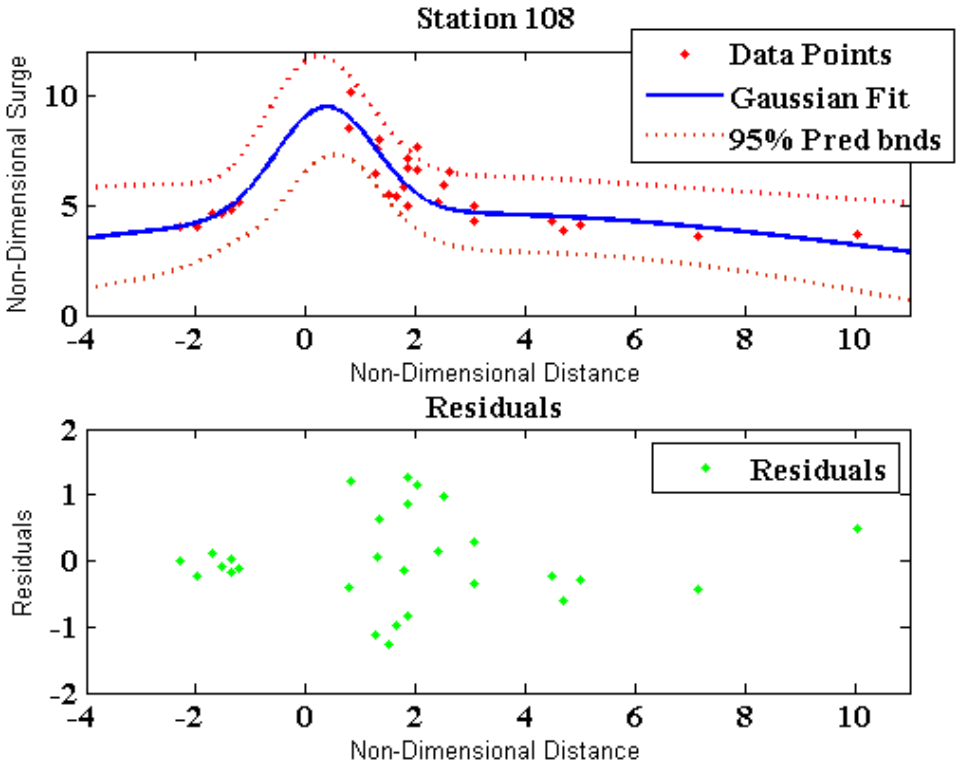

Figure 51 SRF for station 108, R-square 0.82

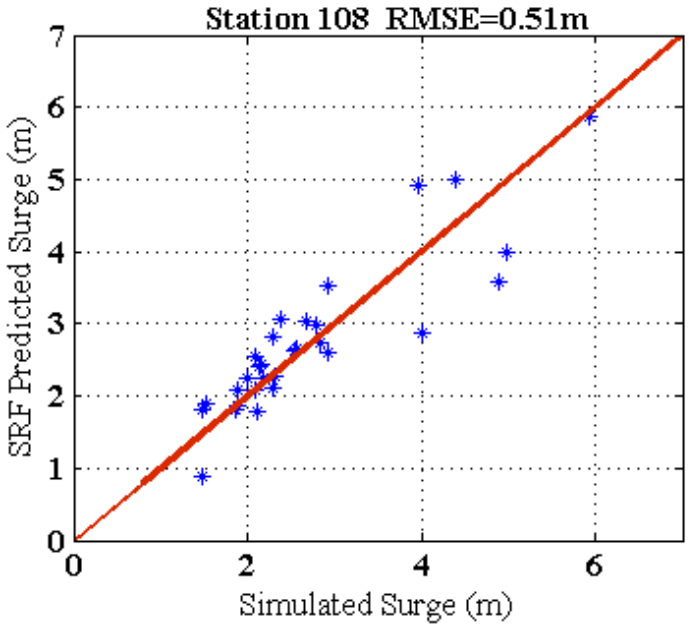

Figure 52 Simulated Vs SRF Predicted

The plots show the predicted SRFs, 95% prediction bound for SRFs and the comparison between the SRF predicted surge and the simulated surge. Except one simulation at station 108 all of the simulations results are within the 95% prediction bound. Residuals plots shows scatter around zero which shows that the fit is unbiased. R-square values for Gaussian fit at Galveston bay lies in 0.81 to 0.88. The R-square value for Galveston is lower than that of Matagorda Bay, thus the fit in this region is not as good as Matagorda Bay. The Figure 49 and Figure 52 show comparison between simulated storm surge values and the SRF predicted surge. RMSE for Galveston Bay is between 0.30m to 0.57m. RMSE at Galveston is higher than that of Matagorda Bay; this can be attributed to the bigger size of bay and the variation in the continental shelf width which has not been taken into account. Also we need to have more data in region where non-dimensional distance approaches zero to define SRFs more accurately.

6.4 Preliminary Application to Corpus Christi

A contour map and the key features for Corpus Christi are discussed in chapter 3. Here we will apply the methodology developed for Matagorda Bay to Corpus Christi Bay. The key parameters which change for Corpus Christi bay are

- Center of gravity of bay
- Size of Bay (10Km)
- Lambda value=0.74 (based upon the Song 2009)
- Constant c ($0.01/m^2$)

Tracks considered for Corpus Christi bay are tracks A and track B, which are same as that for Matagorda Bay. Figure 53 shows the position of the tracks A and B with respect to the Corpus Christi Bay.

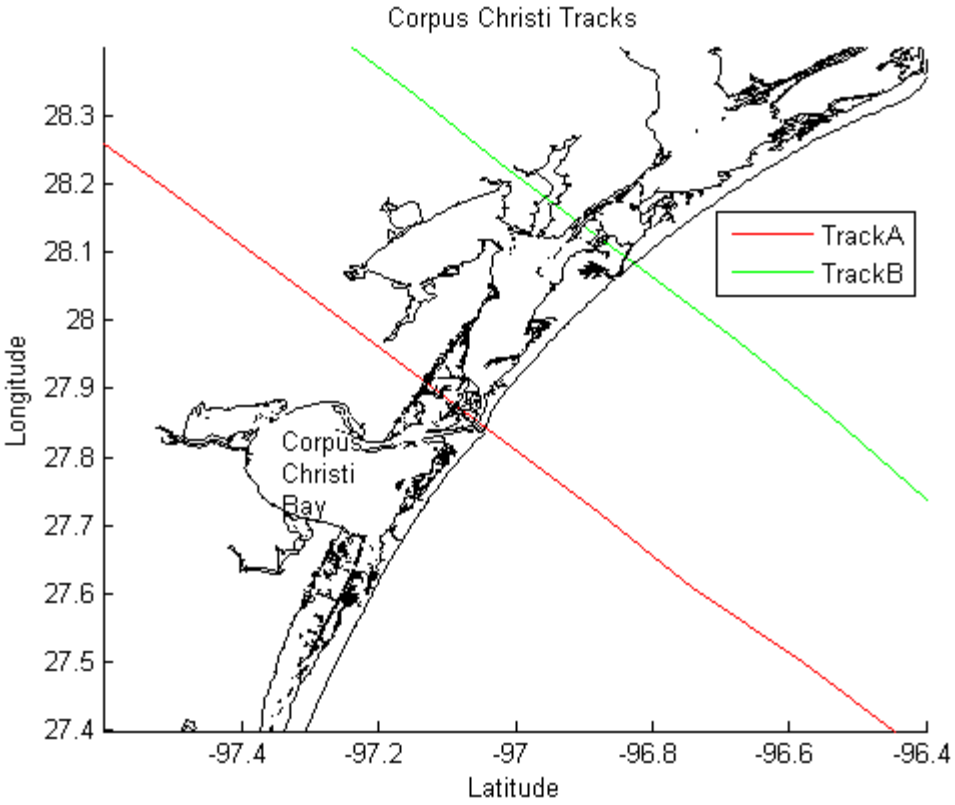

Figure 53 Corpus Christi Bay Tracks

Figure 54 through Figure 57 shows non dimensional plots at station 56, 67, 84, 95 for Corpus Christi. The methodology works well in Corpus Christi for Tracks A and B as simulations collapse on to a single function.

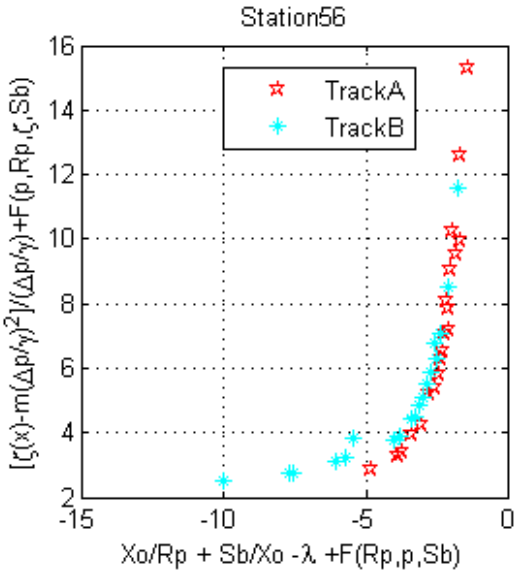

Figure 54 Non-dimensional Plot Corpus Christi Station 56

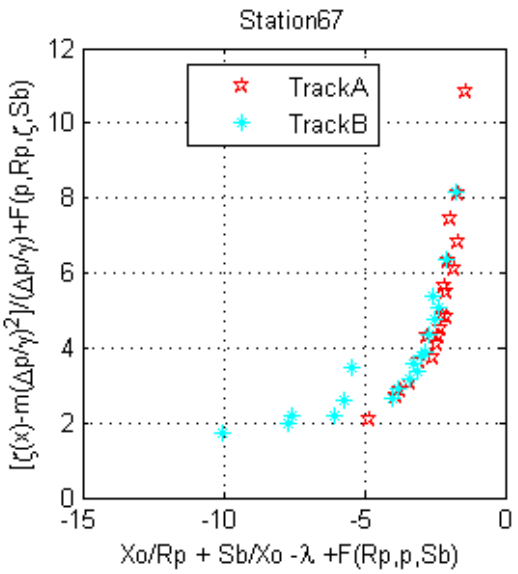

Figure 55 Non-dimensional Plot Corpus Christi Station 67

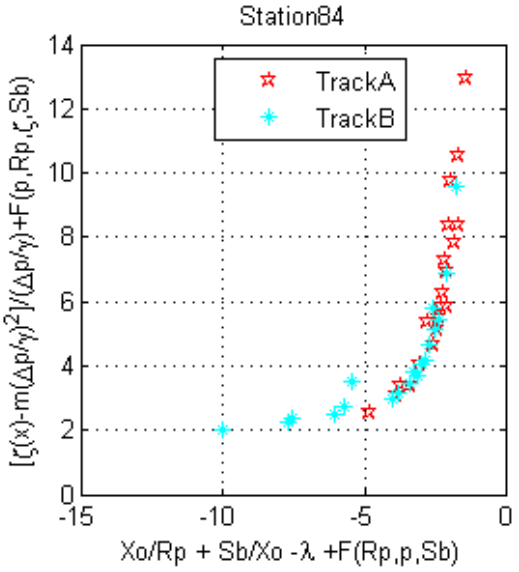

Figure 56 Non-dimensional Plot Corpus Christi Station 84

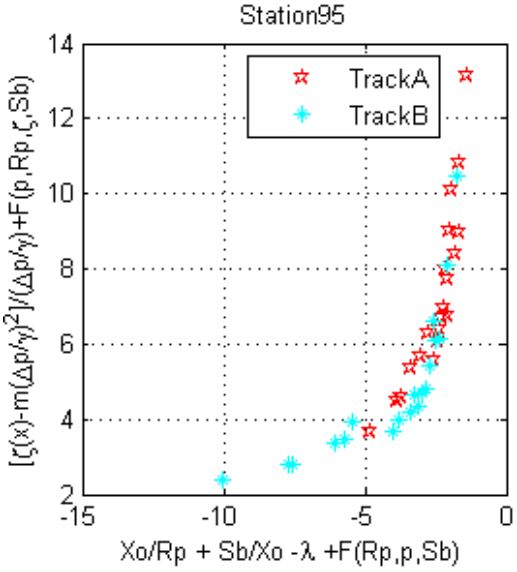

Figure 57 Non-dimensional Plot Corpus Christi Station 95

The SRFs for Corpus Christi show promising results, but to generate the SRFs for positive non-dimensional distance, more simulation on tracks towards the west side of Corpus Christi needs to be added. Figure 58 to Figure 61 shows the Gaussian function fitted to non dimensional data and comparison between the SRF predicted surge and the simulated surge for selected Corpus Christi Bay location.

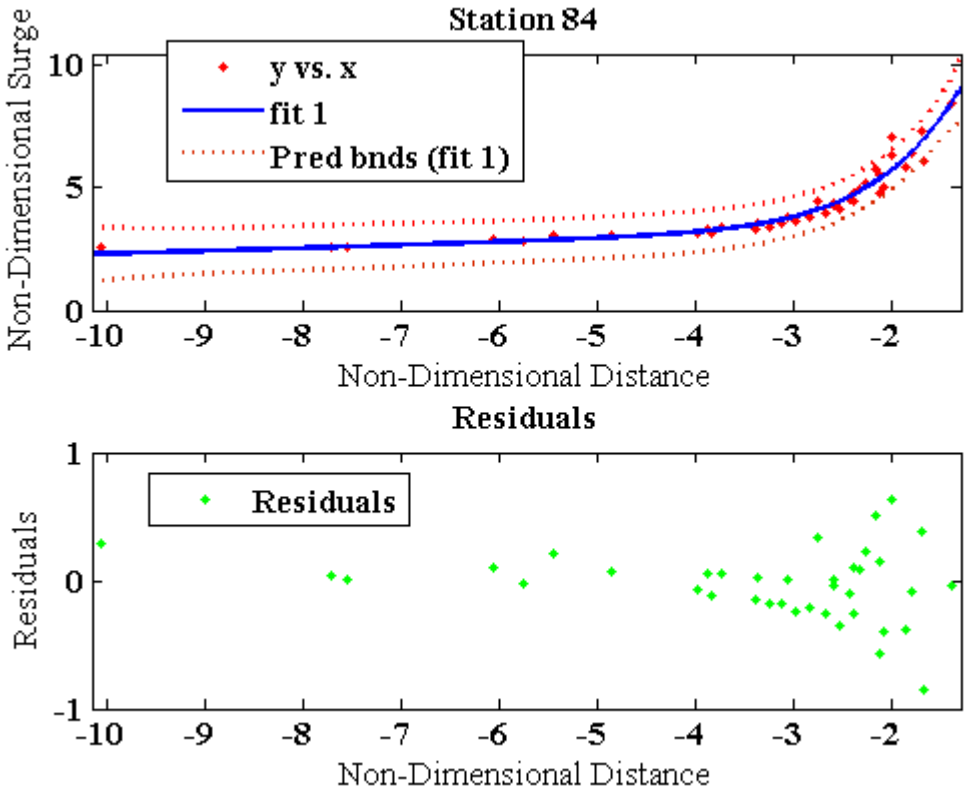

Figure 58 SRF for station 84, R-square 0.94

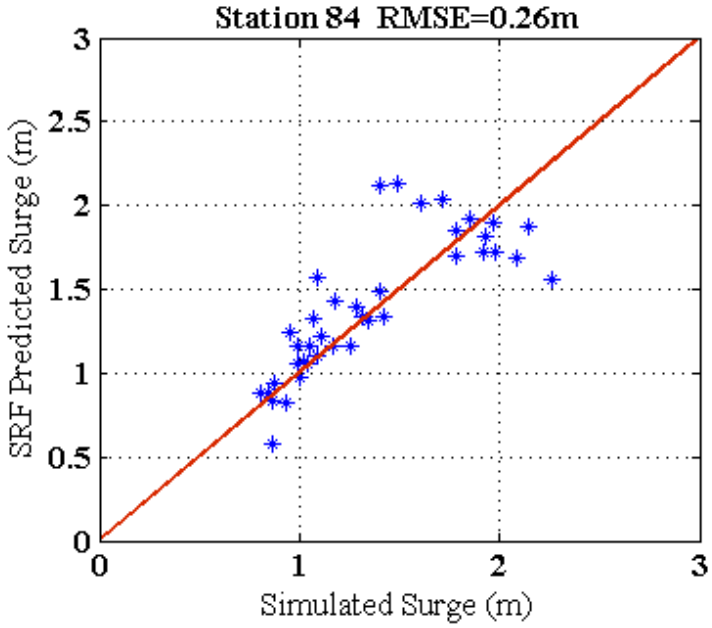

Figure 59 Simulated Vs SRF Predicted

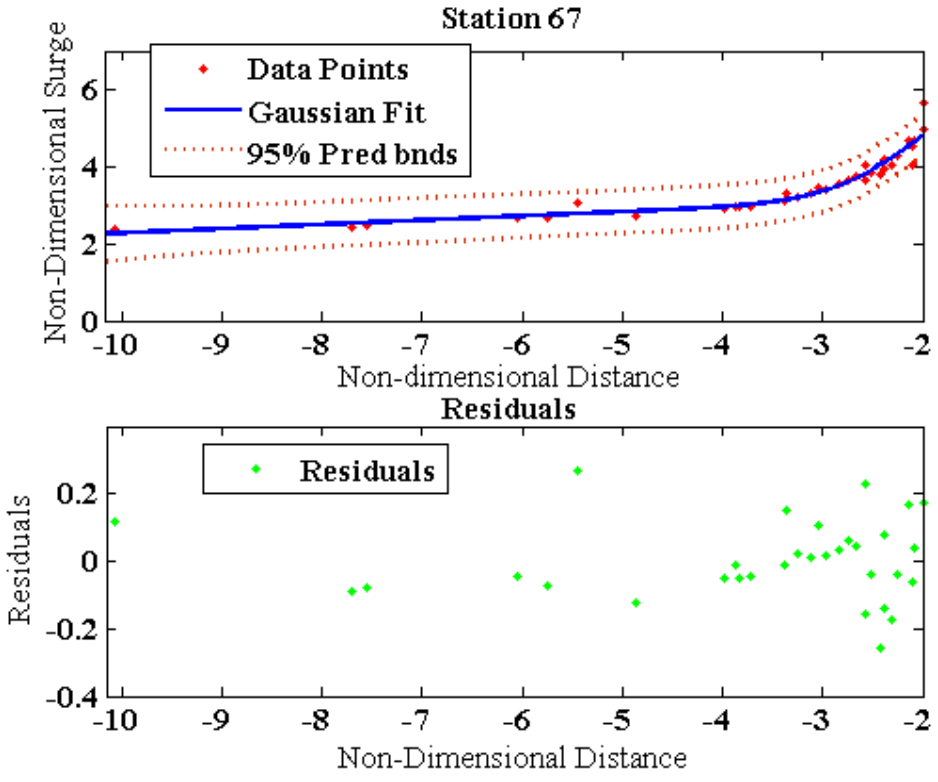

Figure 60 SRF for station 67, R-square 0.95

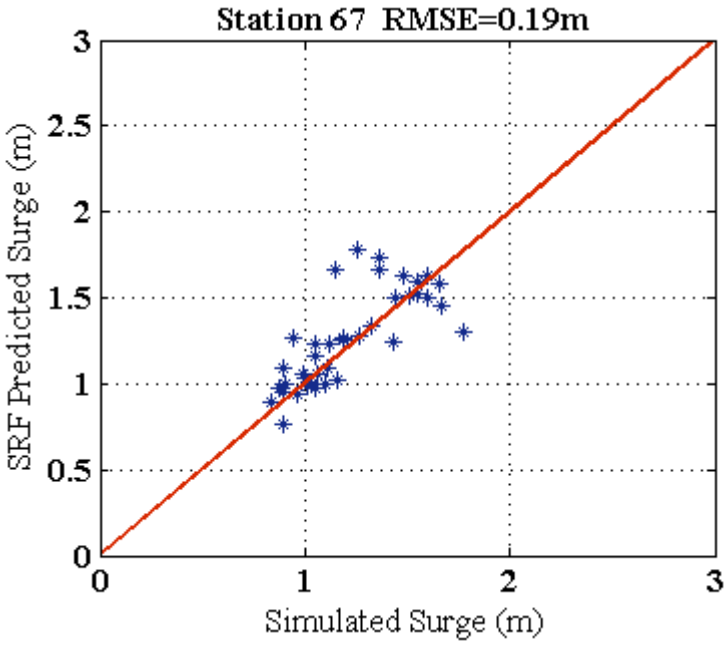

Figure 61 Simulated Vs SRF Predicted

SRFs predicted for Corpus Christi work well for track A and B as all simulation lies in 95% prediction bound. The residual plots have a scatter around the zero, which shows for unbiased fit. R-square value for Gaussian fit at Corpus Christi Bay stations lies in range of 0.92 to 0.97, which is comparable to that of Matagorda Bay. Figure 59 and Figure 61 show the comparison between simulated and SRF predicted surge values at station 84 and 67 inside Corpus Christi Bay. The values lies close to the bisection line (y=x), expect for region where non-dimensional value approaches zero. This can be attributed to fact that we did not consider any track on right hand side of zero in non-dimensional plot. Thus fit in this region is not accurate. Thus more simulations on tracks to the south side of Corpus Christi are required to predict SRFs completely. The RMSE between SRFs predicted and simulated surge values for Corpus Christi stations lie in range of 0.17 to 0.32.

Chapter VII

Summary and Discussion

In this thesis, development of SRFs for bays has been explored. The importance of various relevant parameters for SRFs is determined. As shown in Chapter V, storm surge inside bays is not affected by a location of channel, timing of surge, and inlet width. Also, surge inside the bay is correlated with the center of gravity of bay, characteristic size of bay, intensity of storm, and size of storm. Based upon these parameters non-dimensional distance and surge values are defined, these non-dimensional quantities are used to predict the Surge Response Functions inside Matagorda Bay. The methodology developed for predicting SRFs for Matagorda Bay shown to have worked inside Galveston and Corpus Christi Bay. Although RMSE error for Galveston Bay is higher as compared to Matagorda Bay, but the methodology developed gives the general trend for storm surge values. For Corpus Christi Bay, RMSE is comparable with RMSE of Matagorda bay. It should be noted that for predicting SRFs at Corpus Christi more storms towards south side of Bay should be considered.

Also, for three bays most of simulated results lie in 95% confidence interval. R-square values for Gaussian fit at Matagorda and Corpus Christi Bay are identical with values between 0.9 to 0.97, while at Galveston Bay R-square values are relatively lower with R-square values between 0.78 - 0.88. Also based upon this we have seen higher RMSE at Galveston Bay compared to Matagorda or Corpus Christi Bay.

Also, for non-dimensional surge inside the bay, the value of constant ‘c’ has been varied for three bays. Corpus Christi has c=0.05, Matagorda Bay c=0.03 and for Galveston c=0.01. This can be attributed to change in continental shelf width as one move from Corpus Christi to Galveston Bay. The values for λ based upon open coast work (song 2009) have worked well for inside bays also.

Comparison of SRFs (open coast, Irish et. al 2009) with SLOSH Model data base is also presented. While SLOSH model gives one value of surge for a given category of storm, SRF approach gives range of values based upon the landfall location, intensity and size of storm.

Thus SRFs methodology developed for Matagorda Bay has shown promising results in both Galveston and Corpus Christi Bay. Thus, this method can be used to predict the surge levels in the bay with accuracy defined for 3 bays in earlier chapters. The values of ‘c’ proposed here for 3 bays seems to be related to the continental shelf width, but more work needs to be done to find the exact relation between the constant ‘c’ and the shelf width. To define the SRFs in the region where non-dimensional distance approaches zero (Maximum value for SRF), more simulation results are required for all three bays. To further improve SRFs inside bays, parameters like track angle and forward speed of storm should be considered and the response of bay to these changes should be studied.

REFERENCES

Aldama, A, Aguilar, A, Kolar, R, and Westerink, J.J (2000). "A mass conservation analysis of the GWCE formulation." *Computational Methods in Water Resources XIII*, 2, 907-912.

Cardone, V. J., H. C. Graber, R. E. Jensen, S.Hasselmann, M. J. Caruso (1994). "In search of the true surface wind field in SWADE IOP-1: Ocean wave modelling perspective". The Global Atmosphere and Ocean System, 3, 107-150.

Cardone, V.J., Greenwood, C. V., and Greenwood, J.A. (1992). "Unified program for the specification of hurricane boundary layer winds over surfaces of specified roughness." Contract Report CERC-92-1, US Army Corps of Engineers, Vicksburg, MS. Chow, S. H. (1971). "A study of the wind field in the planetary boundary layer of a moving tropical cyclone," M.S. Thesis, New York Univ., New York.

Donald T. R. and Westerink, J. J. (2008). "Modeling the Physics of Storm Surges." *American Institute of Physics*, feature article.

FEMA (Unknown) “Hurricane Hazards”

[http://www.fema.gov/hazard/hurricane/hu_hazard.shtm]

Gray, W. G. (1982). "Some inadequacies of finite element models." *Adv. WaterResources*, 5(September), 171-177.

Greenberg, D. A., Dupont, F., Lyard, F. H., Lynch, D. R., and Werner, F.E. (2007). "Resolution issues in numerical models of oceanic and coastal circulation." *Continental Shelf Research*, 27(2007), 1317-1343.

Irish, J.L., and Resio, D.T. (2009) "A hydrodynamics-based surge scales for hurricanes." Ocean Eng., in press.

Irish, J. L., and Cañizares, R., (2009). "Storm-Wave Flow through Tidal Inlets and Its Influence on Bay Flooding." *J. Waterw. Port C.,* 135(2), 52-60.

Irish, J. L., Resio, D. T., and Cialone, M. A. (2008). “A surge response function approach to coastal hazard assessment—Part 2: quantification of spatial attributes of response functions." *Nat Hazards*, 10.1007/s11069-009-9381-4.

Irish, J. L., Resio, D. T., and Ratcliff, J. J. (2008). "The influence of storm size on hurricane surge." *J. Phys. Oceanogr.*, 38(9), 2003-2013.

Luettich, R.A., Westerink, J. J., and Scheffner, N.W. "ADCIRC: An advanced three dimensional circulation model for shelves, coasts, and estuaries: Report 1: Theory and Methodology of ADCIRC-2DDI and ADCIRC-3DL", *Technical Report DRP-92-6*, US Army Corps of Engineers, Washington, DC.

Lynch, D. R. (1983). "Progress in hydrodynamic modeling, review of U.S. Contribution." *Rev. Geophys, Space Phys*, 21(3), 741-754.

Lynch, D. R. and Gray W. G. (1979). "A wave equation model for finite element tidal computations." *Comput. Fluids* 7, 207–228 Navon, I. M. (1988). " A review of finite-element methods for solving the shallow-water equations." *Computer Modeling in Ocean Engineering*, 273-278.

Mark,D.J. and ScheffnerN.W.(1993) “ Validation of continental scale storm surge model for the coast of Delaware.” *Estuarine and Coast. Modeling conference, ASCE., New York, NY, 249-263.*

NOAA. (Unknown) “Hurricane Preparedness” [http://www.nhc.noaa.gov/HAW2/english/intro.shtml]

Older, M.E. (1981) “A two-dimensional finite-element advection model with variable resolution”. M. Sc. Thesis. Naval Post Graduate School Report ADA107511: Monterey, CA.

Provost. C. Le, Bernier.C and Balyo.E (1994). “A comparison of two numerical methods for integrating a quasi-geotropic multilayer model of ocean circulations: Finite Element and Finite Difference method” *Computational Physics 110, 341-359.*

Resio, D. T. and Irish, L. J. (2009). "A surge response function approach to coastal hazard assessment. Part 1: Basic concepts." *Nat. Hazards*, 2009, 10.1007/s11069-009-9379-y

Resio, D.T. and Westerink, J. J. (2008). "Modeling the physics of storm surges." *Physics today,*September 2008, feature article.

Song, Y.K (2009) “Extreme Hurricane Surge Estimation for Texas Coastal Bridges Using Dimensionless Surge Response Functions” M.S Thesis, Texas A&M University

Taylor,A and Berger, H(2008) “SLOSH display package” *Evaluation Branch, Meteorological Department Lab, NOAA.*

Thompson, E. F., and Cardone, V.J. (1996). "Practical modeling of hurricane surface wind fields." *Journal of Waterway, Port, Coastal, and Ocean Engineering*, July/August 1996, 198-205.

Vickery, P. J. and Wadhera, D.H., Powell, M. D., Chen, Y. (2008). "A hurricane boundary Layer and wind field model for use in engineering applications." *Journal of applied meteorology and climatology*, 48, 381-405.

Westerink, J.J., Luettich, R. A., Feyen, J.C., Atkinson, J.H., Dawson, C., Roberts, H.J., Powell, M.D., Dunion, J.P., Kubatko, E.J., and Pourtaheri, H. (2008). "A basinto channel-scale unstructured grid hurricane storm surge model applied to southern Louisiana." *Monthly Weather Review*, 136, March 2008, 833-864.

Westerink J.J., Luettich, R. A., and Scheffner N.W. (1994). "ADCIRC: An advanced three-dimensional circulation model for shelves, coasts, and estuaries: Report 4: Hurricane strom surge modeling using large domains." *Technical Report DRP- 92-6,* US Army Corps of Engineers, Washington, DC.

Westerink, J.J., Luettich, R. A., Baptista, A. M., Scheffner, N.W., and Farrar, P. (1992). "Tide and storm surge perdictions using finite element model." *Journal of Hydraulic Engineering*, 118(10), 1373-1390.

Westerink, J. J., Muccino, J. C., and Luettich, R. A. (1991). "Tide and storm surge computations for the Western North Atlantic and Gulf of Mexico." *Esturine and coastal modeling*, 538-550.

APPENDIX A

Development of Parameterized Surge Response Functions for Coastal Bays

Table 5 Stations Location inside Matagorda Bay

Station No.	Lon	Lat
1	-96.4019	28.3452
2	-96.3938	28.3601
3	-96.3812	28.3761
4	-96.3663	28.3888
5	-96.3548	28.4025
6	-96.3376	28.4106
7	-96.3135	28.4232
8	-96.2860	28.4393
9	-96.2630	28.4576
10	-96.2366	28.4737
11	-96.2079	28.4886
12	-96.1827	28.5024
13	-96.1540	28.5161
14	-96.1345	28.5253
15	-96.1116	28.5322
16	-96.0966	28.5414
17	-96.0783	28.5471
18	-96.0576	28.5552
19	-96.0301	28.5666
20	-96.0140	28.5781
21	-96.3776	28.4195
22	-96.3559	28.4343
23	-96.3424	28.4479
24	-96.3208	28.4587
25	-96.3018	28.4709
26	-96.2761	28.4871
27	-96.2545	28.5033
28	-96.2288	28.5169
29	-96.2031	28.5236
30	-96.1828	28.5344
31	-96.1598	28.5480
32	-96.1327	28.5561
33	-96.1165	28.5669
34	-96.0867	28.5750
35	-96.0651	28.5872

Station No.	Lon	Lat
36	-96.0380	28.5994
37	-96.0191	28.6075
38	-96.3938	28.4384
39	-96.4033	28.4627
40	-96.4195	28.4857
41	-96.4506	28.5047
42	-96.4790	28.5142
43	-96.5156	28.4966
44	-96.5385	28.4871
45	-96.5074	28.5412
46	-96.5223	28.5601
47	-96.5372	28.5710
48	-96.5615	28.5831
49	-96.4249	28.4195
50	-96.4209	28.4303
51	-96.4317	28.4560
52	-96.4466	28.4790
53	-96.4682	28.4912
54	-96.4871	28.4939
55	-96.4993	28.4790
56	-96.5467	28.4668
57	-96.5737	28.4830
58	-96.5710	28.5074
59	-96.5385	28.5182
60	-96.5304	28.5439
61	-96.5548	28.5601
62	-96.5710	28.5601
63	-96.5994	28.5628
64	-96.5818	28.5926
65	-96.6129	28.5831
66	-96.6102	28.6210
67	-96.6197	28.6562
68	-96.6414	28.6873
69	-96.6224	28.7117
70	-96.5940	28.7117
71	-96.5751	28.6873
72	-96.5791	28.6535

Station No.	Lon	Lat
73	-96.5426	28.6359
74	-96.5183	28.6332
75	-96.4993	28.6061
76	-96.6387	28.6481
77	-96.6576	28.6684
78	-96.6806	28.6981
79	-96.6305	28.7319
80	-96.6035	28.7414
81	-96.5548	28.7279
82	-96.5602	28.7089
83	-96.5588	28.6846
84	-96.5588	28.6616
85	-96.5372	28.7130
86	-96.5223	28.6805
87	-96.5061	28.6778
88	-96.4736	28.6088
89	-96.4682	28.6264
90	-96.4493	28.6143
91	-96.4276	28.5899
92	-96.4060	28.6007
93	-96.3884	28.6210
94	-96.4127	28.6494
95	-96.4087	28.6792
96	-96.3965	28.6792
97	-96.3681	28.6548
98	-96.3532	28.6210
99	-96.3248	28.6332
100	-96.3072	28.6427
101	-96.2923	28.6589
102	-96.2748	28.6738
103	-96.2436	28.6846
104	-96.2125	28.6900
105	-96.2220	28.6670
106	-96.2369	28.6427
107	-96.2207	28.6264
108	-96.2409	28.5953
109	-96.2315	28.5804

Station No.	Lon	Lat
110	-96.2085	28.5764
111	-96.1855	28.5831
112	-96.1692	28.5926
113	-96.1517	28.6021
114	-96.1300	28.6075
115	-96.4263	28.6143
116	-96.4276	28.6454
117	-96.4330	28.6873
118	-96.3708	28.6914
119	-96.3505	28.6643
120	-96.3289	28.6670
121	-96.3059	28.6968
122	-96.2802	28.7076
123	-96.2504	28.7049
124	-96.2247	28.7238
125	-96.1936	28.6657
126	-96.2031	28.6359
127	-96.1625	28.6359
128	-96.1368	28.6359

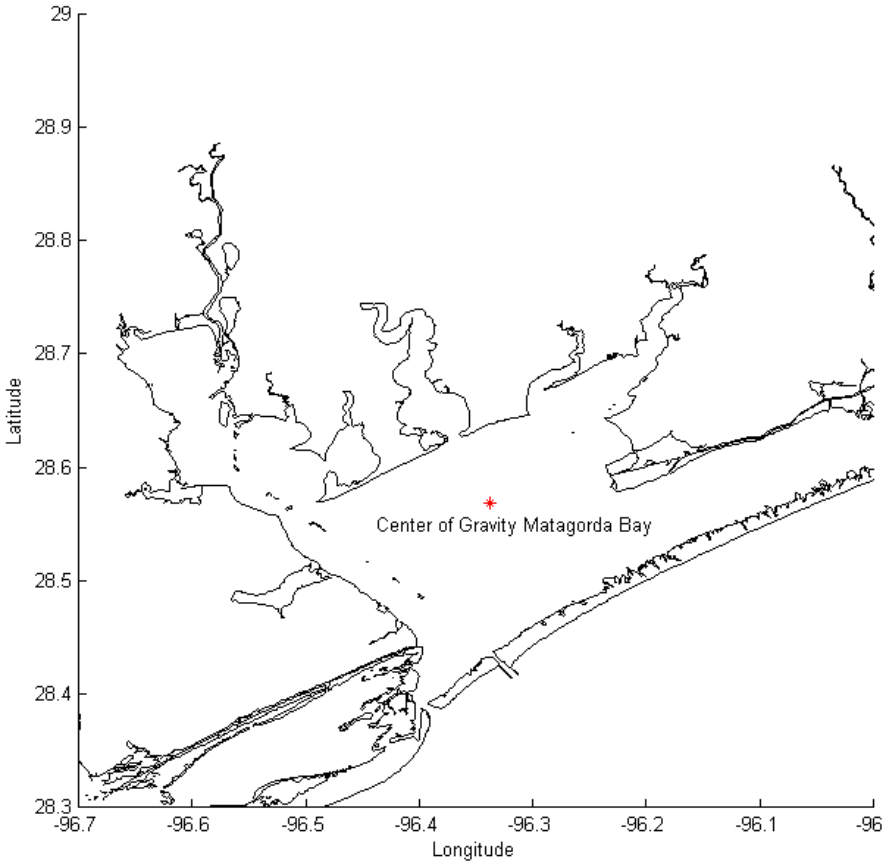

A- 1 Center of Gravity, Matagorda Bay

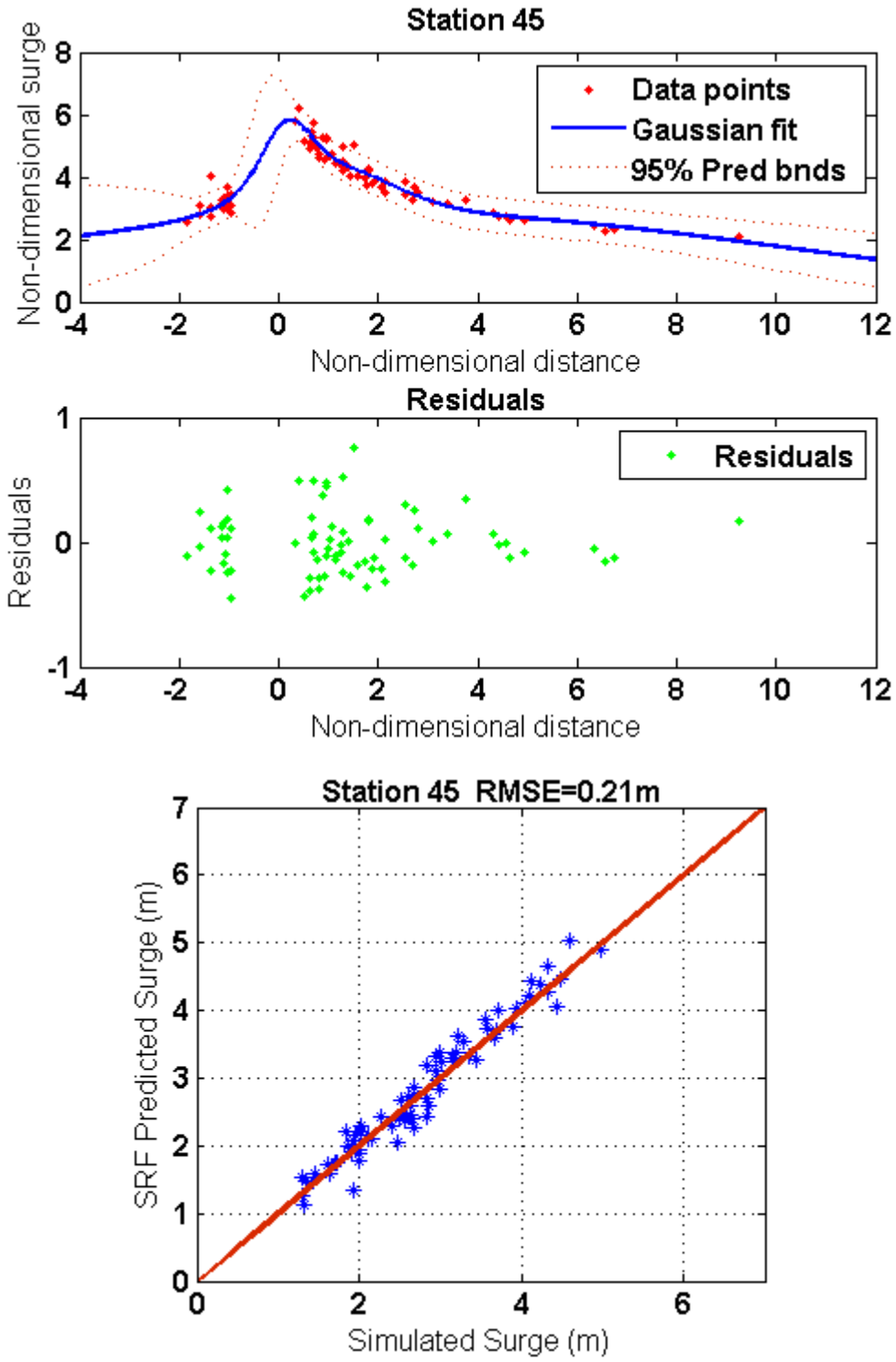

A- 2 SRF at station 45 inside Matagorda Bay.

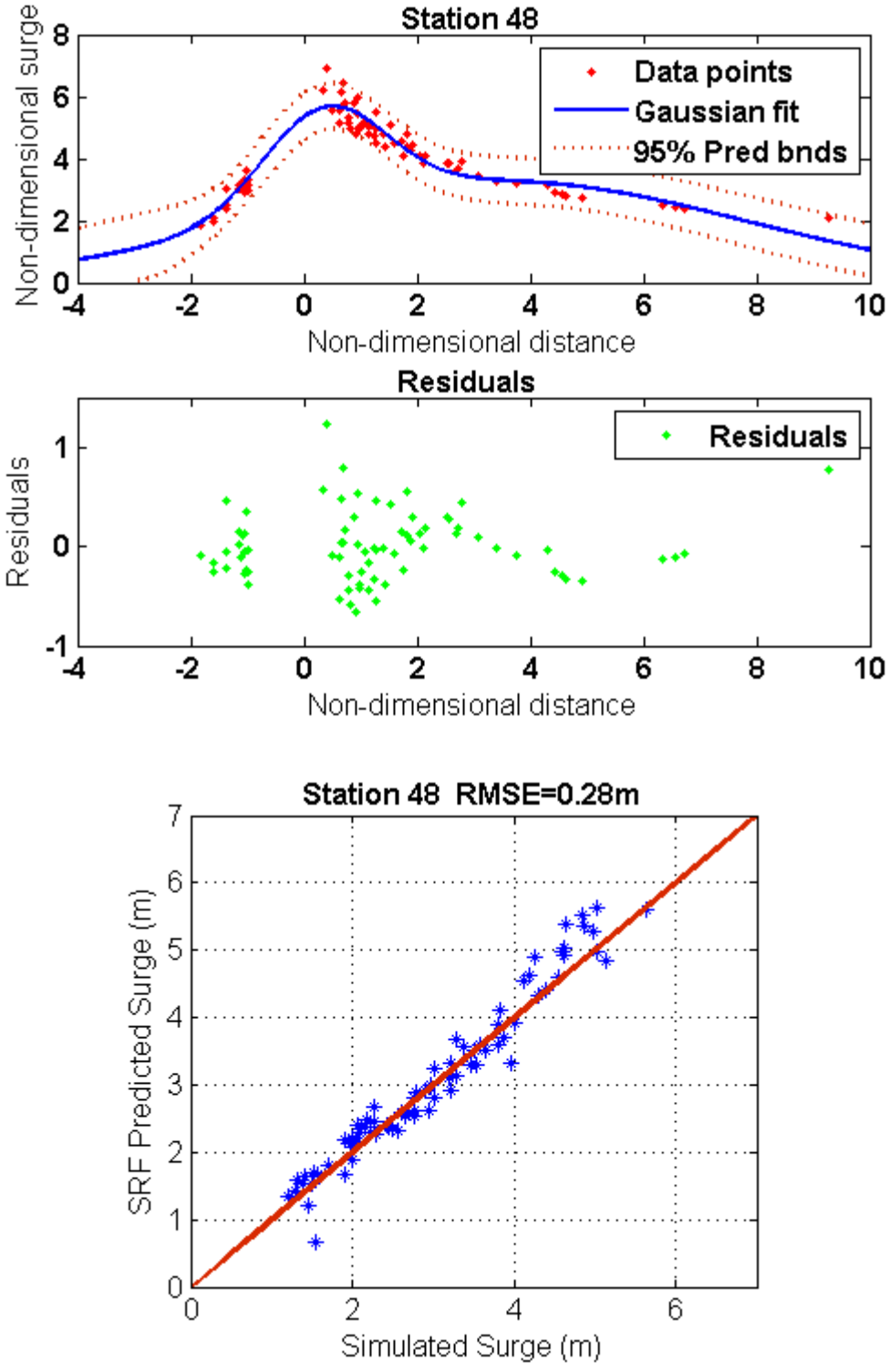

A- 3 SRF at station 48 inside Matagorda Bay

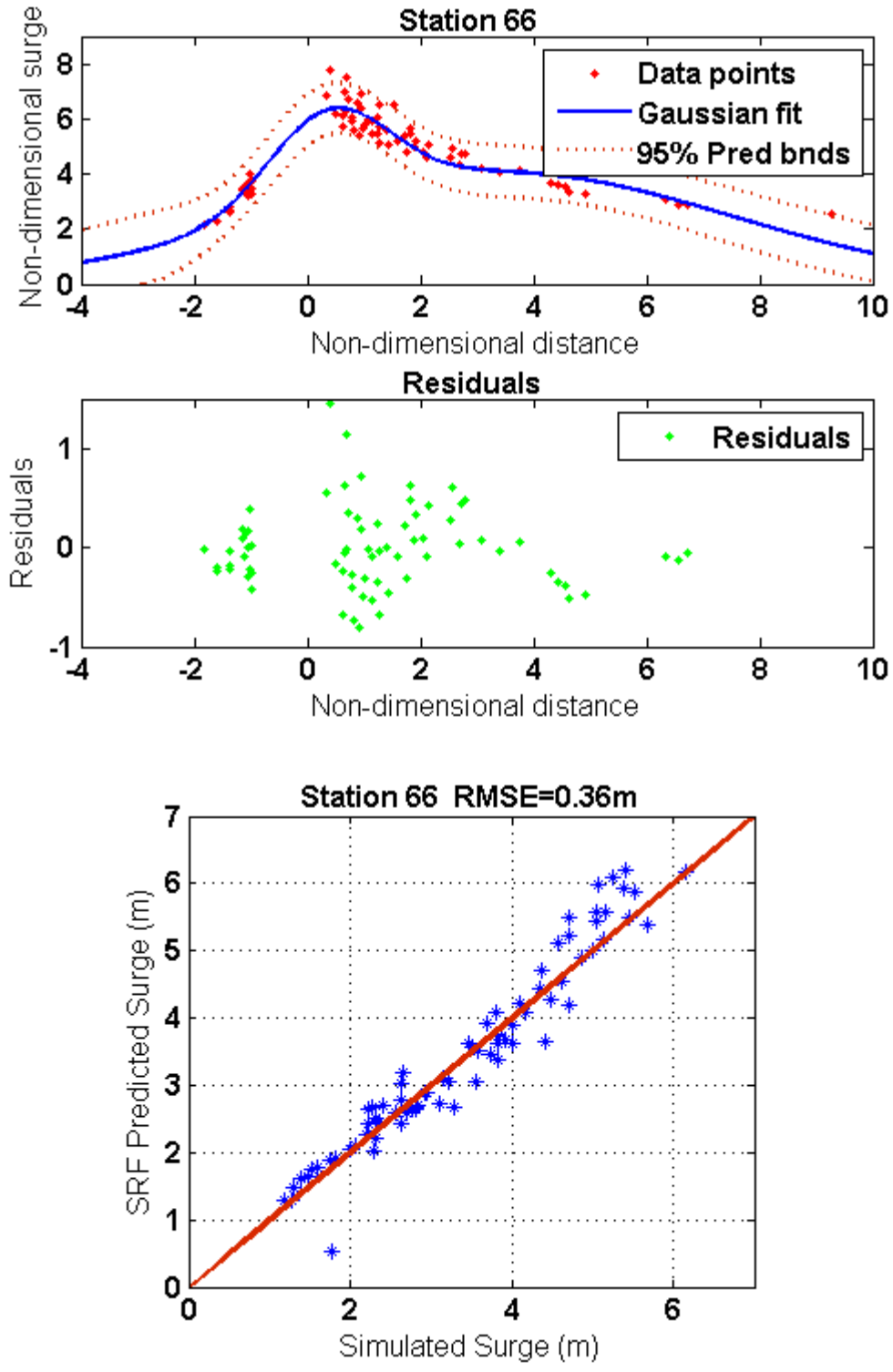

A- 4 SRF at station 66 inside Matagorda Bay

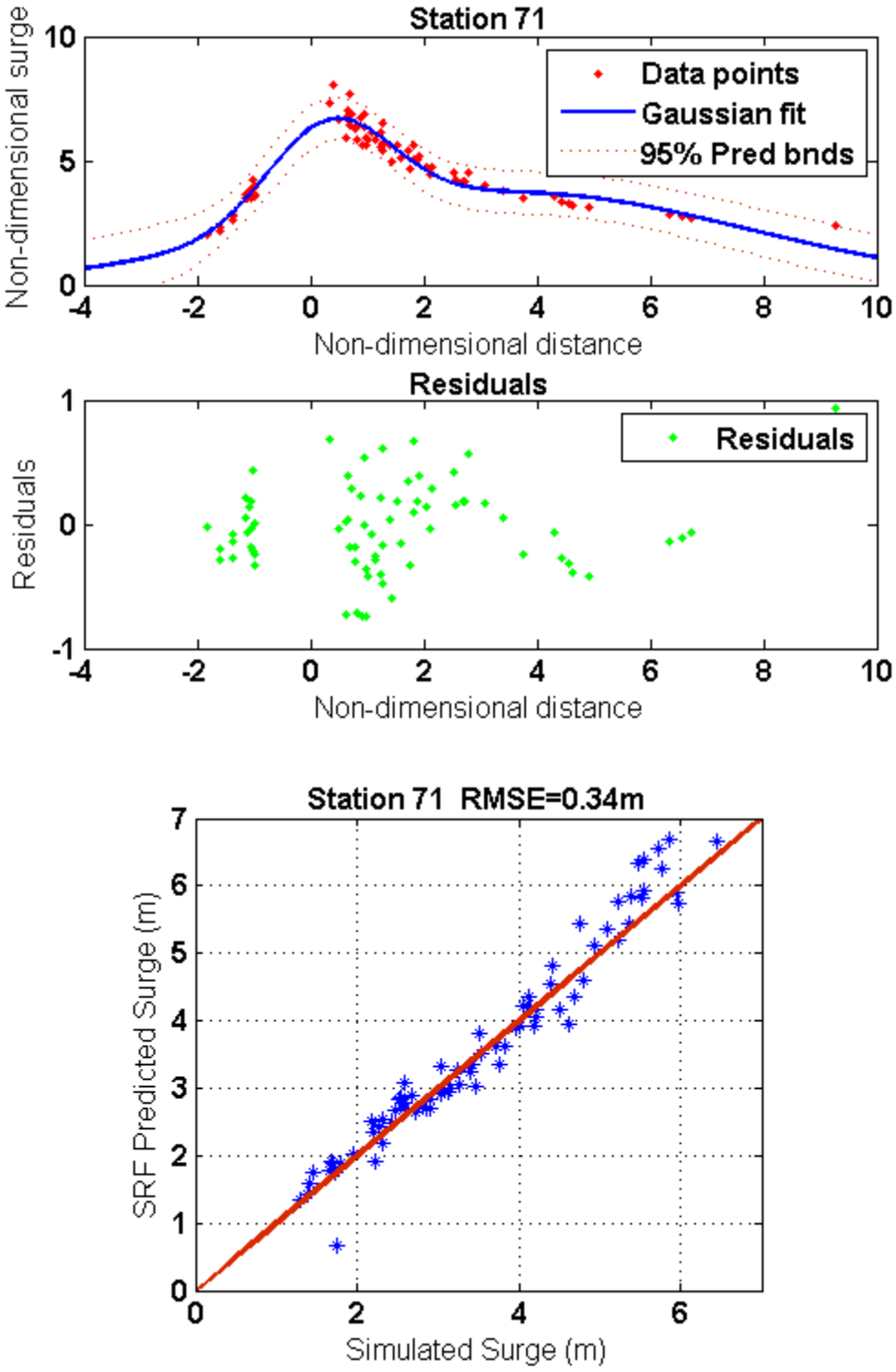

A- 5 SRF at station 71 inside Matagorda Bay

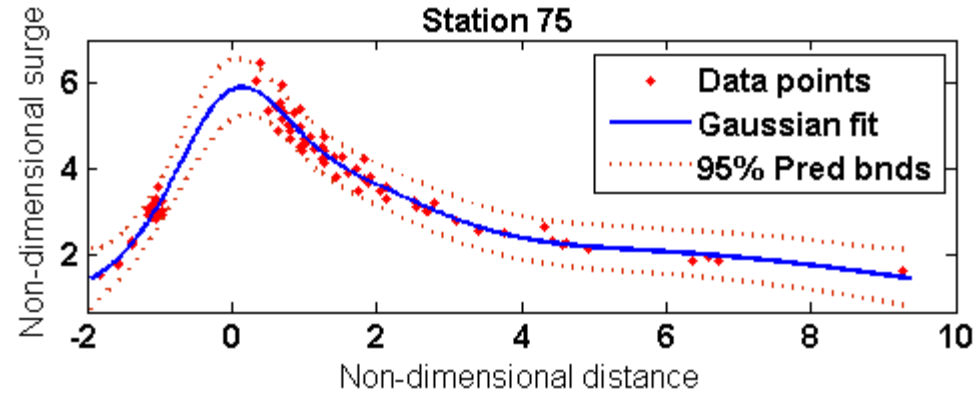

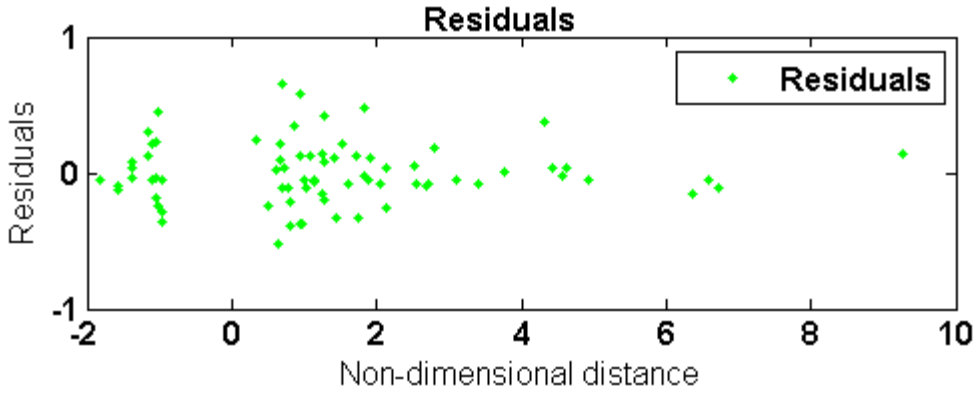

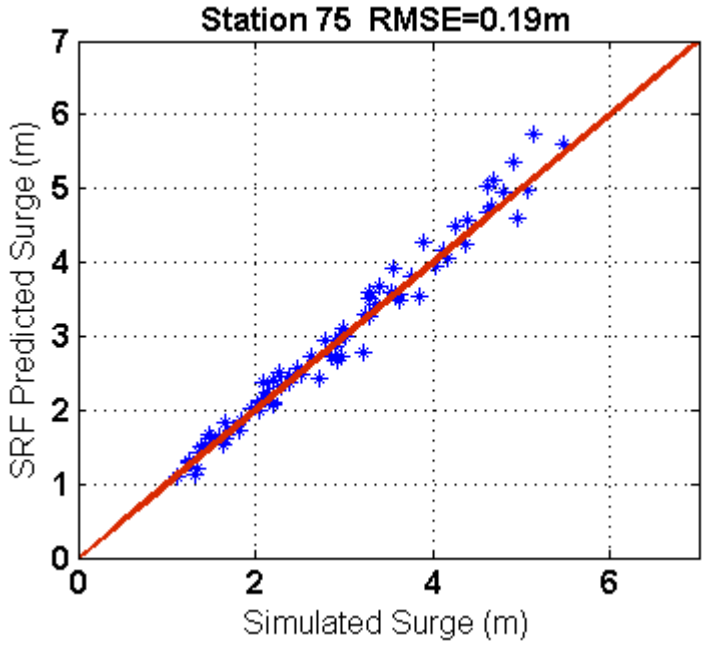

A- 6 SRF at station 75 inside Matagorda Bay

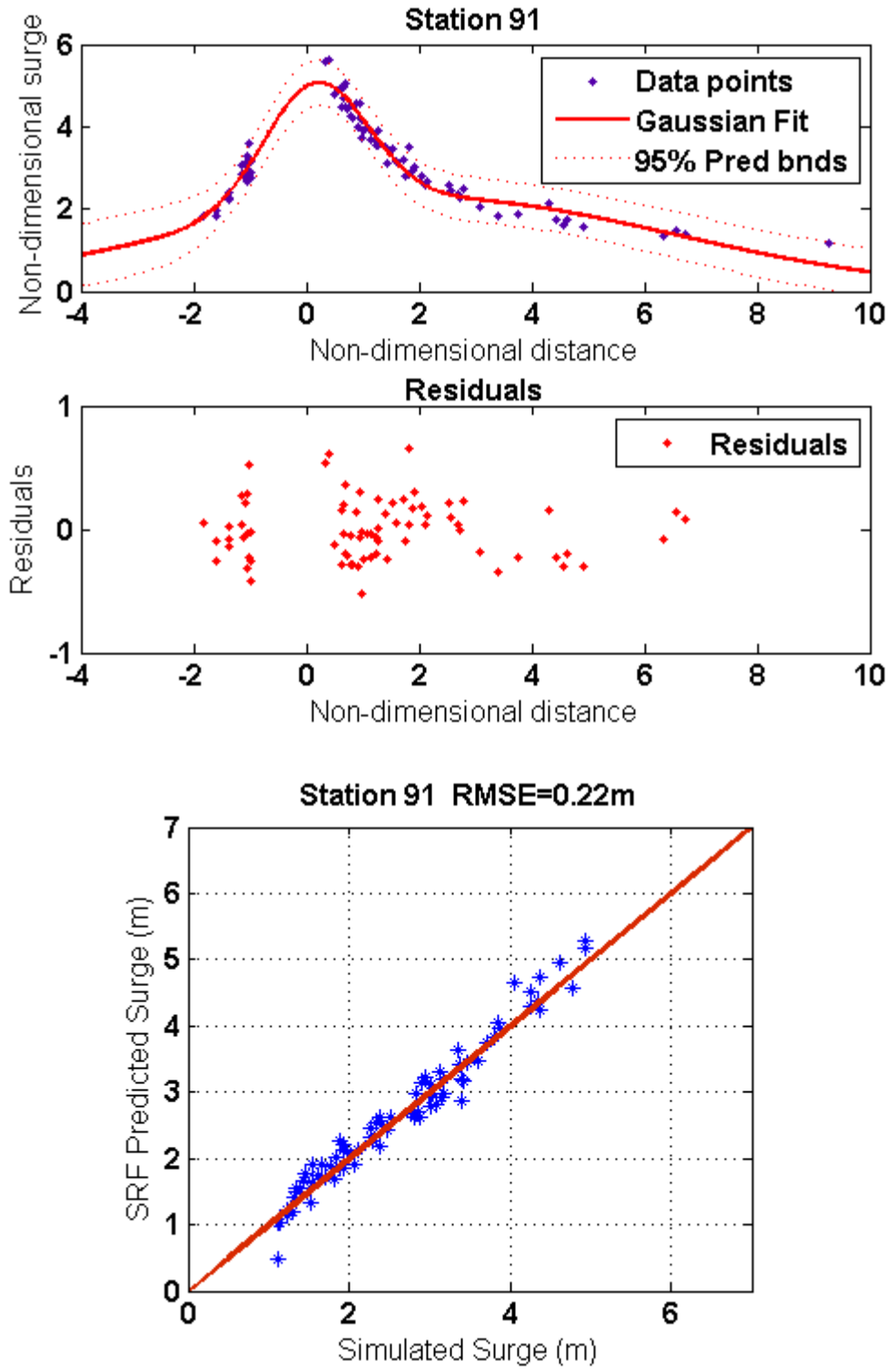

A- 7 SRF at station 91 inside Matagorda Bay

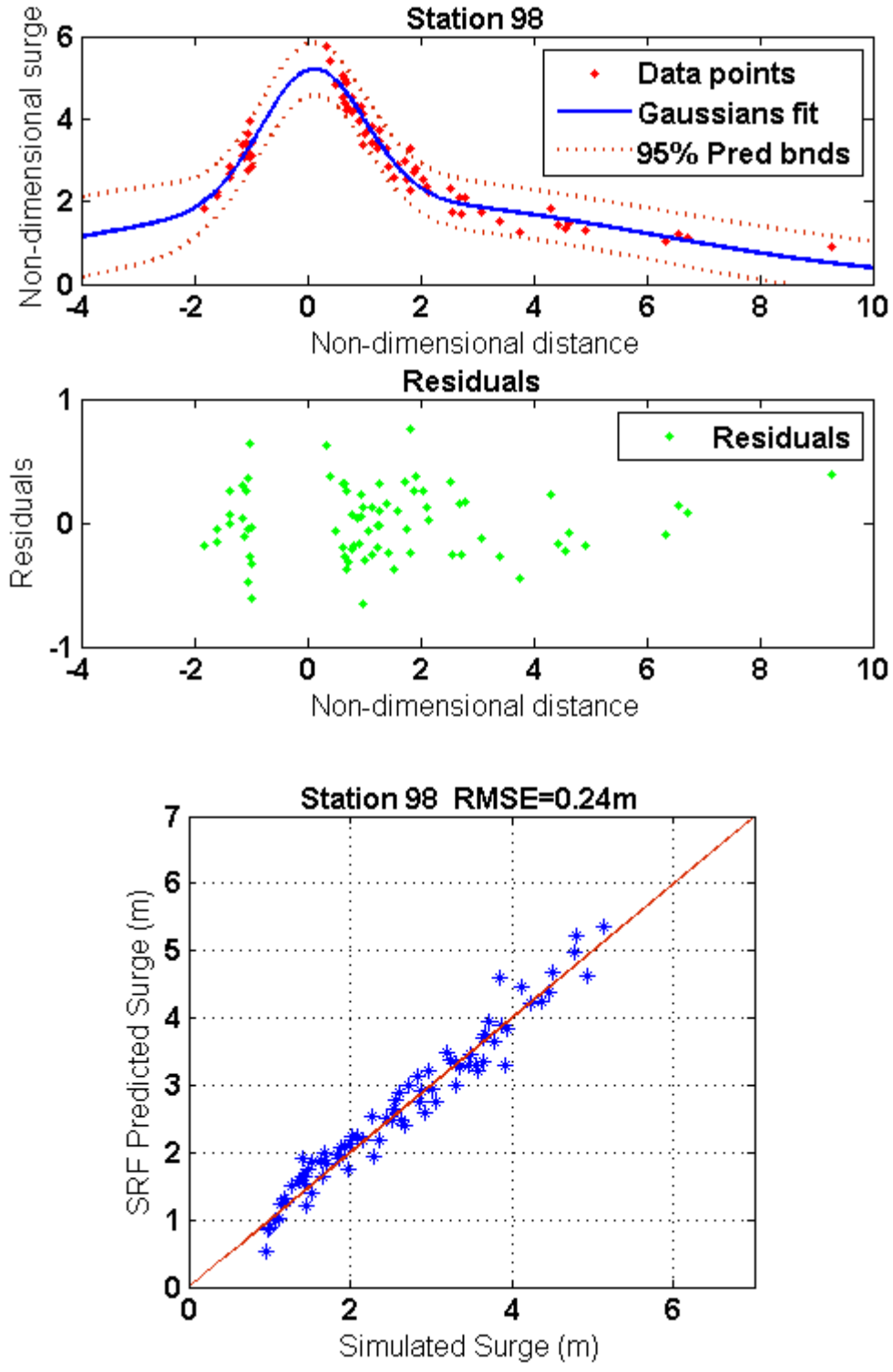

A- 8 SRF at station 98 inside Matagorda Bay

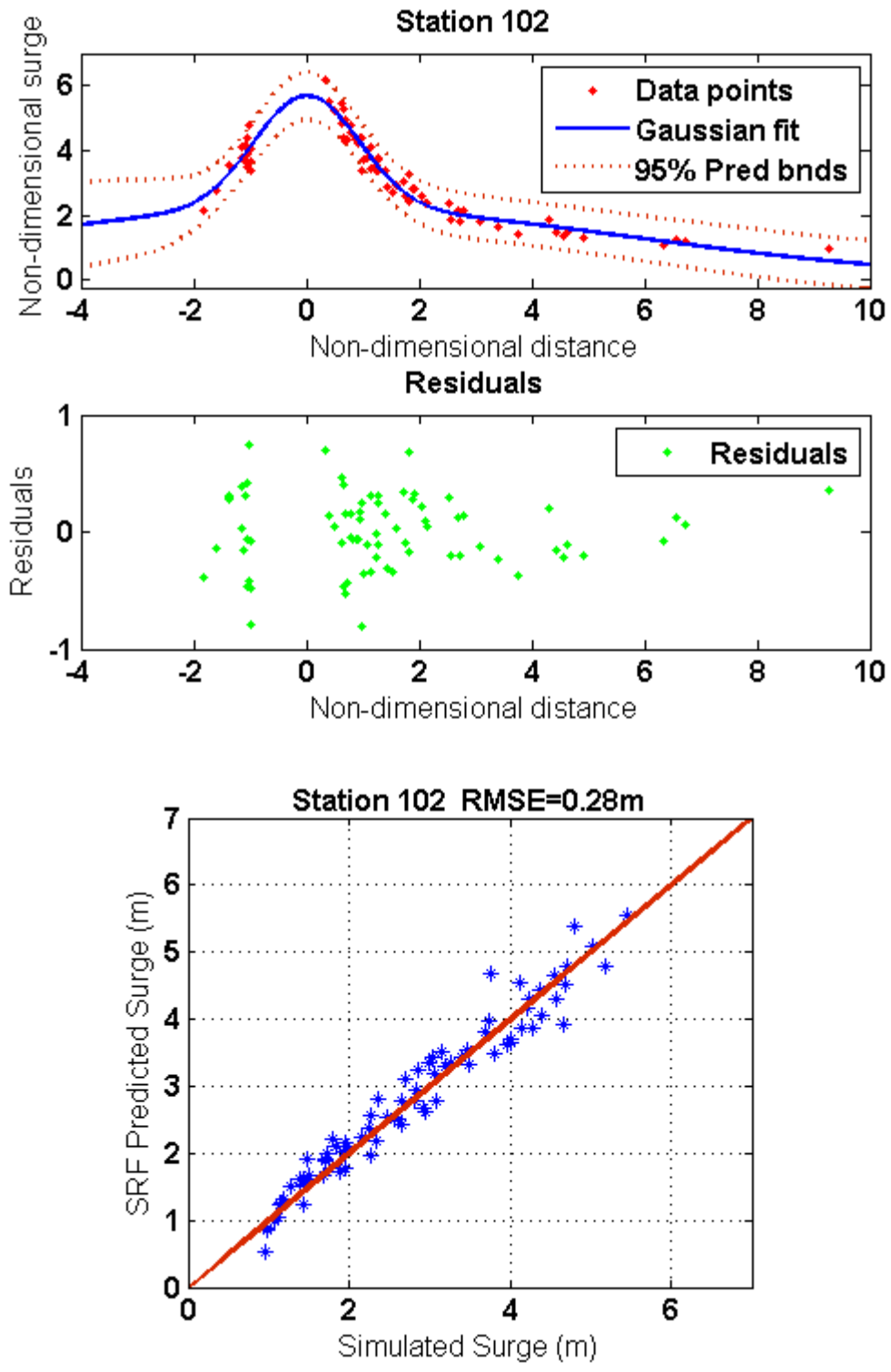

A- 9 SRF at station 102 inside Matagorda Bay

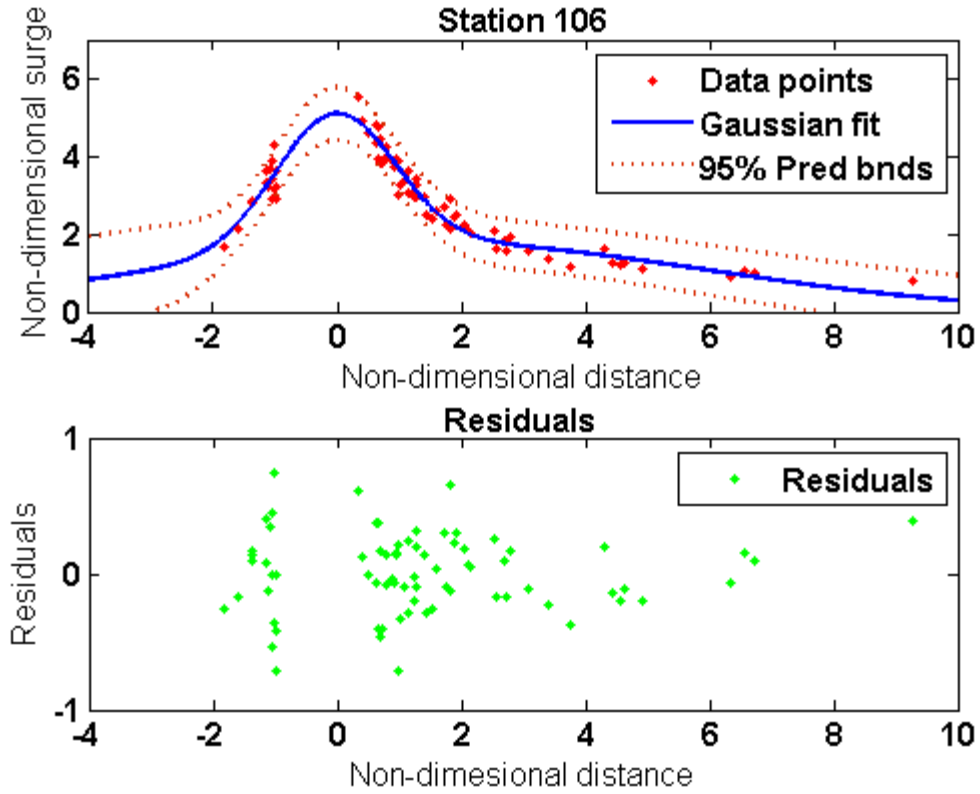

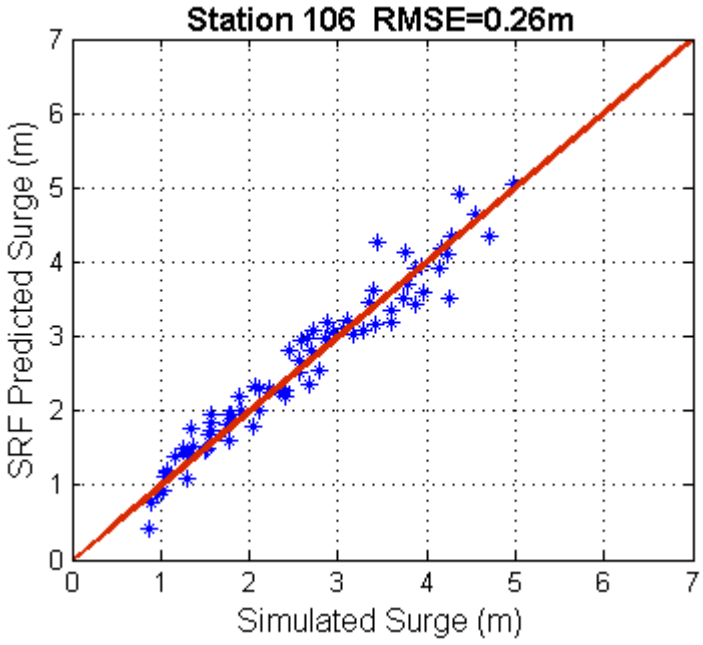

A- 10 SRF at station 106 inside Matagorda Bay

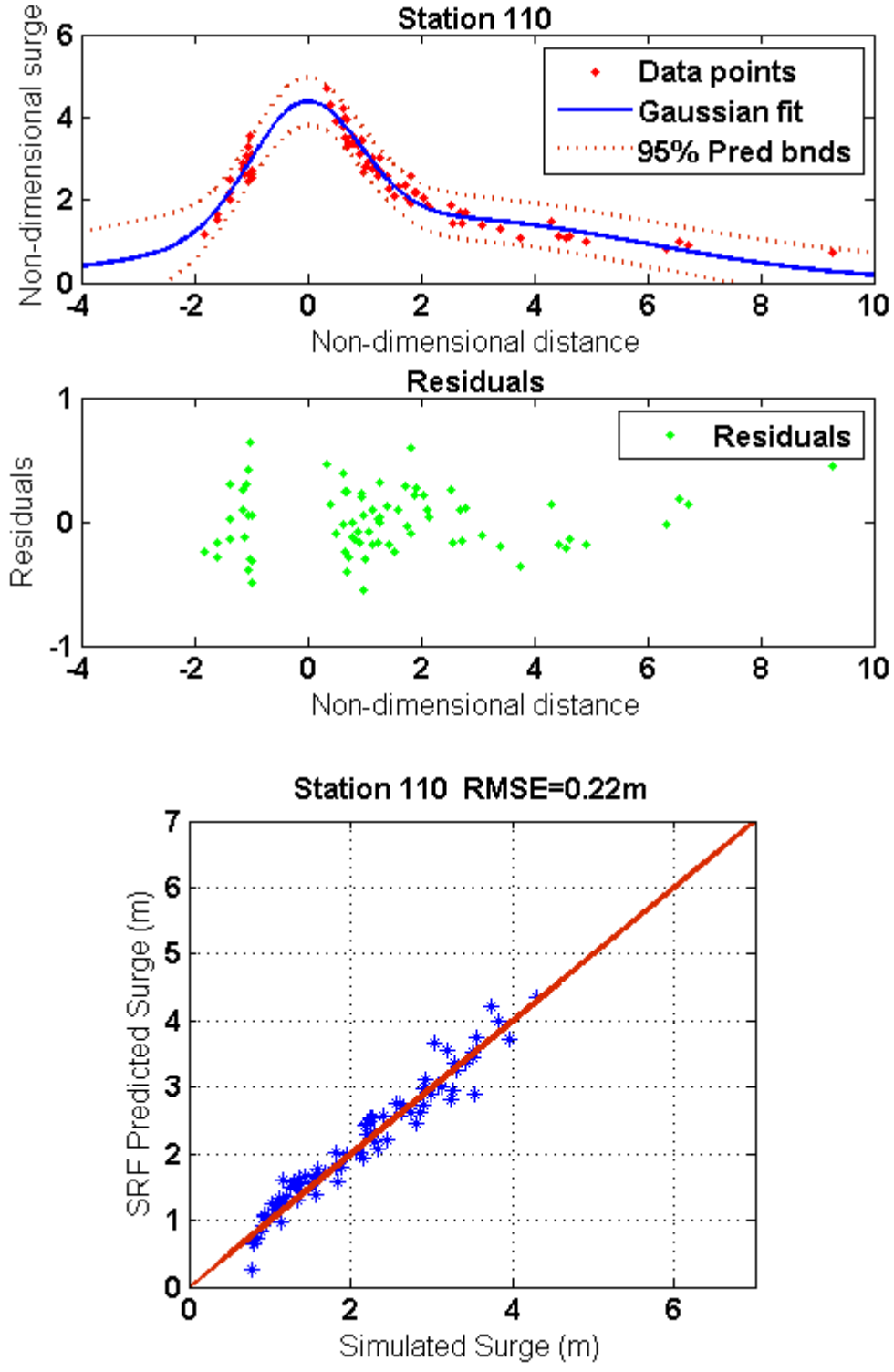

A- 11 SRF at station 110 inside Matagorda Bay

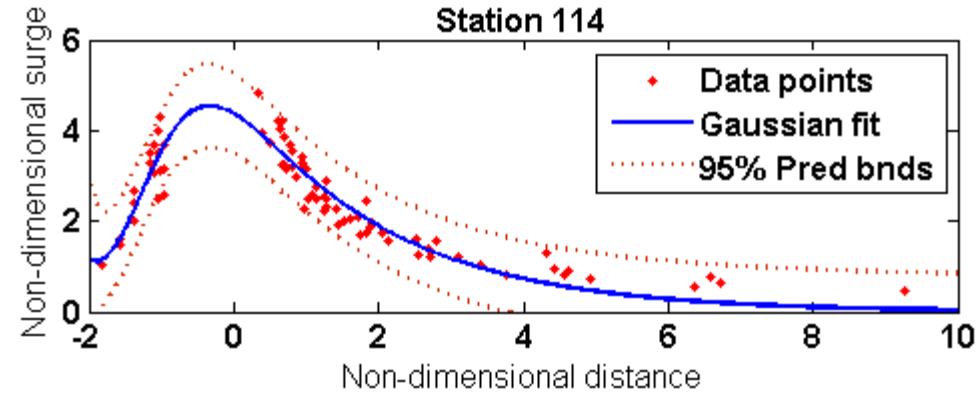

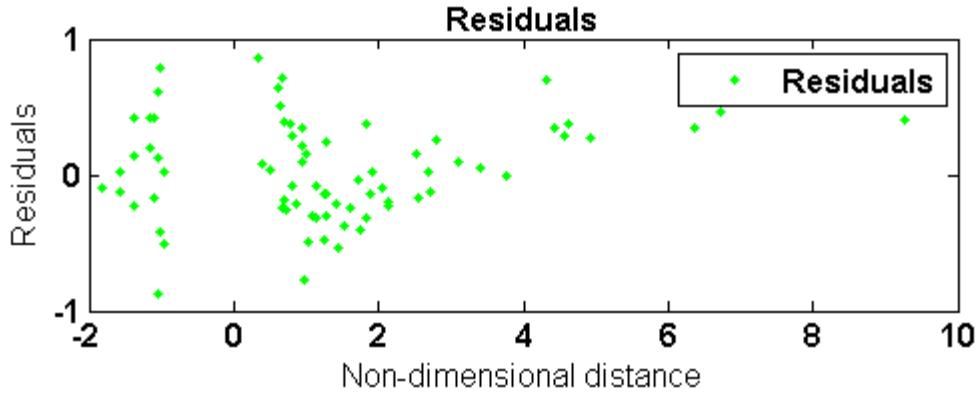

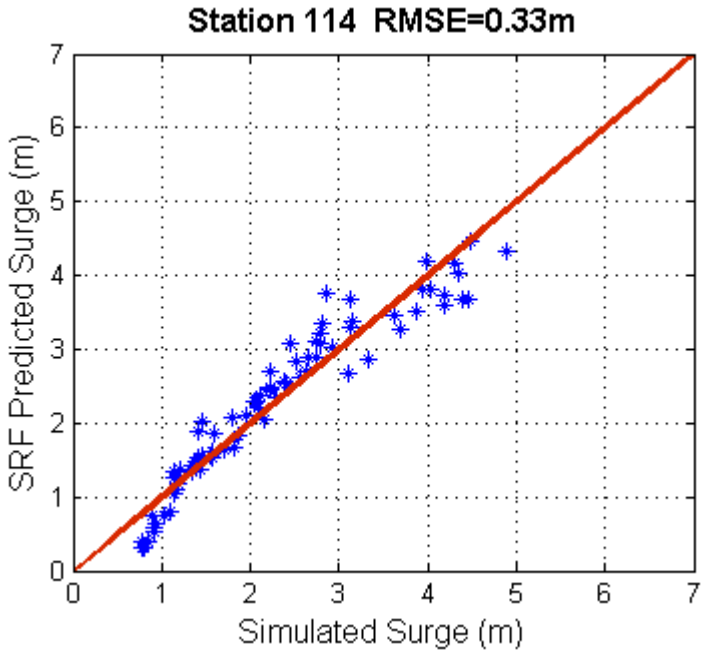

A- 12 SRF at station 114 inside Matagorda Bay

Table 5 Stations Location inside Galveston Bay

Station No.	Lon	Lat
1	-94.9282	29.2033
2	-94.9173	29.2112
3	-94.9026	29.2200
4	-94.8829	29.2308
5	-94.8672	29.2406
6	-94.8446	29.2485
7	-94.8289	29.2544
8	-94.8112	29.2692
9	-94.7925	29.2829
10	-94.7748	29.2957
11	-94.7640	29.3055
12	-94.7492	29.3164
13	-94.7335	29.3262
14	-94.7148	29.3262
15	-94.7227	29.3645
16	-94.7286	29.3714
17	-94.7197	29.3832
18	-94.7128	29.3940
19	-94.6991	29.4029
20	-94.6922	29.4147
21	-94.6745	29.4255
22	-94.6568	29.4343
23	-94.6430	29.4432
24	-94.6263	29.4520
25	-94.6096	29.4609
26	-94.5919	29.4678
27	-94.5693	29.4756
28	-94.5496	29.4845
29	-94.5339	29.4933
30	-94.5123	29.4973
31	-94.9655	29.2131
32	-94.9400	29.2308
33	-94.9213	29.2436
34	-94.9065	29.2603
35	-94.8859	29.2682
36	-94.8761	29.2751

Station No.	Lon	Lat
37	-94.8790	29.2908
38	-94.8721	29.2967
39	-94.8495	29.3026
40	-94.8348	29.3085
41	-94.8318	29.3173
42	-94.8289	29.3311
43	-94.8259	29.3478
44	-94.8180	29.3557
45	-94.7787	29.3891
46	-94.7659	29.4029
47	-94.7532	29.4147
48	-94.7355	29.4275
49	-94.7246	29.4432
50	-94.7060	29.4579
51	-94.6922	29.4717
52	-94.6686	29.4786
53	-94.6529	29.4845
54	-94.6430	29.4864
55	-94.6332	29.4855
56	-94.6185	29.4923
57	-94.6057	29.4982
58	-94.6027	29.5159
59	-94.5909	29.5287
60	-94.5683	29.5346
61	-94.5506	29.5346
62	-94.5369	29.5307
63	-94.5142	29.5277
64	-94.8937	29.3095
65	-94.8859	29.3173
66	-94.8888	29.3321
67	-94.8908	29.3439
68	-94.8898	29.3547
69	-94.8839	29.3645
70	-94.8751	29.3714
71	-94.8829	29.3862
72	-94.8819	29.3960
73	-94.8829	29.4088
74	-94.8869	29.4304

Station No.	Lon	Lat
75	-94.9026	29.4402
76	-94.9164	29.4422
77	-94.9321	29.4284
78	-94.9331	29.4461
79	-94.9301	29.4619
80	-94.9213	29.4766
81	-94.9095	29.4874
82	-94.9154	29.5022
83	-94.9380	29.5051
84	-94.9626	29.5120
85	-94.9901	29.5218
86	-95.0078	29.5327
87	-95.0166	29.5503
88	-95.0117	29.5631
89	-95.0009	29.5759
90	-94.9871	29.5916
91	-94.9783	29.5975
92	-94.9852	29.6103
93	-94.9989	29.6221
94	-95.0088	29.6359
95	-95.0058	29.6546
96	-94.9970	29.6614
97	-94.9862	29.6732
98	-94.9763	29.6841
99	-94.9832	29.6998
100	-94.9803	29.7214
101	-94.9695	29.7195
102	-94.9577	29.7116
103	-94.9409	29.7086
104	-94.9331	29.6978
105	-94.9291	29.6821
106	-94.9183	29.6673
107	-94.8967	29.6654
108	-94.8810	29.6703
109	-94.8613	29.6870
110	-94.8534	29.7096
111	-94.8446	29.7293
112	-94.8279	29.7450

Station No.	Lon	Lat
113	-94.8259	29.7617
114	-94.8230	29.7784
115	-94.8112	29.7814
116	-94.7994	29.7794
117	-94.7846	29.7814
118	-94.7718	29.7883
119	-94.7551	29.7952
120	-94.7394	29.8001
121	-94.7276	29.7971
122	-94.7217	29.7893
123	-94.7237	29.7775
124	-94.7079	29.7775
125	-94.6932	29.7853
126	-94.6961	29.7666
127	-94.6942	29.7558
128	-94.7001	29.7421
129	-94.6971	29.7234
130	-94.6991	29.7086
131	-94.6991	29.6890
132	-94.7040	29.6723
133	-94.7060	29.6546
134	-94.7069	29.6359
135	-94.7158	29.6241
136	-94.7197	29.6133
137	-94.7305	29.5966
138	-94.7394	29.5887
139	-94.7414	29.5769
140	-94.7591	29.5612
141	-94.7738	29.5562
142	-94.7826	29.5317
143	-94.7699	29.5228
144	-94.7541	29.5199
145	-94.7374	29.5209
146	-94.7227	29.5248
147	-94.7040	29.5317
148	-94.6824	29.5366
149	-94.6637	29.5376
150	-94.6421	29.5425

Station No.	Lon	Lat
151	-94.6165	29.5494
152	-94.5968	29.5553
153	-94.5742	29.5612
154	-94.5614	29.5749
155	-94.5467	29.5671
156	-94.5359	29.5562
157	-94.5270	29.5435
158	-94.5162	29.5405
159	-94.5034	29.5405

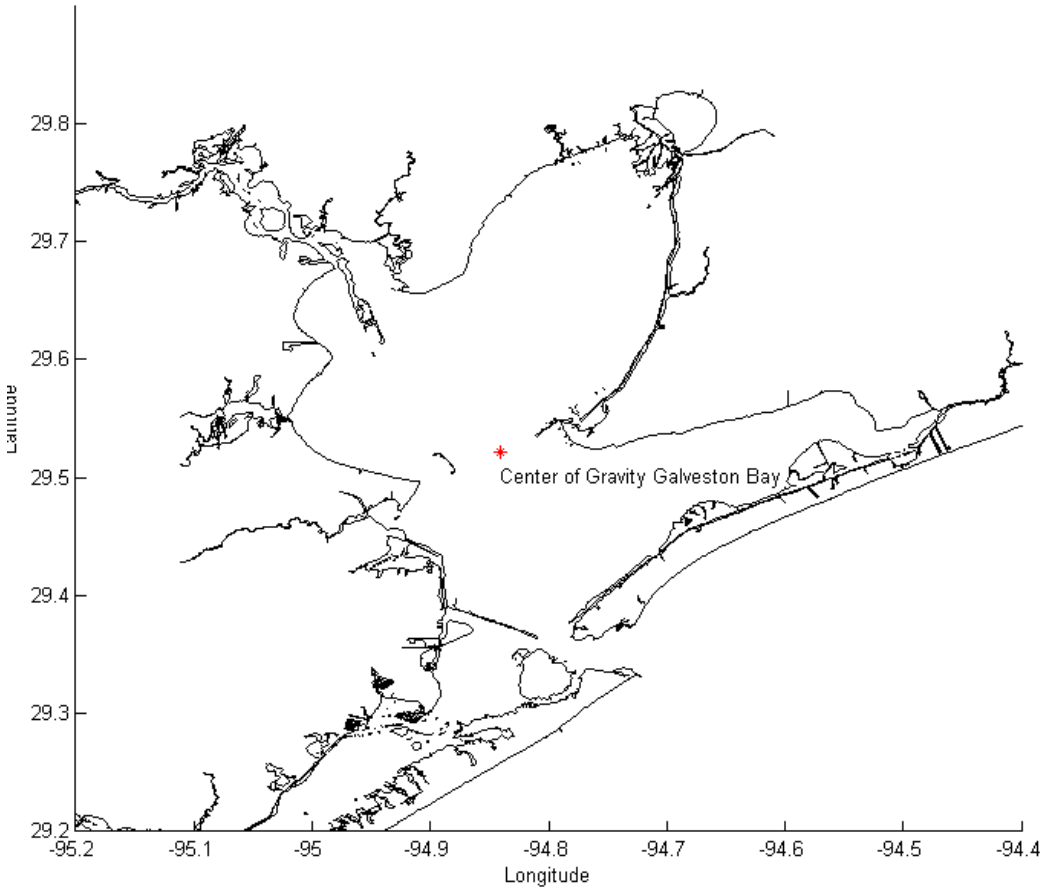

A- 13 Center of Gravity, Galveston Bay

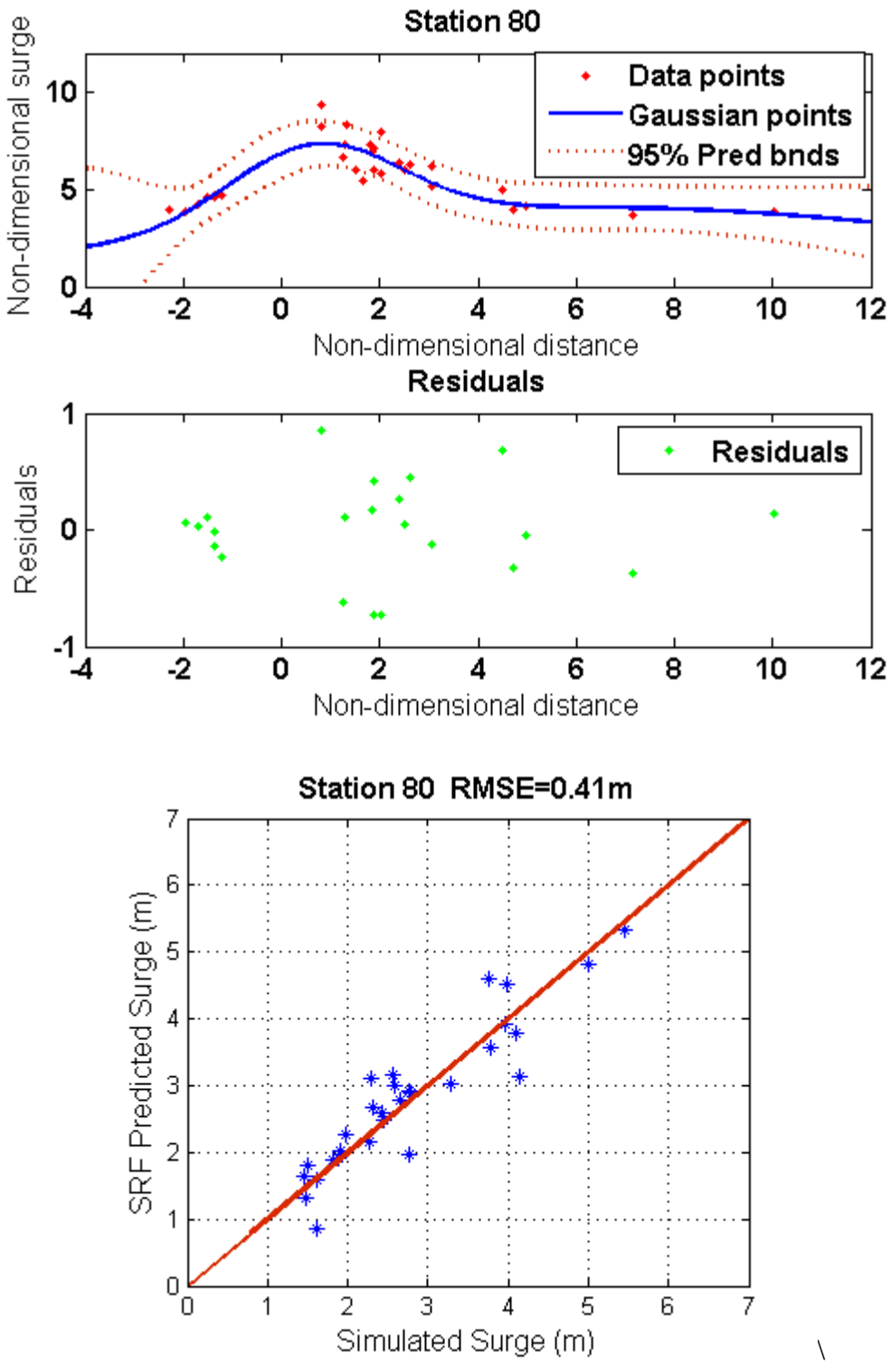

A- 14 SRF at station 80 inside Galveston Bay

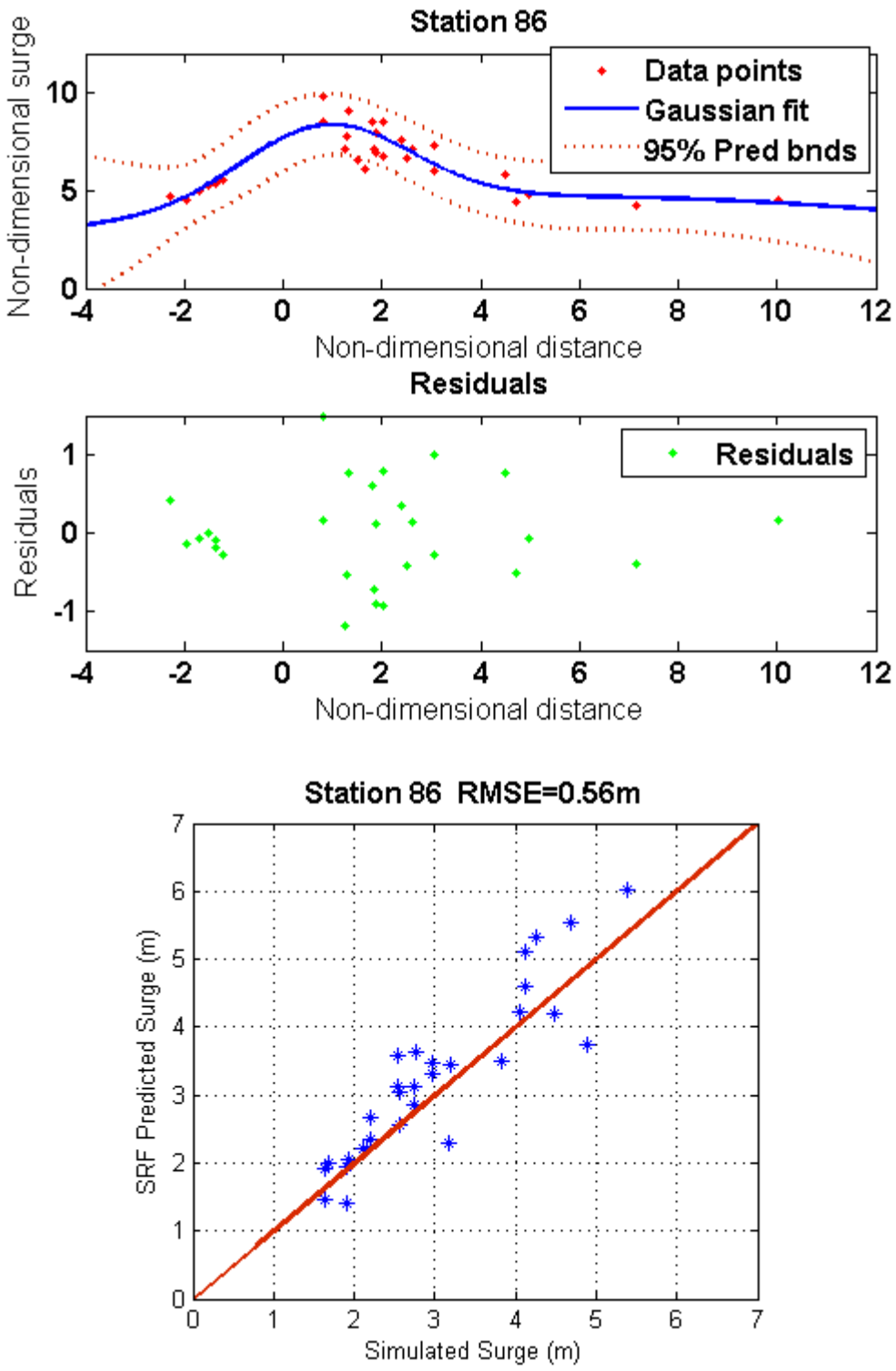

A- 15 SRF at station 86 inside Galveston Bay

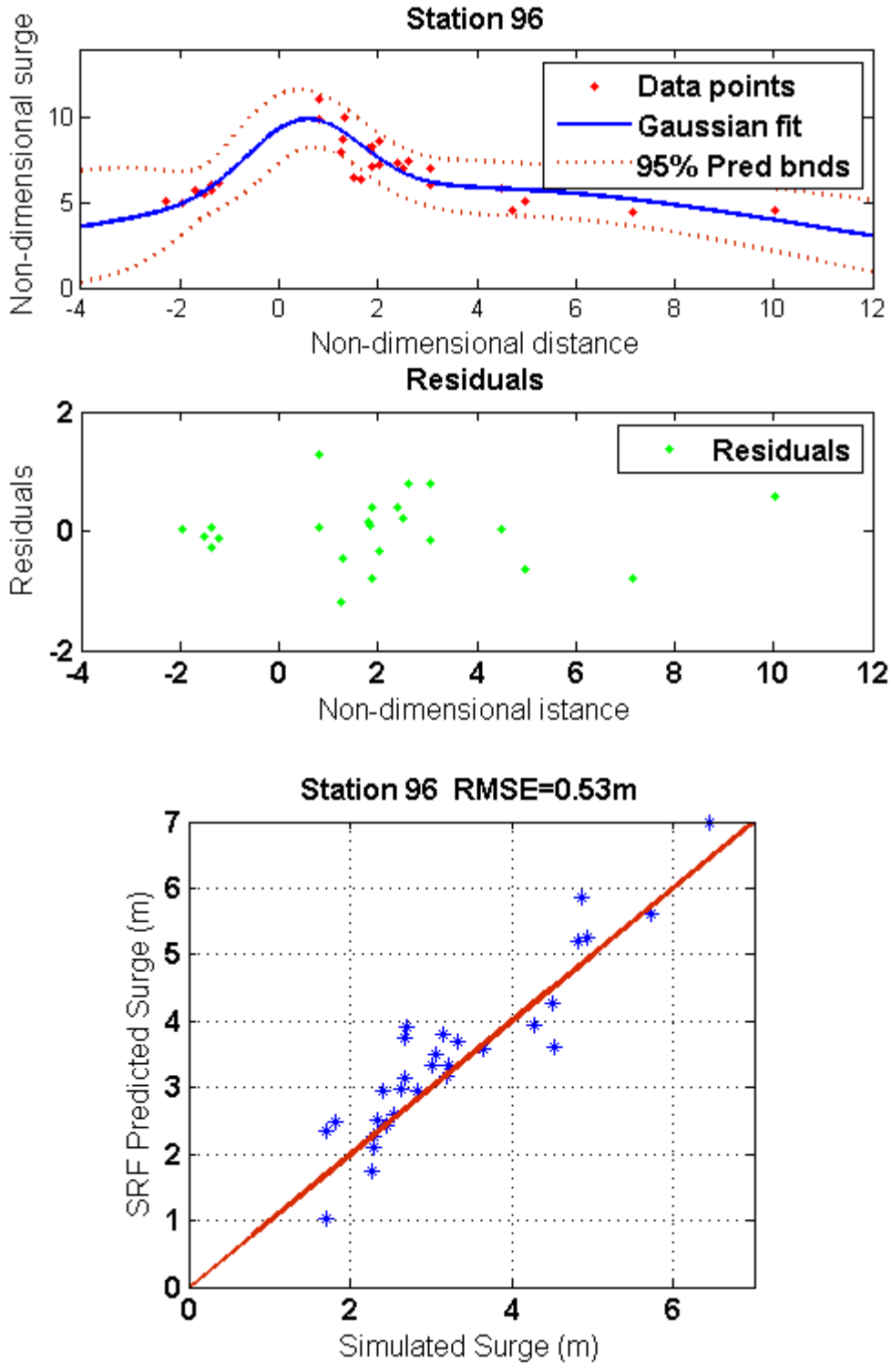

A- 16 SRF at station 96 inside Galveston Bay

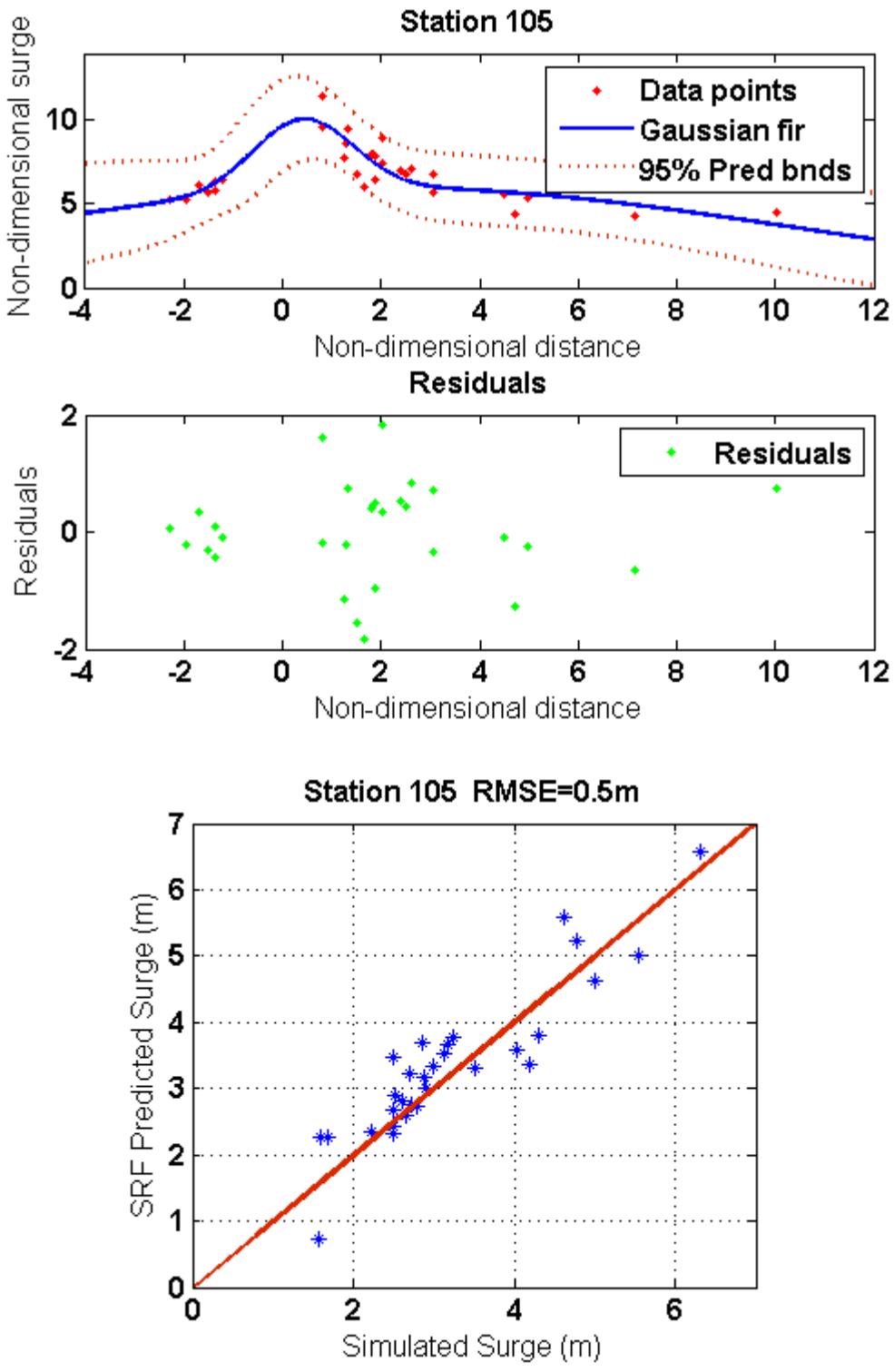

A- 17 SRF at station 105 inside Galveston Bay

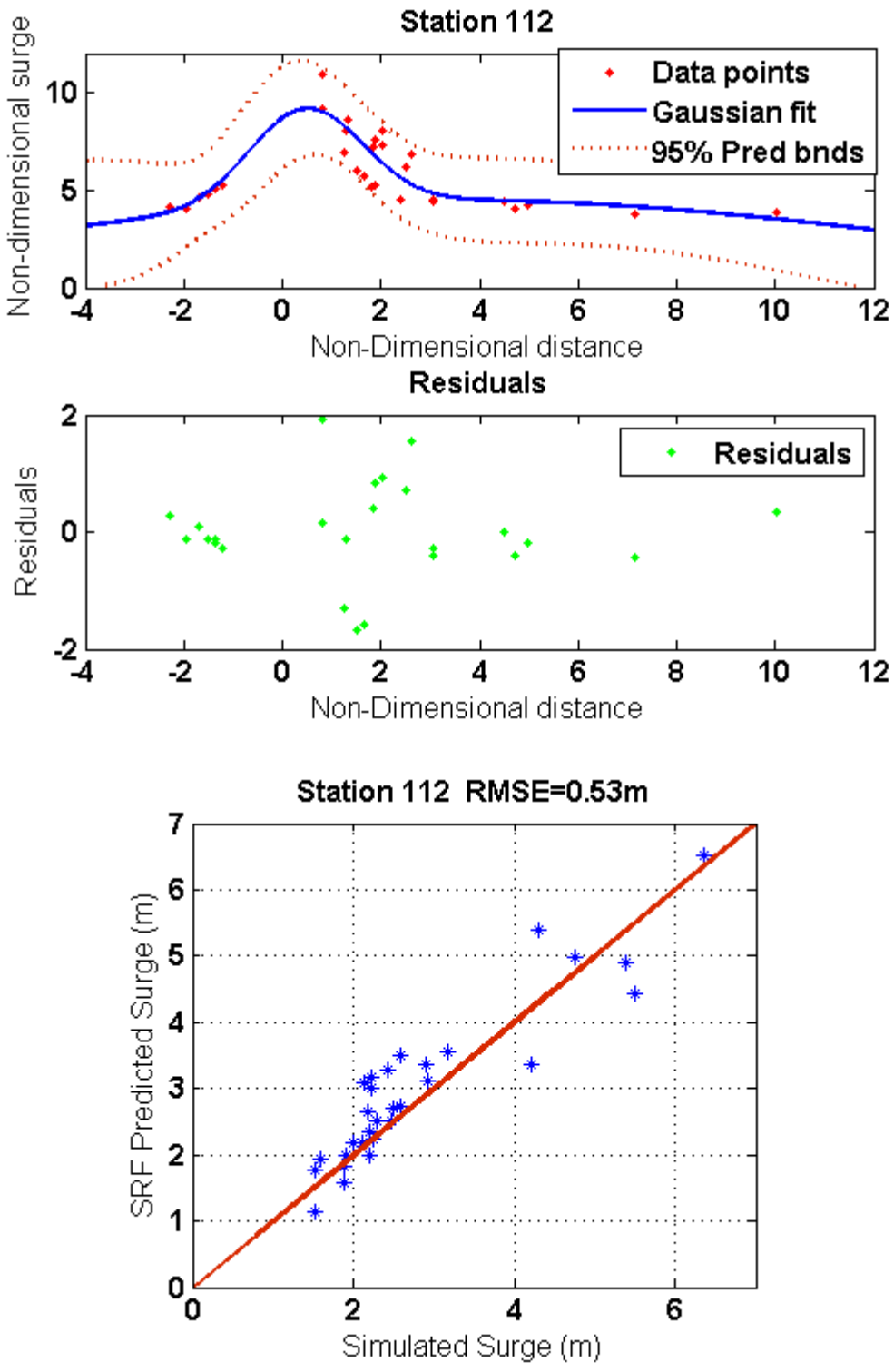

A- 18 SRF at station 112 inside Galveston Bay

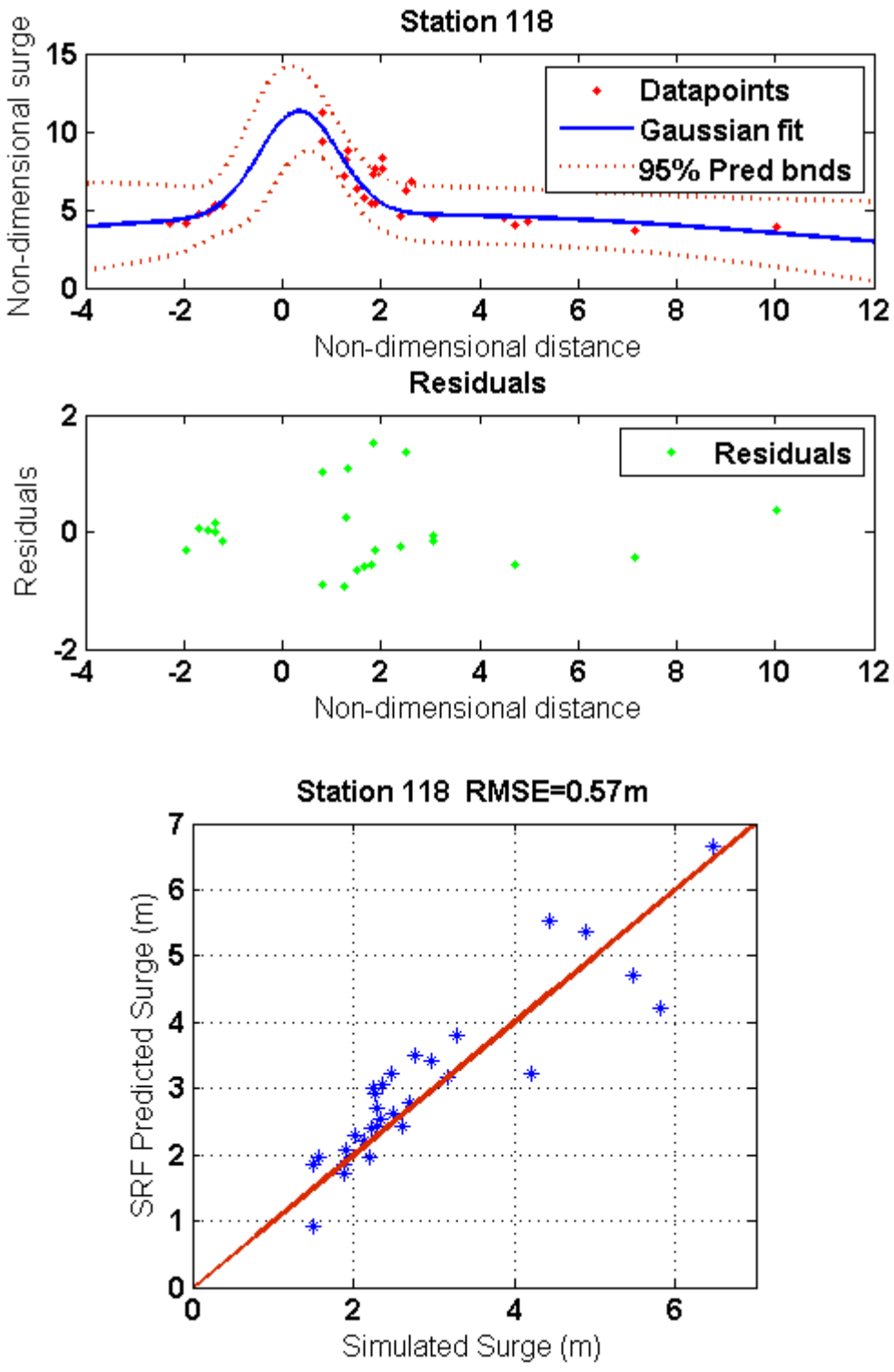

A- 19 SRF at station 118 inside Galveston Bay

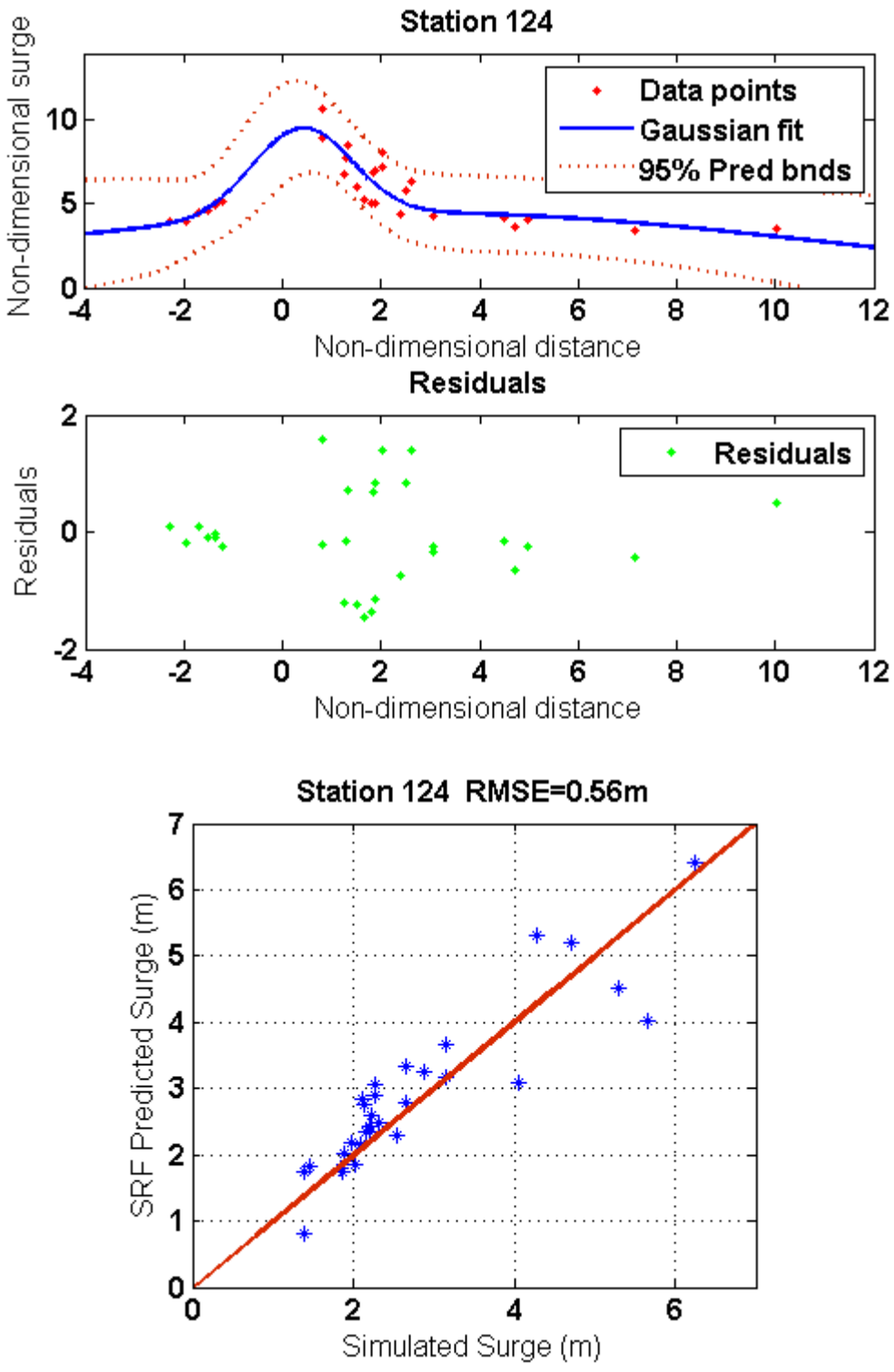

A- 20 SRF at station 124 inside Galveston Bay

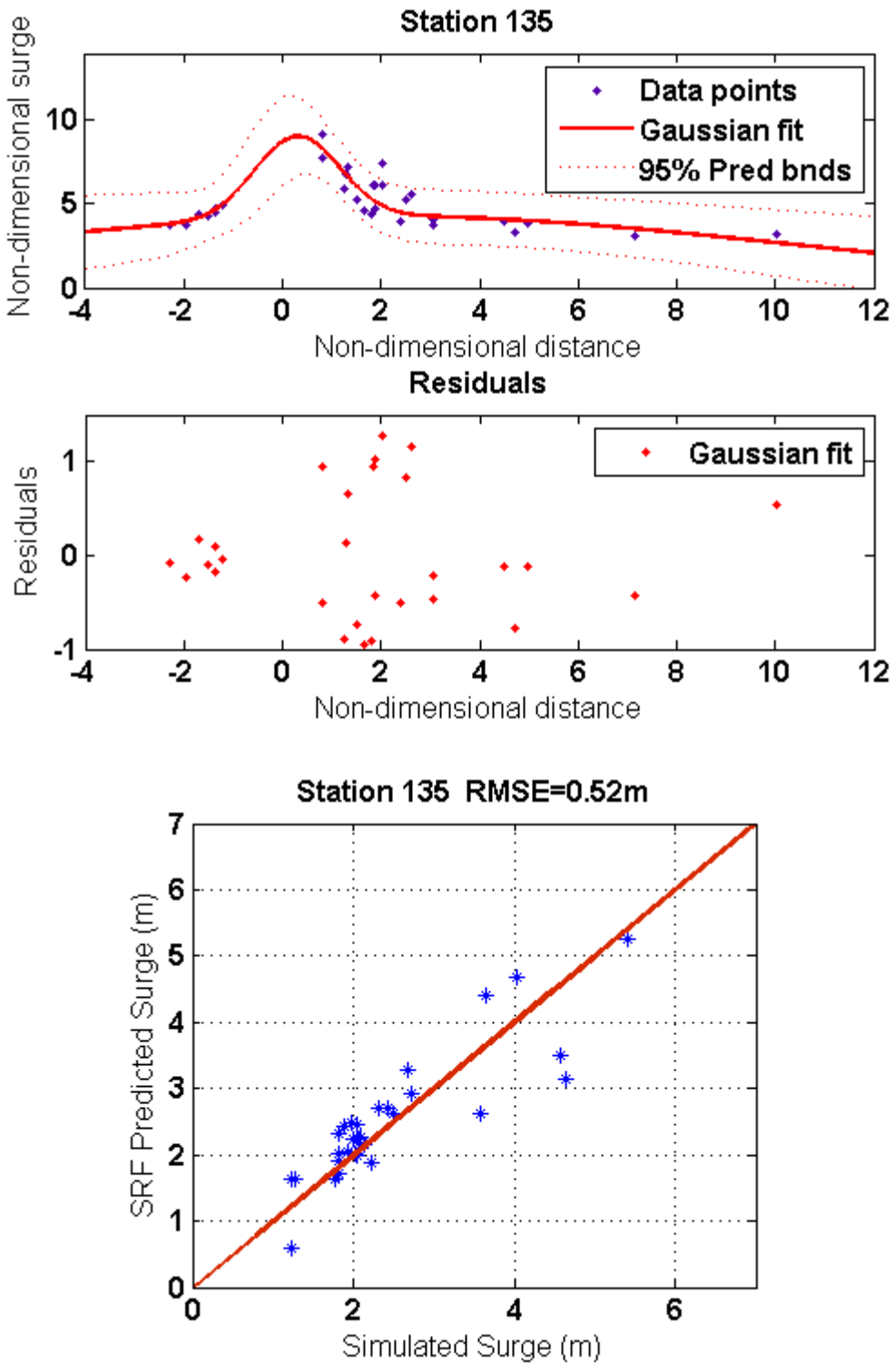

A- 21 SRF at station 135 inside Galveston Bay

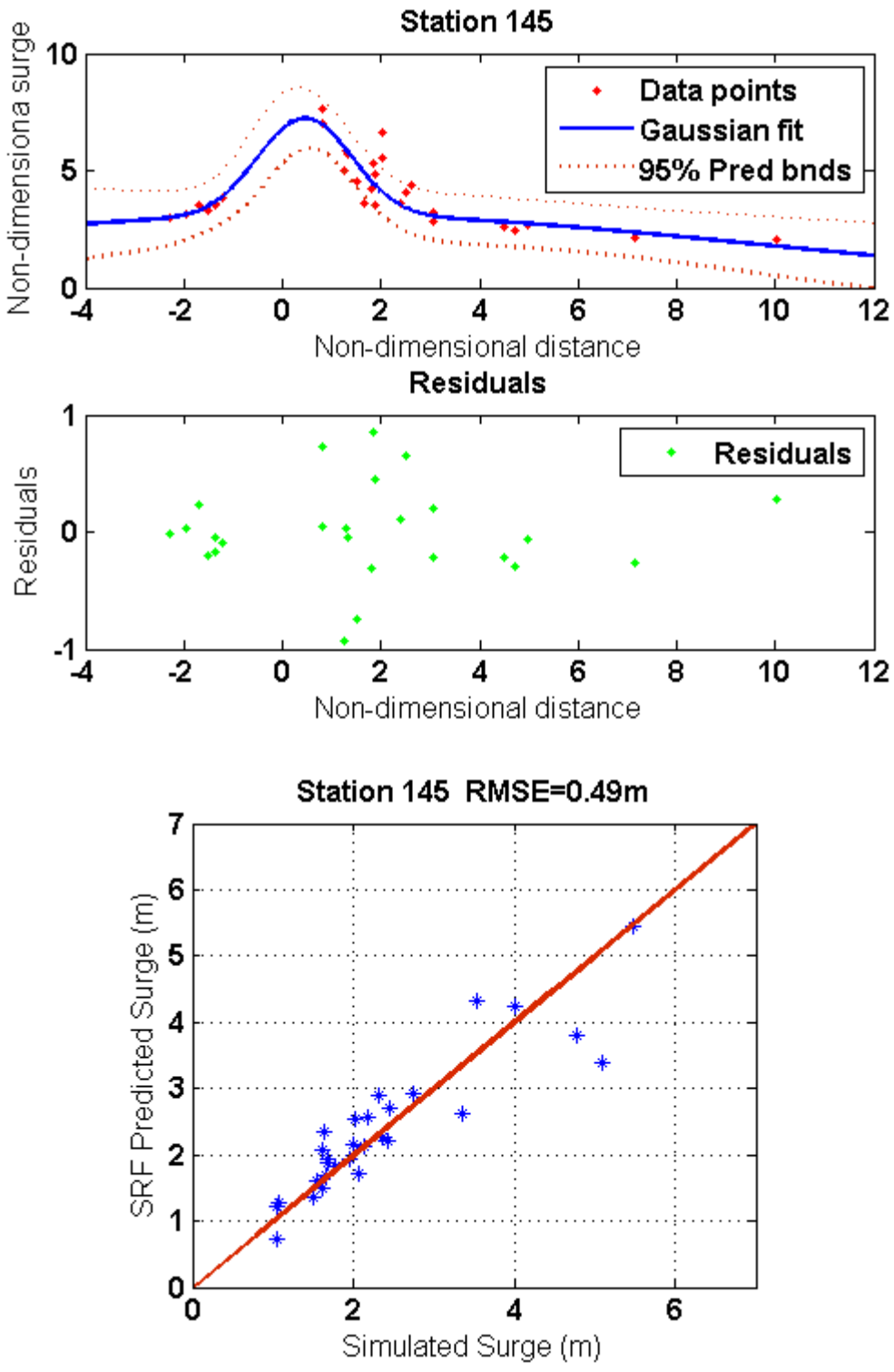

A- 22 SRF at station 145 inside Galveston Bay

Table 6 Stations Location inside Corpus Christi Bay

Station No.	Lon	Lat
1	-97.2052	27.6093
2	-97.2002	27.6202
3	-97.1943	27.6336
4	-97.1851	27.6453
5	-97.1751	27.6612
6	-97.1667	27.6771
7	-97.1609	27.6913
8	-97.1500	27.7072
9	-97.1391	27.7147
10	-97.1358	27.7264
11	-97.1291	27.7373
12	-97.1216	27.7432
13	-97.1115	27.7557
14	-97.1040	27.7674
15	-97.0965	27.7808
16	-97.0856	27.7892
17	-97.0773	27.8025
18	-97.0714	27.8134
19	-97.0580	27.8243
20	-97.0505	27.8301
21	-97.0430	27.8494
22	-97.0388	27.8636
23	-97.0313	27.8703
24	-97.0262	27.8812
25	-97.0154	27.8912
26	-97.2169	27.6369
27	-97.2069	27.6470
28	-97.2052	27.6645
29	-97.2002	27.6821
30	-97.1960	27.6972
31	-97.1843	27.7105
32	-97.1701	27.7281
33	-97.1559	27.7356
34	-97.1433	27.7499
35	-97.1366	27.7616
36	-97.1283	27.7724

Station No.	Lon	Lat
37	-97.1141	27.7892
38	-97.1065	27.8025
39	-97.0990	27.8092
40	-97.1090	27.8218
41	-97.1074	27.8469
42	-97.0940	27.8536
43	-97.0547	27.8619
44	-97.0463	27.8770
45	-97.2922	27.6169
46	-97.2813	27.6369
47	-97.2730	27.6587
48	-97.2679	27.6771
49	-97.2596	27.6888
50	-97.2629	27.7039
51	-97.2847	27.7097
52	-97.2989	27.7114
53	-97.3048	27.6988
54	-97.3064	27.6855
55	-97.3240	27.7005
56	-97.3357	27.7256
57	-97.3524	27.7390
58	-97.3758	27.7532
59	-97.3834	27.7674
60	-97.3942	27.7883
61	-97.3959	27.8051
62	-97.3901	27.8209
63	-97.3834	27.8327
64	-97.4009	27.8393
65	-97.4193	27.8335
66	-97.4277	27.8310
67	-97.4469	27.8318
68	-97.4687	27.8318
69	-97.4837	27.8377
70	-97.5005	27.8486
71	-97.5164	27.8578
72	-97.5205	27.8720
73	-97.5105	27.8862
74	-97.4988	27.8828

Station No.	Lon	Lat
75	-97.4896	27.8762
76	-97.4804	27.8644
77	-97.4670	27.8661
78	-97.4612	27.8787
79	-97.4503	27.8745
80	-97.4269	27.8720
81	-97.4110	27.8720
82	-97.3917	27.8720
83	-97.3733	27.8720
84	-97.3625	27.8803
85	-97.3491	27.8803
86	-97.3407	27.8795
87	-97.3441	27.8611
88	-97.3248	27.8678
89	-97.3098	27.8720
90	-97.2905	27.8745
91	-97.2771	27.8795
92	-97.2604	27.8720
93	-97.2437	27.8586
94	-97.2378	27.8519
95	-97.2303	27.8435
96	-97.2270	27.8310
97	-97.2204	27.8228
98	-97.2129	27.8216
99	-97.1938	27.8265
100	-97.1835	27.8429
101	-97.1776	27.8565
102	-97.1607	27.8709
103	-97.1463	27.8819
104	-97.1361	27.8946
105	-97.1277	27.9107
106	-97.1166	27.9293
107	-97.1090	27.9403
108	-97.0997	27.9547
109	-97.0887	27.9674

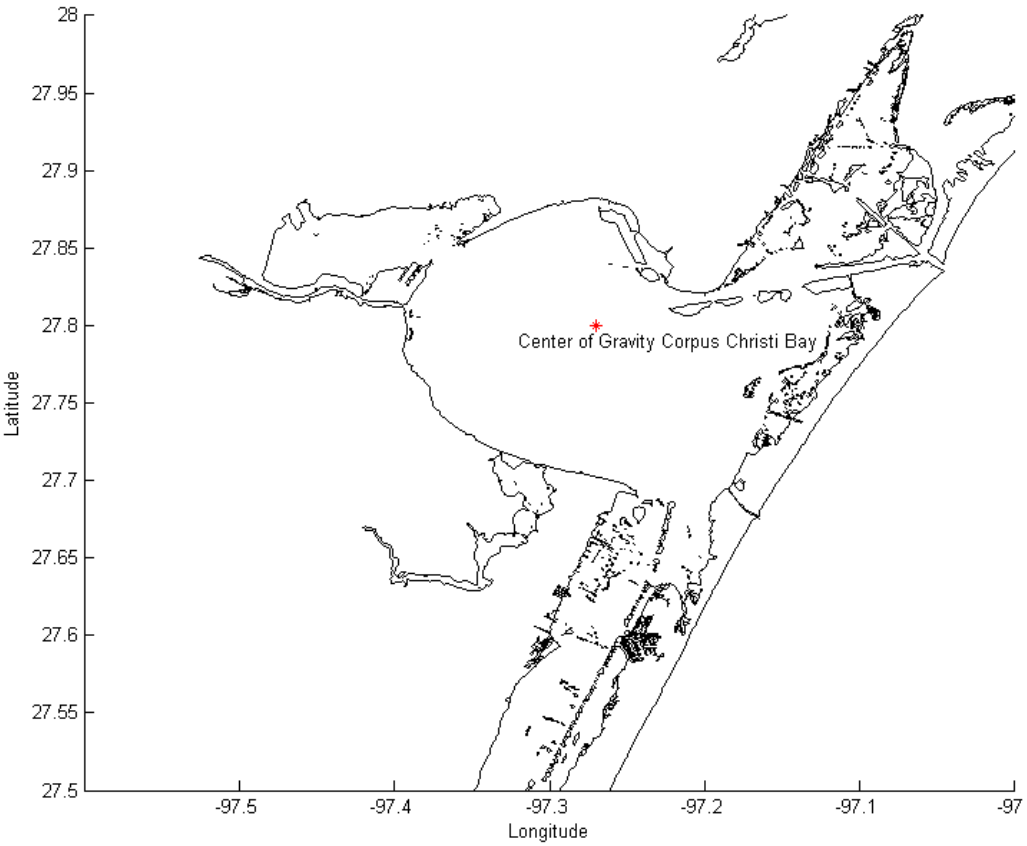

A- 23 Center of Gravity, Corpus Christi Bay

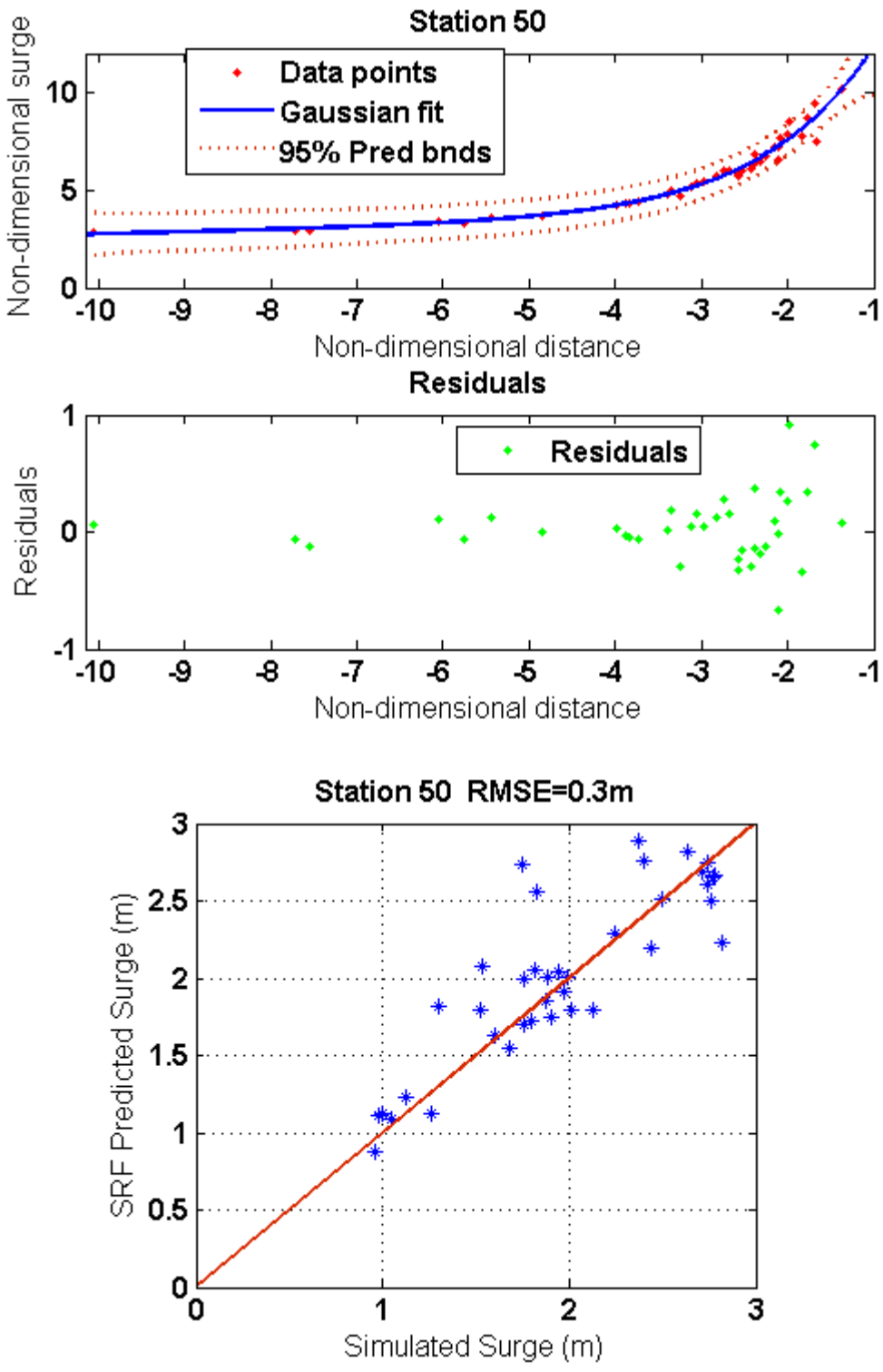

A- 24 SRF at station 50 inside Corpus Christi Bay

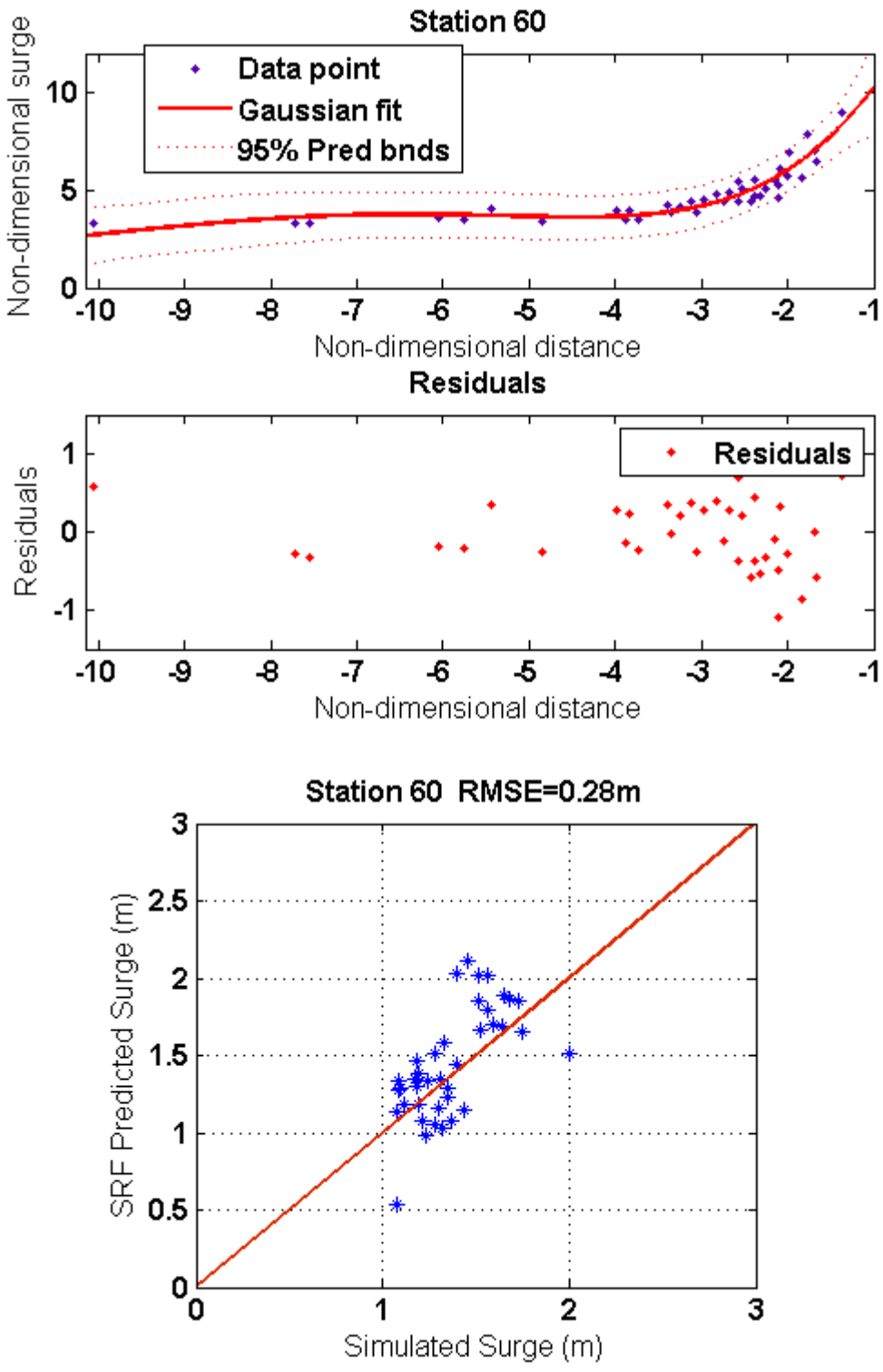

A- 25 SRF at station 60 inside Corpus Christi Bay

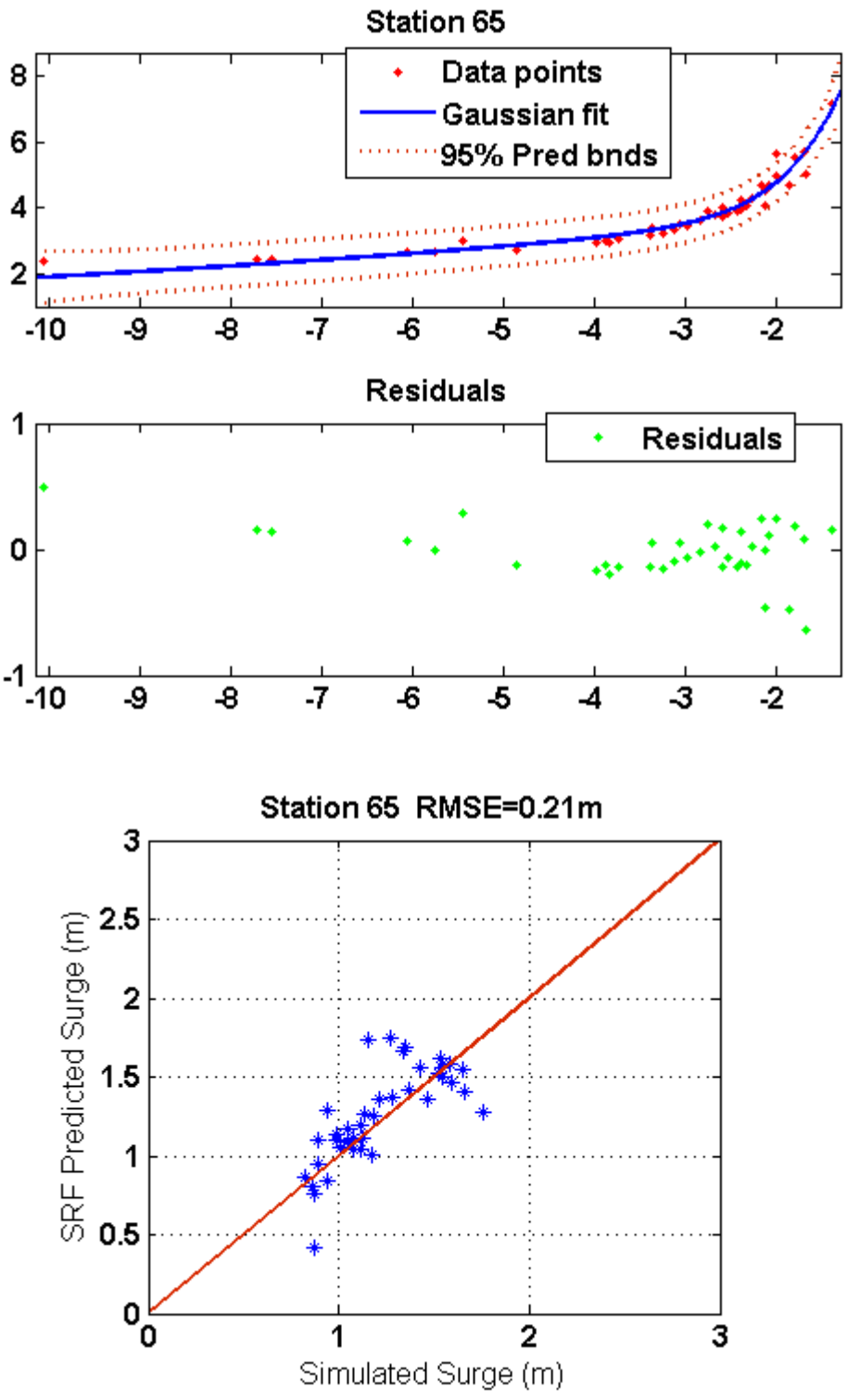

A- 26 SRF at station 65 inside Corpus Christi Bay

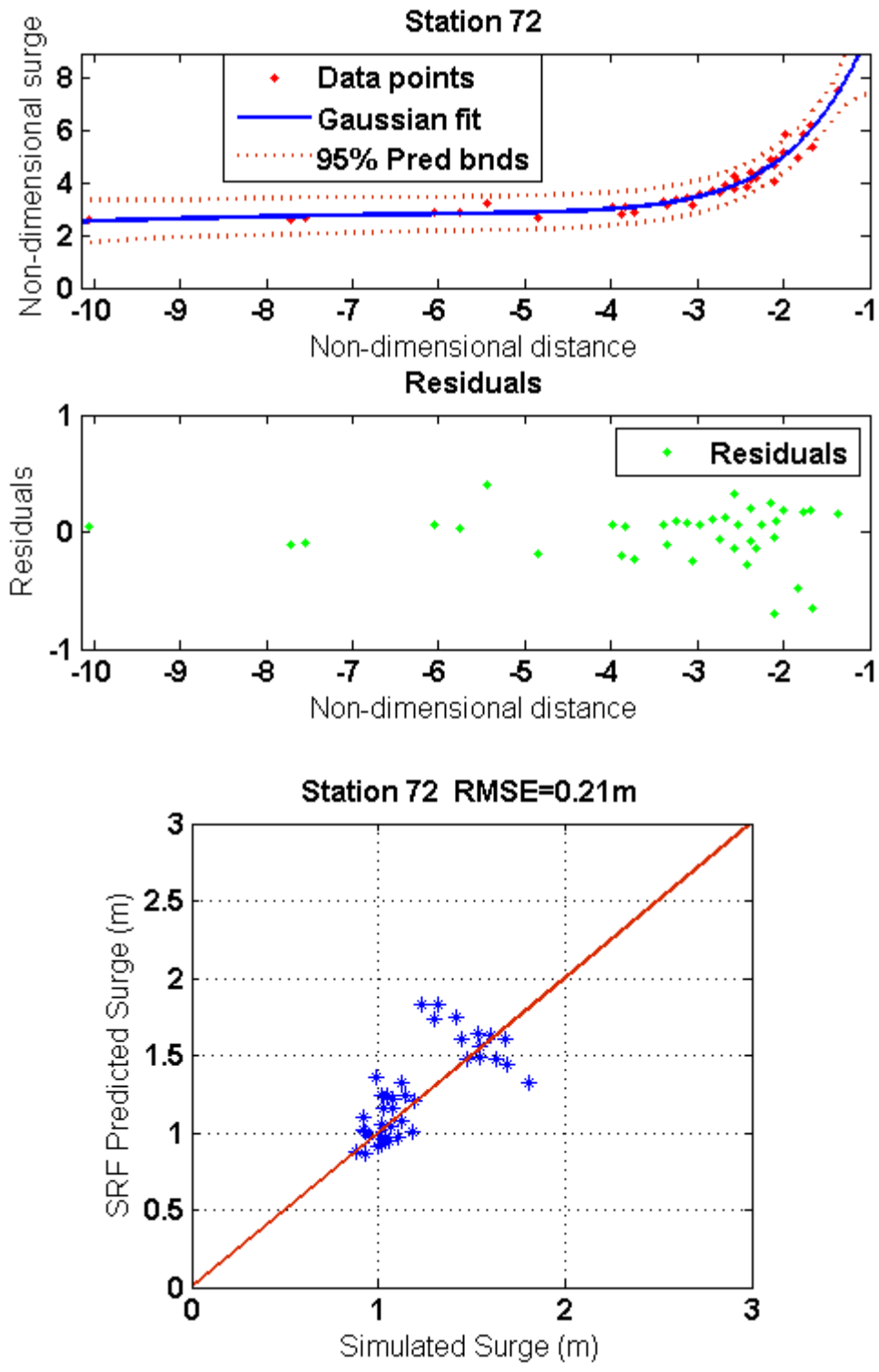

A- 27 SRF at station 72 inside Corpus Christi Bay

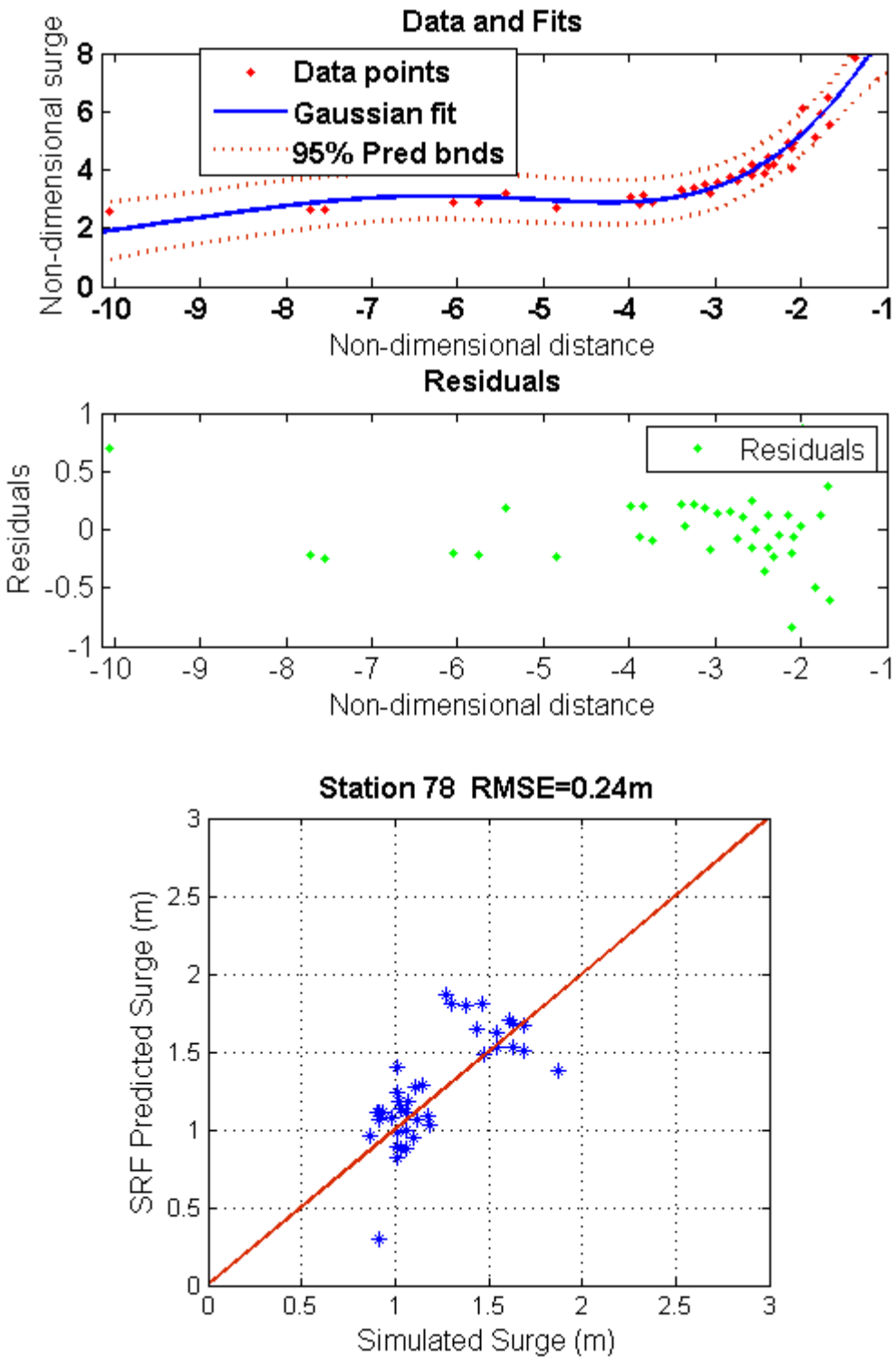

A- 28 SRF at station 78 inside Corpus Christi Bay

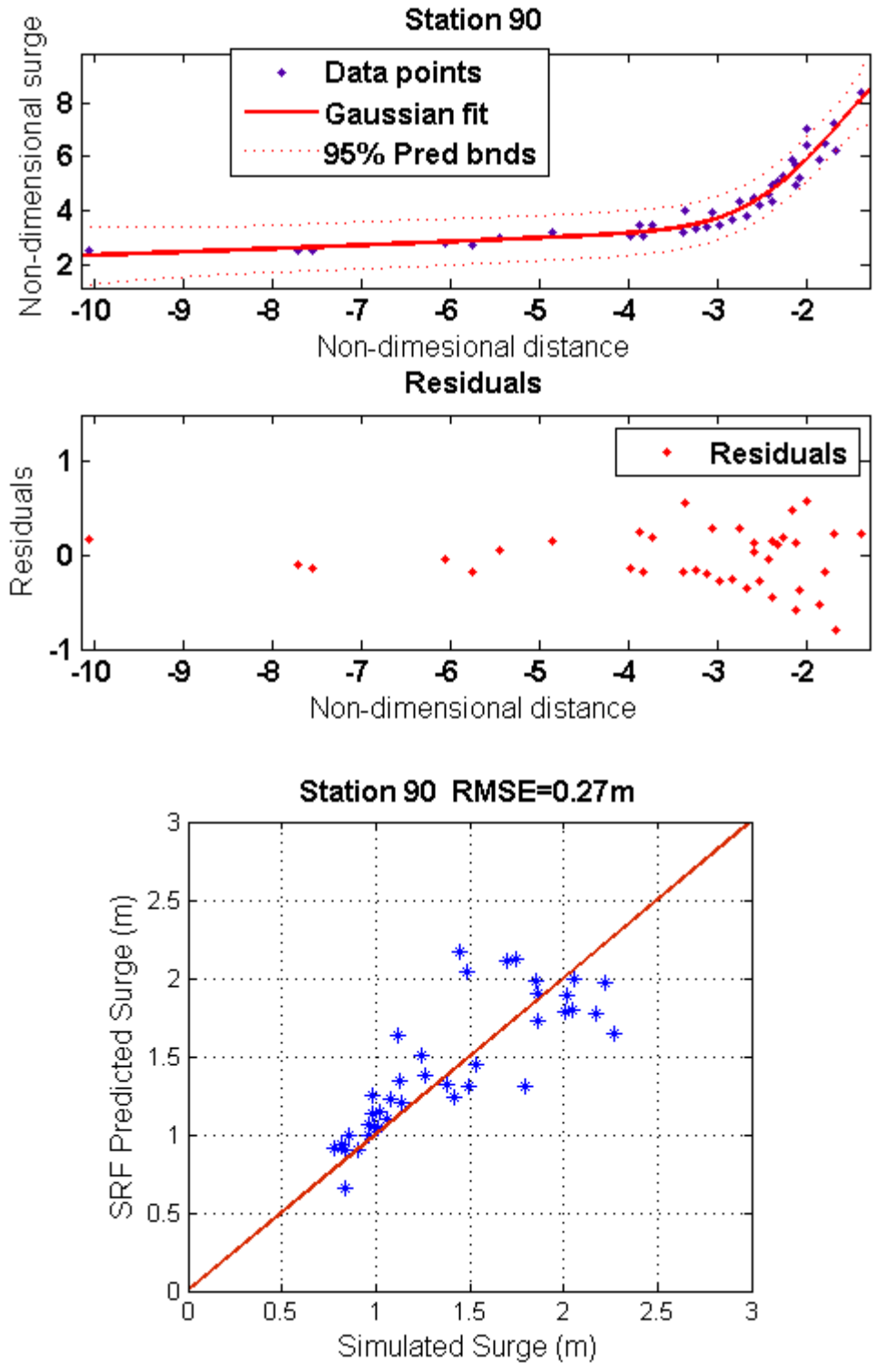

A- 29 SRF at station 90 inside Corpus Christi Bay

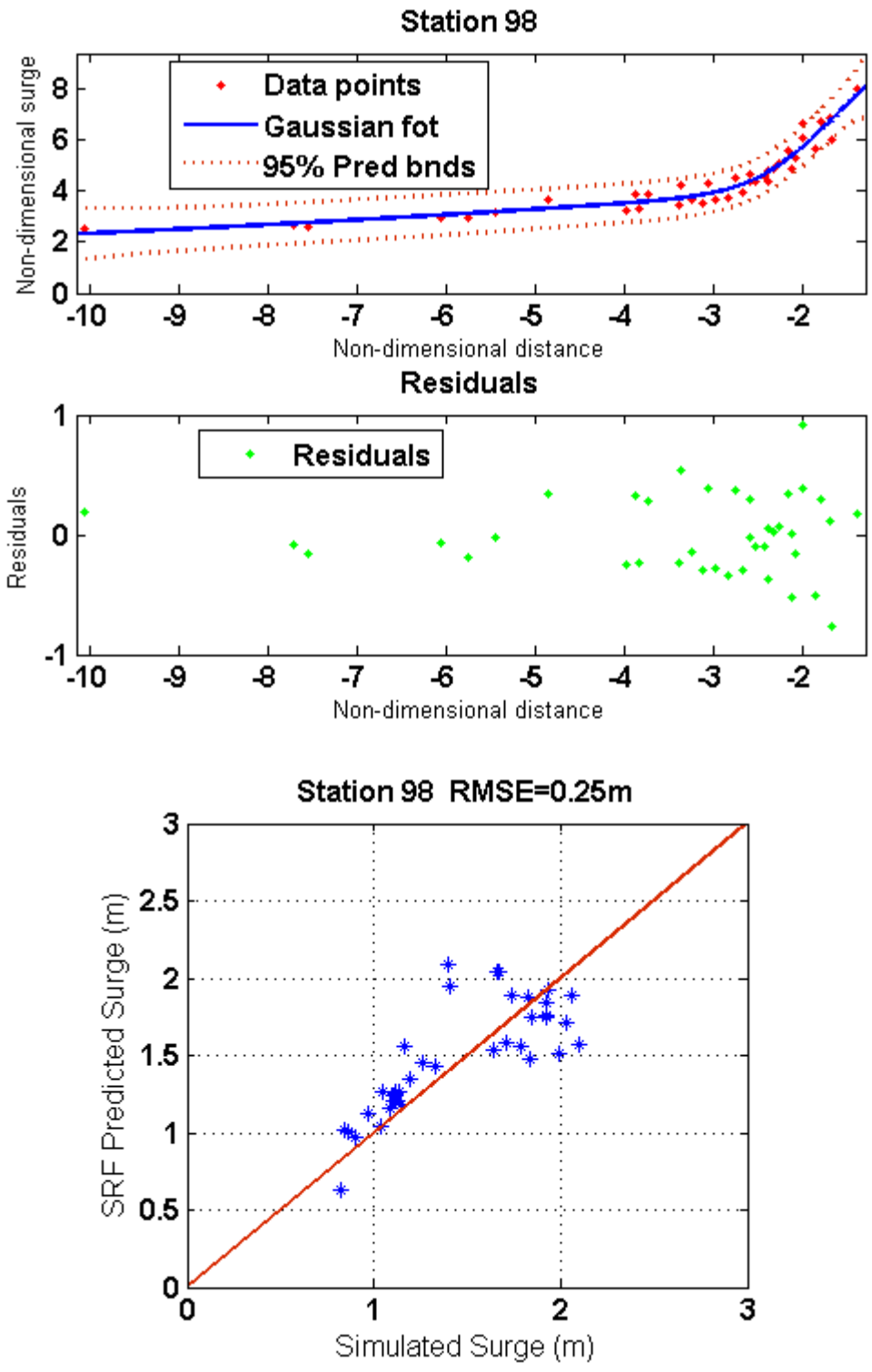

A- 30 SRF at station 98 inside Corpus Christi Bay

Estuarine, Coastal and Shelf Science 84 (2009) 625–636

Contents lists available at ScienceDirect

Estuarine, Coastal and Shelf Science

journal homepage: www.elsevier.com/locate/ecss

Sensitivity of hurricane surge to morphological parameters of coastal wetlands

N.M. Loder [a], J.L. Irish [a,*], M.A. Cialone [b], T.V. Wamsley [b]

[a] Zachry Department of Civil Engineering, Texas A&M University, 3135 TAMU, College Station, TX 77843, USA
[b] Coastal & Hydraulics Laboratory, US Army Research and Development Center, 3909 Halls Ferry Road, Vicksburg, MS 39180, USA

ARTICLE INFO

Article history:
Received 14 January 2009
Accepted 31 July 2009
Available online 12 August 2009

Keywords:
flooding
hurricanes
marsh
storm surge
surge response
wetlands
USA
Gulf of Mexico

ABSTRACT

Given the history and future risk of storm surge in the United States, functional storm protection techniques are needed to protect vital sectors of the economy and coastal communities. It is widely hypothesized that coastal wetlands offer protection from storm surge and wave action, though the extent of this protection is unknown due to the complexities of flow through vegetation. Here we present the sensitivity of storm-surge numerical modeling results to various coastal wetlands characteristics. An idealized grid domain and 400-km^2 marsh feature were used to evaluate the effects of marsh characteristics on hurricane surge, including the effects of bottom friction, elevation, and continuity (the ratio of healthy marsh to open water area within the total wetland area).

Through coupled hydrodynamic and wave model simulations, it is confirmed that increased bottom friction reduces storm-surge levels for most storms. However, increases in depth associated with marsh elevation loss generally results in a reduction of surge. As marsh continuity is decreased, coastal surge increases as a result of enhanced surge conveyance into and out of the marsh. Storm surge is parameterized in terms of marsh morphology, namely marsh elevation, frictional characteristics, and degree of segmentation, which will assist in the justification for and optimization of marsh restoration in terms of storm protection.

1. Introduction

Coastal wetlands have the potential to reduce surge levels through several mechanisms, including vegetative drag within the water column, reduction in wave setup, and the sheltering of surface wind. However, while there exists a moderate body of literature regarding the reduction of hurricane wave heights due to vegetation, there are a comparatively limited number of publications regarding the potential for coastal wetlands to reduce storm surge (e.g., USACE, 1961; Fritz et al., 2008; Resio and Westerink, 2008; Wamsley et al., 2009, in press). Flow resistance afforded by vegetation is a three-dimensional, complex problem governed by processes both within and outside the bottom boundary layer (Reid and Whitaker, 1976; Kouwen et al., 1981; Kadlec, 1990; Nepf, 1999; Peterson et al., 2004; Green, 2005; Tanino and Nepf, 2008). Green (2005) categorizes vegetative resistance into 1) momentum transfer at the bottom of the water column due to bottom friction, and 2) drag throughout the water column. Thus, vegetation effects introduce two terms into the water flow momentum balance:

$$\text{Momentum transfer by vegetation} = \tau_{\text{bed}} + F_{\text{Drag}} \quad (1)$$

where τ_{bed} is resistance due to the bottom boundary layer and F_{Drag} is resistance due to vegetative drag. Drag is particularly important in the case of dense vegetation, as velocities within a stand of vegetation are greatly reduced, and flow tends to be diverted around areas of dense growth. Important factors relating to vegetative drag include stem height, diameter, flexibility, and impeded flow area (Nepf, 2004). Determining plant drag coefficients and densities over a large-scale area, such as that affected by a hurricane, would be difficult. For practical analysis, two-dimensional, depth-integrated hydrodynamic models for storm-surge simulation approximate impacts of vegetation on flow through a bottom shear stress term, τ_b such that:

$$\tau_b \approx \tau_{\text{bed}} + F_{\text{Drag}} \quad (2)$$

Since the vertical velocity profile is highly variable in vegetated flows, the above approximation is ill suited for the study of exact flow structure. However, Eq. (2) can give a first-order approximation of water-level response. To evaluate coastal wetlands in terms of storm protection, two-dimensional, depth-integrated numerical modeling is used in this study to estimate the storm-surge reduction potential associated with characteristic qualities of coastal

* Corresponding author.
E-mail address: jirish@civil.tamu.edu (J.L. Irish).

0272-7714/$ – see front matter © 2009 Elsevier Ltd. All rights reserved.
doi:10.1016/j.ecss.2009.07.036

Nomenclature

b_y	y-intercept (Irish et al., 2008)
c	Marsh continuity (%)
C_f	Nonlinear bottom-friction coefficient
C_p	Hurricane minimum central pressure
d	Still water depth
F_{Drag}	Drag force
f	Coriolis parameter
g	Magnitude of gravitational acceleration
h	Total water depth ($d+\zeta$)
$\hat{k}$	Vertical unit vector
m_s	Slope (Irish et al., 2008)
M	Dimensionless surge function
MSL	Mean sea level
n	Manning's roughness coefficient
p	Barometric pressure
R_p	Radius of pressure (km)
t	Time
$\vec{U}$	Depth-averaged horizontal velocity vector
U	Depth-averaged horizontal velocity magnitude in x
V	Depth-averaged horizontal velocity magnitude in y
Δp	Difference between hurricane minimum central pressure and ambient atmospheric pressure (mb)
ρ	Fluid density
τ_{bed}	Resistance due to the bottom boundary layer
τ_b	Bottom shear stress
τ_s	Free-surface shear stress
τ_w	Wave radiation shear stress
ζ	Surge
ζ_{base}	Average surge within BASE case marsh square
$\zeta_{peak-base}$	Peak along-coast surge for the BASE case, taken at the coastline

marsh. Three parameters are varied within an idealized marsh to observe their relative impact on hurricane storm surge: bottom friction, marsh elevation, and marsh continuity (i.e. a fully continuous marsh versus a marsh delineated by 2-m deep channels). Bottom friction directly impacts the amount of momentum transfer in the flow due to bottom shear stress (first term in Eq. (2)) while marsh elevation impacts the amount of momentum transfer in the flow due to both vegetative drag and bottom shear stress. Marsh

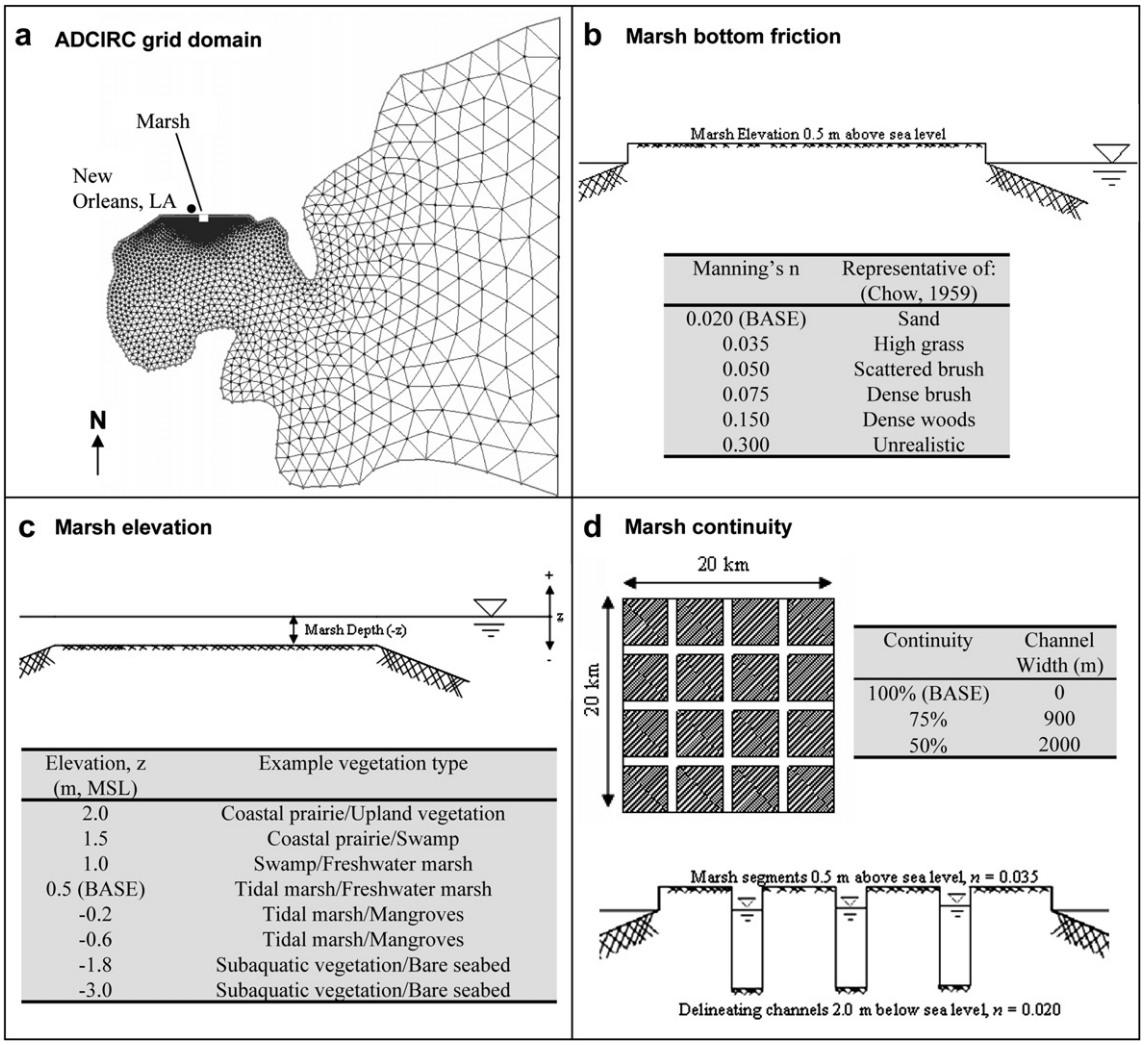

Fig. 1. ADCIRC grid domain (a) and idealized marsh parameters investigated in this study, including bottom friction (b), elevation (c), and continuity (d). Vegetation types given on pane (c) are for example only; exact vegetation type by elevation is highly site specific.

Table 1
Suite of storms used in idealized simulations. Surge potential is mean surge over marsh feature while peak surge is peak along-coast surge.

Storm	Landfall minimum central pressure (mb)	Landfall pressure radius (km)	Forward speed (m/s)	Surge potential for BASE grid (ζ_{base})	Peak surge over BASE grid ($\zeta_{peak\text{-}base}$, m)
Storm 1	900	20.4	5.6	4.4	6.5
Storm 2	900	38.9	5.6	5.2	7.1
Storm 3	900	74.1	5.6	6.0	7.5
Storm 4	941	38.9	5.6	3.5	4.8
Storm 5	975	20.4	5.6	1.8	2.8
Storm 6	975	38.9	5.6	2.2	3.1

continuity, which considers discontinuous bottom friction and marsh elevation throughout the marsh system also impacts the amount of momentum transfer in the flow due to both vegetative drag and bottom shear stress. It is recognized that vegetated flow is substantially approximated in this study through the use of a bottom stress term; nevertheless, findings will be useful in estimating the impacts of marsh degradation and restoration in terms of storm-surge protection.

2. Methods

2.1. Numerical models

To simulate hurricane surge, the finite-element Advanced Circulation (ADCIRC) hydrodynamic model was applied (Westerink et al., 2008) in its two-dimensional, depth-integrated form (ADCIRC-2DDI V46.57). Continuity (Eq. (3)) and momentum equations (Eq. (4)) were

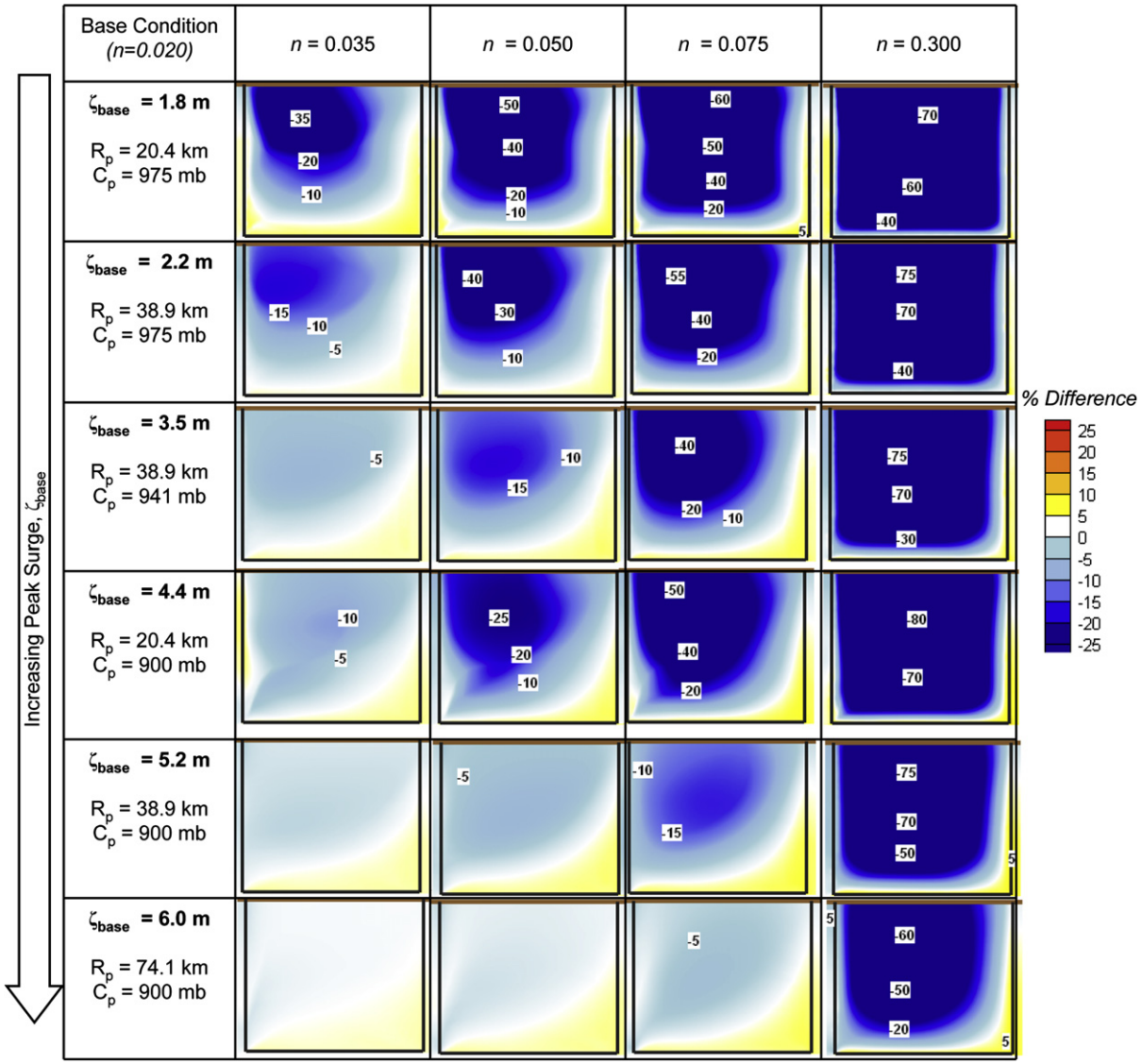

Fig. 2. Results depicting sensitivity of surge levels to bottom friction. Plots depict percent changes in surge relative to the same storm condition on a marsh characterized by a Manning's n of 0.020 (BASE case). Black lines represent marsh boundaries, with the coastline (landward marsh edge, shown in brown) oriented at the top of each plot. Warm colors indicate surge increases, while cool colors indicate surge decreases. Rows represent each storm condition, increasing in storm surge potential from top to bottom. In each case, storms makes landfall at a 90° angle to the coast, with core passage at a location that results in maximum surge at the center of the marsh.

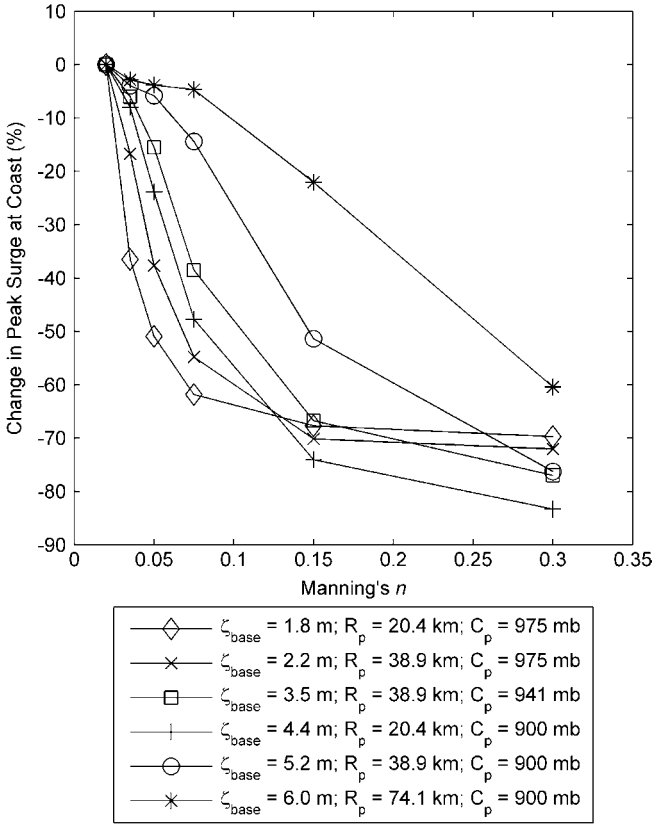

Fig. 3. Percent change in peak surge along the coast due to bottom friction. Percent change shown is referenced to simulated peak surge at the coast for the sandy bottom case, with a Manning's n of 0.020 (BASE case).

solved by the model for each elemental area (Luettich and Westerink, 2004), given by:

$$\frac{\partial h}{\partial t} + \nabla_h(\vec{U}h) = 0 \tag{3}$$

$$\frac{\partial \vec{U}}{\partial t} + (U\cdot\nabla_h)\vec{U} = -g\nabla_h\left(\zeta + \frac{p(x,y)}{g\rho}\right) + f\hat{k}\times\vec{U} + \frac{\vec{\tau_s}}{h\rho} - \frac{\vec{\tau_b}}{h\rho} + \frac{\vec{\tau_w}}{h\rho} \tag{4}$$

where h is water depth [L], t is time [T], $\vec{U}$ is the depth-integrated horizontal velocity [LT^{-1}], g is gravitational acceleration [LT^{-2}], $p(x,y)$ is spatially-variable atmospheric pressure [$ML^{-1}T^{-2}$], ρ is fluid density [ML^{-3}], f is the Coriolis parameter [T^{-1}], $\hat{k}$ is the vertical unit vector [–], τ_s is surface shear stress [MLT^{-2}], and τ_w is wave radiation stress [MLT^{-2}]. Bottom stress is given by:

$$\vec{\tau_b} = \frac{C_f\vec{U}|\vec{U}|}{h} \tag{5}$$

where the nonlinear bottom drag coefficient, C_f, is a function of the Manning's n friction coefficient.

The ADCIRC model was forced by wind, pressure, and wave radiation stress inputs (Loder, 2008; Loder et al., 2009). Wind and pressure fields were obtained from the Planetary Boundary Layer Model developed by Cardone et al. (1992), while wave radiation stress was simulated using the Steady-State Spectral Wave Model, STWAVE (Smith, 2007; Smith et al., 2001), in which offshore wave conditions were specified using output from the global Wave Prediction Model (WAMDI Group, 1988; R.E. Jensen, personal communication). Given the idealized nature of this study, astronomical tidal forcing was not included. ADCIRC output included water surface elevation and velocity at each computational node at 15-min time intervals.

2.2. Coastal wetland parameters

To provide a basis for general application along a number of coastlines, an idealized grid for the northern Gulf of Mexico (Irish et al., 2008) having a uniform continental shelf slope and smooth bathymetry was selected (Fig. 1(a)). Since the goal of this study is to isolate the impacts of various marsh parameters on hurricane surge response, the idealized grid does not include other coastal features, such as beaches and dunes. Several profiles offshore of southeastern Louisiana were analyzed to assist in the selection of a continental shelf slope representative of the northern Gulf of Mexico. Profiles ranged from 1:800 to 1:1600, resulting in the selection of a 1:1000 continental shelf slope for the idealized grid. A 400-km^2 marsh feature was added to the grid, where a 1:250 slope transitioned between the marsh feature and the 1:1000 continental shelf slope. The marsh feature has a minimum grid resolution of 200 m. Outside the limits of the idealized marsh, bottom friction for the sea floor was specified by a Manning's n of 0.020, representative of a sandy surface (Chow, 1959).

This base marsh configuration was used to compare and evaluate surge response due to changes in 1) bottom friction, 2) marsh elevation, and 3) continuity. First, a set of six grids was developed to model surge over a marsh-like feature of increased bottom friction. Marsh elevation was held constant at 0.5 m above mean sea level (MSL) for each idealized grid, representing a typical high-water tidal marsh elevation in the Gulf of Mexico. Bottom friction was implemented by applying various Manning's n, ranging between 0.020 and 0.300 over the 20-km by 20-km marsh area, as shown in Fig. 1(b). The marsh regions represented by the Manning's n values in this study range from sandy bottom (as implemented elsewhere in the grid) to extremely rough (to provide an upper bound in model simulations).

Second, surge response due to changes in marsh elevation was investigated in eight grids of varying marsh elevation. To isolate the effects of elevation, Manning's n across the idealized feature was held constant at 0.020 for these four grids. Elevations were chosen to represent regions of upland vegetation, through swamp, mangroves, and tidal marsh, to bare sea bottom, from 2.0 m above MSL to 3.0 m below MSL, respectively. These elevations can also be considered to represent varying levels of marsh elevation degradation and sea-level rise. Fig. 1(c) provides a cross-section of the idealized marsh and presents the characteristics of the grids used for investigating elevation effects. The reference BASE grid (see Fig. 1(b)) used in the bottom-friction analysis is a part of this suite, as it features the same bottom friction ($n = 0.020$) as the other elevation grids.

Third, variation of marsh continuity, defined as the area of marsh at an elevation of 0.5 m above MSL divided by the total area of the marsh system (400 km^2) multiplied by 100%, was investigated to analyze surge sensitivity to a fragmented marsh compared with a continuous marsh. For example a marsh continuity of 100% indicates fully continuous marsh coverage while a marsh continuity of 0% indicates the complete absence of marsh. To achieve a non-continuous marsh, uniform channels were introduced, dividing the 20-km by 20-km square marsh feature into 16 squares of equal marsh area, elevation, and bottom friction. The small marsh segments had an elevation of 0.5 m and bottom friction of $n = 0.035$ (tall grass). Channels delineating the marsh segments had a 2.0-m depth and a bottom friction of $n = 0.020$ (sandy bottom). Fig. 1(d) depicts the marsh in both cross-section and plan view. In this study, two non-continuous marshes having continuities of 75% and 50%, fragmented by 900-m- and 2000-m-wide channels, respectively, were evaluated.

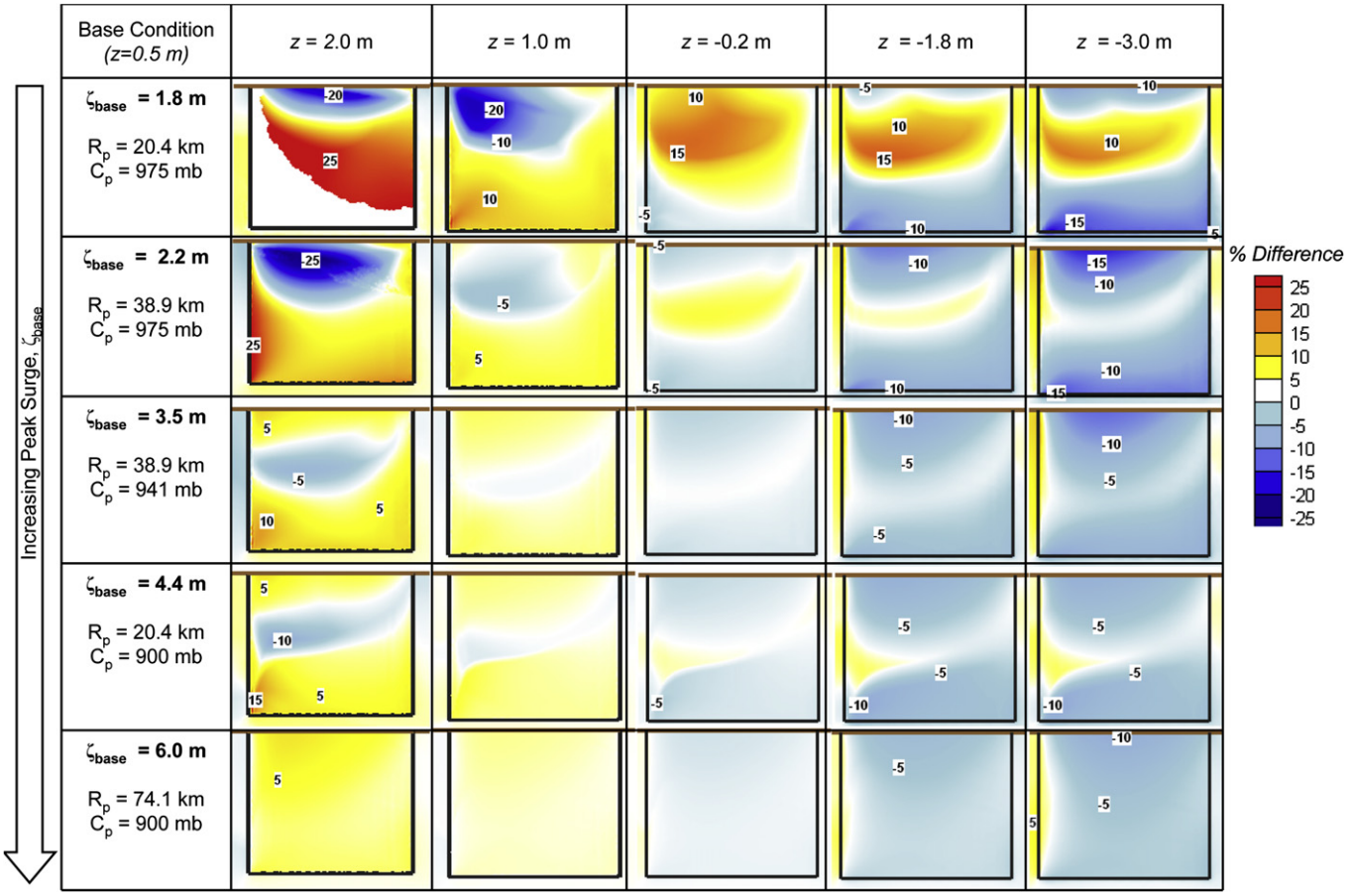

Fig. 4. Results depicting sensitivity of surge levels to marsh elevation. Plots depict percent changes in surge relative to that for a marsh elevation of 0.5 m above MSL (BASE case). Black lines represent marsh boundaries, with the coastline (landward marsh edge, shown in brown) oriented at the top of each plot. Hot colors indicate surge increases while cool colors indicate surge decreases. Rows represent each storm condition, increasing in storm-surge potential from top to bottom.

2.3. Hurricane parameters

To provide a wide range of surge conditions, a suite of storms with varying hurricane size and minimum central pressure was selected for simulation. Six synthetic hurricanes with minimum central pressures between 900 and 975 mb and scale pressure radii (R_p) (e.g., Thompson and Cardone, 1996) between 20.4 and 74.1 km were simulated. Forward speed was held constant for all storms at a typical value of 5.6 m/s (10.9 kts). The use of multiple storms having varying characteristics provides insight into the storm protection value of a marsh during a wide range of storm conditions, including both surge magnitude and surge alongshore extent (Irish et al., 2008). Large storms generate a widespread alongshore surge distribution, while smaller storms produce a more focused surge response at the coast. Table 1 lists properties of the simulated storms. To provide maximum surge levels at the marsh, storm tracks were shifted so that the marsh was located to the east of the storm by approximately one pressure radius R_p at landfall, based on the findings of Irish et al. (2009) who showed that for 75 synthetic hurricanes in the Gulf of Mexico the along-coast distance between peak surge and hurricane landfall location was between 75 and 115% of R_p. These six storms were used to evaluate the relative surge response as a function of bottom friction, marsh elevation, and marsh continuity, as discussed below.

3. Results

In the following, simulation results for varying bottom friction, elevation, and continuity are presented and compared to the BASE simulation case, where Manning's $n = 0.020$ (sandy bottom) and marsh elevation is $z = 0.5$ m. Table 1 lists the mean surge over the marsh feature, or "surge potential" (ζ_{base}), and the peak along-coast surge ($\zeta_{peak\text{-}base}$, taken at the coastline) as computed on the BASE grid for each of the six hurricane conditions considered here. The base case (BASE) surge potential for the six storms ranges from $\zeta_{base} = 1.8$ to 6.0 m. The surge results for the BASE case indicate that a range of hurricane surge conditions are considered. The relative gradient in surge distribution across the marsh for the BASE case is dictated by storm size, and is indicated by the ratio $\zeta_{peak\text{-}base}/\zeta_{base}$, which has values of about 1.50, for small storms with relatively large changes in peak surge elevation across the marsh feature, to about 1.25, for large storms with relatively small changes in peak surge elevation across the marsh feature. Wave setup contributes on the order of 0.1 and 0.5 m to the surge level on the marsh feature, with highest contributions generally seen over the seaward half of the marsh feature (Loder, 2008; Loder et al., 2009). The relative reduction in wave setup contributions at the coast is most likely attributed to the discontinuity in wave setup between the marsh feature and adjacent shorelines, results in release of wave-induced floodwaters to the sides of the marsh.

3.1. Influence of bottom friction

Total surge levels generally decrease with increasing bottom friction. Fig. 2 provides percent difference plots with respect to surge generated on the BASE bottom-friction case (Manning's $n = 0.020$), relating surge response to changes in bottom friction.

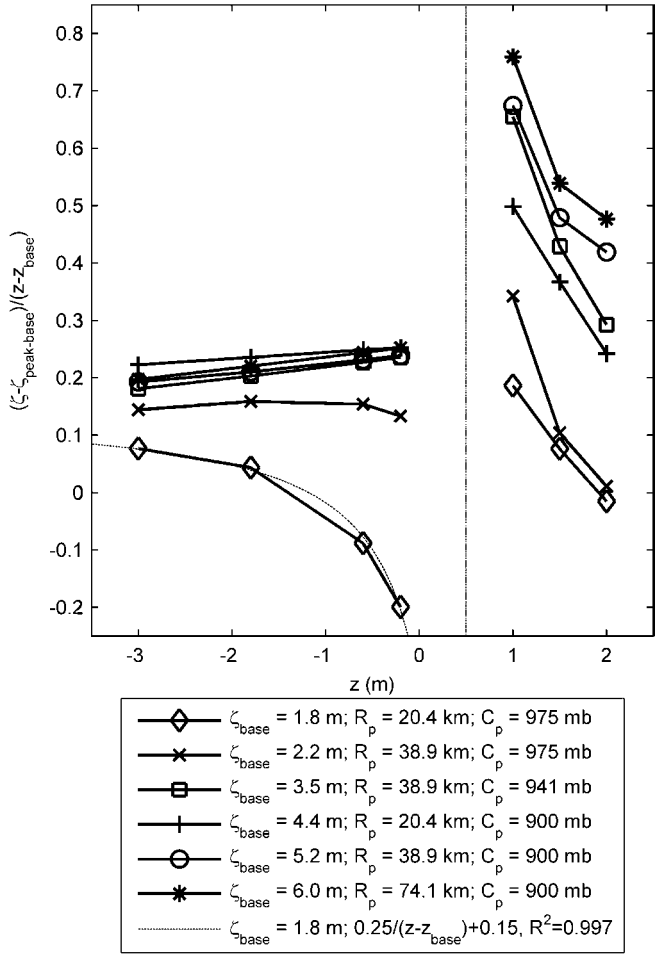

Fig. 5. Change in peak surge at the coast normalized by change in marsh elevation as a function of marsh elevation. Reference elevation (z_{base}) is 0.5-m above MSL, and $\zeta_{peak\text{-}base}$ is the corresponding peak along-coast surge for this reference elevation (BASE case).

Results are presented in order of increasing surge potential, where surge potential refers to the spatial average of peak surge within the square marsh feature for the BASE marsh case, providing a metric to classify storms according to the amount of surge they induce. As shown in Fig. 2, when Manning's n is increased from 0.020 to 0.035, a decrease in peak surge levels of 35% is observed for the storm of lowest surge potential ($\zeta_{base} = 1.8$ m). For the same storm (indicated on the first row of graphics in Fig. 2), surge levels decrease further, reaching a 50% surge decrease for a Manning's n of 0.050, and ultimately reaching a 70% surge decrease for the upper bound value of Manning's friction coefficient ($n = 0.300$). As ζ_{base} increases, bottom friction generally has less impact on peak surge levels, due to the fact that the bottom stress term is inversely proportional to depth (see Eq. (5)). There is one exception to this generalization: when comparing the storms of 3.5- and 4.4-m surge potential (third and fourth rows of graphics in Fig. 2), it is evident that the storm of higher surge potential shows a greater reduction in peak surge levels. This is a deviation from the overall increased sensitivity to changes in bottom friction due to decreased surge potential (as noted in all other results presented in Fig. 2). For example, the 4.4-m surge potential event results in surge decreases of 10%, 25%, and 50% for Manning's n of 0.035, 0.050, and 0.075, respectively. The storm of next-lowest surge potential ($\zeta_{base} = 3.5$ m) results in 5%, 15%, and 40% decreases in surge for the same respective Manning's n cases. The storm of 4.4-m surge potential features a pressure radius of 20.4 km and a minimum pressure of 900 mb, while the storm of 3.5 m has a pressure radius of 38.9 km, and minimum pressure of 941 mb. This suggests that storm size, which drives the alongshore distribution of surge (Irish and Resio, in press), is an additional factor contributing to the marsh's ability to reduce storm surge. Here, the larger, weaker storm produces a surge magnitude along the coast that varies slowly, resulting in relatively low gravity-driven currents, and, consequently, relatively less damping by bottom friction than for the stronger, smaller storm. Therefore, surge sensitivity to bottom friction (in terms of percent differences) is primarily affected by total water depth (ζ_{base}), and secondarily affected by the alongshore distribution of surge.

In alongshore areas to the sides of the marsh (where bottom friction is held constant at $n = 0.020$ for all conditions, not shown in Fig. 2), changes in surge are limited to ±10%. At hurricane landfall, flow is predominantly oriented from east to west (shore-parallel) due to the counterclockwise flow of winds around the core of the storm. As surge propagating in this direction experiences frictional resistance within the marsh, the flow is slowed, and a slight buildup of water levels (with respect to the sandy bottom condition where Manning's $n = 0.020$) is noted along the eastern edge of the marsh. Accompanying the increase in surge east of the marsh is a decrease in surge to the west of the marsh, also caused by the decreased flow within the marsh. In this way, the marsh acts similarly to a shoreline protrusion, causing shadowing to the west and a buildup of surge to the east. As the hurricane moves northward, winds transition from easterly to westerly. Surge waters react accordingly with a change in flow direction, flowing first to the west then to the east. This reverses the previously mentioned buildup and shadowing effect. Therefore, as the hurricane is positioned landward of the marsh (to the north), there is a water level increase to the west and a decrease to the east. This translates to changes in the peak water levels (maximum water surface elevation observed at each node point at any given time step). In all cases, peak water levels increase southeast of the marsh by no more than 5%. Decreases in peak surge of up to 10% are noted to the west of the marsh for most simulated cases.

Fig. 3 presents percent reductions in surge along the coast due to increased bottom friction for all six storm events. As shown in the lower lines in Fig. 3, up to a Manning's n of 0.075, storms of low ζ_{base} are associated with the greatest reductions in surge levels at the coast. Storms of moderate ζ_{base} (middle lines) result in the greatest decreases due to increases in bottom friction beyond a Manning's n of 0.075. Storms of greatest ζ_{base} (upper lines) indicate a relationship between maximum surge reduction and bottom friction that is overall less sensitive to increasing bottom friction.

3.2. Influence of marsh elevation

Fig. 4 depicts the surge response to increasing depths in terms of percent differences, with respect to the $z = 0.5$ m elevation case (BASE). As expected, for marsh features below MSL, with negative elevations ($z < 0$), simulation results generally show that decreases in marsh elevation (or increases in depth) result in decreases in surge. This is due to the inversely proportional relationship between surge and total water depth, as shown in the momentum balance (see stress terms in Eq. (4)). Storms of high surge potential (ζ_{base} for BASE case) are shown in the lower lines of the figure, while storms of low surge potential are depicted in the upper lines. An exception to this trend is the storm of lowest surge potential ($\zeta_{base} = 1.8$ m), shown on the first line of Fig. 4. Because of the relatively high base case marsh elevation ($z = 0.5$ m above MSL) and relatively low surge potential, in this case the marsh feature remains dry initially. Thus, surge propagation into the marsh is impeded. Areas of slight surge increases (less than 5%) are also visible in the storm of second lowest surge potential, but for most other storms, a uniform decrease in

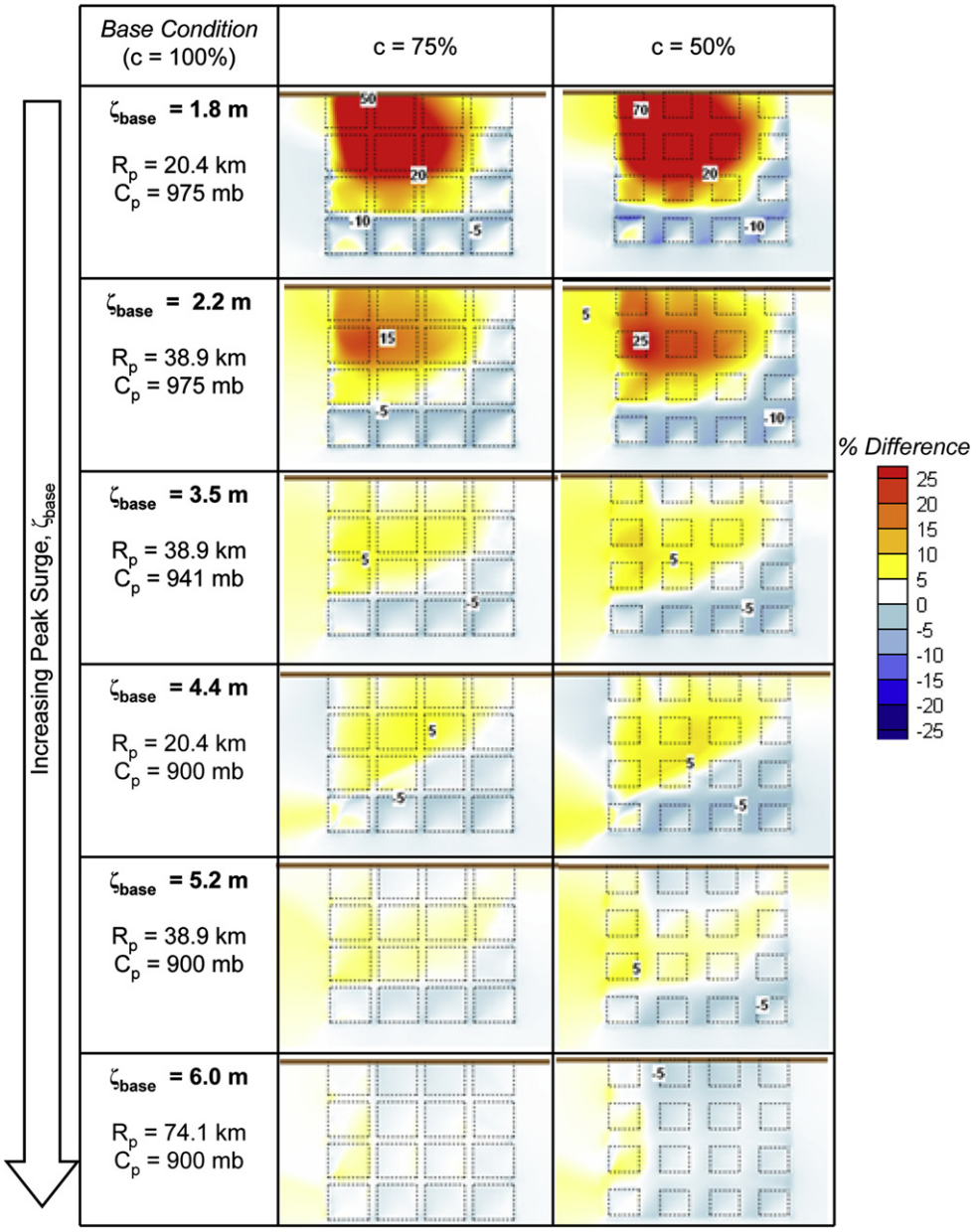

Fig. 6. Results depicting sensitivity of surge levels to marsh continuity. Plots depict percent changes in surge from a marsh having a continuity of $c = 100\%$ (BASE case). Black lines represent marsh boundaries, with the coastline (landward marsh edge, shown in brown) oriented at the top of each plot. Hot colors indicate surge increases while cool colors indicate surge decreases. Rows represent each storm condition, increasing in storm-surge potential from top to bottom.

surge is noted within the marsh. Surge at the coast is increased by no more than 10% for the marsh elevations of 0.2 and 0.6 m below MSL. As marsh elevation is further lowered to 1.8 and 3.0 m below MSL, surge decreases along the coast by as much as 10% are observed. Decreases in coastal surge levels are most substantial for the storm of second lowest surge potential ($\zeta_{base} = 2.2$ m). Associated with this storm are decreases in surge at the coast of as much as 15% for a marsh lowered to a depth of 3.0 m.

A three-part effect is seen within the marsh due to lowered marsh elevation. In most of the simulations (particularly those of moderate to low surge potential), surge is: 1) decreased along the coastline (landward edge of marsh), 2) increased within the marsh, and 3) decreased along the seaward edge of the marsh. Areas of lowered peak surge along the landward and seaward edge of the marsh are a result of the inverse relationship between surge and depth. The increased peak surge within areas central to the marsh is a result of increased conveyance of water across the marsh boundary due to lowered marsh elevation. This three-part effect is most dramatic in storms of low surge potential. For example, from the coastline to the edge of the marsh, surge is decreased by 10%, increased by 10%, and once again decreased by 15% due to a lowered marsh elevation 3.0 m below MSL in the case of the storm of lowest surge potential ($\zeta_{base} = 1.8$ m). Surge levels become less sensitive to lowered bathymetry as surge potential increases.

For marsh features above MSL, with positive elevations ($z > 0$), the surge response is highly sensitive to surge potential. For larger surge events, surge at the coast increases, with respect to the BASE case, with increasing surge due to the relatively shallow region which develops well before the time of peak surge. Surge near the coast increases by as much as 5% for these higher-elevation

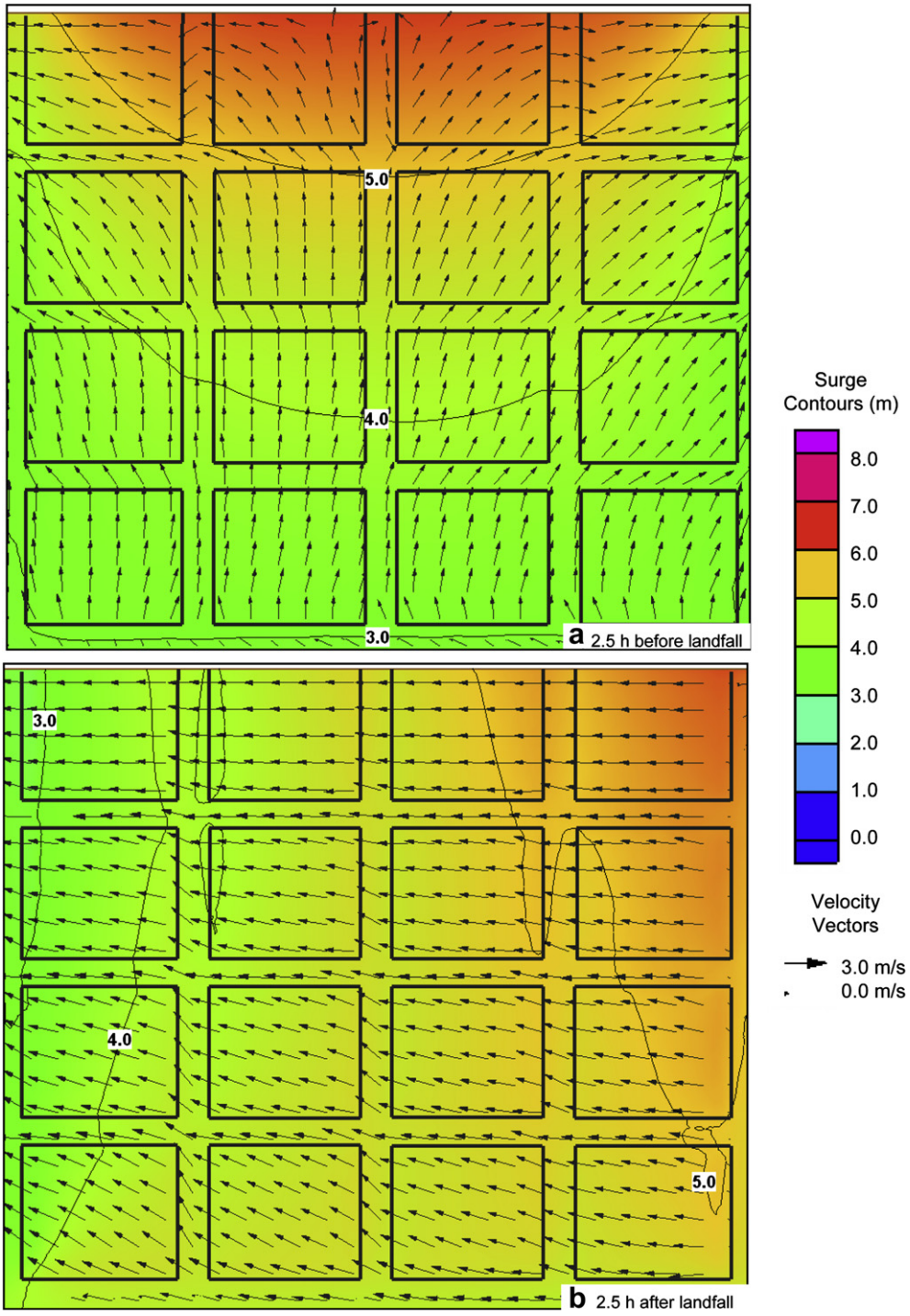

Fig. 7. Instantaneous water surface elevation and depth-integrated velocity vectors for 2.5 h before (a) and 2.5 h after (b) hurricane landfall (Storm 1) for the $c = 75\%$ marsh configuration.

configurations. However, for smaller surge events, surge at the coast generally decreases with respect to the BASE case, due to the limited duration over which the elevated feature is inundated. Surge near the coast is reduced by 5–25% due to the marsh feature being above surge level during a large portion of the time of storm passage.

Fig. 5 shows the relative change in peak surge at the coast, with respect to peak surge when the marsh is 0.5 m above MSL ($\zeta_{\text{peak-base}}$), normalized by change in marsh elevation over the range of $-3 \leq z \leq 2$ m. For elevations below MSL ($z < 0$), this figure shows that when change in total depth is substantial, as for the case of lowest surge potential, $\zeta_{\text{base}} = 1.8$ m, the relative change in surge is sensitive to change in mean depth and increases as mean depth decreases such that peak surge can be described as a linear function of $(z - z_{\text{base}})^{-1}$; where this function can be considered a measure of the relative importance of depth in the stress terms in Eq. (4). This linear function of $(z - z_{\text{base}})^{-1}$ is shown on Fig. 5 for the storm of lowest surge potential. This trend is also weakly exhibited for the case when $\zeta_{\text{base}} = 2.2$ m. However, as surge potential increases further, relative change in peak surge is only weakly-dependent on

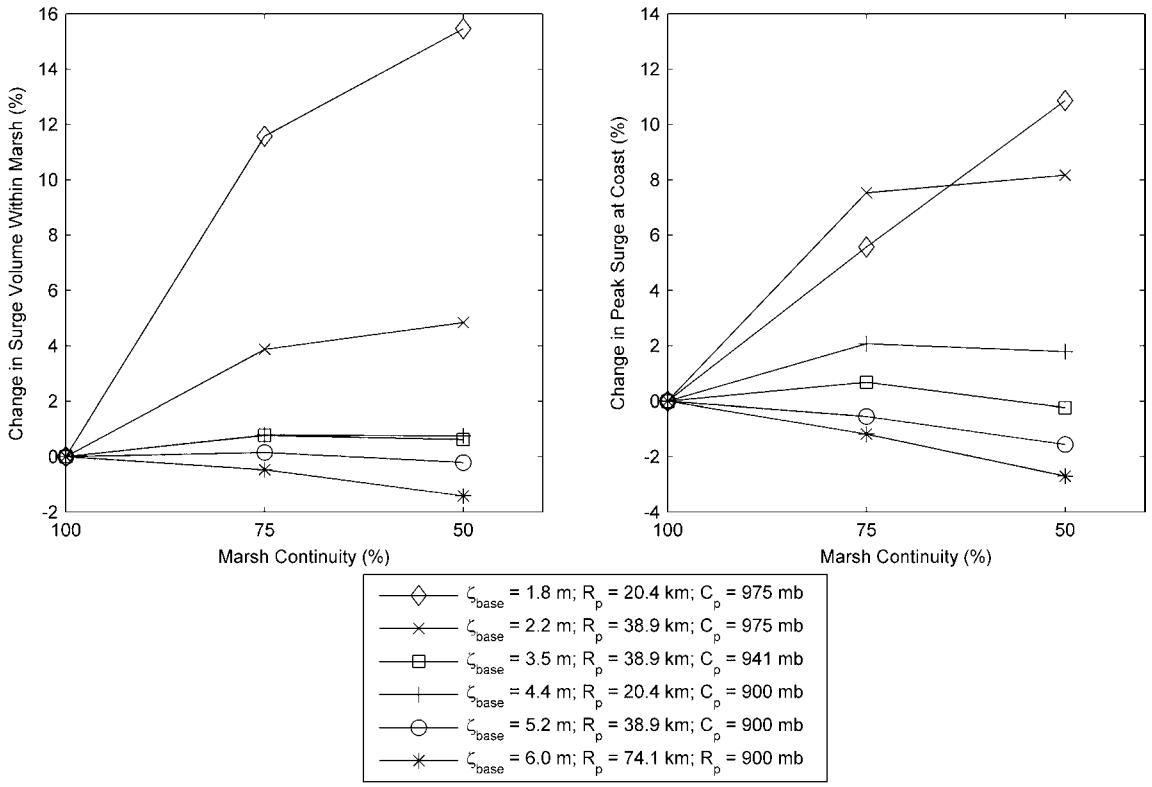

Fig. 8. Change in surge volume within the marsh (left) and change in peak along-coast surge (right) due to decreased marsh continuity.

$(z - z_{base})^{-1}$. When bed elevation is above MSL ($z > 0$), all but the storm of smallest surge potential exhibit an increase in surge, with respect to the BASE case, which can also be described as a linear function of $(z - z_{base})^{-1}$. Since in this elevation regime the marsh feature is initially dry and gradually becomes submerged over the duration of the storm, relative change in peak surge at the coast is strongly dependent on the term $(z - z_{base})^{-1}$. For the storm with smallest surge potential, peak surge at the coast decreases slightly, with respect to the BASE case; this is attributed to the relatively long duration that the marsh feature remains dry before storm landfall.

3.3. Influence of wetland continuity

Changes in surge due to increased marsh continuity, shown in Fig. 6, are a function of conveyance of water into and out of the marsh. The relative impact of marsh continuity couples the relative influence of change in depth on surge generation (see stress terms in Eq. (4)) and the relative influence of bottom friction (see bottom stress term in Eq. (4)) while changing flow pathways via channelization. For a decreased marsh continuity of $c = 75\%$, coastal surge increases by as much as 50% in the case of the storm of lowest surge potential ($\zeta_{base} = 1.8$ m). A further reduction in continuity to $c = 50\%$ results in a 70% increase in peak surge at the coast. Increases in peak surge along the coast are a result of the transmission of water through the marsh channels (Fig. 7). As marsh channel width increases continuity further decreases, resulting in greater conveyance of water into the coastal boundary of the marsh. To show this process, peak water surface elevation and depth-integrated velocity vectors 2.5 h before hurricane landfall are presented in Fig. 7(a). While the flow field is different in the case of real vegetation, the depth-integrated velocity field gives a qualitative indication of general flow patterns during hurricane passage. Wider channels within the marsh also allow water to flow out of certain areas of the marsh, as depicted in Fig. 7(b), at 2.5 h after hurricane landfall. In comparing Fig. 7(a) and (b), it can be seen that while the storm is approaching, water is being conveyed through the marsh, from east to west. After storm landfall, outward flow is observed, diverging from the marsh's center to the east and west. This is also evident in the decreased peak surge along the seaward edge of the marsh, especially prominent in the storm of lowest surge potential (first line of Fig. 6). In this scenario, a 5–10% decrease in surge is noted within marsh channels due to the shifting of surge from the seaward marsh boundary to the landward marsh boundary. As surge potential increases, these decreases become less pronounced.

While storms of low surge potential induce an increase in coastal surge levels with decreasing marsh continuity, an opposite effect is associated with the storms of high surge potential. In these cases, surge decreases at the coast by as much as 5% in the case of $c = 50\%$ continuity for the storm of highest surge potential ($\zeta_{base} = 6.0$ m). This is a result of increased conveyance within the marsh, allowing an outflow of surge from the marsh during times of peak surge. Nevertheless, increases in peak surge are still noted within the marsh due to channeling from the seaward to central areas of the marsh.

The relationship between marsh continuity and volume of surge (total volume of water stored within the marsh due to peak water levels) within the marsh is depicted in Fig. 8 (left pane). A drastic increase in surge volume within the marsh is noted for the storm of lowest surge potential, by more than 15% when $c = 50\%$. However, with increasing surge potential, marsh continuity has a less significant effect on surge volume. For the storm of highest surge potential (lower line in Fig. 8, left pane), surge volume within the marsh decreases slightly with decreasing marsh continuity, up to 2%, indicating an outward flow dominating at times of peak surge. This indicates that segmented marshes have more potential for

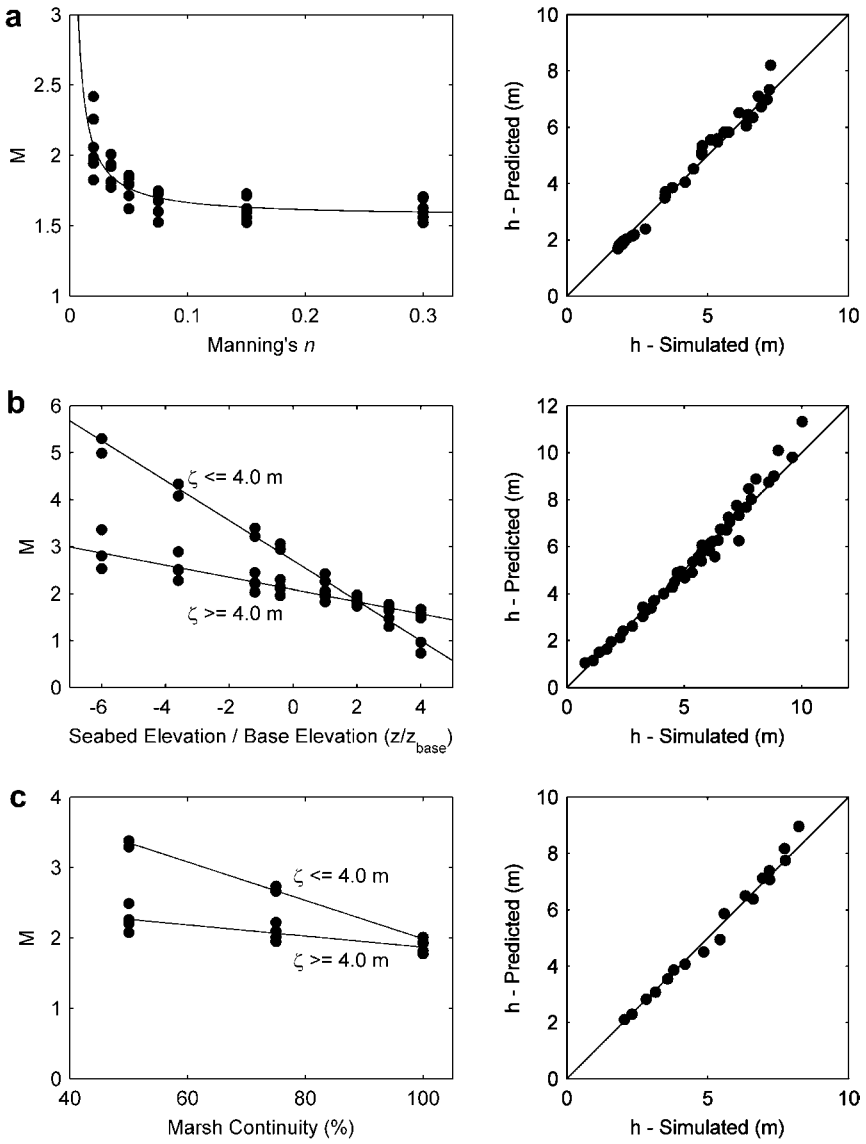

Fig. 9. Relationship between characteristic surge function M and Manning's n (a), marsh elevation (b), and marsh continuity (c) with exponential best-fit curve (left panes). Predicted values of peak water depth based on Eqs. (8)–(10) as compared with simulated peak water depth are shown in right panes.

holding back floodwaters during small storm-surge events than during large storm-surge events.

A similar effect is noted for changes in peak surge at the coastline due to decreased marsh continuity. As presented in Fig. 8 (right pane), peak surge at the coast increases substantially (5–10%) with decreasing marsh continuity for the low potential storms (as indicated by the upper two lines). However, as surge potential increases to storms of intermediate surge potential, continuity has a negligible effect on surge at the coast. For the storms of highest surge potential, a small decrease in peak surge at the coast is observed (lower two lines of Fig. 8, right pane).

4. Discussion

The data were further analyzed to develop relationships for estimating the surge response at the coast as a function of marsh bottom friction, elevation, and continuity.

Results provide an indication of the value of marshes for storm-surge reduction. It is shown that the relative impact of bottom friction decreases with increasing ζ_{base}. Here, the simulation results were reviewed to develop a series of relationships for estimating the relative impact of vegetation on surge response. To develop an equation based on Manning's n and storm parameters, peak flood depths from ADCIRC simulation results were plotted based on the linear relationship between ζ normalized by the hurricane's central pressure deficit (Δp) and R_p, as presented in Irish et al. (2008) for an idealized continental shelf of uniform 1:1000 slope without a marsh feature:

$$\zeta/\Delta p = m_s R_p + b_y \tag{6}$$

where the slope $m_s = 1.34 \times 10^{-4}$, and the y-intercept $b_y = 0.02511$. Using Eq. (6), a characteristic dimensionless surge function, M, can be developed:

$$M = (h/\Delta p)/(m_s R_p + b_y) \tag{7}$$

In this equation, total depth (h) replaces the peak surge (ζ) in Eq. (6). This substitution is justified as peak surge referenced by Irish et al. (2008) is based on peak surge at the coastline of an idealized

grid, where the total depth equals peak surge (ζ). Fig. 9 (a, left) presents this parameter as a function of Manning's n for all 36 bottom-friction and storm condition scenarios. The best-fit curve to these data (Fig. 9a, left) yields an equation for peak water depth at the coast as a function of marsh Manning's n and hurricane parameters (Δp and R_p):

$$h = 0.01017 n^{-1} \Delta p (m_s R_p + b_y) \quad (8)$$

Fig. 9 (a, right) depicts peak water depths observed through ADCIRC simulations compared with peak water depths calculated through Eq. (8). Surge predicted by Eq. (8) has an R^2 value of 0.985 and a root-mean-square error in surge prediction of 0.27 m, with respect to the numerical data used to derive this equation.

To condense the simulation results for surge response to changing marsh elevation, the characteristic surge function in Eq. (7) is revisited. As shown in Fig. 9 (b, left), two similarly scaled data sets emerge according to peak surge, one class for high surge events ($\zeta > 4$ m) and another class for lower surge events ($\zeta \leq 4$ m). Best-fit lines through these two surge classes yield the following relationship between peak water depth at the coast and marsh-feature elevation and hurricane meteorological parameters:

$$h = (0.8508z + 2.701)(m_s R_p + b_y)\Delta p \quad \text{if } \zeta \leq 4.0 \text{ m} \quad (9a)$$

$$h = (0.2580z + 2.087)(m_s R_p + b_y)\Delta p \quad \text{if } \zeta > 4.0 \text{ m} \quad (9b)$$

The accuracy of these equations in predicting peak surge as simulated by ADCIRC is shown in Fig. 9 (b, right). The comparison has an R^2 value of 0.978 and a root-mean-square error in surge prediction of 0.39 m, with respect to the numerical data used to derive this equation.

Following the approach used to develop Eqs. (8) and (9), a relationship between marsh continuity and estimated peak surge was developed. Fig. 9 (c, left) presents the characteristic surge function (M) versus marsh continuity for all hurricane simulations. As with marsh elevation, two classes of surge response are evident, yielding the following relationship for peak water depth at the coast based on storm parameters and marsh continuity:

$$h = (-0.02727c + 4.715)(m_s R_p + b_y)\Delta p \ \text{ if } \zeta \leq 4.0 \text{ m} \quad (10a)$$

$$h = (-0.007973c + 2.662)(m_s R_p + b_y)\Delta p \ \text{ if } \zeta > 4.0 \text{ m} \quad (10b)$$

The accuracy of these relationships is illustrated in Fig. 9 (c, right), with an R^2 of 0.986 and a root-mean-square error in surge prediction of 0.28 m, with respect to the numerical data used to derive this equation. Eqs. (8)–(10) provide a means to simplify estimating the relationship between coastal vegetation and hurricane surge. They also serve as a way to quickly estimate the relative impact of marsh degradation on surge response. However, the above relationships do not consider the relative influence on surge of storm forward speed and approach angle or marsh planform shape.

5. Conclusions

Due to global sea-level rise, land subsidence, manmade canal construction, and land development, coastal wetlands are at risk of degradation. Surge response to wetland degradation is complex and often associated with an increase in coastal storm-surge risk levels. The idealized numerical investigation discussed here generally indicates that vegetated coastal regions indeed have potential to reduce hurricane surge. Specifically, bottom friction, marsh elevation, and marsh continuity have a definite and wide-ranging effect on peak surge levels. Increased bottom friction results in decreases in storm-surge levels, particularly for cases of low to moderate levels of storm surge (less than 2.0 m of peak surge). The lowering of marsh elevation generally induces a decrease in surge levels due to the inverse proportional relationship between surge and total depth. While the segmentation, or reduction of marsh continuity, results in increased coastal surge levels for low to moderate surge potential events, slight decreases in surge are expected for high surge potential events. In some cases, a comparable degree of surge protection may be provided by both a continuous and non-continuous marsh. On the other hand, care should be taken when planning marsh restoration, since a rise in elevation may lead to larger surge levels, particularly during severe surge events.

While Eqs. (8)–(10) were developed using idealized simulations and by making simplified assumptions regarding the vegetated response, they can be used to give a relative indication of the benefit of marshes for surge reduction. However, for more detailed applications, evaluation of these relationships should be carried out by to quantify their performance with respect to real measurements. Though approximate, these relationships assist in understanding the storm protection value of a proposed or existing coastal wetland, and may provide an approximation of the relative impact of marsh degradation and restoration in terms of coastal storm protection. Ultimately, the potential of wetlands to attenuate surges is dependent not only on wetland characteristics evaluated here, but also on the surrounding coastal landscape and the strength and duration of the storm forcing.

Acknowledgements

All work was funded by the US Army Engineer Research and Development Center and the Louisiana Coastal Area Science and Technology Program through grant number C08-00010. The use of trade names does not constitute an endorsement in the use of these products by the US government.

References

Cardone, V.J., Greenwood, C.V., Greenwood, J.A., 1992. Unified Program for the Specification of Hurricane Boundary Layer Winds over Surfaces of Specified Roughness. Contract Report CERC-92-1. US Army Corps of Engineers, Vicksburg, MS, 131 pp.

Chow, V.T., 1959. Open Channel Hydraulics. McGraw-Hill Book Co, NY, 680 pp.

Fritz, H.M., Blount, C., Sokoloski, R., Singleton, J., Fuggle, A., McAdoo, B.G., Moore, A., Grass, C., Banks, T., 2008. Hurricane Katrina storm surge reconnaissance. Journal of Geotechnical and Geoenvironmental Engineering, American Society of Civil Engineers 134, 644–656.

Green, J.C., 2005. Modeling flow resistance in vegetated streams: review and development of new theory. Hydrological Processes 19, 1245–1259.

Irish, J., Cialone, M., Resio, D., 2009. A surge response function approach to coastal hazard assessment, part II: quantification of spatial attributes of response functions. Natural Hazards. doi:10.1007/s11069-009-0381-4.

Irish, J.L., Resio, D.T. A hydrodynamics-based surge scale for hurricanes. Ocean Engineering, in press, doi:10.1016/j.oceaneng.2009.07.012.

Irish, J.L., Resio, D.T., Ratcliff, J.J., 2008. The influence of storm size on hurricane surge. Journal of Physical Oceanography 38, 2003–2013.

Kadlec, R.H., 1990. Overland flow in wetlands: vegetation resistance. Journal of Hydraulic Engineering 116, 691–706.

Kouwen, N., Li, R., Simons, D.B., 1981. Flow resistance in vegetated waterways. Transactions of the American Society of Agricultural Engineers 81, 685–690.

Loder, N.M., 2008. An Evaluation of the Potential of Coastal Wetlands for Hurricane Surge and Wave Energy Reduction. Master's thesis. Texas A&M University, College Station, TX, 99 pp.

Loder, N., Cialone, M., Irish, J., Sleath, A., 2009. Reducing storm impacts through marsh restoration: idealized evaluation of wave condition sensitivity to marsh parameters. In: Proceedings of the 2008 International Conference on Coastal Engineering, vol. 2 1024–1036.

Luettich, R., Westerink, J., 2004. Formulation and Numerical Implementation of the 2D/3D ADCIRC Finite Element Model Version 44.XX. <http://adcirc.org/adcirc_theory_2004_12_08.pdf> (accessed 25.08.08).

Nepf, H.M., 2004. Vegetative flow dynamics. In: Fagherazzi, Marain, Blum (Eds.), The Ecogeomorphology of Tidal Marshes. Coastal and Estuarine Studies 59, 137–163.

Nepf, H.M., 1999. Drag, turbulence, and diffusion in flow through emergent vegetation. Water Resources Research 35, 479–489.
Peterson, C.H., Luettich, R.A., Fiorenza, M., Skilleter, G.A., 2004. Attenuation of water flow inside seagrass canopies of differing structure. Marine Ecology Progress Series 268, 81–92.
Reid, R.O., Whitaker, R.E., 1976. Wind-driven flow of water influenced by a canopy. Journal of the Waterways, Harbors and Coastal Engineering Division WW1, 61–77.
Resio, D.T., Westerink, J.J., 2008. Modeling the physics of storm surges. Physics Today 61 (9), 33–38.
Smith, J.M., 2007. Full-plane STWAVE with Bottom Friction: II. Model Overview. ERDC TN = SWWRP-07-5. US Army Corps of Engineers Engineer Research and Development Center, Vicksburg, MS.
Smith, J.M., Sherlock, A., Resio, D., 2001. STWAVE: Steady-State Spectral Wave Model User's Manual for STWAVE, Version 3.0. US Army Corps of Engineers Engineer Research and Development Center, Vicksburg, MS, 66 pp.
Tanino, Y., Nepf, H.M., 2008. Laboratory investigation of mean drag in a random array of rigid, emergent cylinders. Journal of Hydraulic Engineering 134, 34–41.
Thompson, E.F., Cardone, V.J., 1996. Practical modeling of hurricane surface wind fields. ASCE Journal of Waterway, Port, Coastal, and Ocean Engineering 122, 195–205.
USACE, 1961. Interim Survey Report: Mississippi River Delta at and Below New Orleans, Louisiana. US Army Corps of Engineers New Orleans District, New Orleans, LA.
WAMDI Group, 1988. The WAM model – a third-generation ocean wave prediction model. Journal of Physical Oceanography 18, 1775–1810.
Wamsley, T.V., Cialone, M.C., Smith, J.M., Atkinson, J.H., Rosati, J.D. The potential of wetlands in reducing storm surge. Ocean Engineering, in press, doi:10.1016/j.oceaneng.2009.07.018.
Wamsley, T.V., Cialone, M.C., Smith, J.M., Ebersole, B.A., Grzegorzewski, A.S., 2009. Influence of landscape restoration and degradation on storm surge and waves in southern Louisiana. Natural Hazards. doi:10.1007/s11069-009-9378-z.
Westerink, J.J., Luettich, R.A., Feyen, J.C., Atkinson, J.H., Dawson, C., Roberts, H.J., Powell, M.D., Dunion, J.P., Kubatko, E.J., Pourtaheri, H., 2008. A basin- to channel-scale unstructured grid hurricane storm surge model applied to southern Louisiana. Monthly Weather Review 136, 833–864.